Site-specific evaluation of safety issues for high-level waste disposal in crystalline rocks

- Final Report -

Site-specific evaluation of safety issues for high-level waste disposal in crystalline rocks

- Final Report -

Authors:

[1]Jobmann, M. (Editor)
[2]Flügge, J.
[3]Hammer, J.
[1]Herold, P.
[1]Krone, J.
[3]Kühnlenz, T.
[1]Li, S.
[1]Lommerzheim, A.
[2]Meleshyn, A.
[2]Wolf, J.

[1]DBE TECHNOLOGY GmbH, Eschenstraße 55, D-31224 Peine.
[2]Gesellschaft für Anlagen- und Reaktorsicherheit (GRS) gGmbH, Theodor-Heuss-Straße 4, D-38122 Braunschweig.
[3]Bundesanstalt für Geowissenschaften und Rohstoffe (BGR), Stilleweg 2, D-30655 Hannover

This report was produced during the R&D project: **URSEL**
(Untersuchungen zur Robustheit der Sicherheitsaussage zu HAW-Endlagersystemen in magmatischen Wirtsgesteinen)

Auftraggeber: KIT (PTKA-WTE) FKZ: 02E10750/60

Berichtsnummer: TEC-28-2015-AB

31.03.2016

The research work that is the basis of this report was funded by the German Federal Ministry for Economic Affairs and Energy (BMWi = Bundesministerium für Wirtschaft und Energie) under the contract numbers FKZ 02E10760 (DBETEC) and 02E10750 (GRS). The authors alone, however, are responsible for the contents of this study.

Table of contents

1 Introduction

In the past, German research and development (R&D) activities regarding the disposal of radioactive waste, including spent nuclear fuel, focused mainly on domal rock salt because rock salt was the preferred host rock formation. In addition, generic R&D work regarding alternative host rocks (crystalline rocks and claystones) had been performed as well for a long time but with lower intensity.

Around the year 2000, as a consequence of the moratorium on the Gorleben site, the Federal Government decided to have argillaceous rocks and crystalline rocks investigated in more detail. As Germany does not have any underground research and host rock characterization facilities, international cooperation received a high priority in the German R&D programme for high-level waste (HLW) disposal in order to increase the knowledge regarding alternative host rocks. Major cornerstones of the cooperation are joint projects and experiments conducted especially in underground research laboratories (URL) in crystalline rocks at the Grimsel Test Site (Switzerland) and the Hard Rock Laboratory (HRL) Äspö (Sweden) and in argillaceous rocks at the URL Mont Terri (Switzerland) and Bure (France).

In 2001, the topic of radioactive waste disposal was integrated into the agreement between the former Russian Ministry of Atomic Energy (Minatom, now Rosatom) and the German Ministry of Labor (BMWA), now Ministry of Economic Affairs and Energy (BMWi), on cooperation regarding R&D on the peaceful utilization of nuclear power (agreement on “Wirtschaftlich-Technische Zusammenarbeit” WTZ). The intention was to have a new and interesting opportunity for international R&D cooperation regarding HLW disposal in crystalline rocks and the unique possibility to perform site-specific work, to test the safety demonstration tools available, and to expand the knowledge to all aspects specific to these host rocks. Another motivation for joining this cooperation was the intent to assist Russian engineers and scientists in their integration into the international scientific community concerned with radioactive waste disposal and to share advanced safety approaches.

Based on the WTZ agreement, a comprehensive and versatile cooperation has been implemented in the past 13 years. Joint R&D activities and projects regarding HLW disposal in crystalline (magmatic) host rocks based on site investigation activities in the Krasnoyarsk region have been a permanent part of this cooperation. The Russian side has been led by VNIPI Promtekhnologii (VNIPI PT), while three major R&D organizations, the Federal Institute for Geosciences and Natural Resources (BGR) in Hanover, Gesellschaft für Anlagen- und Reaktorsicherheit (GRS) gGmbH in Brunswick, and DBE TECHNOLOGY GmbH (DBE-TEC) in Peine have been the permanent participants from the German side.

The corresponding joint R&D activities were pooled in the following three R&D BMWi-funded projects:

- ASTER “Requirements for Site Investigation for a HLW Repository in hard rock Formations” (2002 – 05), (Krone et al., 2005)
  Main Objective: To develop a well-justified methodological approach for site investigation and selection in the Nizhnekansk granitoid formation near Krasnoyarsk, exemplarily for the disposal of conditioned HLW sludge from formerly produced weapons-grade plutonium and vitrified HLW from reprocessing

- WIBASTA “Performance investigation of engineered and geologic barriers of a HLW repository in magmatic host rocks” (2005 – 08), (Jobmann et al., 2008)
  Main Objective: Performance analysis of the system of geologic and engineered barriers based on safety functions, exemplarily for the proposed HLW disposal facility at the Yeniseysky site

- URSEL “Site-specific evaluation of safety issues for HLW disposal in crystalline rocks” (2008 – 16)
  Main Objective: Investigation of the robustness of the safety and of the safety assessment of e repository in crystalline rocks. The proposed HLW disposal facility at the Yeniseysky site was taken as an example site.

In parallel to the bilateral R&D cooperation, the Russian R&D work has undergone a considerable evolution. In the last decade of the 20th century, site investigation activities started in various preselected regions of the Nizhnekansky granitoid formation east of Krasnoyarsk. Starting in 2003, preference was given to the Yeniseysky site, which is located several kilometres south east of the underground former production facilities for weapons-grade plutonium of the Mining Chemical Combine (MCC) at Zheleznogorsk. In the beginning, these investigations were performed for the eventual disposal of conditioned HLW sludge from weapons-grade plutonium production and vitrified HLW from reprocessing of the planned reprocessing plant RT-2 at Zheleznogorsk. Recently, priority has been given to so-called class 1 waste (HLW) of the existing reprocessing plant RT-1 in Mayak and other so-called class 2 waste; i.e. long-lived radioactive waste that according to the latest IAEA[1] recommendations for waste classification is called intermediate level waste (ILW). In addition, in the course of various disposal concept optimizations, modifications have been taken into account; e.g., the lengths, diameters, and spacing of disposal boreholes have been modified several times.

This report provides a condensed overview of the corresponding manifold site-specific safety investigations regarding HLW disposal in crystalline host rocks. The investigations were carried out by BGR, GRS, and DBE TECHNOLOGY GmbH in the last years in close cooperation with VNIPI PT and other Russian organizations involved in the investigation of the Yeniseysky site near Zheleznogorsk in the Krasnoyarsk region.

The investigations have been performed at different times based on different states of knowledge on the site characteristics and different states of the disposal concept. Because both are still evolving, it is practically impossible to completely exclude inconsistencies between the different parts of the safety investigations. However, most of these inconsistencies could be accepted for the purpose of the investigations, which focus on methodological and general safety aspects.

The next two chapters summarize the state of knowledge available regarding the characterization of the considered site Yeniseysky (chapter 2, work package 1) and regarding the characterization of the relevant host rocks (chapter 3, work package 2 and 3). They are followed in chapter 4 (work package 2) by an overview of the waste data available and in chapter 5 by a description of the most current repository concept (work package 4).

The evaluation of the barrier performance in chapter 6 as core part of the safety investigations performed is divided into three parts: The performance of the geotechnical and technical barriers (work package 4), the performance of the geologic barrier (work package 5), and the sensitivity analysis (work package 5).

A brief summary of the investigation results and recommendations for necessary future investigations are provided in the concluding chapter 7 (work package 6).

[1] International Atomic Energy Agency

2 Characterization of the site considered

Overviews about the geological exploration of the Yenisey region since the beginning of the 1990s and the geological conditions at the Yeniseysky site were given in Krone et al. (2005) and Jobmann et al. (2008). In the last 3 to 4 years, new geological and geophysical investigations were provided by Krasnoyarskgeologiya. They include 12 exploration boreholes, up to 600 – 700 m deep, 4 hydrogeological boreholes each 200 m deep, square geophysical surveying (magnetic survey 100 m x 10 m – 6,2 km^2; vertical electrosounding and seismic survey – 6,2 km^2) and geophysical logging in boreholes (natural radioactivity, density, electric properties, magnetic susceptibility, inclinometry, flowmetry, resistivimetry). These investigations have enhanced the knowledge about the geology at the site and about the barrier properties of the potential host rocks (Ozerskiy, 2012; Ozerskiy & Karaulov, 2012). Basing on new geologic-geophysical data (first of all on seismic and gravimetric data), a new geological 3D model will be prepared by responsible Russian institutions, which will more precisely show the geologic-tectonic structure of the Yeniseysky site as illustrated in Jobmann et al. (2008).

2.1 Regional geological position of Yeniseysky site

The Yeniseysky site is situated in South Siberia, nearly 50 km from city Krasnoyarsk in NE direction (Fig. 2-1 and Fig. 2-2). The site lies in the southwest edge of the Siberian Shield in the area of the Angara-Kansk anticlinorium in the Yeniseysky mountain belt or Yeniseysky ridge (Fig. 2-2). It is composed of Archean to Proterozoic basement rocks, which are part of the intensively folded margin of the more than one-billion-year-old Siberian Platform. The basement rocks are covered by Quaternary rocks.

The long-term safety assessment for a planned HLW repository in this region requires a detailed exploration and modelling of the vertical and horizontal movements of the geological units in which the repository is planned to be built. The Yeniseysky area is in a region in which three geotectonic units with different histories meet (Fig. 2-2). At the present time the West Siberian platform in the west is sinking at a rate of about 6 – 15 mm/a, and the Altai-Sayan Fold Belt in the south is rising at a rate of 5 – 10 mm/a. The Siberian Platform is rising at slow rate of 0.2 – 5 mm/a. The Yeniseysky site belongs to a relatively calm geodynamic regime with individual tectonic blocks that have distinctly elevated uplift rates (Morozov et al., 2007).

Fig. 2-1: Geographical location of the studied Yeniseysky site (modified after Shabalev, 2009)

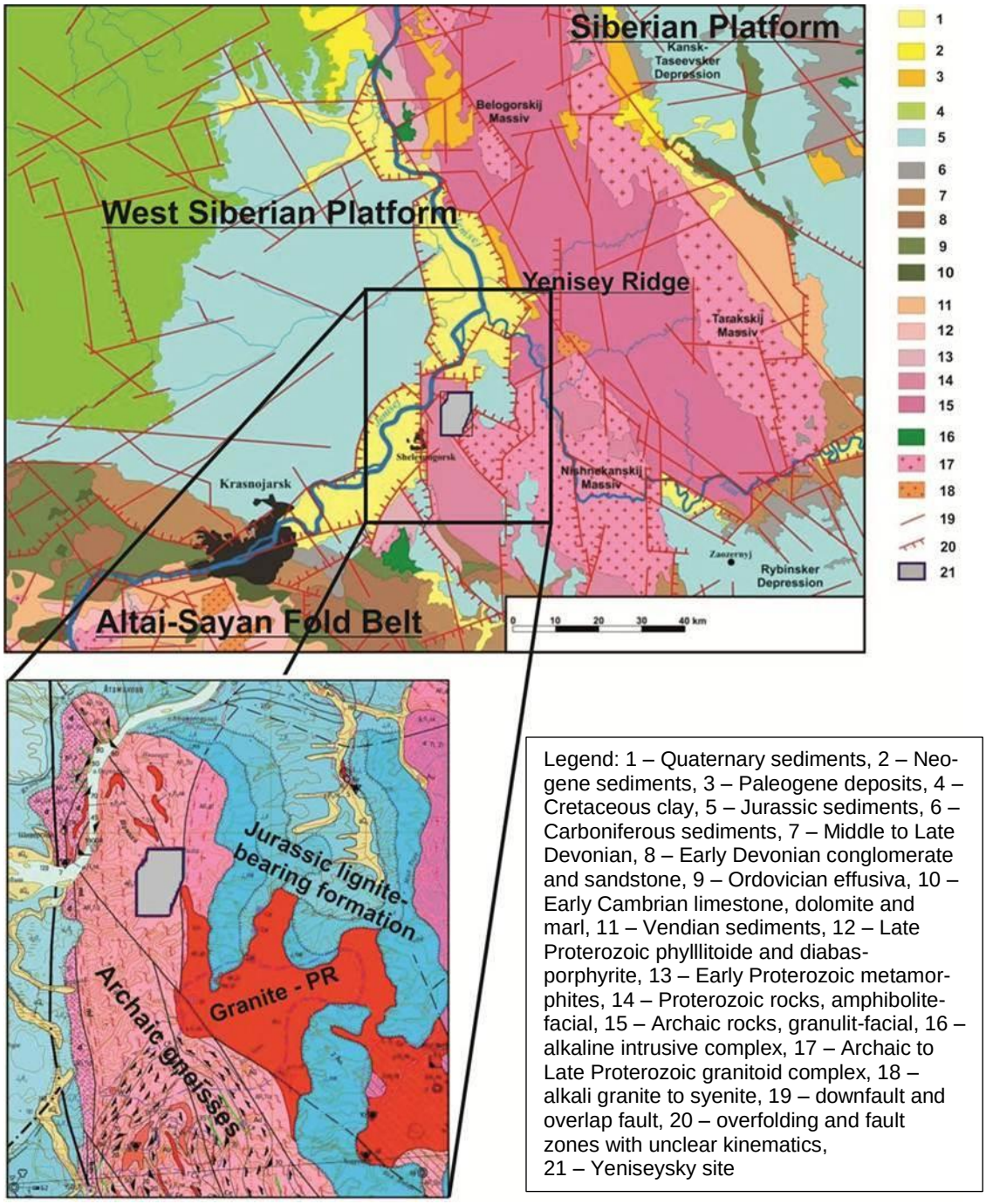

Fig. 2-2: The location of Yeniseysky site at the southwestern edge of the Siberian Platform based on Geological map of the area in the scale 1 : 750 000. Upper map from Krone et al. (2005), lower map from Ozerskiy (2013).

2.2 Relief, hydrology and climate

From a hydrological point of view the region belongs to the catchment area of Yenisey river. The density of the hydrological network is 0.45 km/km^2. The Yeniseysky site is situated on the watersheds of the rivers Bolshaja Tel and Yenisey (Fig. 2-3). The watersheds show a weakly distinct topography. The watersheds, as stable blocks, are only slightly influenced by the faults that are situated in the periphery of the blocks. Apart from any possible hazards through floods, through the binding of rivers to fault and cataclasis zones and through the ascent character of the groundwater in these regions, the river valleys are not suitable as a site for the HLW repository. In general, the relief of the site is influenced by its location in the

southern part of Yeniseysky ridge. The area between the rivers Yenisey and Kan is characterized by stepwise surface relief with relatively low vertical movements of the separate crustal blocks against one another. The height above sea level of Yeniseysky ridge varies between 110 m to 573 m (Fig. 2-3).

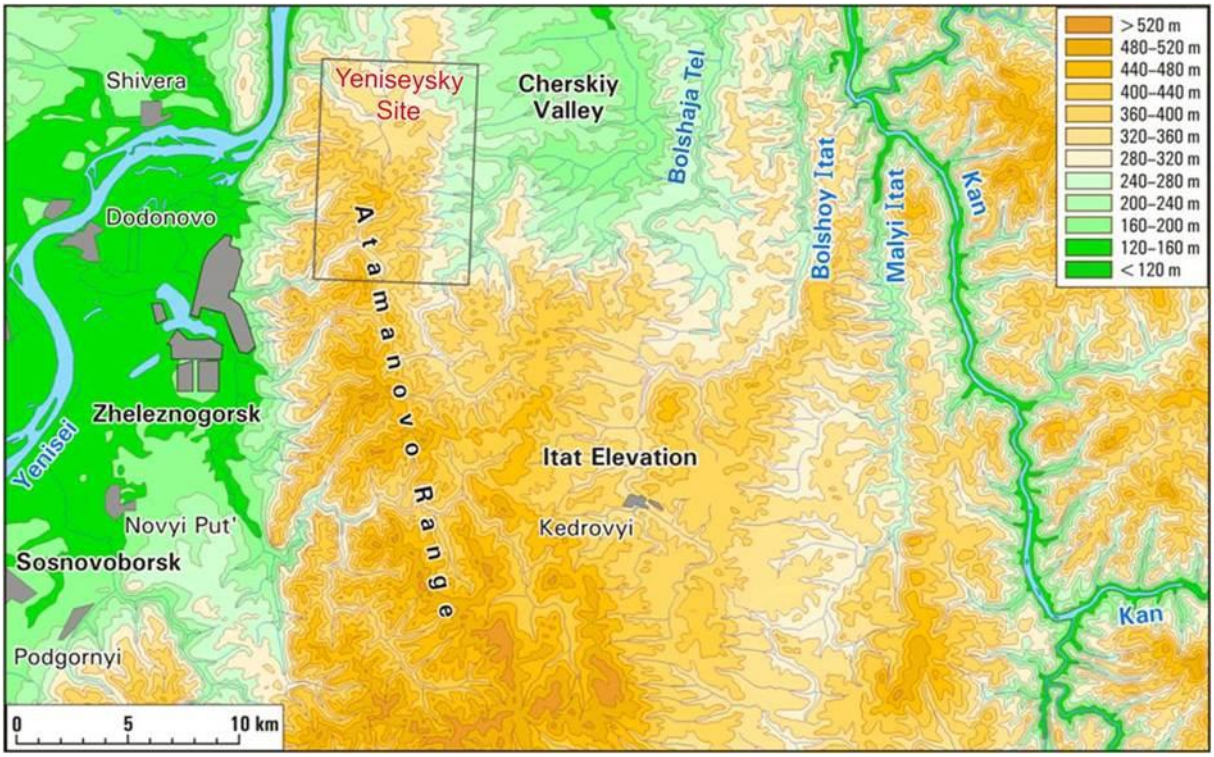

Fig. 2-3: Relief and hydrology of the study area (Shabalev, 2009)

The orientation of the river valleys is not even. The straight sections are typical for the areas with outcrops of crystalline rocks. They are interspersed with strongly meandering sections of the river that are adapting in its orientations to the crossing fault zones ("tectonic meandering"). The width of the river valleys varies from several hundred meters to 3-4 km.

The climate in the study area is continental with a long, cold winter and a short, warm summer. The average temperature in January is around -20°C to -24˚C, in July +18°C to +20˚C (Fig. 2-4). The difference in temperature between winter and summer is up to 65°C. The mean annual temperature varies between -0.6°C and -3.2˚C. There are no permafrost conditions in the study region. The soils freeze to a depth of 67-94 cm to maximal 210-300 cm. Until the end of July the soils thaw fully. Until springtime the rivers are covered by permanent ice (Anderson et al., 1993).

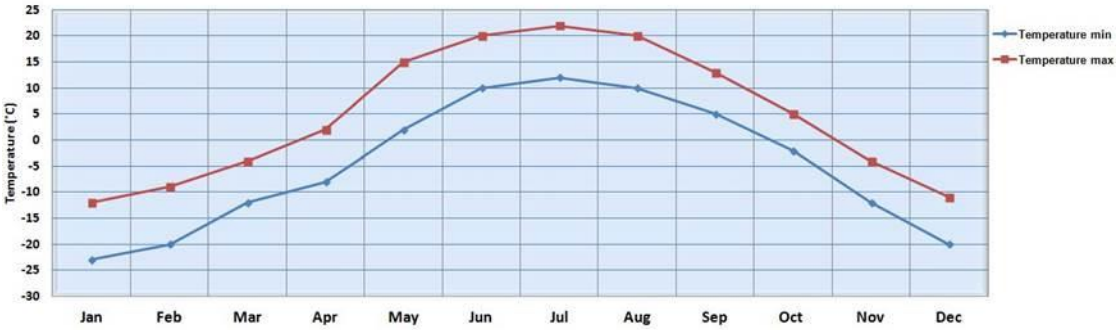

Fig. 2-4: Average minimum and maximum temperature over the year in the Krasnoyarsk region (Data source: http://www.weather-and-climate.com/average-monthly-Rainfall-Temperature-Sunshine,Krasnoyarsk,Russia)

The sea level air pressure varies during the year between 992.1 hPa in February and 974.8 hPa in July (Tab. 2-1). The highest relative moisture is registered in December and in January and amounts to 70-80 %. The lowest moisture level is in May to June (54-68 %).

Tab. 2.1: Seasonal fluctuations of the sea level air pressure in the region Krasnoyarsk (see also Jobmann et al., 2008)

	Jan	Feb	Mar	Apr	May	Jun	Jul	Aug	Sep	Oct	Nov	Dec
Air pressure (hPa)	991.7	992.1	985.6	984.4	980.4	977.1	974.8	977.9	982.0	986.9	989.1	991.5
Standard deviation (hPa)	3.4	4.1	15.5	3.1	1.7	1.5	1.3	1.2	6.2	2.2	3.7	3.9
Averaging years	23	23	23	20	21	22	21	17	21	20	21	22
Averaging period: 1971 – 1994												

The annual precipitation is 300-500 mm in average, the largest volume of which (75-80 %) falls in summer (Fig. 2-5; Anderson et al., 2011). The annual evaporation losses of up to 480-500 mm and the hydraulic properties of the near-surface layers lead to a relatively low runoff of the surface waters, which is between 2.5 to 3.0 l/(s km^2) in Proterozoic-Archaean metamorphites (Anderson et al., 1993).

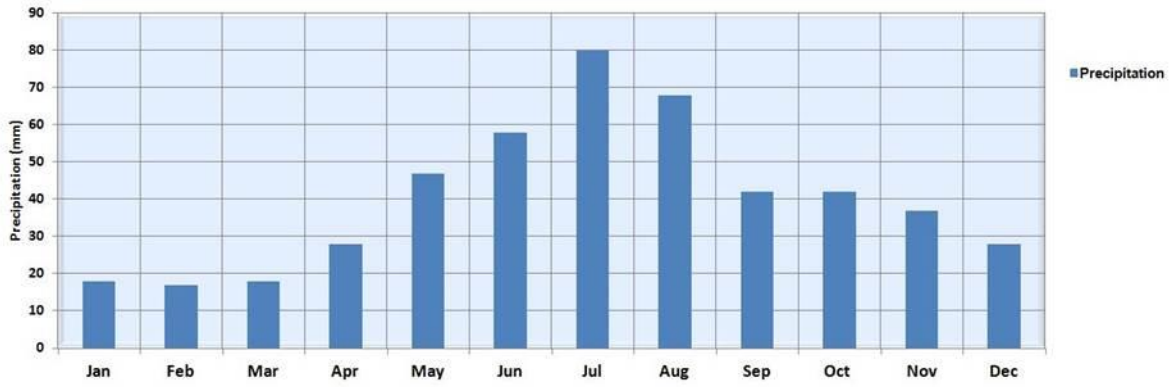

Fig. 2-5: Average monthly precipitation over the year in the Krasnoyarsk region (Source: http://www.weather-and-climate.com/average-monthly-Rainfall-Temperature-Sunshine,Krasnoyarsk,Russia)

The hydrological studies confirm the essential role of the groundwater for the recharge of the surface waters. The following hydrogeological properties are characteristic for the region:

- In a substantial part of the territory an intensive water exchange between the uppermost part of hydrogeological profile and the groundwater level can be observed. The reason for this is the effective infiltration of the precipitation
- The precipitations participate in river recharge by means of underground flow. For this reason, the chemical composition of surface water is remotely similar to the chemical composition of the precipitations
- The total mineralization of the precipitations in the region is 20 mg/l. Chloride-hydrocarbon Na-K components predominate in the water (Anderson et al., 2011).

2.3 Extension of past glaciations in central Siberia

Considering the extension of past glaciations is important for the assessment of the climatic evolution in the future and thus for the long-term safety evaluation. It is significant to consider the possible factors that could have an influence on the safety of the planned repository for HLW in the future. The study of glaciations in the investigated region in the past has a special meaning, because the glaciations can affect the hydrogeological and geochemical

evaluation in the region. The growth and retreat of ice sheets can change permeability, water turnover, groundwater pressure, groundwater flow and composition (Cedercreutz, 2004) as well as topography.

The climatic changes in the past were also evaluated in other international projects for the planning and construction of a repository in granitic rocks, among others in the Finnish project Olkiluoto. The main difference of Olkiluoto compared to Yeniseysky site regarding the evaluation of the glaciations is the geographical position (Fig. 2-1). While Scandinavia was covered four times with a thick ice sheet during the past 1 Mio. years, the region of Yeniseysky site stayed free from the ice cover.

The ice ages and connected land glaciations in Alps, Northern and Central Europe and Siberia took place not exactly simultaneously, but the ice periods overlap, so it is possible to parallelize some of them (Tab. 2.2).

Tab. 2.2: Classification of the Quaternary ice ages in the Alps, Northern Germany and central Siberia.

Ice Age in Alps	Ice Age in Northern Germany	Period, a (according to Skupin et al., 2003)	Ice Age in Siberia	Period, a (according to Artjushkov, 1969)
Wuerm	Weichselian	110.000 – 10.000	Zyrjansk	70.000 – 60.000
Riss	Saalian	280.000 – 125.000	Samarovsk	150.000 – 100.000
Mindel	Elsterian	480.000 – 320.000		
Guenz	Menapian	700.000 – 540.000		

The whole ice age history of central Siberia lies in the period 10 to 560+/-60 thousand years (Velichko, 1987). The exact spreading of glaciations in Siberia is difficult to recognize due to lack of reliable traces and difficult conditions of investigations in Siberian regions. Diverse authors postulate for the Siberian regions different glaciations with deviating period. Only two glaciations in central Siberia can be determined with certainty: the last Zyrjansk glaciation and the maximal Samarovsk glaciation (Thiel, 1951).

As centre of glaciations for central Siberia served the Norilsk Plateau and the Taimyr peninsula. The ice sheet moved from this region in the SW direction, i.e. in the direction of the investigated area (Thiel, 1951).

The last Zyrjansk glaciation in central Siberia can be parallelized with the Weichselian ice age in Europe (Tab. 2.2). According to Thiel (1951) and Svendsen et al. (2004) this glaciation was particularly poorly developed and reached barely Yenisey river (Fig. 2-6). The central Siberian platform had no closed ice sheet. The sheet was only locally developed and had only a low thickness. The exact geographical extension of this glaciation was not possible to identify (Thiel, 1951). The approximately spread of this glaciation in the period about 60 ka can be found in the works of Svendsen et al. (2004) and Mangerud et al. (2004) (see Fig. 2-6).

The maximum glaciation in central Siberia is called Samarovsk. It took place approximately synchronic to the Alps Riss or to North European Saalian glaciations (Tab. 2.2).

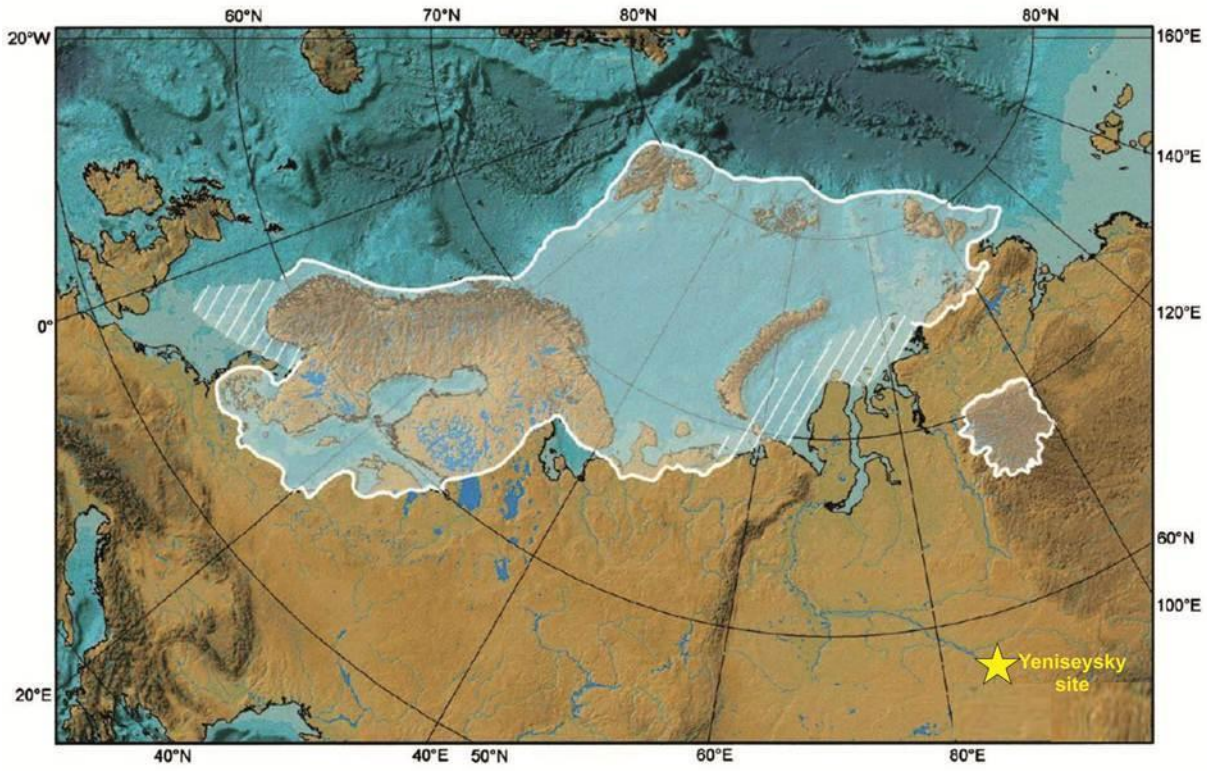

Fig. 2-6: Extension of the Eurasian ice sheet in the period 60-50 ka ago corresponds approximately to the Zyrjansk glaciation in Siberia (modified after Svendsen et al., 2004)

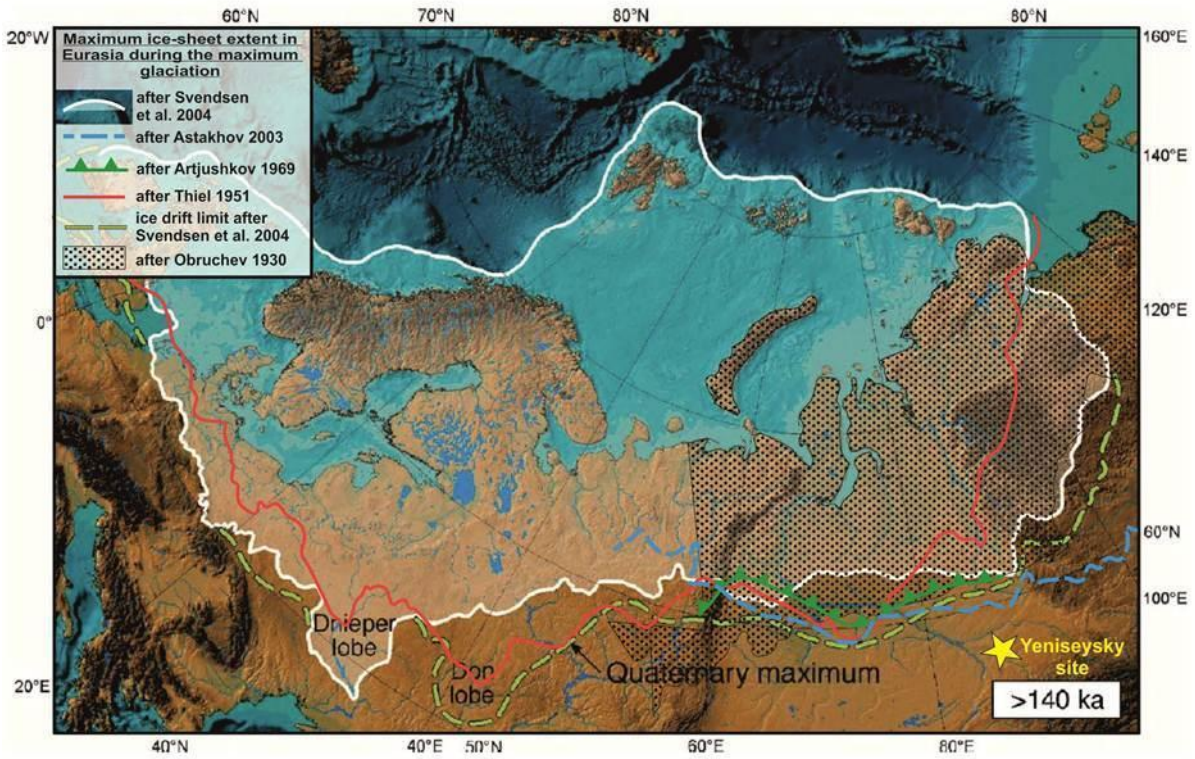

Fig. 2-7: Reconstruction of the maximum ice-sheet extension in Eurasia during the Saalian (c. 160-140 ka), corresponding to the Samarovsk glaciation in Siberia according to different authors (modified after Svendsen et al., 2004; based on Astakhov, 2003; Artjushkov, 1969; Thiel, 1951; Obruchev, 1930).

According to many authors, the maximum extension of this glaciation in central Siberia reached as far south as 60° of north latitude (Artjushkov, 1969; Thiel, 1951; Obruchev, 1930; Svendsen et al., 2004; Astakhov, 2003; see Fig. 2-7). Whereby, in the area of Yenisey the ice traces (moraine) from the North were detected only as far as 61°N. It is not clear whether the moraine material was brought by ice sheet or by the transport within the lumps of ice that were floating back with the Yenisey (Thiel, 1951). Since the investigated area is at approximately 56°15' of northern latitude, the level of the Yeniseysky site remained unattainable by a wide margin even by the maximum land glaciations. In the south of the investigated area, in the Sayan and Altai mountain regions glaciations had just a local character and did not set out the confines of the mountains (Obruchev, 1930). Therefore, the investigated area lies in a geographical position that was not influenced by the ice sheet during the past ice ages.

This overview of the past glaciation events in central Siberia leads to the assumption, that glaciations are not to be expected to reach the Yeniseysky site in the period relevant to the long-term safety assessment of a repository.

2.4 Tectonic structure and regional tectonic development

To assess the barrier properties of the geological near and far-fields, detailed information is needed about the jointing and fracturing of the potential host rocks of the planned repository and about the occurrence of regional and local fault zones in the study area.

Fig. 2-8: Left: System of main fault zones in the studied area, basing on aerial photographs, geomorphological and geophysical data (from: Shabalev, 2009). Right: Comparison of the fault zones within the 3D geological model of BGR (blue/green – rocks with high electric conductivity, orange/yellow – rocks with low electric conductivity) (from Jobmann et al., 2008)

Several regional fault zones were interpreted from the aerial photographs and the seismic, gravimetric and geoelectric data (Fig. 2-8). The available voluminous data base was partly

inconsistent and made it difficult to determine with certainty the precise position and spatial orientation of fault zones. It was assumed that only the Telsky fault (extends along the eastern edge of the area, separating it from the Jurassic sediments to the east) and the Meridional fault zone (located in the middle of the Yeniseysky area) extend to considerable depths, all other faults should reach only shallow depths and are characterized by weak geophysical anomalies (Gupalo et al., 2004a, 2007).

Moreover, the exploration experiences of the Russian institutions in similar rock massifs lead to the assumption that relatively flat dipping faults developed only to the depth of 100-150 m from the earth surface and disappear completely with increasing depths. According to Russian assumptions, steeply dipping faults reach depths of several hundred meters.

The Russian authors assume that the majority of faults has been filled by dykes and show no recent tectonic activity. The rates of relative movement of the blocks on either side of faults in the Yeniseysky area vary between 0.077 and 0.3 mm/a. Radon and helium measurements indicate no recent tectonic activity (Gupalo et al., 2007).

However, the results of latest analyses of the seismological data from six seismological stations near the investigation site do not confirm the existence of some active vertical faults that were assumed within the area earlier (Fig. 2-8, Fig. 2-9). On Fig. 2-9 is shown that the faults Baikalsky, Meridional and the great section of the Shumichinsky fault have not been confirmed. This conclusion is based also on new data from teleseismic registration of a strong earthquake (in Antarctic region, 17.11.2013, magnitude of 7.7) near the investigation site. According to these studies, there is no indication for deep reaching fault zones in the site because of missing of velocity changes in seismic waves in the site (Lukishov et al., 2014).

Systematic studies of the fracturing of rocks, the position and spatial orientation of fault zones, as well as the strain and deformation regimes have not been done, because of bad conditions of exposure in the Siberian taiga. Results of systematic structural-geological investigations of core material from exploration boreholes are not available. The comparison of such data from different methods shows distinct differences. Comparing the zones of intensive weathering (= fault zones) observed in the geoelectric data and visualized in the 3D geological model of BGR (Fig. 2-8 right; Jobmann et al., 2008) with the fault zones designated by the local exploration geologists, there are many inconsistences. The blue areas in the geological 3D model represent especially deep parts of the top surface of the gneiss complex that is only very weakly jointed/fractured (top surface of the area with a resistivity of more than 3,000 ohm·m). The comparison shows great differences, which are due to the small amount of structural data for the area and in part conflicting investigation results. A transfer of the voluminous structural results from the underground excavations of the Mining Chemical Combine (MCC) to the Yeniseysky area can be done only with much uncertainty; e. g. possibly another tectonic block is present.

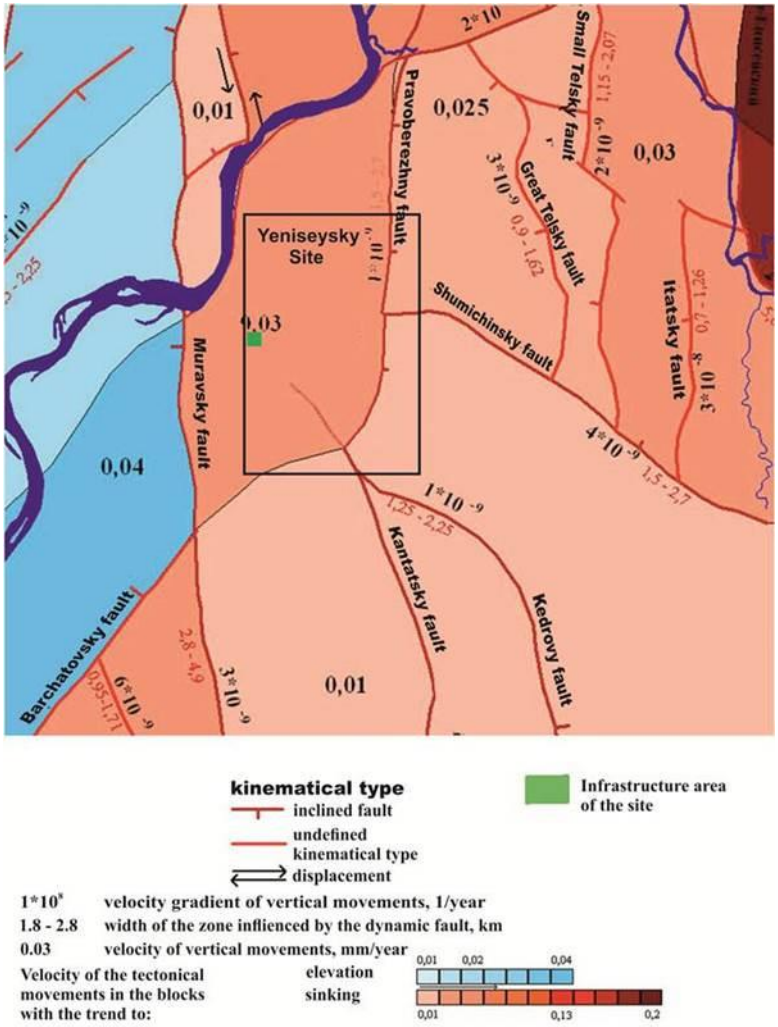

Fig. 2-9: System of main fault zones in the studied area, basing on teleseismic measurements (Lukishov et al., 2014).

The Yeniseysky site is characterized by a compression regime oriented ca. NE–SW (Morozov et al., 2007), which is associated with thrust structures oriented ca. NW–SE (e.g., the Shumichinsky and Baikalsky faults, Fig. 2-8). Considering this orientation of the maximum main compression vector with an approximate strike of 230 – 240º, NW–SE joints and fault zones are particularly likely to develop in hydraulically active groundwater migration paths as a result of tectonically caused opening. Analyses of the orientation of the intensive alteration zones in the 3D geological model confirm the prevalent NW–SE orientation of these zones of weakness within the geologic barrier (Fig. 2-8). According to Belov et al. (2007) in the plagiogneisses of the Yeniseysky area there are two systems of steeply dipping joints with a NW–SE or NE–SW strike; joints/fractures with a slight dip are not observed. On the other side, in the magmatic granitic rocks of Nizhnekansky massif, two systems of steeply dipping joints with either submeridional orientation or an approximately E–W strike, as well as a joint system with a very slight dip, are observed.

Basing on data from Belov et al. (2007) strain within the gneissic rocks varies between 10 MPa (N–S) and 30 MPa (ca. E–W). These values are of the same order of magnitude as the results of measurements using the stress-release method in the area of the underground excavations (biotite gneiss 27.9 MPa maximum, metadiabase 15.6 MPa, and amphibolite 22.1 MPa maximum; Morozov et al., 1999).

There is no detailed data available about joints and fault zones in cores of the 12 deep exploration boreholes, drilled in the last 3 to 4 years. Until now, on the basis of the last studies only general assumptions about the distribution and properties of the joints and fault zones can be made (see Fig. 2-16, Fig. 2-17). But, the drill core descriptions and the borehole geophysical measurements in the three 100 m boreholes indicate relatively frequent 1 – 2 m thick fault zones (approximately every 20 m starting at a depth of 30 m; see Jobmann et al., 2008). Most of the faults zones and joints observed in the boreholes have a steep dip (70 – 90º) or a moderate dip (40 – 60º). Horizontal joints were seldom observed and were usually closed (hair joints with opening widths smaller than 1 mm).

Regional tectonic development of the study area
The long-term geodynamic evolution of the region is characterized by uplift trend. The uplift was not constant and was accompanied by tectonic compression with a NE-SW directed vector (Belov et al., 2007). As a result of this, from the structural-geological point of view the region is represented by series of blocks with NNW orientation. Belov et al. (2007) carried out morphostructural analyses in the region. As a result of it they identified several relief-forming blocks within the Nizhnekansky massif and Yeniseysky ridge. It should be noted that the blocks in the western part of the region (the location of the Yeniseysky site) reach the absolute height of 430 m to 280 m. In opposite, the blocks in the eastern part of the region (east from Malyi Itat) are located higher (530 m to 380 m). That means, that the region located to the west of Malyi Itat (including the Yeniseysky site) has a lower intensity of vertical movements and can be classified as a tectonic stable region in contrast to the eastern part (Belov et al., 2007; Gvishiani et al., 2008).

Structural-geological analyses suggest a dominant uplift trend during the neotectonic development of the study area. The uplift in the region was not continuous and led to the separation of the blocks from each other by faults. This is visible in the relief. According to Kolmogorova & Kolmogorov (2004) the actual rate of movement of the blocks is up to about 8 mm/a (see also Gvishiani et al., 2008). Belov et al. (2007) suppose that in respect to NE-SW oriented tectonic compression the uplift trend that is determined in the region shall be preserved for a long time. The exact uplift rate is difficult to predict. But on the basis of reconstructed erosion rate it could be supposed that the rates will not exceed a few centimetres in thousand years (Belov et al., 2007).

A relatively low uplift rate was determined for the sub-recent geological history for the Zheleznogorsk region by an analysis of the vertical movement of the Neogene and early Quaternary sediments and terraces (Lukina, 1996 and 2001). Average uplift in the region due to neotectonic activity varies from 0.051 mm/a in the western part of the study area to 0.093 mm/a in the eastern part. On this basis, an uplift of the groundwater divides in the potential repository area can be predicted to be a maximum of ca. 90 cm in 10.000 years and a maximum of ca. 10 m in 130.000 years. The mean erosion by the rivers during the next 10.000 years amounts to 24 cm by the rivers in the western part of the area and 52 cm in the eastern part.

Uplift will occur very slowly and will have only a minimal effect on the stability and hydraulic properties of the rock massif. The vertical movement will occur along thick fault zones, i.e., there will be large blocks of rocks moving against each other. While this is occurring, the interior of these blocks (bounded by fault zones), i.e., the potential repository regions, will not or only weakly be deformed. The nearly constant uplift rate is distinctly smaller than 1 mm/a since the Pliocene and was calculated by Lukina (2001) from geomorphological data. This defines the region of the planned repository as a stable platform area. Precise geodetic measurements for estimating the recent uplift rates in the Yeniseysky mountain belt (Kolmogorova & Kolmogorov, 2004) showed significantly lower values (up to 10 mm/a) for the study area in contrast to the central part of the mountains (between the cities Yeniseysk, Novaya Yeruda, and Yartsevo, which is situated about 500 km northwards from the Yeniseysky site)

with a significantly higher uplift rate. This difference in the uplift rates is due to the fact that the northern part of Yeniseysky mountain belt is an accretionary prism, while the investigated area in the south lies within a stable micro-continent.

Determination of vertical movement from 1963 to 1986 at points along an E–W line about 450 km long through Krasnoyarsk, Kansk, and Tayshet (Fig. 2-10) resulted in uplift rates of 0 – 1.5 mm/a for the region of planned repository. According to Kolmogorova & Kolmogorov (2002) the measured uplift tendency in the area of the MCC is also significantly lower than in the Altai-Sayan region further to the southwest. At the same time, uplift anomalies were revealed in the Yeniseysky mountain range by a grid of measuring points set up to demonstrate neotectonically active fault zones.

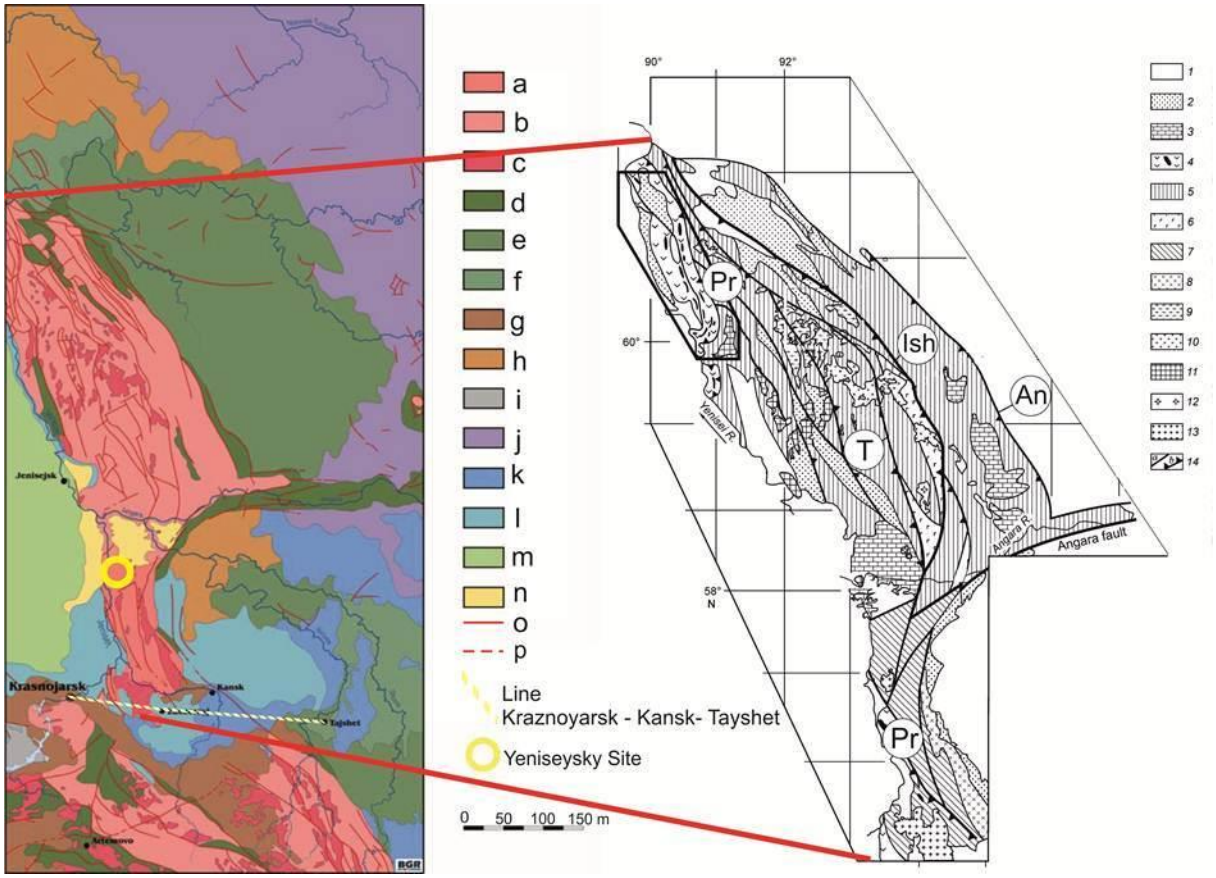

Legend: a – Archaean rocks („Dzheltulinsky Serie“ and analogues), sporadic Early to Late Proterozoic rocks and Archaic alkaline/ultrabasic and acidic intrusive rocks, b - Early to Late Proterozoic rocks (inclusive Riphean-Vendian) with alkaline/ultrabasic and acidic intrusive rocks, c - granitoid intrusions primarily Late Proterozoic to Early Cambrian or Devon, d – Cambrian rocks, partly Ordovician, e – primarily Late Cambrian to Ordovician rocks with Triassic gabbroid occurrences, f – primarily Silurian rocks, with gabbroids and Ordovician sediments, g – primarily Devonian sediments and vulkanites, minor Carboniferous material, h – Devon-Carboniferous, minor Permian rocks with gabbroids, i – Carboniferous sediments, minor Devonian, j – primarily Triassic vulkanites with alkaline compositions, with gabbroid intrusions and Carbonifeous-Permian material and minor Jurassic and Neogen, k – Early Jurassic sediments, local combined with Carboniferous-Permian rocks, l – Middle Jurassic sediments, m – primarily Upper Cretaceous sediments, minor Lower Cretaceous- and Neogen material, n - Neogen or Paleogen-Neogen material, o –fault zones, proved from the surface, p – supposed fault zones
1 – nappe (Paleozoic-Cenozoic), 2 – molasse (Neoproterozoic), 3 – mostly carbonate deposits (Neoproterozoic), 4 – ophiolite and island-arc complex of Priyenisey Belt (Neoproterozoic), plagiogranites aged 700-630 Ma, 5 – greenschist- to amphobolite-facies-metamorphosed flysch deposits (Mesoproterozoic-Neoproterozoic), 6 – ophiolites of the Rybanaya-Ishimba belt (Mesoproterozoic-Neoproterozoic), 7 – granulite-amphibolite complexes (Proterozoic).
Granitoids: 8 – Taraka (1840 Ma), 9 – Teya and Eruda (880-865 Ma), 10 – Ayakhta (760-750 Ma), 11 – Glushikha (750-720 Ma), 12 – Tatarka (630 Ma), 13 – Posol´ny and Nizhnekansk (511-445 Ma), 14 – faults and thrusts: Ish – Ishimba, T – Tatarka, Pr – Priyeniseysky; An - Angara

Fig. 2-10: Schematic tectonic map of the Yeniseysky ridge. Left: part of the Geological Map of Russia, Scale: 1 : 750 000; Right: from Vernikovsky & Vernikovskaya (2006)

With the exception of the Ishimba fault zone (Fig. 2-10), which is located in other structural position, the thick, neotectonically active fault zones in the southwestern part of the Siberian platform (e.g., the Tatarka, Priyeniseysky and Angara faults; Fig. 2-10) do not extend as far as the area of the MCC (Kolmogorova & Kolmogorov, 2004). Geomonitoring in the underground excavations of the MCC Zheleznogorsk confirm the assignment of the study area to a stable, seismically inactive platform region. Vertical movement of +0.09 mm/a (mean from 1976 to 1998) was reported to occur at the level of the MCC excavations (Gupalo, 2003).

2.5 Seismic activity

To be taken into consideration as a potential site for a nuclear waste repository, Russian regulations require that intensive seismic activity must be proven to be absent within 200 km of the proposed site. Most of the data for such an assessment is available in earthquake catalogues and recent seismic measurements in the region. The presence of seismically active fault zones in magmatites and metamorphites in the proposed repository area must be excluded with a high probability in a long-term safety assessment.

Seismological data has been recorded in Siberia only in the last 250 years. The Siberian platform is considered to be a seismically inactive region. A list of earthquakes that have occurred since 1727 in the southwestern part of the Siberian platform has been compiled by Arzhannikov et al. (2004) (Tab. 2.3).

Tab. 2.3: List of earthquakes in SW part of Siberian Platform (from: Arzhannikov et al., 2004)

Epicentre of earthquake	Time	Magnitude
Vercholensk	1910	5.0 ± 0.5
Kirensk	1727	6.25
Kirensk	1827	6.5
Kirensk	1856	5.0
140 km SE Bratsk	26.02.1996	4
	1786	5.4
Cheremchovo	1908	4.4 ± 0.6
Zima-Balagansk	1913	4.7 ± 0.6
Rybnaja Basin	29.08.1892	3.9 ± 0.7
Rybnaja Basin	25.04.1938	4.9 ± 0.5

Within its environmental monitoring tasks, the Krasnoyarsk Research Institute for Geology and Mineral Resources (KNIIGIMS) has carried out an extensive program to register seismic activity where the old Siberian craton, the young West Siberian platform, and the Altai-Sayan orogenic belt meet (Fig. 2-2). The systematic records of seismic activity from 1963 to the present show a complete absence of earthquakes with a Richter-scale magnitude of greater than 5 in the Krasnoyarsk region. Only occasional weak seismic activity was registered in that region; this activity was related to earthquakes in the north-western part of the Eastern Sayan Mts. (Anderson et al., 1998).

The relatively short period of systematic recording of earthquakes and a clear distinction between naturally and anthropogenically (e.g., through mining and large construction projects) induced quakes permit only a rough assessment of seismic risk in the Zheleznogorsk region on the basis of a statistical evaluation. The available data are inconsistent with respect to intensity, location, and time. For example, the earthquake with an epicentre 120 – 130 km south of Krasnoyarsk on 10 June 1958 listed by Anderson et al. (1998) does not appear in the earthquake catalogue of Shebalin & Leydecker (1997). The lack of information about epicentres and epicentre intensities over a long historical period (for comparison, the earthquake catalogue for Germany covers the period from 800 AD till today (Leydecker, 2005)

makes it difficult to make statements about the statistical probability of an earthquake of a particular intensity.

Despite the difficulty of obtaining data, the BGR together with the Laboratory for Strong Earthquakes of the Institute for the Physics of the Earth of the Russian Academy of Sciences, developed a historical earthquake catalogue for the territory of the former Soviet Union for the time period from 500 BC to 1988 AD (Shebalin & Leydecker, 1997). Compiled on the basis of the epicentre locations, focal depths, intensity and magnitude given in this catalogue, earthquakes with an intensity of more than 4 in the region considered are shown in Tab. 2.4. A similar compilation on the basis of the earthquake catalogue of the International Seismic Center (ISC-Bulletin, 2001) is given in Tab. 2.5. This table presents data until 2000. The earthquakes in the period from 2003 to 2014 are shown in the Tab. 2.6. This data comes from catalogues of Minregion of Russian Federation (2003-2009 years) and of European-Mediterranean Seismological Center - EMSC (2011-2014 years) and gives the intensity according to the Medvedev-Sponheuer-Karnik MSK-64 scale.

Tab. 2.4: Overview of the data according earthquakes intensity with magnitude of more than 4 in the region between 52° to 60° latitude North and 88° to 98° eastern longitude (earthquake catalogue from Shebalin & Leydecker (1997)), earthquakes data collected until 1988, epicentral intensity according to 12-degree Medvedev-Sponheuer-Karnik scale

Date	Time	Latitude	Longitude	Depth (km)	Magnitude	Intensity
1806/08/08	11:00	55.90	92.60	5	3.6	6.0
1858/06/11	06:15	56.00	93.00	10	4.7	6.0
1879/03/27	12:00	52.10	92.50	18	5.6	7.0
1885/07/07		53.50	91.40	16	4.5	5.0
1892/08/29	13:30	55.60	95.50	10	3.9	5.0
1903/05/16	06:18	53.60	92.50	11	4.5	6.0
1905/03/15	17:55:00	52.70	92.60	30	6.1	5.0
1908/06/19		55.90	97.90	15	4.0	5.0
1914/03/13	20:00	57.60	93.20	5	2.6	4.0
1926/08/27		56.00	92.60	5	2.6	4.0
1927/05/10	19:59:27	52.00	88.50	22	5.3	7.0
1938/02/21	13:49:37	52.00	93.50	28	5.4	6.0
1938/04/25	10:13:39	56.90	97.00	22	4.9	5.0
1949/01/09	10:49:38	53.70	89.20	20	4.2	
1952/04/17	09:22:12	52.60	97.00	20	5.0	
1954/11/11	06:23:53	53.00	90.00	20	4.0	
1964/02/29	04:31:40	53.40	91.00	15	4.0	
1964/08/31	13:55:59	53.70	97.30	15	4.0	
1969/10/30	12:17:17	52.57	95.47	20	4.7	
1971/08/24	16:33:20	52.17	91.42	24	5.6	6.0
1971/08/24	16:38:14	52.02	91.32	30	4.0	
1971/10/21	23:07:50	54.19	91.00	12	4.4	5.0
1972/08/31	14:03:15	52.40	95.30	25	5.5	
1972/09/28	12:04:52	52.00	96.43	20	4.0	
1972/09/29	06:21:15	52.38	95.33	20	4.6	
1978/08/03	06:07:33	52.20	96.93	11	5.8	8.0
1982/06/09	13:10:02	54.25	90.46	6	4.1	6.0

Tab. 2.5: Overview of the data according earthquakes in the region between 52° to 60° latitude North and 88° to 98° eastern longitude (ISC-Catalogue; ISC-Bulletin, 2001)

Date	Time	Latitude	Longitude	Depth (km)	Magnitude	Intensity
1927/05/10	19:59:20	52.00	88.50	35	5.6	
1928/11/07	18:36:45	52.50	95.00			
1938/04/25	10:14:03	55.00	92.00			
1960/04/27	22:47:42	53.00	97.00			
1964/02/29	04:31:41	53.55	91.00	33	4.7	
1969/10/30	12:17:22	52.35	95.73	33	5.0	
1971/08/24	16:33:21	52.18	91.56	12	5.4	
1971/08/24	16:38:13	52.37	92.20	0		
1971/10/21	23:07:53	54.31	91.22	43	4.7	
1972/02/27	22:15:05	55.05	93.11	39		
1972/08/31	14:03:15	52.36	95.31	21	5.5	
1972/09/28	12:05:00	52.41	95.98	52		
1972/09/29	06:21:20	52.47	95.13	36	4.7	
1973/05/22	02:15:04	52.85	89.54	22		
1978/08/03	06:07:33	52.15	96.94	8	5.2	
1978/08/09	10:17:45	52.14	96.99	33	4.7	
1979/01/29	06:27:30	52.45	97.91	1	4.8	
1981/04/25	15:28:47	54.89	96.90	46	3.1	
1987/09/16	17:57:23	52.16	95.78	10	4.8	
1989/03/21	05:29:37	54.59	90.45	33	4.6	
1989/12/10	19:55:27	55.32	97.76	33	4.1	
1996/01/10	08:14:03	54.08	91.21		3.2	
1996/01/13	13:11:06	54.90	97.17	33	3.7	
1996/05/08	08:30:12	54.39	90.46		3.5	
1997/03/10	13:28:40	54.57	88.78	17	3.7	
1997/11/19	05:15:39	53.36	89.80	32	3.9	
1997/12/02	11:56:13	58.74	89.37		4.0	
1998/12/15	11:19:26	52.66	94.98	44	4.0	
1998/12/26	08:32:10	55.58	92.00	33	4.0	
1999/03/05	10:45:30	54.34	90.70	0	3.0	
1999/11/02	05:09:27	52.74	95.99	10	4.8	
1999/12/31	02:54:44	52.12	93.88	10	3.7	
2000/10/07	08:57:56	52.99	88.47	10	4.2	
2000/10/27	00:08:50	54.82	95.07	10	5.8	
2000/10/27	00:08:54	54.71	95.01	33	5.2	
2000/11/09	06:39:53	53.47	95.12	0	3.9	
2000/11/09	06:40:13	56.22	94.61	33	3.9	
2000/12/01	05:02:55	53.03	96.61	10	4.3	

Tab. 2.6: Overview of the data according earthquakes in the region between 50° to 60° latitude North and 85° to 105° eastern longitude, scala MSK-64. a) Period of 2003-2009, based on the catalogue of Minregion of Russian Federation (www.seismorus.ru), b) period of 2011-2014 based on EMSC (www.emsc-csem.org/Earthquake/))

Date	Time UTC	Latitude	Longitude	Depth (km)	Magnitude	Intensity
03.02.03	16:23:00	54.97	94.72	10	3.3	0.2
27.09.03	11:33:00	50.01	87.74	24	7.3	3.8
01.10.03	01:03:00	50.13	87.7	10	6.9	3.2
08.05.04	08:53:00	54.71	95.17	15	4	0.9

Date	Time UTC	Latitude	Longitude	Depth (km)	Magnitude	Intensity
27.04.05	07:36:00	51.15	98.23	14	4.9	0.5
25.10.06	06:20:00	64.67	93.59	12	3.3	0.0
19.01.08	07:32:00	51.39	98.05	10	4.7	0.3
16.08.08	04:01:00	52.2	98.23	15	5.5	1.7
16.08.08	04:06:00	52.22	98.28	17	4.6	0.3
24.03.09	11:08:00	54.88	93.16	11	3.3	0.2
04.08.09	16:20:00	50.62	96.89	14	5	0.6
10.02.11	5:35:17	52.14	91.72	18	5.4	1.7
17.04.11	23:07:23	53.36	86.76	20	4.4	0.0
25.09.11	12:36:43	51.19	93.29	23	4.8	0.6
27.12.11	23:43:51	52.09	95.63	15	4.4	0.2
27.12.11	20:19:12	51.65	96.37	30	4.8	0.6
27.12.11	15:53:07	51.81	96.1	10	4.8	0.7
27.12.11	15:21:57	51.84	95.85	10	6.5	3.3
28.12.11	23:40:42	51.67	96.12	10	4.4	0.0
28.12.11	21:35:01	51.55	96.23	10	4.5	0.1
28.12.11	15:25:41	51.73	96.06	10	4.5	0.2
28.12.11	13:54:35	51.92	96.17	10	4.6	0.4
28.12.11	4:45:53	51.72	96.03	10	4.4	0.1
28.12.11	4:23:41	51.82	95.75	10	4.7	0.6
28.12.11	0:40:32	52.03	95.81	5	4.7	0.6
01.01.12	11:07:19	51.79	96.24	10	4.4	0.1
04.01.12	13:08:14	51.71	95.96	30	4.8	0.7
09.01.12	19:33:06	51.48	96.02	2	4.7	0.4
09.01.12	18:55:29	51.7	95.9	10	4.8	0.7
16.01.12	5:13:37	51.73	96.16	10	4.9	0.8
26.02.12	19:59:31	51.64	95.93	10	4.7	0.5
26.02.12	13:17:33	51.53	95.6	10	4.5	0.2
26.02.12	13:06:36	51.84	95.97	10	4.9	0.8
26.02.12	12:50:21	51.73	96.14	10	4.7	0.5
26.02.12	11:59:05	51.76	96	10	5.3	1.4
26.02.12	11:50:48	51.59	96.05	10	4.5	0.2
26.02.12	11:07:41	51.66	96.15	10	5.2	1.2
26.02.12	7:49:01	51.72	96.09	10	4.4	0.1
26.02.12	6:52:39	51.76	96.22	10	5.0	1.0
26.02.12	6:17:19	51.72	95.99	10	6.6	3.4
27.02.12	12:54:34	51.68	95.91	10	4.7	0.5
27.02.12	8:56:04	51.49	96.12	10	4.5	0.1
27.02.12	2:54:56	51.62	95.97	10	4.6	0.3
29.02.12	20:19:37	51.56	96.23	10	4.8	0.6
29.02.12	12:03:19	51.62	96	10	4.7	0.5
01.03.12	19:46:22	51.51	96.11	10	4.5	0.1
04.03.12	23:33:45	51.55	95.72	46	4.4	0.0
04.03.12	15:59:05	51.69	95.96	10	4.6	0.4
04.03.12	0:01:22	51.45	96.24	10	4.7	0.4
06.03.12	6:49:50	51.49	95.73	50	4.5	0.1
07.03.12	14:33:55	51.44	96.09	2	4.9	0.7
18.03.12	5:00:06	51.55	95.99	10	4.5	0.2
21.03.12	18:00:29	51.78	95.99	10	4.6	0.4
06.04.12	9:55:45	55.19	91.19	10	3.4	0.1
11.04.12	3:13:05	51.49	95.78	10	4.5	0.2
16.04.12	2:18:37	54.37	95.09	10	4.4	1.3

Date	Time UTC	Latitude	Longitude	Depth (km)	Magnitude	Intensity
26.04.12	4:11:08	51.58	95.58	10	4.5	0.2
14.05.12	16:24:25	51.9	95.85	10	4.7	0.6
06.06.12	22:39:01	51.8	96.12	10	4.4	0.1
06.06.12	16:16:19	51.82	96.21	10	4.8	0.7
06.06.12	14:04:14	51.69	96.01	2	5.2	1.3
27.07.12	3:58:13	51.56	96.03	10	4.7	0.5
30.07.12	22:30:42	50.64	87.4	10	5.0	0.4
28.08.12	7:40:35	51.81	96.11	10	4.8	0.7
03.09.12	7:52:29	51.81	95.7	10	4.5	0.3
30.04.13	1:03:35	51.32	92.44	10	5.3	1.3
18.06.13	23:02:08	54.27	86.27	2	5.2	1.29
03.11.13	6:14:47	51.74	98.99	10	4.8	0.43
21.12.13	17:51:50	53.44	91.76	10	5.0	1.64
17.01.14	7:01:25	58.56	101.74	2	4.6	0.32

As can be seen in Tab. 2.4, in historical time only a few earthquakes are known to have occurred within 200 km of the potential HLW repository. An example of a relatively strong earthquake occurred about 100 km south of the Kan-Man watershed on 25.04.1938 with a magnitude of 4.9. The distribution of the earthquakes in the region around Krasnoyarsk compiled from the data of Shebalin & Leydecker (1997) is shown as a function of magnitude and epicentre intensity in Fig. 2-11, Fig. 2-12 and based on the data from catalogue of Minregion of Russian Federation and of EMSC, according to scale MSK-64 is shown in Fig. 2-13.

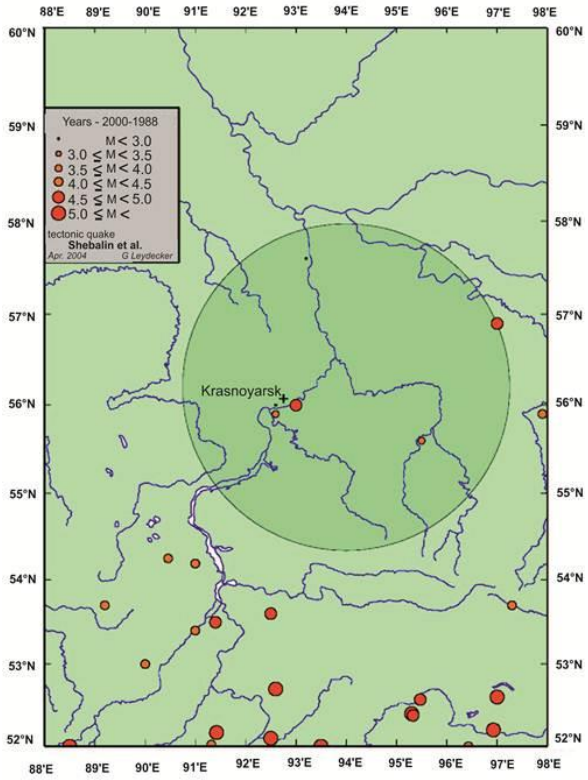

Fig. 2-11: Distribution of earthquakes with different magnitudes in the area of Krasnoyarsk city, based on the data base of Shebalin & Leydecker (1997). The circle has a diameter of 200 km.

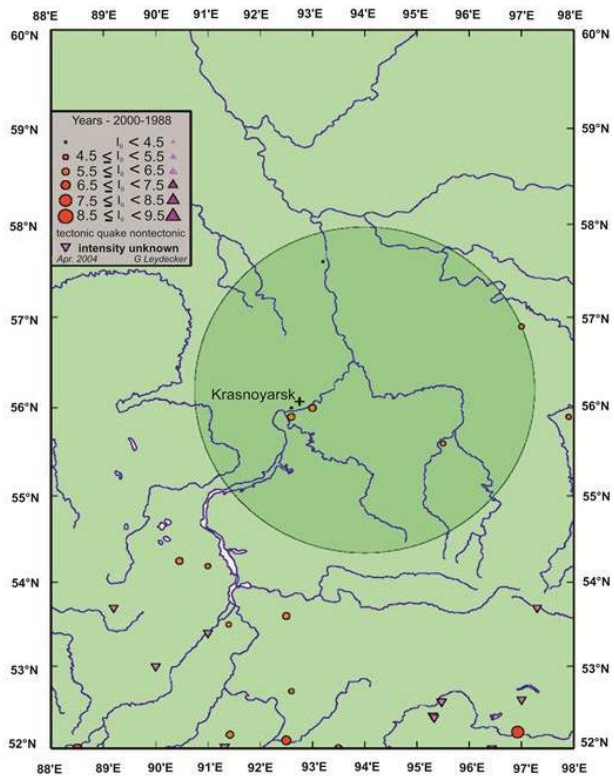

Fig. 2-12: Distribution of the earthquakes with different intensities in the area of Krasnoyarsk city. Epicentre intensity according to 12-degree Medvedev-Sponheuer-Karnik scale (diameter of the cycle: 200 km (Shebalin & Leydecker, 1997)

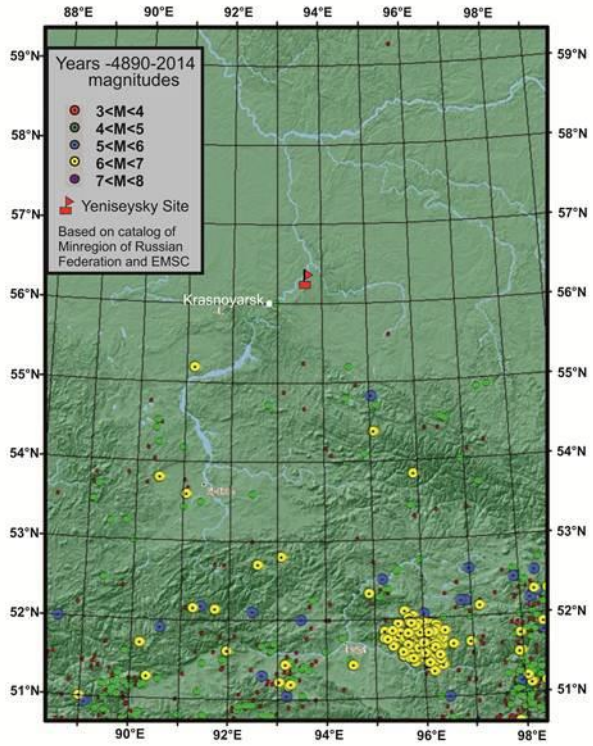

Fig. 2-13:

Distribution of earthquakes with magnitudes higher 3 near the area of Krasnoyarsk city, based on the data from catalogue of Minregion of Russian Federation and of EMSC, according to scale MSK-64 (based on www.seismorus.ru (-10000 to 2010 years) and www.emsc-csem.org/Earthquake/ (2011 to 2014 years))

The long-term monitoring of seismic activity and the geomorphological studies of the region confirm that the potential repository site lies in a stable platform region with low seismic and neotectonic activity and a low tendency for uplift. The exponentially rapid decrease in earthquake energy with increasing distance from the epicentre greatly weakens the effects of seismic activity in neighbouring active zones. For example, the Karagansk earthquake at the end of September 2003 was much stronger (magnitude of 5.2 – 5.8) where it originated in the Altai-Sayan Mts., than felt in the area of planned repository (maximum of 1.5 – 4 on the Richter scale). There were no negative effects on the numerous technical structures in the area (for example, the hydroelectric plants and the underground excavations of MCC).

In addition to the data from the monitoring of seismic activity, the Map of General Seismic Subdivision of the Territory of the Russian Federation (OSR–97–S), published by the Institute of the Physics of the Earth of the Russian Academy of Sciences, serves as an official document for the assessment of suitable repository sites (Morozov et al., 2001). On the basis of the subdivision of the territory of the former Soviet Union into earthquake units, the study area is characterized by a low propensity for seismic activity of category 6 (Fig. 2-14). This means that only once in 5000 years an earthquake can be expected with an intensity of 6. This is an earthquake that will cause cracks in the plaster, walls and chimneys.

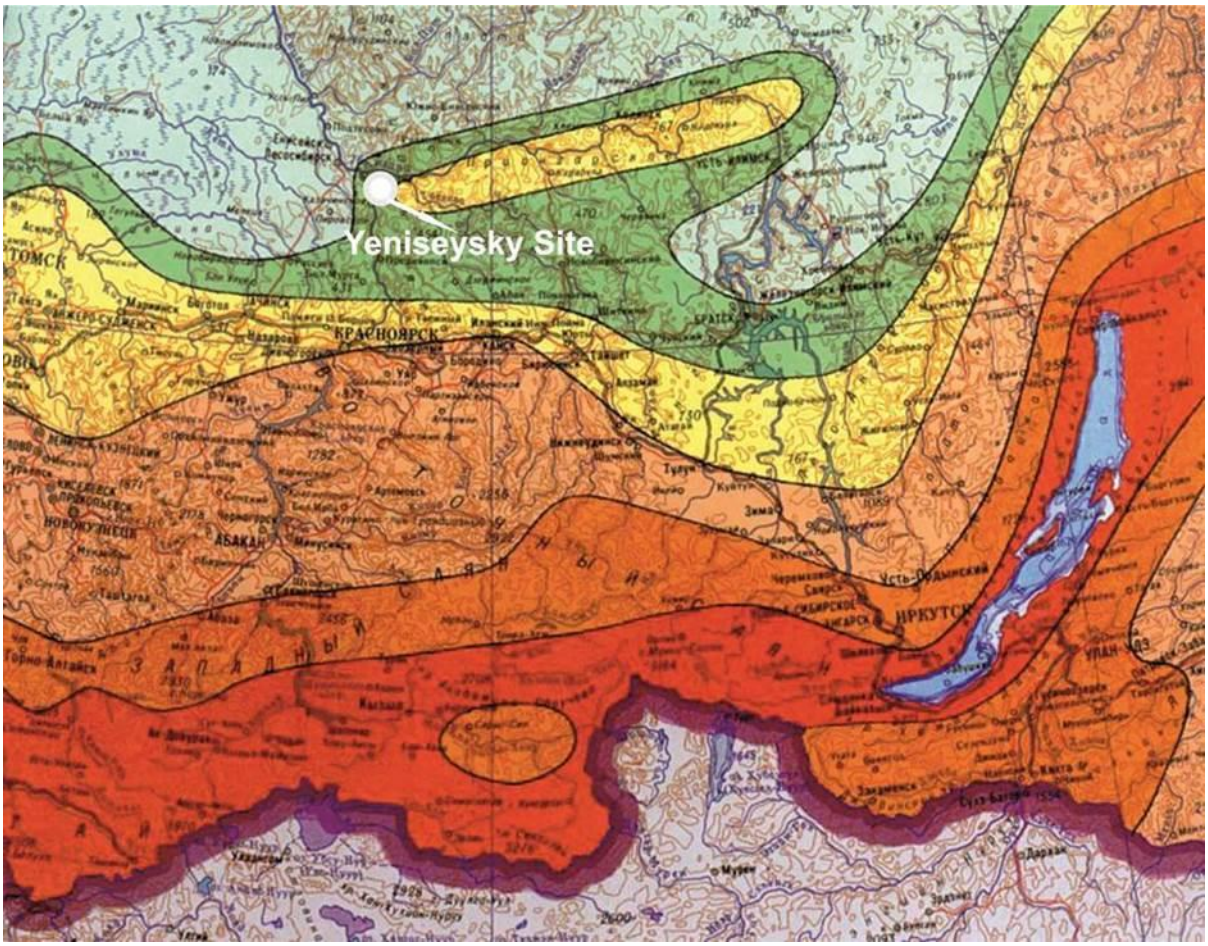

Legend: violet – state border of Russia, dark red – intensity 10 and more, orange – intensity 9, brown – intensity 8, yellow – intensity 7, green – intensity 6. Intensity values for regions mean that the earthquakes with certain intensities have a repetition period of 5000 years

Fig. 2-14: The Yeniseysky site at the "Map of general seismic activity for the territory of Russian Federation ("ORS-97 – S")"

All known epicenters in central Siberia, e.g., the Baikal Rift zone as well as the southern and southeastern parts of the Altai-Sayan region (marked red in Fig. 2-14), are several hundred to thousand kilometres from the study area. The effects of earthquakes with a magnitude of 8 in those regions have been calculated to have maximum magnitudes of 5 in the Yeniseysky area (Morozov, pers. comm.).

The last analysis of the seismic data showed that the seismic regime of the investigation site is caused by the waves of the regional earthquakes and technogenic stress. It has been observed that the lineament zones do not serve as a source of seismic activity (Lukishov et al., 2014).

2.6 Hydrogeology

Extensive hydrogeological and hydrochemical investigations were made in the Yeniseysky area in last years (Ozerskiy, 2012; Ozerskiy & Karaulov, 2012). Numerous pumping tests were conducted to determine the permeability of rocks. Additionally, hydro-chemical and isotope geochemistry studies were conducted to obtain information about the origin and content of dissolved substances in the groundwater of the study area, as well as the groundwater retention times, i.e., ages, and for assessing recent tectonic activity.

It is important for the characterization of the groundwater system and the hydraulic conditions at the planned repository site that the maximum thickness of the weathering zone in the gneisses and basic rocks was determined to be ca. 55 m. For the 12 deep exploration boreholes no detailed data concerning the thickness of the weathering zone was available. The estimated thickness of the weathering zone is shown on the hydrogeological profile (Fig. 2-17 and Fig. 2-18).

The groundwater is alkaline Ca-Na bicarbonate water with a total mineralization between 140 and 641 mg/l (mean: 367 mg/l). The groundwater is reducing (mean Eh is 44.8 mV) and the pH values are slightly lower than 8.0. The ages of groundwater were determined with tritium and radiocarbon methods only for waters collected from 100 m deep exploration boreholes E-1 to E-3 and from borehole 1-E (500 m deep, Fig. 2-15). Tritium analyses (carried out by VSEGINGEO) and radiocarbon measurements (carried out at the University of St. Petersburg) of the groundwater samples indicate high groundwater retention times, i.e., low exchange rates with surface water.

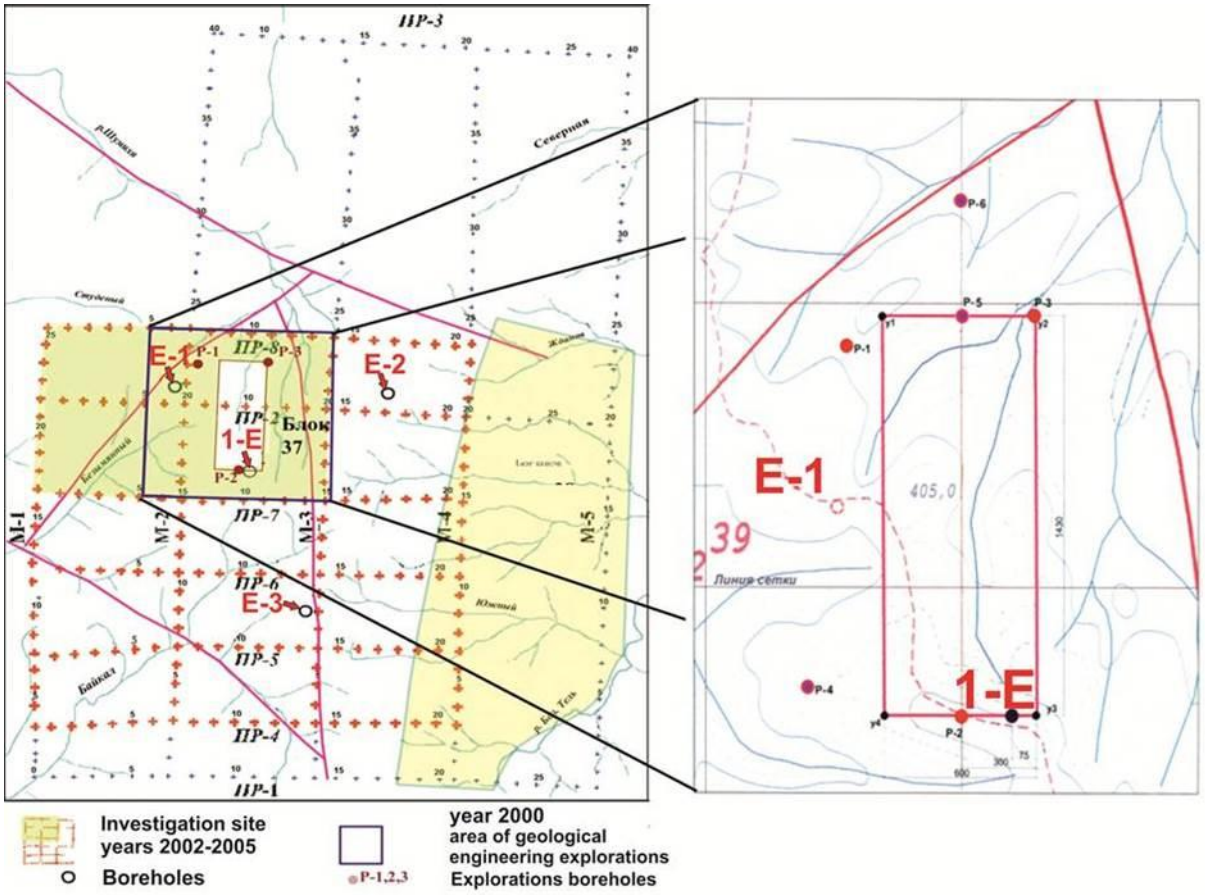

Fig. 2-15: Overview of the position of exploration boreholes on the Yeniseysky site (work status in 2008, VNIPI PT). Right is the enlarged section of the area. The boreholes E-1 and 1-E on the both maps serve as an orientation.

These findings are in contradiction to assumption of Anderson et al. (2011, see also subchapter 2.2) which still needs clarification. The groundwater ages determined with the tritium method vary from 70 to more than 1000 a; the ^{14}C groundwater ages for four samples from borehole 1-E (collected from depths between 100 and 500 m) range from 6000 to 8000 a (Gupalo et al., 2007).

After nearly 10 years of exploration works in Yeniseysky area there are a large amount of data available concerning permeability and porosity of rocks. Filtration coefficients (K_f, hydraulic conductivities) were determined at different stages of drilling for up to 50 m long

intervals to the bottom of boreholes E-1 to E-3 (Gupalo et al., 2004b): $2.2 \cdot 10^{-7}$ - $8.1 \cdot 10^{-7}$ $m \cdot s^{-1}$ down to 50 m depth; $6.6 \cdot 10^{-8}$ - $6.9 \cdot 10^{-8}$ $m \cdot s^{-1}$ down to 100 m depth. The filtration coefficients of borehole intervals of 25-50 m vary between $7.8 \cdot 10^{-11}$ $m \cdot s^{-1}$ (borehole 1-E, 504-550 m depth) and $2.19 \cdot 10^{-7}$ $m \cdot s^{-1}$ (borehole E-3, 9.8 - 50 m depth; Gupalo et al., 2007). Permeabilities for water and gas were determined in GRS laboratories for some samples from boreholes E-1 to E-3. Permeabilities for water varied from $7.16 \cdot 10^{-18}$ to $2.77 \cdot 10^{-21}$ m^2. They are comparable to the permeabilities of the granitoids of the Nizhnekansky massif ($1.4 \cdot 10^{-18}$ - $3.7 \cdot 10^{-20}$ m^2, Laverov et al., 2002).

In 2013, eight core samples from the deep exploration borehole R-12 were made available by NO.RAO and Krasnoyarskgeologiya to the German project partners. Gas permeabilities were determined in GRS laboratories for these eight samples between 2013 and 2015 (see Annex). Values range from $2.73 \cdot 10^{-17}$ to $4.21 \cdot 10^{-22}$ m^2 (Annex Tab. 9.11). Lowest values were observed for the biotite plagiogneisses from a depth below approx. 420 m below ground surface (bgs). Higher gas permeabilities were observed for biotite plagiogneiss samples from lower depths (approx. 170 m bgs), and for migmatites and the contact between the dolerite and the lamprophyre in depths deeper ca. 440 m bgs. Water permeabilities could not be determined for all eight samples (Annex Tab. 9.12) due to the technical limits of the experimental setup. Water permeabilities of the samples are lower than the gas permeabilities with a factor of one to three orders of magnitude, which is commonly observed in lowly permeable rocks. Determined water permeabilities range from $1.28 \cdot 10^{-18}$ for the migmatite to $3.67 \cdot 10^{-20}$ m^2 for the biotite plagiogneisses from approx. 477 m bgs (Tab. 9.12).

Numerous pumping tests were conducted in the last years by Krasnoyarskgeologiya. The interval pumping tests were carried out in the exploration boreholes with an interval of ca. 50 m. In total 150 pumping tests were achieved. 125 filtrations coefficients were derived after the analysis of the results from the pumping tests. Sporadic areas with distinct higher filtration coefficients up to ca. $1.7 \cdot 10^{-7}$ $m \cdot s^{-1}$ (0.015 m/day) were evidenced only in the surface-near areas (up to ca. 150 m above sea level) (Tab. 2.7, Fig. 2-17). From the earth surface to depths of 700 m impermeable rocks with the filtration coefficient of $5.8 \cdot 10^{-8}$ $m \cdot s^{-1}$ (0.005 m/day) are dominant.

Additionally, Gupalo (2003) made filtration experiments in the underground cavities of the MCC. The maximum filtration coefficients of the gneiss blocks with only few joints at the depth level of the excavations (nearly ca. 200 m below earth surface) were $4 \cdot 10^{-9}$ $m \cdot s^{-1}$. The schistose zones (up to $8.1 \cdot 10^{-8}$ $m \cdot s^{-1}$) and contact zones between mafic dykes and their metamorphic wall rock (up to $5.7 \cdot 10^{-8}$ $m \cdot s^{-1}$) have elevated porosities and permeabilities. Unfortunately, these results are available only for 25 - 50 m long borehole intervals, owing to the unavailability of smaller packer systems for the pumping tests. Besides these overall data (25 m to 50 m long pumping intervals) there are no data for fault zones themselves. Nevertheless, the presence of zones with significantly higher permeabilities (up to $1.16 \cdot 10^{-5}$ $m \cdot s^{-1}$, Gupalo, 2003) cannot be excluded (Fig. 2-16).

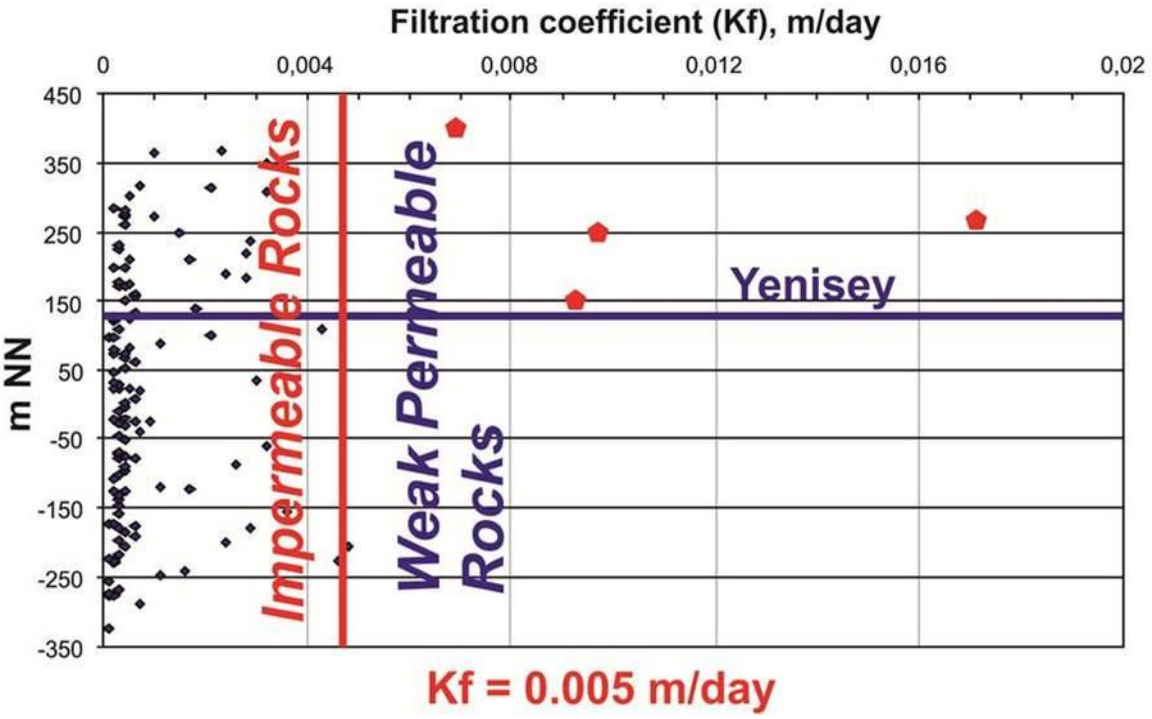

Fig. 2-16: Vertical distribution of filtration coefficients (=hydraulic conductivities; 0.005 m/day = $5.79 \cdot 10^{-8}$ m·s^{-1}) in the rocks of the Yeniseysky site based on Ozerskiy & Karaulov (2012)

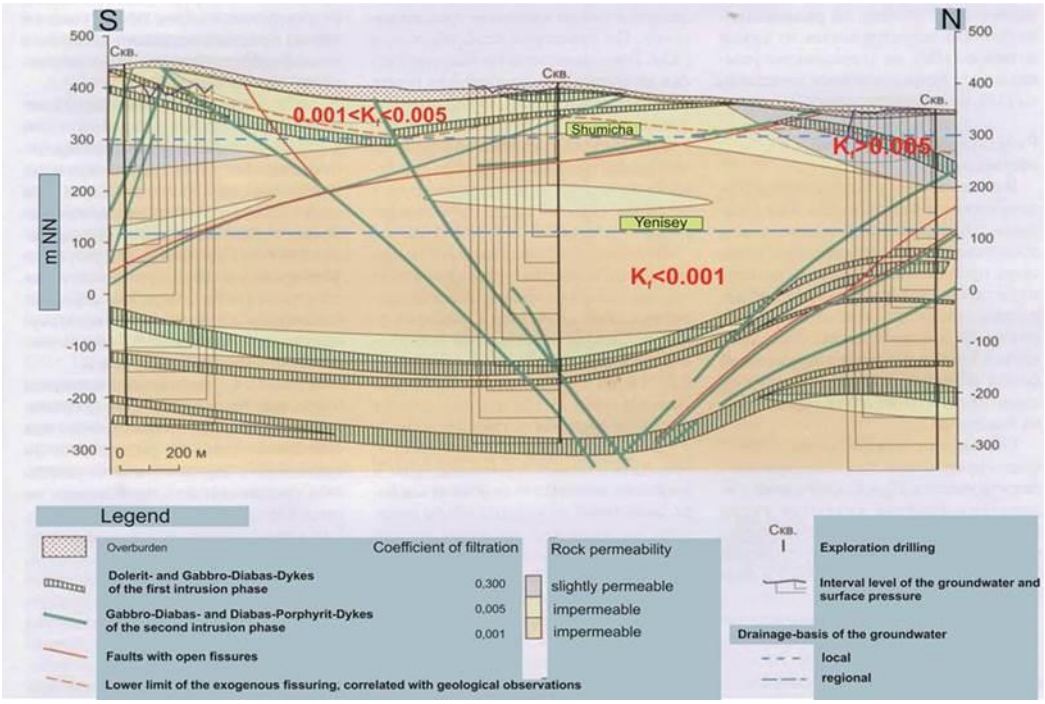

Fig. 2-17: Schematic meridional hydrogeological profile across the Yeniseysky site based on Ozerskiy & Karaulov (2012); (0.001 – 0.005 m/day = $1.16 \cdot 10^{-8}$ – $5.79 \cdot 10^{-8}$ m·s^{-1})

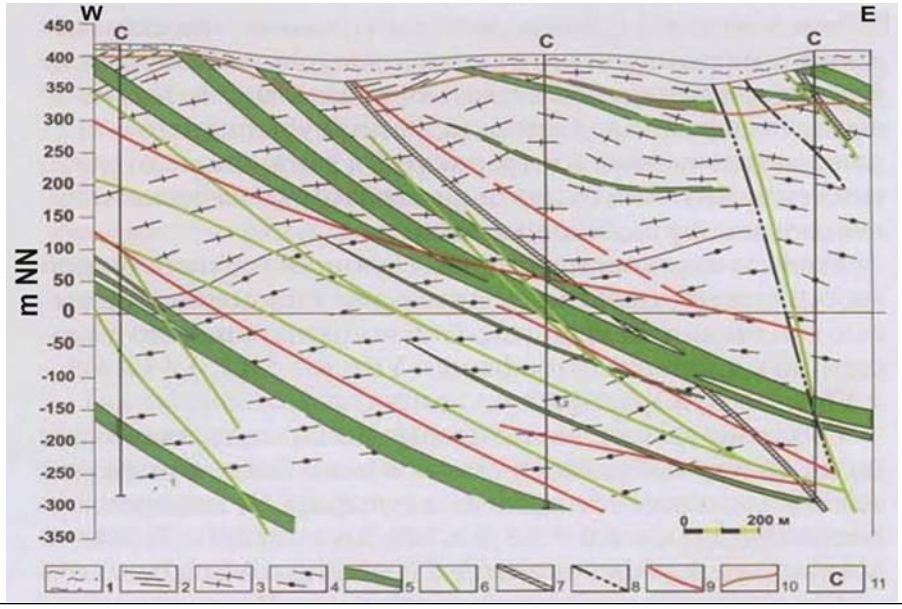

Legend: 1 – quaternary clay, sand and clay sand; 2 – biotitic gneiss, two mica gneiss and crystalline shale; 3 – biotitic plagiogneiss; 4 – biotitic cordierite-gneiss; 5 – dolerite- and gabbro-diabas-dykes; 6 – gabbro-diabas- and diabas-porphyry-dykes of the second intrusive phase, 7 – zone of cemented breccias of the earlier phase of the fault dislocation; 8 – faults with open fissuring; 9 – zone of tectonic breccias that are cemented by quartz-microcline material; 10 – lower border of the exogenous fissuring; 11 – exploration boreholes

Fig. 2-18: Schematically W-E- hydrogeological profile across the Yeniseysky site (Ozerskiy, 2012)

Only limited information is available on the distribution and hydraulic properties of the fault zones and the connections between them in the area of the planned repository. The presence of fault zones with significantly higher filtration coefficients cannot be excluded in long-term safety assessments for the repository, even in the already measured boreholes. Measurements of hydraulic permeability of the individual fault zones or of the contact zones between different types of rock (e.g., gneiss in contact with basic dykes) have not been made due to a lack of suitable instruments. The only information available is that the fault zones at a depth are healed and that groundwater flow rates are only 10^{-7} und 10^{-6} m^3 s^{-1} in the 100 m deep boreholes (Gupalo et al., 2004b).

The analysis of the distribution of the hydraulic conductivity (K_f) as a function of the depth position of the investigated interval (zone structure of the k_f-value according to Tab. 2.7, Fig. 2-16 and Fig. 2-17) allows understanding the dependencies: The highest zone that lies over the local drainage basis has the highest average and median K_f-value and includes rocks with a low hydraulic conductivity of $K_f > 5.79 \cdot 10^{-8}$ $m \cdot s^{-1}$ ($K_f > 0.005$ m/d^{-1}). During the pumping tests made by Krasnoyarskgeologiya the zone of exogenous fissuring in the top interval (up to 50-70 m deep) does not show increased filtration coefficients. The transmissivity in the top zone is $1.88 \cdot 10^{-2}$ m^2 s^{-1} and in average $5.79 \cdot 10^{-1}$ m^2 s^{-1}. The mid zone that is between local and regional drainage basis (300-120 m above sea level) shows decreasing average and median K_f-values. That means that in this zone rocks with a low water transfer capability are present. Both zones that are situated under the regional drainage basis have approximately the same average and median K_f-values. According to Fig. 2-16, all rocks in these zones are impermeable to water (Tab. 2.7).

Tab. 2.7: Permeability of the Archaean rocks at the Yeniseysky site (Ozerskiy & Karaulov, 2012)

Permeability of the Archaean rocks				
Depth zones	***Location in relation to the drainage basal plane***	***Altitude [m]***	***Filtration coefficient K_f [m/day]***	
			Average	***Median***
top zone	*above the local*	*>+300*	*0.0025*	*0.0023*
middle zone	*between the local and the regional*	*+300 + +120*	*0.0018*	*0.0005*
bottom zone	*between the regional and the global*	*+120 + 0*	*0.0007*	*0.0004*
depth zone	*under the global*	*0+ -350*	*0.0008*	*0.0004*

Krasnoyarskgeologiya provided porosities as well as gas and water permeabilities from laboratory studies for the gneiss and dolerite samples from the deep geological boreholes. The investigations show very low porosity values (0.35% for gneiss and 0.25% for dolerite, Tab. 2.8) and low gas permeability (median for gneiss $1.97 \cdot 10^{-17}$ or $9.87 \cdot 10^{-18}$ m^2 parallel or perpendicular to the bedding and for dolerite $8.88 \cdot 10^{-18}$ m^2). Laboratory tests show that the average open porosity is 0.35 % and never more than 1% (Tab. 2.8). The average porosity of gneiss is 1.5 times larger than the porosity of metadolerite. The comparison of the K_f-values from the laboratory (for pore collectors) and from in-situ-studies in the rock massif (for pore and fissure collectors) shows that the share of pore collectors in total geofiltration is ca. 1% and is not higher than 3%.

Tab. 2.8: Mean open porosity and permeability values of the Archaean rocks in Yeniseysky site (Ozerskiy & Karaulov, 2012)

Mean values for the open porosity and permeability of the Archaean rocks*						
Rocks	**N**	**open porosity, %**	**parallel to bedding**		**perpendicular to bedding**	
			k [m^2]	K_f [m/day]/ K_f [m/s]	k [m^2]	K_f [m/day]/ K_f [m/s]
Gneiss	24	0.35	$1.97 \cdot 10^{-17}$	$1.2 \cdot 10^{-5}$/ $1.39 \cdot 10^{-10}$	0.014	$8.3 \cdot 10^{-6}$/ $9.6 \cdot 10^{-11}$
Metadolerite	8	0.25	$8.88 \cdot 10^{-18}$	$5.4 \cdot 10^{-6}$/ $6.25 \cdot 10^{-11}$	0.009	$5.4 \cdot 10^{-6}$/ $6.25 \cdot 10^{-11}$
*N - number of samples; k - gas permeability; K_f - filtration coefficient (hydraulic conductivity)						

The permeability of the rocks is very low. Thereby the gneisses which have a higher open porosity show also a higher permeability which is 1.5 - 2 times higher than of the metadolerite. A very important difference between gneisses and metadolerite is represented by the anisotropic permeability of the gneisses. The metadolerites are hydraulically isotropic (Tab. 2.8). All values of the filtration coefficient K_f obtained for the rocks studied allow the attribution of these rocks to water impermeable rocks according to GOST (2011).

The metadolerite dykes build “water impermeable” layer-like bodies in the rock massif of water impermeable rocks. The anisotropy of the gneisses supports sub-horizontal groundwater migration in opposite to the vertical filtration. During geological exploration it was impossible to identify a so-called “aquifer with open fissuring” within the rock massif. The distribution of hydraulic pressure in the groundwater is controlled by the morphology of earth surface (Fig. 2-19). The pressure decrease occurs with average hydraulic gradient of I=0.05 in two directions – NNW (in the direction of the local drainage) and W (in the direction of the regional drainage – Yenisey valley).

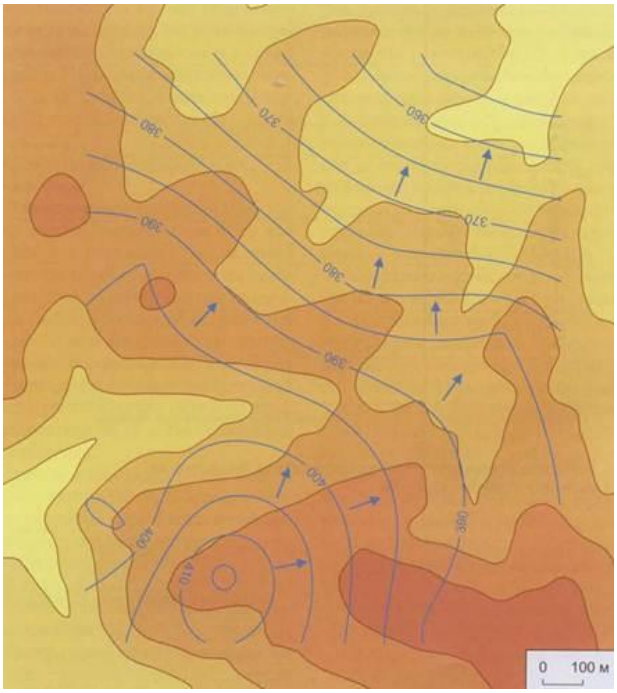

The subsurface zonation of the site underground into four depth zones is reflected in the chemical composition of the groundwater (Tab. 2.9). The average groundwater composition in the top zone of the massif is calcium-hydrocarbonatic. Directly beneath the top zone the composition changes into sodium-calcium composition. In the deepest zone the total dissolved solids and the concentration of the major ions is substantially lower. This is caused by the dissolution resilience of the rocks and the hydrolytic disintegration resilience of the silicates. The decrease (from top to bottom) of the total mineralization and of the concentrations of the major ions until depth level 0 m above sea level is characteristic for the three upper zones. The very low water content and very low permeability of the rocks are typical for the rocks of the lowest zone of the massif and result in increasing concentrations.

Fig. 2-19: Hydrodynamic map for the ground level 0 m above sea level: numbers – depth level of groundwater table, arrow – direction of the pressure decrease (from: Ozerskiy & Karaulov, 2012)

Tab. 2.9: Average chemistry of groundwater in Yeniseysky site (from: Ozerskiy & Karaulov, 2012)

Average chemistry of groundwater				
Component	**Concentration, mg/l, in the massifs zones**			
	top zone	**middle zone**	**bottom zone**	**depth zone**
HCO_3^-	220	232	247	215
Cl^-	4	5	6	5
SO_4^{2-}	19	26	21	16
Ca^{2+}	56	42	54	44
Mg^{2+}	11	10	12	9
Na^+	19	33	26	25
K^+	2.6	2.7	2.6	2.7
Fe_{total}	1.4	4.4	3.1	4.1
total dissolved solids	369	376	394	343

The results of the newly provided hydrogeological investigations at the Yeniseysky site show that the massif consists substantially of water impermeable rocks with filtration coefficients of ten thousandth m per day. Weak water conducting intervals are present only locally and only higher than the local drainage basis, ca. 150 m higher than the level of the planned repository. In the present state of knowledge the massif has no permeable, water conducting layers or zones and also no “underground water lenses” or fissure zones along which the water can reach the underground excavations and thereby cause their flooding. The zones of tectonic fissuring are substantially filled with dykes of intrusive rocks and with secondary minerals. These zones do not have any increased filtration coefficients and cannot serve as hydraulic ways that can connect the disposal level with the earth surface (Ozerskiy & Karaulov, 2012).

3 Characterization of the host rocks

The geological exploration shows that the Yeniseysky area has a complicated geological structure resulting from multi-phase regional metamorphism, folding, and faulting due in part to its contact to the east with the Nizhnekansky granitoid massif (Gupalo et al., 2004a). The high-grade metamorphic rocks of Archaean to early Proterozoic age are characterized by granulite facies as well as amphibolite facies. The Archaean rocks of the Kansk Series (up to 8000 m thick) are subdivided into the Atamanov and Kuzeev Formations. The early Proterozoic rocks are subdivided into the Isaevsk and Serednyansk Formations. The metamorphites, which correlate with the ancient rocks of eastern Siberia, are mostly biotite gneisses, biotite-garnet gneisses, quarzites, amphibolites, and mica schist (Rundkvist & Mitrofanov, 1988).

3.1 Petrography, mineralogy and geochemistry of rocks

The Yeniseysky site includes Quaternary sediments (4 – 30 m thick), patches of fine-clastic to sandy Jurassic sediments and high-grade Proterozoic and Archaean gneiss complexes. Occurrences of Nizhnekansky granitoid complex are found at the east edge of the Yeniseysky site as thin apophyses in gneisses (Gupalo et al., 2004a, 2007). On the other hand, it is highly probable that there are small anatectic granitic bodies within the high grade gneiss complex. The thickness of the weathering crust in the gneisses and basic rocks varies greatly, with a maximum of nearly 55 m. The surface of the area is covered by Quaternary eluvial-deluvial sediments – clay, silt, loam/loess, sand with inclusions of wood residuals and gravel from the underlying rocks. The covering layers are composed of weak permeable rock (Fig. 2-17). The predominant rocks in the Yeniseysky site are high-grade plagiogneisses (biotite gneiss, biotite-amphibole gneiss, or garnet-biotite gneiss) which in part show a amphibolite to granulite facies owing to the occurrence of sillimanite, garnet, cordierite, and kyanite (Petrov et al., 2008). The gneisses are composed of 3-50% quartz, 25-70% plagioclase, 5-20% potash feldspar, 5-30% biotite, 15-20% muscovite, and 3-10% sillimanite.

Basic intercalations (amphibolite, metabasite) and numerous discordant basic veins and intrusive bodies are present with increasing depth in the plagiogneisses of the Isaevsk Complex. The gneisses of the investigated area are penetrated with dykes of dolerite and gabbro-diabase. They belong to at least two intrusions phases. The dolerite dykes are high metamorphic rocks. This means they were transformed in orthoamphibolite owing to regional metamorphosis. This is why they are called metadolerite (for more details see Annex). The mineralogical composition of dykes consists of plagioclase (20-60%), actinolite (5-60%) or hornblende (up to 40-45 %), diopside (3-35%) and quartz (3-10%).

Systematic petrographic and physical-mechanical studies of the rocks were provided by Krasnoyarskgeologiya in the past years, using cores of exploration boreholes. 91 thin sections were investigated in detail, 452 samples were analysed regarding their physical-mechanical and deformational behaviour and chemical (205 samples), including gamma-spectrometric analyses (101 analyses) were done. Additionally, preliminary data on the petrographic composition, on the degree of alteration, and on the petrophysical properties of the plagiogneisses were notified by Petrov et al. (2008). The data are from drill cores from boreholes E-1 to E-3 (Fig. 2-15). Owing to missing information and rock samples, especially from fault zones and lithological contacts, nothing can be said about the distribution and frequency of rocks and alteration types, or about age relationships. It also makes impossible a detailed characterization of the lithological contacts, fault zones, and jointing relevant for long-term safety analyses. The geochemical composition of the rocks has been analysed by BGR. The data on main components is given in the Tab. 3.1. The trace element composition of the samples was determined by X-ray fluorescence analysis and is presented in the Tab. 3.2. In addition, for the quantification of other trace elements the samples were analysed by ion coupled plasma mass spectrometry (Tab. 3.3).

Tab. 3.1: Main element composition of the rocks of the Yeniseysky site determined by RFA.

RFA, wt. %	Sample	rock type*	SiO2	TiO2	Al2O3	Fe2O3	MnO	MgO	CaO	Na2O	K2O	P2O5	LOI	Sum of main components
	E1_56,3	**Bg**	71.6	0.53	12.2	4.46	0.04	1.91	1.40	2.36	1.93	0.06	3.15	99.63
	E1_63,5	**Bg**	74.2	0.40	11.1	4.57	0.06	2.03	2.46	2.43	1.04	0.06	1.44	99.77
	E1_75	**Bg**	66.2	0.20	18.5	2.16	0.03	1.52	5.26	4.10	1.03	0.11	0.66	99.79
	E1_83	**Bg**	66.8	0.65	14.7	6.19	0.08	2.33	2.79	2.80	2.22	0.07	1.04	99.71
	E1_98,7	**Bg**	66.1	0.66	15.0	6.34	0.08	2.46	2.12	2.22	3.21	0.08	1.39	99.7
	E2_15,5	**Bg, w**	57.7	0.58	17.6	5.67	0.08	3.80	4.18	2.14	1.52	0.03	6.49	99.77
	E2_25,3	**Bg, w**	72.7	0.53	12.7	4.41	0.14	1.39	3.16	2.09	1.02	0.12	1.52	99.72
	E2_30,1	**Bg, w**	62.8	0.23	19.6	2.43	0.04	1.98	5.23	3.27	1.05	0.05	3.22	99.82
	E2_40,4	**Bg, w**	46.9	1.05	21.5	12.64	0.07	4.58	1.07	0.26	5.42	0.07	5.98	99.55
	E2_68,2	**Bg**	67.6	0.65	14.2	5.74	0.07	2.38	3.46	2.82	1.77	0.07	1.01	99.75
	E2_84,1	**A**	49.6	1.63	14.8	13.99	0.23	5.65	9.45	2.16	0.93	0.19	1.05	99.65
	E3_32,1	**Bg, w**	58.2	0.87	17.5	9.53	0.10	3.12	1.77	2.13	4.98	0.08	1.28	99.65
	E3_61,5	**Bg**	61.7	0.80	16.7	8.37	0.08	2.71	1.99	2.26	3.62	0.09	1.19	99.66
	E3_78,3	**Bg**	64.2	0.63	15.8	6.73	0.08	2.81	1.68	1.91	4.34	0.10	1.34	99.63

* Bg-biotite gneiss, Bg,w- weathered biotite gneiss, A- amphibolite; LOI – loss of ignition

Tab. 3.2: Composition of rocks of the Yeniseysky site according to X-ray fluorescence analysis

RFA, mg/kg	Sample:	rock type*	As	Ba	Ce	Co	Cr	Cs	Cu	Ga	Hf	La	Nb	Nd	Ni	Pb	Rb	Sc	Sm	Sn	Sr	Ta	Th	V	Y	Zn	Zr
	E1_56,3	**Bg**	2	131	61	12	75	<3	14	16	<7	14	29	28	27	73	90	8	17	1303	94	31	12	71	11	69	178
	E1_63,5	**Bg**	<1	167	113	11	76	<3	15	14	<7	55	15	53	26	71	46	17	<15	87	169	14	22	56	21	75	183
	E1_75	**Bg**	<1	204	24	7	39	<3	7	16	<7	<13	7	<16	9	52	38	5	<14	315	446	5	<3	26	3	35	38
	E1_83	**Bg**	<2	572	72	18	90	<3	6	19	8	27	13	39	41	38	110	16	<16	107	183	<5	17	82	17	82	185
	E1_98,7	**Bg**	<2	841	55	19	98	5	<3	20	<7	28	11	<17	45	27	143	18	<16	24	137	<5	18	94	14	88	256
	E2_15,5	**Bg, w**	<1	371	25	21	99	<3	8	20	<7	<13	6	<16	48	26	72	15	<15	49	227	<5	<3	97	4	67	75
	E2_25,3	**Bg, w**	5	460	91	9	58	<3	22	16	8	32	14	27	27	19	45	11	<15	21	328	<5	18	67	22	59	182
	E2_30,1	**Bg, w**	2	187	18	9	48	<3	6	17	<7	<13	4	<16	20	23	41	6	16	51	332	<5	<3	35	<3	31	46
	E2_40,4	**Bg, w**	3	1420	133	33	142	<3	<3	42	<8	60	20	54	72	25	155	32	<17	10	47	<6	30	215	33	182	181
	E2_68,2	**Bg**	<2	316	89	16	67	<3	3	19	<7	46	8	40	28	29	71	14	18	61	214	<5	18	86	19	74	218
	E2_84,1	**A**	2	222	21	42	167	8	165	21	<8	<14	10	34	73	10	31	37	<18	15	165	10	4	330	32	145	152
	E3_32,1	**Bg, w**	2	1113	99	27	101	<3	12	28	<8	49	13	47	54	35	200	20	<17	17	142	<6	25	139	25	139	172
	E3_61,5	**Bg**	<2	992	124	22	87	<3	6	25	<7	50	13	57	47	26	138	16	<16	7	162	<5	26	116	28	93	195
	E3_78,3	**Bg**	2	1170	123	17	66	<3	5	24	12	56	15	57	35	26	166	16	<16	18	200	<5	29	83	35	97	278

* Bg-biotite gneiss, Bg,w- weathered biotite gneiss, A- amphibolite

Tab. 3.3: Composition of rocks of the Yeniseysky site according to ion coupled plasma mass spectrometry analysis

ICP, mg/kg	Sample:	rock type*	As	Ba	Ce	Co	Cr	Cs	Cu	Ga	Hf	La	Li	Mn	Nb	Ni	Pb	Rb	Sc	Sr	Ta	Th	U	V	Y	Zn	Pr
	E1_56,3	**Bg**	1.48	141	69	14	68	2.2	11	17	4.1	34	23	269	21.1	29	73	100	9	100	24.4	12	1.9	75	11.1	74	7.9
	E1_63,5	**Bg**	1.76	180	117	14	72	0.9	9	19	3.4	57	17	455	15.7	26	78	50	21	190	15.1	24	1.3	68	18.7	81	13.4
	E1_75	**Bg**	0.61	214	11	8	42	1.0	6	18	1.7	5	17	257	8.0	10	53	46	5	493	8.5	0	0.3	29	4.5	38	1.3
	E1_83	**Bg**	1.05	578	65	19	88	1.4	3	20	4.4	32	23	589	8.4	40	44	113	17	196	2.6	15	1.1	97	9.2	90	6.9
	E1_98,7	**Bg**	0.99	824	53	22	94	2.0	2	22	5.2	27	25	562	9.8	46	27	144	20	144	3.1	17	1.2	106	8.7	91	5.6
	E2_15,5	**Bg, w**	0.40	365	19	22	98	1.4	11	21	3.1	9	19	583	6.6	49	26	72	17	240	1.3	1	0.6	112	3.5	71	1.8
	E2_25,3	**Bg, w**	0.78	446	65	10	51	0.6	24	18	6.0	33	10	988	10.2	21	21	49	12	346	4.4	11	1.8	75	17.6	61	7.2
	E2_30,1	**Bg, w**	0.42	169	7	9	50	0.7	9	18	2.3	3	12	255	3.7	21	23	9	5	330	1.2	0	0.2	34	2.3	32	0.9
	E2_40,4	**Bg, w**	1.00	1383	89	37	143	1.7	1	44	4.1	44	35	475	16.6	72	27	157	36	47	1.6	18	2.3	228	18.2	182	10.4
	E2_68,2	**Bg**	0.96	313	83	16	67	0.7	2	22	4.4	43	16	500	5.8	28	29	64	15	225	1.4	16	1.0	99	14.2	78	9.4
	E2_84,1	**A**	0.98	217	36	44	158	1.5	188	21	4.6	16	8	1455	10.0	70	13	35	37	162	1.4	4	1.0	336	34.6	135	4.5
	E3_32,1	**Bg, w**	0.96	1030	75	26	98	2.8	5	28	3.1	36	24	692	9.0	53	32	163	19	138	0.8	16	1.3	145	13.2	136	8.9
	E3_61,5	**Bg**	0.84	842	66	21	83	1.8	1	24	3.2	30	18	532	9.1	44	21	66	14	150	1.2	15	1.2	119	11.3	93	7.7
	E3_78,3	**Bg**	0.73	903	54	17	64	1.9	1	24	7.6	23	18	542	12.5	33	25	51	12	173	0.9	15	2.1	98	11.0	95	6.4

ICP, mg/kg	Sample:	rock type*	Nd	Sm	Eu	Gd	Tb	Dy	Ho	Er	Tm	Yb	Lu
	E1_56,3	**Bg**	29	4.9	1.0	4.3	0.5	2.5	0.4	1.1	0.1	0.7	0.1
	E1_63,5	**Bg**	49	8.3	1.2	7.2	0.9	4.1	0.7	1.8	0.2	1.3	0.2
	E1_75	**Bg**	5	1.1	0.4	1.0	0.1	0.8	0.2	0.5	0.1	0.4	0.1
	E1_83	**Bg**	26	4.5	1.2	4.0	0.5	2.2	0.4	0.9	0.1	0.6	0.1
	E1_98,7	**Bg**	21	3.6	1.1	3.3	0.4	1.9	0.3	0.9	0.1	0.6	0.1
	E2_15,5	**Bg, w**	7	1.2	0.4	1.1	0.1	0.7	0.1	0.4	0.1	0.5	0.1
	E2_25,3	**Bg, w**	27	4.9	1.1	4.5	0.6	3.4	0.7	1.8	0.2	1.6	0.2
	E2_30,1	**Bg, w**	3	0.7	0.2	0.6	0.1	0.5	0.1	0.3	0.0	0.2	0.0
	E2_40,4	**Bg, w**	37	6.8	1.2	6.2	0.8	4.1	0.7	1.8	0.2	1.2	0.2
	E2_68,2	**Bg**	33	5.6	1.3	5.0	0.6	3.1	0.5	1.4	0.2	1.1	0.2
	E2_84,1	**A**	20	5.0	1.5	5.8	1.0	6.2	1.3	3.7	0.5	3.5	0.5
	E3_32,1	**Bg, w**	32	5.9	1.3	5.3	0.7	3.2	0.5	1.3	0.1	0.7	0.1
	E3_61,5	**Bg**	30	5.5	1.1	4.9	0.6	3.1	0.5	1.2	0.1	0.6	0.1
	E3_78,3	**Bg**	25	4.9	0.8	4.5	0.6	3.2	0.5	1.3	0.2	0.9	0.1

* Bg-biotite gneiss, Bg,w- weathered biotite gneiss, A- amphibolite

The mineralogical compositions of the samples analysed petrographically by Petrov et al. (2008) are given in Tab. 3.4. Only one sample from the coarse porphyric gabbro diabase (sample E2-84.1) was available. Most of the samples show distinct evidence of metasomatism. Some of the samples show distinct signs of deformation – they are in part cataclastic, brecciated and jointed, whereby most joints have a mineral filling. Samples from borehole E-1 (Fig. 2-15), which is the furthest from the contact of the gneisses with the Nizhnekansky granitoids, show much less cataclastic deformation than the rocks from boreholes E-2 and E-3.

Microscopic analyses were conducted to determine the degree of metasomatism and to assess the influence of alteration on the petrophysical properties (Petrov et al., 2008). Weathering has formed smectite, illite-smectite, kaolinite, and sometimes vermiculite in most of the samples collected near the ground surface. The occurrence of these clay minerals in the altered samples increases the capacity of sorption of radionuclides by the geological barrier. Altered samples from greater depths often contain secondary sericite, chlorite, and carbonate. Talc was identified by radiography in the gabbro-diabase.

Tab. 3.4: Mineralogical composition of rocks of the Yeniseysky site (investigation of core samples from the boreholes E-1 to E-3, Petrov et al., 2008)

№	Rock	Depth (m)	Q, %	Pl, %	Am, %	Bt, %	Mu, %	Kfs, %	Ser, %	Chl, %	Kar, %
E1-56.3	Biotite plagiogneiss	56.3	30	20				10	15	15	8
E1-63.5	Biotite granitgneiss	63.5	35	20		10		15	8	6	3
E1-75.0	Plagiogneiss	75.0	30	37		9		10	(8)		2
E1-83.0	Biotite plagiogneiss	83.0	25	30		15		15	5	(15)	
E2-40.4	Muscovite biotite-rich gneiss	40.4				34	35		20		
E2-68.2	Muscovite biotite plagiogneiss	68.2	25	25		20	10	10			
E2-84.1	Amphibolite gabbro-diabas	84.1		30	41				10	5	
E3-32.1	Muscovite biotite plagiogneiss	32.1	25	30		25	13	5			
E3-61.5	Muscovite biotite plagiogneiss	61.5	20	30		28	15	5			

Legend: Q – quartz, Pl – plagioclase, Am – amphibole, Bt – biotite, Mu – muscovite, Kfs – orthoclase feldspar, Ser – sericite, Chl – chlorite, Kar - carbonate

The rocks of the Yeniseysky area are more heterogeneous (frequently alternating lithologies) and usually exhibit multi-phase metasomatism, when comparing with data for the granitoids of the Verchne-Itatsky area within Nizhnekansky granitoid complex (Laverov et al., 2002). The contact of gneisses with intrusive bodies in the Yeniseysky area has an especially strong metasomatism. This is logical when considered that these are zones of weakness during deformation and metamorphism. For the investigation of a potential repository site, these zones should be especially looked for and characterized in detail.

In addition to petrographic studies on rock samples from boreholes E1, E2 and E3, six samples of crystalline rocks (gneisses, migmatite and metadolerite) drilled in the Krasnoyarsk area in 2013 (borehole R-12) were investigated using a petrographic microscope and a medical computertomograph (see Annex). The aim of the study was to reveal the deformation microstructures, deformation mechanisms and conditions of deformations. Particular attention was paid to possible open pores and fractures, which could serve as pathways for fluid phases.

The gneisses are probably paragneisses (metasediments) because of roundish zircons, which are accessory minerals interpreted to be detrital. During orogenesis (mountain-building processes), these metasediments underwent both volume diffusion and dislocation creep under high-grade metamorphic conditions as is indicated by serrated phase boundaries between feldspar and quartz and by perpendicular sets of subgrain boundaries in quartz, the latter suggesting deformation in the high-quartz field at T >650°C (see Annex). The anatectic melt and the growth of randomly oriented laths of orthopyroxene post-date this deformation phase. Both the orthopyroxene and the minerals of the leucosomes (quartz, plagioclase, muscovite) are entirely free from high-temperature deformation fabrics.

The intrusion of the (meta)dolerite, on the other hand, postdates the anatectic event. The metadolerite is not foliated and does not show any ductile deformation fabric. However, the metadolerite was deformed in the brittle field under metamorphic conditions of the prehnite-actinolite facies (T = 240-350 °C, P <2 kbar). During this deformation phase discrete dilational shear zones and extensional veins developed, which are mineralized with prehnite, actinolite, chlorite, and calcite. As the calcite of these structures is not twinned, the differential stress since the formation of these brittle structures was very low, and significant deformation did probably not occur.

Despite the presence of the late brittle structures, there is no evidence for open fractures and open pores, which could serve as pathways for fluids (see Annex). This is valid for all of the investigated rocks.

3.2 Physical properties

Petrov et al. (2008) determined the saturation rate with water by hydrostatic weighting and the effective porosity of eight plagiogneiss and one gabbro-diabase samples (Tab. 3.5). The effective porosity of most of the samples was less than 0.5 %, only the samples from weathered, near-surface zones exhibited higher porosities (1.45 and 3.48 %). The porosity decreased with increasing depth of the sample, and the time to saturate the sample increased. The results are not representative owing to the small number of samples, but are in the range of normal values for granitoids or gneisses (for example, see Laverov et al., 2002).

New measurements of the petrophysical properties were conducted between 2013 and 2015 for different samles of the borehole R-12. The bulk density, grain density, total porosity, and the effective porosity are summarised in Tab. 9.5. The bulk density of the samples ranges from 2655 m^3 kg^{-1} to 3485 m^3 kg^{-1} with a mean value of 2890 m^3 kg^{-1}. The dolerite and the contact between the dolerite and the lamprohyre are observed to have a higher bulk density than the plagiogneisses. A dependence of the bulk density on the depth could not be noticed. The grain densities are in the same range as the bulk densities. They vary between 2728 m^3 kg^{-1} and 3509 m^3 kg^{-1} with a mean value of 2956 m^3 kg^{-1}. The total porosity is generally below 3 % with an outlier at 7.37 %. The archimedic determination of the total porosity confirms the values below 3 %. Again, there is no dependence of the porosity on the depth of the samples. The effective porosity was quantified for all samples. It ranges between 0.15 % and 1.49 % with a mean at 0.48 %. Only the migmatite samples from ca. 577 m bgs show an elevated effective porosity with values at 1.49 % and 1.06 %. These samples showed the highest total porosities of 2.62 % (archimedic determination) and 2.86 %, respectively. All other samples showed effective porosities below 0.6 %. These values are in good agreement with the analyses by Petrov et al. (2008).

The water content at reception of the samples and the water content of the saturated samples are listed in Tab. 9.6. The water content at reception was measured to vary between 0.04 and 0.16 %. These values are not significant regarding the long transport times of the samples. Nevertheless, they can be an indication of the low porosities of the samples. The saturated water content, determined during the analyses of the thermo-physical properties of

the samples, varies between 0.05 and 0.56 %. The saturated water content correlates with the water content at reception, but no dependency on the depth or the mineralogical composition of the samples can be identified.

The geomechanical properties of the rocks envisaged for the repository as well as the behaviour of the rock under stress and heat must be assessed for the long-term safety analysis. This data together with information on the distribution of rock types with different geomechanical and thermo-physical properties is needed to predict the behaviour of the rocks in the near and far-fields of the repository, for the planning of the mining work and for modelling the migration of radionuclides. High-grade metamorphic rocks usually have strongly pronounced anisotropies with respect to composition and petrophysical properties as a result of intensive regional metamorphism. Textures in rocks of the Yeniseysky site that are typically associated with elevated anisotropy and inhomogeneous, oriented distribution of the mineral components are shown in Fig. 3-1 and Fig. 3-2.

Tab. 3.5: Saturation behaviour, effective porosity and mineral density of samples of Yeniseysky site (Petrov et al., 2008)

No	A, %	m1, %	m2, %	m3, %	m4, %	m5, %	P_{eff}, %	T ½ hour	ρ, g/cm^3
Time of Saturation:	1min	10 min	70 min	24 h	72 h	168 h			
E1-56.3	0.10	0.15	0.30	0.80	0.10	0.00	1.45	2.8	2.73
E1-63.5	0.00	0.08	0.08	0.16	0.04	0.00	0.36	1.7	2.79
E1-75.0	0.00	0.04	0.04	0.16	0.12	0.00	0.36	7.8	2.71
E1-83.0	0.00	0.14	0.09	0.05	0.09	0.00	0.37	0.5	2.77
Average value	0.02	0.1	0.13	0.29	0.09	0	0.64	3.21	2.75
E3-32.1	0.05	0.05	0.10	0.14	0.10	0.00	0.43	3.30	2.82
E3-61.5	0.04	0.04	0.00	0.08	0.12	0.00	0.29	24.0	2.84
Average value	0.04	0.04	0.05	0.11	0.11	0	0.36	13.6	2.83
E2-40.4	0.31	0.78	1.04	1.24	0.00	0.10	3.48	0.8	2.82
E2-68.2	0.04	0.00	0.04	0.12	0.08	0.00	0.29	8.8	2.79
E2-84.1	0.04	0.00	0.04	0.16	0.21	0.04	0.49	26.8	3.00
Average value	0.13	0.26	0.37	0.51	0.1	0.05	1.42	12.1	2.87

Legend: A – “immediate saturation”, m – degree of volume saturation by different time intervals, P_{eff} – effective porosity, T ½ - mid-time of saturation, ρ – mineral density

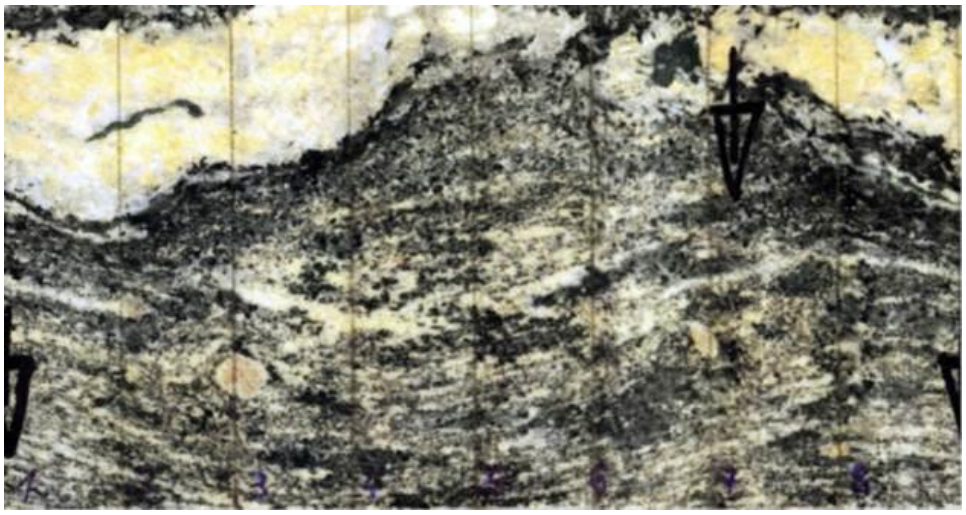

Fig. 3-1: View of the surface of a heterogeneous composed core cylinder (sample E3-78,3) for illustration of the rocks texture (height of the cylinder is ca. 5 cm)

Fig. 3-2: View of the surface of a core cylinder (sample E3-61,5) for illustration of the rocks texture (height of the cylinder is ca. 7 cm)

Ultrasonic measurements were made on several drill cores to characterize lithological inhomogeneities more exactly and to determine microscopic joints (potential groundwater migration paths). The velocities of the acoustic waves in both the axial and radial directions in the sample cylinders were measured and are compiled in Tab. 3.6 and Tab. 3.7. These values were used to calculate the dynamic elasticity of the samples (Tab. 3.7 and Tab. 3.8).

Tab. 3.6: Results of the ultrasonic transmission of the samples from the Yeniseysky site - V_p and V_s in axial and radial direction under dry and wet conditions (Petrov et al., 2008)

	Axial direction				**Radial direction**			
sample	V_P, Dry km/s	V_S, Dry km/s	V_P, Wet km/s	V_S, Wet km/s	V_P, Dry km/s	V_S, Dry km/s	V_P, Wet km/s	V_S, Wet km/s
E1-63.5	5.584	3.587	5.808	3.583	5.808	3.621	5.941	3.641
E1-75.0	6.105	3.471	6.165	3.197	6.166	3.572	6.207	3.582
E1-98.7	5.544	3.502	5.800	3.496	5.607	3.470	5.848	3.505
E2-15.5	1.474	1.081*	--	--	3.379	1.593	3.555	--
E2-68.2	5.591	4.097	5.641	4.11	5.844	3.523	5.912	3.488
E2-84.1	6.317	3.685	6.366	3.752	6.419	3.714	6.428	3.718
E3-61.5	5.972	3.344	5.554	3.361	5.884	3.588	5.865	3.587
E3-78.3	5.426	3.899	5.587	3.322	5.779	3.526	5.899	3.541

Comment: * - high uncertainty

The data show that besides relatively homogenous gneissic rocks with very few joints, there are also highly heterogeneous rocks that have hydraulically active joints, even down to the bottom of the 100 m deep boreholes.

Tab. 3.7: Compilation of the sound running period and of the dynamic elastic parameters for the samples from the Yeniseysky site (from: Jobmann et al., 2008)

Core (sample)	Diameter, d	Total density, ρ_{tot}	Longitudinal wave velocity, V_p	Transversal wave velocity V_s	Dynamic Young's modulus E_{dyn}	Dynamic Poisson's ratio ν
	mm	g/cm^3	m/s	m/s	MPa	-
C1 (56,3)	50.0	2.671	5070	3298	65841	0.133
C1 (63,5)	60.6	2.345	6211	3768	80486	0.209
C1 (75,0)	60.0	2.362	6601	3899	88491	0.232
C1 (83,0)	50.0	2.880	5600	3449	81848	0.195
C1 (98,7)	56.3	2.703	5459	3521	76660	0.144
C2 (15,5)	49.9	2.441	3357	2246	26964	0.095
C2 (25,3)	50.2	2.645	3108	n. m.	n. m.	n. m.
C2 (30,1)	50.0	2.465	5029	2161	31923	0.387
C2 (68,2)	53.3	2.709	5529	n. m.	n. m.	n. m.
C2 (84,1)	55.0	2.931	6410	3920	108196	0.201
C3 (32,1)	50.0	2.795	5617	3552	82301	0.167
C3 (61,5)	56.1	2.834	5760	3646	87843	0.166
C3 (78,3)	55.8	2.714	5646	3267	72319	0.248

n.m.: not measurable

Tab. 3.8: Dynamic moduli of the samples from the Yeniseysky site (calculated according to the results of the ultrasonic transmission of the samples in axial and radial direction under dry and wet conditions (Petrov et al., 2008)

	Axial direction						Radial direction					
Sample	K, GPa Dry	μ, GPa Dry	K, GPa Wet	μ, GPa Wet	ν Dry	ν Wet	K, GPa Dry	μ, GPa Dry	K, GPa Wet	μ, GPa Wet	ν Dry	ν Wet
E1-63.5	39.1	35.9	46.4	35.8	0.15	0.19	45.3	36.6	49.1	37	0.18	0.20
E1-75.0	57.5	32.7	66.1	27.7	0.26	0.32	56.9	34.6	58	34.8	0.25	0.25
E1-98.7	39.8	34.0	48	33.9	0.17	0.21	42.6	33.3	49.4	34	0.19	0.22
E2-15.5	3.3	1.7	--	--	0.28	--	22.6	7.1	--	--	0.36	--
E2-68.2	46.8	24.8	47.1	25.9	0.27	0.27	49.1	34.6	52.2	34	0.21	0.23
E2-84.1	65.4	40.7	65.2	42.2	0.24	0.23	68.4	41.4	68.7	41.5	0.25	0.25
E3-61.5	59.0	31.8	44.8	32.1	0.27	0.21	49.6	36.6	49	36.5	0.2	0.2
E3-78.3	43.0	26.0	46.7	31.2	0.25	0.23	47.6	35.2	51.2	35.5	0.2	0.22

Comments: K – Young's modulus; μ – shear modulus, ν – Poisson's ratio

The elasticity values derived from the ultrasonic measurements of the Yeniseysky samples (Tab. 3.7 and Tab. 3.8) differ only little from the values obtained for the granitoids of the Nizhnekansky pluton (Tab. 3.9) except for the near-surface sample E2-15.5. The data show that the physical-mechanical properties of the rocks depend on their structure and texture, on their mineral composition, as well as their degree of alteration or weathering. Intensively weathered rocks generally have elevated porosities and water saturation capacities, lower resistivity to compression, and are more plastic than before weathering owing to the formation of new clay minerals and chlorites. The data reflect the dependence of the deformation behaviour of a rock on its mineral composition. Rocks with low content of quartz show significantly lower strength and higher plasticity than quartz rich rocks as granite and leucogranite. When subjected to mechanical stress, quartz rich rocks tend to brittle deformation, i.e., cataclasis and joint formation.

Tab. 3.9: Compilation of the important petrophysical parameters for the rocks of the Nizhnekansky granitoid massif (Anderson et al., 1998)

Rock type	Uniaxial compressive strength, σ_{ic}, MPa	Yield point, σ_{is}, MPa	Poisson's ratio, ν	Fracture deformation, ε_{ic}, %	Plastic deformation ε_{pl}, %	Dynamic Young's modulus, $E \cdot 10^4$, MPa	Static Young's modulus, $E_{st} \cdot 10^4$, MPa
Granite	252±8	232±8	0.21±0,01	0.58	0.10	6.59±0.13	6.08±0.8
Cataclastic Granite	273	248	0,24	0.47	0.11	7.57	6.65
Granite-gneiss	298±21	248±21	0.21±0,004	0.50	0.06	7.87±0.19	6.69±0.2
gneiss	264	253	0.21	0.65	0.18	5.98	6.48
Granodiorite	175	139	0.21	0.59	0.30	7.64	5.63
Quartzdiorite	193±7	158±7	0.27±0.01	0.38	0.13	7.10±0.31	6.27±0.2
Spessartite	125	99	—	1.25	0.63	—	1.66 (?)

According to the classification of Protodyakonov (1927; see Burmistrov et al., 2009), the gneisses of the region Yeniseysky belong to relatively hard rocks and the metadolerite to the category of hard to very hard rocks. Depending on the jointing the strength limit of the gneissic samples measured by the uniaxial compressive strength test varies between 78.6 MPa to 102 MPa and for metadolerite between 117 MPa to 182 MPa (Tab. 3.10).

Tab. 3.10: Evaluation of deformation parameters of samples from depth interval 400-600 m

Grade of fissuring	Weakening coefficient	Rock type	Unconfined compressive strength, MPa					
			In the sample			In the massif		
			dry	wet	Type (GOST 2011)	dry	wet	Type (GOST 2011)
Very fissured	0.2	gneiss	78.6	42.9	medium solid	15.7	8.6	low solid
		dolerite	182.0	-	very solid	36.4	-	medium solid
Medium fissured	0.4	gneiss	99.0	77.9	solid	39.6	31.2	medium solid
		dolerite	116.8	79.7	solid	46.7	31.9	medium solid
Weak fissured	0.6	gneiss	101.9	86.1	solid	61.0	51.7	medium solid
		dolerite	123.2	109.2	solid	73.9	65.5	solid

Ultrasonic measurements performed by GRS on four samples received in 2013 showed comparable values for the determined dynamic elastic parameters Poisson's ratio and Young's modulus (Tab. 3.11 and Annex Tab. 9.3, Fig. 9-13, Fig. 9-14). No specific correlation can be identified between the dynamic elastic Young's modulus and the depth of the samples, but some conclusions may be drawn concerning the petrological properties of the samples. While the plagiogneiss samples show values in the same range, the sample from 444.83 m bgs, featuring a contact between the dolerite and the lamprophyre, shows an elevated Young's modulus. The Poisson's ratio is decreasing with depth for the plagiogneisses investigated here.

Tab. 3.11: Measured shear wave and transversal wave velocities and calculated dynamic Poisson's ratios and Young's moduli for the regarded four samples

Direction	Depth [m bgs]	v_s [m s^{-1}]	v_p [m s^{-1}]	Bulk density [kg m^{-1}]	Poisson's ratio [-]	Young's modulus [MPa]
Radial	201.14	5213	3100	3359.3	0.349	85478
	347.64	5975	3703	2716.2	0.187	88981
	444.83	6706	3945	3032.9	0.235	116614
	476.55	5537	3286	2767.7	0.226	71953
Axial	201.14	5578	2831	3359.3	0.316	72341
	347.64	5622	3423	2716.2	0.205	76735
	444.83	6721	3918	3032.9	0.242	115675
	476.55	5389	3389	2767.7	0.172	74537
Mean	201.14	5395	2965	3359.3	0.342	82558
	347.64	5798	3563	2716.2	0.191	82754
	444.83	6714	3931	3032.9	0.237	116379
	476.55	5463	3338	2767.7	0.211	72691

Triaxial tests were performed to determine the static elastic parameters, such as the deviatoric stress, axial deformation, the Young's modulus and Poisson's ratio. In addition to this, the gas permeability was determined in these triaxial experiments. All results are described in detail in chapter 9.1.5. Only four samples were analysed via triaxial tests. The failure behaviour, i.e. deviatoric pressure and the respective axial deformation are depicted in Fig. 9-16. Two of the samples show distinct failure behaviour with failures at a lower deviatoric pressure than the other two samples. The sample of the contact of the dolerite to the lamprophyre shows a higher axial deformation at a lower deviatoric pressure. The sample from the deepest depth at ca. 477 m shows an indefinite failure behaviour due to the absence of a distinct failure state.

As described above (chapter 2.6), there is no clear trend in the permeability of the samples depending on their depth (Fig. 9-18 to Fig. 9-20). All permeability data determined for the drill core samples received in 2013 show the same trend. There is a decreasing trend of the permeabilities of the plagiogneisses with depth. Higher permeability values were determined in the triaxial tests than in the permeability tests. This may be due to the fact that here, pressure was already applied to the samples and new pathways for flow may have been opened during determination of the parameters.

The static Young's modulus of the four samples is in the range of those given in Tab. 3.9. As stated above, the samples with a lower quartz content show a lower strength than those with a higher quartz content. This can be observed in Fig. 9-21 to Fig. 9-24. The plagiogneiss samples feature a significantly higher static Young's modulus than the dolerite. Comparing the dynamic and the static Poisson's ratio (Fig. 9-25 to Fig. 9-28), the results are in the same order of magnitude. Here again, the petrography plays a dominant role in the sample's deformation behaviour. Details on the triaxial tests and their results are given in chapter 9.1.5.

Supplementary investigations of the thermo-physical properties of the drill cores from boreholes E-1 – E-3 were conducted. The results are compiled in Tab. 3.12 (Petrov et al., 2008). The range of variations of the thermo-physical parameters for the granitoids of the Nizhnekansky massif (thermal diffusivity: 6.0 - 15.6·10^{-7} m^2s^{-1}, specific heat capacity: 765 - 1100 J·$kg^{-1}K^{-1}$, thermal conductivity: 1.7 - 3.4 W·$m^{-1}K^{-1}$) differs little from the values for the gneisses of the Yeniseysky site (thermal diffusivity: 5.8 - 15.9·10^{-7} m^2s^{-1}, specific heat capacity: 780 - 980 J·$kg^{-1}K^{-1}$, thermal conductivity: 1.5 - 3.4 W·$m^{-1}K^{-1}$).

Tab. 3.12: Thermo-physical properties of rocks from the borehole E-1, E-2 and E-3 (Petrov et al., 2008)

№	Rock type	Density ρ, kg m^{-3}	Thermal parameters	T = 18°	T = 100°	T = 200°
E1-56.3	Biotite-plagiogneiss	2590	a / 10^{-7} m^2s^{-1} c_p / J kg^{-1} K^{-1} λ / W m^{-1} K^{-1}	15.4 780 3.1	11.2 890 2.5	8.5 980 2.1
E1-63.5	Biotite-granit-gneiss	2700	a / 10^{-7} m^2s^{-1} c_p / J kg^{-1} K^{-1} λ / W m^{-1} K^{-1}	15.9 780 3.3	12.1 890 2.9	9.0 980 2.4
E1-75.0	Plagiogneiss	2740	a / 10^{-7} m^2s^{-1} c_p / J kg^{-1} K^{-1} λ / W m^{-1} K^{-1}	14.5 780 3.1	10.4 890 2.5	7.4 980 2.0
E1-83.0	Biotite-plagiogneiss	2670	a / 10^{-7} m^2s^{-1} c_p / J kg^{-1} K^{-1} λ / W m^{-1} K^{-1}	15.6 780 3.25	11.4 890 2.7	8.7 980 2.3
E2-40.4	Muscovite biotite-rich gneiss	2665	a / 10^{-7} m^2s^{-1} c_p / J kg^{-1} K^{-1} λ / W m^{-1} K^{-1}	12.4 (11.1) 800 (800) 2.65 (2.35)	8.8 (7.7) 910 (910) 2.1 (1.85)	6.5 (5.8) 980 (980) 1.7 (1.5)
E2-68.2	Muscovite biotite-plagiogneiss with amphibole	2720	a / 10^{-7} m^2s^{-1} c_p / J kg^{-1} K^{-1} λ / W m^{-1} K^{-1}	15.2 800 3.3	11.0 910 2.7	8.3 990 2.2
E2-84.1	Amphibolite gabbro-diabas	2910	a / 10^{-7} m^2s^{-1} c_p / J kg^{-1} K^{-1} λ / W m^{-1} K^{-1}	14.5 780 3.3	10.2 890 2.65	7.2 980 2.05
E3-32.1	Muscovite biotite-plagiogneiss	2735	a / 10^{-7} m^2s^{-1} c_p / J kg^{-1} K^{-1} λ / W m^{-1} K^{-1}	14.5 800 3.15	10.1 910 2.5	7.2 980 1.9
E3-61.5	Muscovite biotite-plagiogneiss	2730	a / 10^{-7} m^2s^{-1} c_p / J kg^{-1} K^{-1} λ / W m^{-1} K^{-1}	14.1 800 3.1	10.1 910 2.5	7.2 980 1.9

Comments: a – thermal diffusivity, c_p - specific heat capacity, λ - thermal conductivity. For the sample E2-40.4 in the brackets are the results of a repeating analysis.

The rocks of the gneiss complex generally have a good thermal conductivity as a result of the relatively high contents of the good heat-conducting minerals as quartz, feldspar, and amphibole (in the basic rocks). The parts of the complex with a high mica content (e.g., sample E2-40.4) have a significantly lower thermal conductivity, which can lead to heat accumulation if these parts are large enough. For this reason, these rocks must be well mapped during the geological exploration of the repository site.

It is significant that the thermo-physical values of the gabbro-diabase sample (E2-84.1) are not different from those of the plagiogneisses. The spessartite vein in the Nizhnekansky granitoid massif has significantly lower thermal diffusivity and thermal conductivities (4.2 – $5.5 \cdot 10^{-7}$ m^2s^{-1}, 1.31 - 1.52 $W \cdot m^{-1}K^{-1}$) and higher heat capacities (1020 - 1150 $J \cdot kg^{-1}K^{-1}$), and thus is apparently an especially strongly altered rock type.

Samples received in 2013 were also tested for their thermo-physical properties (Annex, chapter 9.1.3). The specific heat capacity, the heat conductivity and the thermal diffusivity were determined for dry samples in dependence on the temperature ranging from 25 °C to 150 °C. Additionally, samples saturated with water were investigated for the thermo-physical parameters at 25 °C. The temperature dependent thermal conductivity of the dry samples (Tab. 9.7) is in the range of those determined before (Tab. 3.12). The trend of decreasing thermal conductivity with temperature can also be observed for the samples from borehole R-12. A maximum thermal conductivity of 3.869 $Wm^{-1}K^{-1}$ was detected for the migmatite from ca. 460 m depth, while a minimum value of 2.159 $Wm^{-1}K^{-1}$ was observed for the sample from the contact of the dolerite to the lamprophyre from a depth of ca. 418 m. This sample shows an unspecific trend in the thermal conductivity (Fig. 9-6) with the lowest values at the higher temperatures. The thermal diffusivity of the samples differs more at lower temperatures than at higher temperatures (Fig. 9-7). The minimum value of all samples is at $0.849 \cdot 10^{-7}$ m^2 s^{-1}

and the maximum value at $2.097 \cdot 10^{-7}$ m^2 s^{-1}. The specific heat capacity (Fig. 9-8) is generally rising with increasing depth, while the sample from ca. 417 m bgs again is featuring a different trend. No significant difference between the results for the dry and the saturated samples (Tab. 9.10) could be identified during the measurements. This is caused by the low porosities and low water contents of the saturated samples, indicating that the rock matrix is the crucial factor determining the thermo-physical properties.

Studies of sorption behaviour of radionuclides on five rock samples drilled in the deep borehole R12 in the exocontact zone of Nizhnekansky granitoid massif (Yeniseysky site) in the range of depth 166 m – 477 m bgs were carried out. The sorption kinetics and Kd values of the long-lived radionuclides of different chemical behaviour $^{135+137}Cs$, ^{226}Ra, ^{79}Se, $^{237+239}Np$, $^{239,240}Pu$, $^{241,243}Am$ were determined (see Annex). Experiments were performed under the conditions that are relevant for the future high level waste disposal (atmosphere; composition, pH and Eh of the solutions). Digital radiography demonstrated uneven sorption of all the investigated radionuclides and revealed phases with higher sorption capacity. It was established that sorption of metal cations is fast and reaches steady state in a few hours, while Se in the form of selenate-ion sorbs insignificantly.

3.3 Fault zones and fissure systems

In contrast to porous sedimentary host rocks the radionuclide migration through a magmatic/metamorphic rock complex takes place only subordinately through the effective pore space, but predominantly through fissures or joints. The studied Yeniseysky site is characterized by the occurrence of fissures, open to groundwater flow, and distinct foliation, like each metamorphic rock massif. It represents a heterogeneously composed gneissic complex that is penetrated by numerous steeply dipping basic dykes. The fissure zones that were identified during the geological exploration of the region have a thickness of 1-4 cm and a dip of 15-35°. In all cases the fissures are filled with carbonate and feldspars and rarely with quartz.

The steeply dipping (65-70°) basic dykes separate the gneisses into blocks. The distance between the dykes (in direction from West to East) amount 10-30 m to maximal 100-150 m. According to Lukina (2001) the Yeniseysky area represents a tectonically stable block. Newly originated, not healed fault zones were not identified. The observed fissures have no continuous connection and are developed only on short distances. The fissures frequency of the rocks in the deep interval 400-600 m is characterized by fissures modulus M_{fi} = 3-5 (M_{fi} = amount of fissures per meter). Higher fissures modules (10-18) show the contact areas of some dolerite dykes. The length of the fissures is less than 5-7 cm (Beygul et al., 2011).

4 Waste characterization

4.1 HLW from reprocessing

Reprocessing of defence reactor fuel at the Kyshtym site began in 1949 with a process involving sodium uranyl acetate precipitation from nitric acid solution. Reprocessing of commercial reactor fuel is reported to have started in 1976-1978 at the RT-1 plant of the combine "PO MAYAK" at Kyshtym BN-350, BN-600, WWER-440 and naval reactor fuel (Bates et al., 1994; Jain, 1998; Makarchuk et al., 1999). The technology for WWER-440 spent fuel reprocessing is based on the PUREX process. The partition factors from fission products are $1 \cdot 10^7$ for uranium and $1 \cdot 10^8$ for plutonium (Makarchuk et al., 1999).

As of 1994, research had been reported to be conducted in the Russian Federation on separation or partitioning of element fractions from liquid radioactive waste using cobalt dicarboly anion in strong HNO_3, which is especially effective for large ions (Bates et al., 1994). The efficiency of separation of strontium, caesium, rare earths, and transuranic elements had been reported there to reach up to 99%. The use of transmutation for further treatment of a mixture of lithium and transuranic waste (~35% Np-237, ~27% Am-241, and ~44% Cm) in a heavy water reactor had been suggested (Bates et al., 1994). In August 1996 then, a semi-industrial facility was commissioned at the RT-1 plant, which indeed provided a partition of Np-237 from the vitrified waste stream (Makarchuk & Kudryavtsev, 2005).

During the first 10 years of the plant operation, about 2,000 t of civilian reactor fuel were reprocessed (Bates et al., 1994). As of 1998, about 3,000 t of spent fuel were reprocessed (resulting in an accumulation of ~30 t plutonium) (Makarchuk et al., 1999), and this amount increased to about 3,300 t by 2005 (Makarchuk & Kudryavtsev, 2005) and to about 4,000 t by 2008 (Khaperskaya & Kudryavtsev, 2008).

The liquid wastes from reprocessing are vitrified into a final volume of 100–150 l/tU (Bates et al., 1994). 200 l of phosphate glass (vitrified at 1,100–1,150°C (Makarchuk et al., 1999)) are filled in a mild steel pour canister in a batch process with a pour time of 1 to 2 min (Jain, 1998). After lids are welded, three canisters are placed without a preceding decontamination in a stainless steel container, which is then welded up. Except for the visual inspection, there are no leak checks or other quality checks of the welds (Jain, 1998). The containers are placed in a storage building that is designed to cool container heat loads of up to 5 kW/m^3 by a forced-air circulation (Jain, 1998; Makarchuk et al., 1999).

Between 1967 and 1987, several pilot-scale vitrification plants were designed and operated in Russia using non-radioactive simulated wastes as well as radioactive wastes. The first large-scale, liquid-fed melter at Chelyabinsk-65 in Kyshtym started operation in 1986 and was commissioned in February 1987. The melter suffered an electrode failure after twelve months in operation. Between 1987 and 1988, the HLW vitrification facility produced 160 tons of phosphate glass containing $1.4 \cdot 10^{17}$ Bq of radioactivity (Jain, 1998). A second melter, similar in design, started testing operations in December 1990 and was commissioned for radioactive operations on June 25, 1991. This melter has produced more than 2,010 tons of phosphate glass containing $86.9 \cdot 10^{17}$ Bq of radioactivity. The facility was shut down in January 1997, 2.5 years past its operational design life of 3 years (Jain, 1998).

Important characteristics of vitrification process relevant for vitrified waste inventories are the use of molasses (150 g/l) in the feed to trap the volatile radionuclides (Jain, 1998; Makarchuk et al., 1999) and the collection of the steam-gas condensate, which is periodically fed for mixing with the vitrified solutions (Makarchuk et al., 1999). Phosphate glasses, unlike borosilicate glasses, offer higher sulphate solubility but have poor chemical durability and thermal stability. Indeed, at 90°C the release of Pu and Gd from the phosphate glass was 10 times greater than that from borosilicate glass, and the bulk component releases (Si, B, P, Na)

from phosphate glass was two times greater than that from borosilicate glass (Anderson et al., 2000).

4.2 Derivation of the model inventory of vitrified HLW in the Russian Federation

The Russian project partners have provided inventories of vitrified HLW produced in the Russian Federation – supposedly in Kyshtym, which are presented in Tab. 4.1 below along with the data for vitrified waste produced in La Hague. Interestingly, the ratios of two target nuclides of the PUREX process, U-238 and Pu-239, coincide up to the first decimal place, which agrees with the above-discussed statement about the PUREX-based reprocessing at Kyshtym. However, the inventories of transuranic elements Np-237, Am-241, and Am-243 in Russian vitrified waste show remarkable deviations from those reported for vitrified waste from La Hague (Meleshyn & Noseck, 2012).

As mentioned above, since 1996, a semi-industrial facility was commissioned at Kyshtym, which provided a partition of Np-237 from the vitrified waste stream (Makarchuk & Kudryavtsev, 2005). An intention to partition Np-237, Am-241, and Cm in the Russian Federation for a future transmutation was reported earlier as well (Bates et al., 1994). Therefore, it can be assumed that the facility commissioned in 1996 or another facility commissioned later on provides an effective separation of transuranic elements from the reprocessing waste. A similar conclusion can be drawn for fission products regarding the inventories of Se-79, Tc-99, and Cs-135 decreased by a factor of about 6 to 7 in Russian vitrified waste as compared to that from La Hague and the reported effective experimental separation of strontium, caesium and rare earths in Russian Federation (Bates et al., 1994).

Based on the reported production of 2170 t of vitrified waste at Kyshtym till January 1997 (Jain, 1998) and considering that the facility for partitioning the transuranic elements was commissioned in August 1996 (Makarchuk & Kudryavtsev, 2005), it should be concluded that the data on vitrified waste from Kyshtym in Tab. 4.1 may be representative only of the waste produced within half a year. This waste may be estimated to contribute about 10% to the total amount of waste produced in Kyshtym considering the total operational time of 5.5 years of the second melter, which produced a total of 2010 t of glass (Jain, 1998).

Tab. 4.1: Inventories of radionuclides in vitrified waste (g/tU) from Kyshtym, according to the data provided by VNIPI PT, and La Hague /MEL 12/ at the time of vitrification

	^{79}Se	^{99}Tc	^{135}Cs	^{237}Np	^{238}U	^{239}Pu	^{241}Am	^{243}Am
Kyshtym	2.6	476	263	6	13.00	10	27	46
La Hague	18.8	3434	1471	1422	2112	16.3	1744	516
La Hague/ Kyshtym Ratio	7.2	7.2	5.6	237	1.62	1.63	64.6	11.2

Taking further into account that the phosphate glass produced in Kyshtym has a density of 2,500 kg/cm^3, as reported by VNIPI PT, a total of 2,170 t of the vitrified waste production at Kyshtym till 1997 (Jain, 1998) would correspond to about 5800 tU of reprocessed spent nuclear fuel. This amount is well above the reported amount of 3000 t of commercial spent fuel reprocessed at Kyshtym till 1997 (Makarchuk et al., 1999) possibly due to the reprocessed defence reactor fuel.

Based on the volume of 200 l in each of the three canisters within a container as discussed above (Jain, 1998) and the volume of vitrified liquid wastes of 150 l/tU from reprocessing (Bates et al., 1994), one container to be disposed of at the site Yeniseysky contains a waste amount derived from reprocessing of 4 tU. Accordingly, one borehole contains the reprocessing equivalent of 24 tU and the whole repository may contain the reprocessing waste equivalent of ~18,200 tU (assuming that about 4,550 containers are to be disposed of). Thus, the vitrified waste produced at Kyshtym till 1997 corresponds to ~30% of the total projected amount of the vitrified waste to be disposed of at that site.

Considering the above arguments, two source terms may be suggested for the vitrified waste at the site Yeniseysky. The first source term, which applies to ~90% of the vitrified waste produced at Kyshtym till 1997 and to ~30% of the projected vitrified waste amount, may be conservatively assumed to have similar inventories as the vitrified waste from La Hague (Meleshyn & Noseck, 2012) and is given in Tab. 4.2.

The second source term, which applies to ~10% of the vitrified waste produced at Kyshtym till 1997 and to ~70% of the projected vitrified waste amount to be disposed of at the site Yeniseysky, has the inventories as given in Tab. 4.3 for the isotopes listed in Tab. 4.1. For the other isotopes, the inventories given in Tab. 4.2 can be taken. However, as can be seen in Tab. 4.1, these inventories may represent very conservative estimates with probably the only exception of U and Pu isotopes. In view of the missing data, no better estimate can currently be made.

Tab. 4.2: Inventories of radionuclides in vitrified waste (at the time of vitrification) from Kyshtym based on the average data for La Hague (Meleshyn & Noseck, 2012). These inventories are derived based on the assumption that a container with the vitrified waste from Kyshtym results from reprocessing of 4 tU. Only the radionuclides relevant for long-term safety analyses of final repositories for radioactive waste are listed.

Isotope	Decay half-life	Container inventory [TBq]	Borehole inventory [TBq]
^{14}C	5730 a	$5.24 \cdot 10^{-4}$	$31.4 \cdot 10^{-4}$
^{36}Cl	$3.0 \cdot 10^{5}$ a	$3.1 \cdot 10^{-5}$	$18.6 \cdot 10^{-5}$
^{41}Ca	$9.94 \cdot 10^{4}$ a	$2.29 \cdot 10^{-4}$	$13.7 \cdot 10^{-4}$
^{59}Ni	$7.5 \cdot 10^{4}$ a	$2.6 \cdot 10^{-4}$	$15.6 \cdot 10^{-4}$
^{60}Co	5.272 a	2.352	14.11
^{63}Ni	100 a	0.0376	0.2256
^{79}Se	$3.27 \cdot 10^{5}$ a	0.0153	0.0919
^{87}Rb	$4.8 \cdot 10^{10}$ a	$3.2 \cdot 10^{-6}$	$19.2 \cdot 10^{-6}$
^{90}Sr	28.64 a	14228	85368
^{90}Y	64.1 h	14228	85368
^{93}Mo	3500 a	$1.43 \cdot 10^{-4}$	$8.58 \cdot 10^{-4}$
^{93}Zr	$1.5 \cdot 10^{6}$ a	0.404	2.424
^{94}Nb	$2.0 \cdot 10^{4}$ a	$4.11 \cdot 10^{-5}$	$24.66 \cdot 10^{-5}$
^{99}Tc	$2.1 \cdot 10^{5}$ a	3.48	20.88
$^{106}Ru + (^{106}Rh)$	373.6 d (30 s)	1740	10440
^{107}Pd	$6.5 \cdot 10^{6}$ a	0.02596	0.15576
^{125}Sb	2.77 a	164.8	988.8
^{126}Sn	$1.98 \cdot 10^{5}$ a	0.0732	0.4392
^{129}I	$1.57 \cdot 10^{7}$ a	$1.344 \cdot 10^{-4}$	$8.064 \cdot 10^{-4}$
^{134}Cs	2.06 a	2836	17016
^{135}Cs	$2.0 \cdot 10^{6}$ a	0.1148	0.6888
^{137}Cs	30.17 a	22368	134208
$^{144}Ce + (^{144}Pr)$	284.8 d (17.3 m)	1596	9576
^{151}Sm	93 a	47	282
^{154}Eu	8.8 a	680	4080
^{226}Ra	1600 a	$2.89 \cdot 10^{-8}$	$17.34 \cdot 10^{-8}$
^{227}Ac	21.773 a	$1.59 \cdot 10^{-6}$	$9.54 \cdot 10^{-6}$
^{229}Th	7880 a	$1.79 \cdot 10^{-7}$	$10.74 \cdot 10^{-7}$
^{230}Th	$7.54 \cdot 10^{4}$ a	$2.033 \cdot 10^{-5}$	$12.20 \cdot 10^{-5}$
^{231}Pa	$3.276 \cdot 10^{4}$ a	$8.03 \cdot 10^{-6}$	$48.18 \cdot 10^{-6}$
^{232}Th	$1.405 \cdot 10^{10}$ a	$1.26 \cdot 10^{-7}$	$7.56 \cdot 10^{-7}$
^{232}U	68.9 a	$2.50 \cdot 10^{-6}$	$4.64 \cdot 10^{-6}$

Isotope	Decay half-life	Container inventory [TBq]	Borehole inventory [TBq]
^{233}U	$1.592 \cdot 10^{5}$ a	$5.52 \cdot 10^{-6}$	$33.12 \cdot 10^{-6}$
^{234}U	$2.455 \cdot 10^{5}$ a	$1.17 \cdot 10^{-4}$	$7.03 \cdot 10^{-4}$
^{235}U	$7.038 \cdot 10^{8}$ a	$2.15 \cdot 10^{-6}$	$12.89 \cdot 10^{-6}$
^{236}U	$2.342 \cdot 10^{7}$ a	$2.91 \cdot 10^{-5}$	$17.45 \cdot 10^{-5}$
^{238}U	$4.468 \cdot 10^{9}$ a	$4.20 \cdot 10^{-5}$	$25.20 \cdot 10^{-5}$
^{237}Np	$2.144 \cdot 10^{6}$ a	0.0592	0.3552
^{238}Pu	87.74 a	0.56	3.36
^{239}Pu	$2.411 \cdot 10^{4}$ a	0.0596	0.3576
^{240}Pu	6563 a	0.0972	0.5832
^{241}Pu	14.35 a	17.08	102.48
^{242}Pu	$3.75 \cdot 10^{5}$ a	$4.20 \cdot 10^{-4}$	$25.20 \cdot 10^{-4}$
^{244}Pu	$8.0 \cdot 10^{7}$ a	$0.511 \cdot 10^{-10}$	$3.07 \cdot 10^{-10}$
^{241}Am	432.2 a	352.4	2114.4
^{242m}Am	141 a	1.2	7.2
^{243}Am	7370 a	6.08	36.48
^{243}Cm	29.1 a	2.65	15.9
^{244}Cm	18.1 a	584	3504
^{245}Cm	8500 a	0.0652	0.3912
^{246}Cm	4730 a	0.00406	0.02436
^{248}Cm	$3.4 \cdot 10^{5}$ a	$2.01 \cdot 10^{-8}$	$12.06 \cdot 10^{-8}$

Tab. 4.3: Inventories of the radionuclides in vitrified waste (at the time of vitrification) from Kyshtym based on the data reported by VNIPI PT (for isotopes listed in Tab. 4-1).

Isotope	Decay half-life	Container inventory [TBq]	Borehole inventory [TBq]
^{79}Se	$3.27 \cdot 10^{5}$ a	$2.0 \cdot 10^{-3}$	0.012
^{99}Tc	$2.1 \cdot 10^{5}$ a	0.454	2.73
^{135}Cs	$2.0 \cdot 10^{6}$ a	0.0193	0.116
^{238}U	$4.468 \cdot 10^{9}$ a	$2.43 \cdot 10^{-5}$	$14.6 \cdot 10^{-5}$
^{237}Np	$2.144 \cdot 10^{6}$ a	$2.34 \cdot 10^{-4}$	$14.1 \cdot 10^{-4}$
^{239}Pu	$2.411 \cdot 10^{4}$ a	0.0344	0.207
^{241}Am	432.2 a	5.14	30.9
^{243}Am	7370 a	0.51	3.06

5 Repository concept

The disposal facility of the deep underground repository has a total area of 1 km² that is intended to be built in two main stages. The main characteristics of the facility are:

Total capacity:	Disposal of up to 155,000 m³ of long-lived ILW in class 2 packages and 4,500 m³ of vitrified HLW in 7,500 class 1 containers.
Annual capacity:	Radioactive waste class 2: not less than 5,000 m³, radioactive waste class 1: 378 packages.
End of emplacement	2047

5.1 Repository layout

The first stage of the repository consists of a deep underground disposal sector with two emplacement horizons at approx. -450 m (5 m above sea level) and approx. -525 m (-70 m above sea level), respectively (Fig. 5-1).

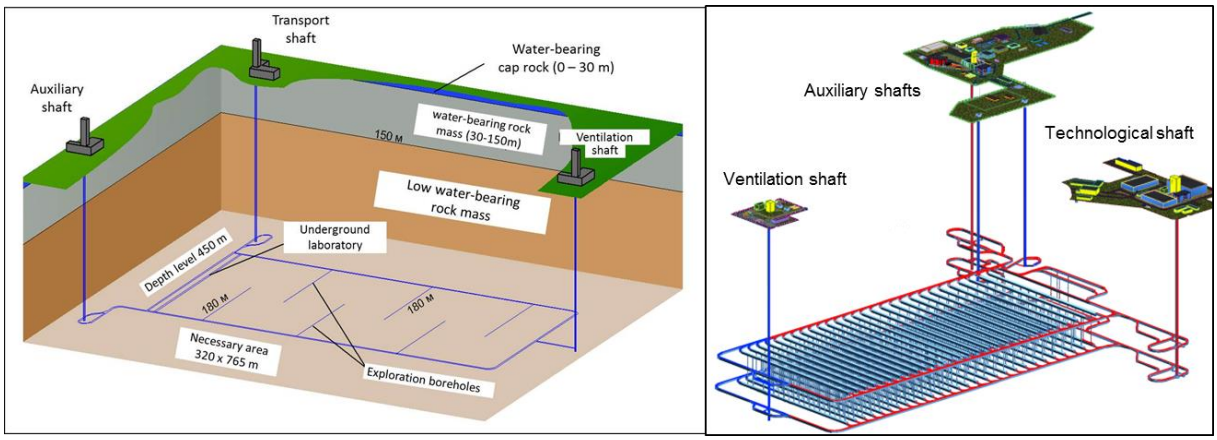

Fig. 5-1: General view of the underground area (modified after VNIPI PT, 2012 and 2013a)

Each horizon has a total of 28 emplacement drifts (Fig. 5-2), which are located between the transport drift at the beginning and the ventilation drift at the end of the emplacement horizon. Both emplacement levels are similar and cover an area of 317 m x 745 m = 236,165 m². The upper and lower levels are planned with a deviation along the horizontal axis by 4.5 m. Both horizons are joined by a ventilation, transport, and auxiliary shaft and have a joint ventilation hole for the storage of backfill material and a ventilation hole where the electric locomotive is charged.

An emplacement horizon consists of:

- near-shaft drifts for the storage of backfill material, for the underground laboratory and the connection between them
- excavations necessary for work in the emplacement level and
- the technological drifts for the emplacement of the long-lived high and intermediate level radioactive waste.

All 28 cross-drifts of each horizon have connections from the auxiliary shaft to the general transport drift and from the transport shaft to the waste transport drift. The widths and the heights of the working areas are similar.

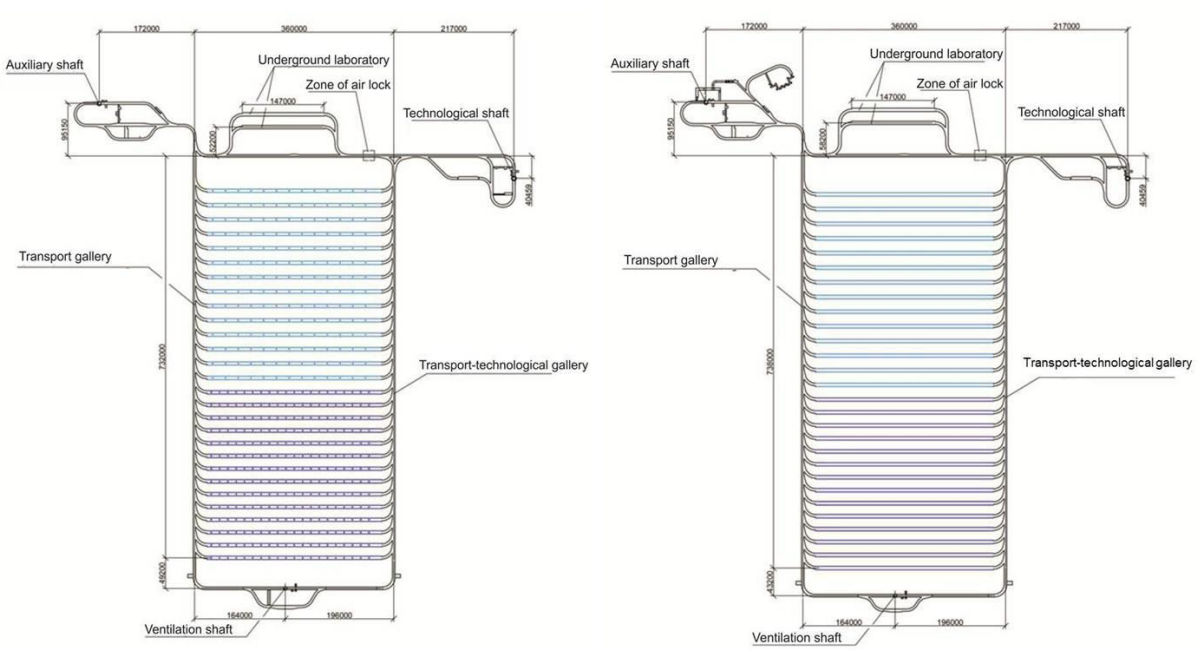

Fig. 5-2: Layout of emplacement levels; left: upper level, right: lower level (modified after VNIPIPT, 2013a)

Radioactive waste class 2 will be distributed over the emplacement levels in such a way that a uniform load of both levels will be achieved. The emplacement chambers in the emplacement horizons are isolated from each other by means of dividing seals. Seals are also placed between the boreholes of the working area and the containers disposed in the emplacement chambers. At the ends of the working area where the emplacement chambers are located, there are seals with a thickness of 0.8 m. The gaps between the containers in the emplacement chambers will be filled with a bentonite-cement mixture. A transverse niche is provided for manoeuvring the emplacement device in the emplacement chambers of the working area. After the bentonite-cement mixture has been poured over the containers in the emplacement chambers, the space between the roof and the bentonite-cement mixture covering of the top containers remains empty. This remaining gap is filled with backfill material (final material still to be determined).

Boreholes with a diameter of 1.2 m and a depth of 75 m for the disposal of HLW in canister (class 1) are planned to be created under the upper emplacement horizon (Fig. 5.2, Fig. 5-3). The upper horizon is separated into two different areas with different amounts of boreholes for the disposal of spent nuclear fuels. The first part of the horizon contains 14 cross-drifts. The distance between these drifts is 23 m; each of them contains 20 boreholes with 18 containers with high-level, long-lived radioactive waste with high heat generation. The remaining space between the container in the borehole and the borehole wall will be filled with bentonite or a similar material. The whole length of this first emplacement zone makes up 23·13 = 299 m. The distance between the boreholes in this part of the emplacement area is 15 m, which amounts to a length of 15·19 = 285 m in this part of the repository.

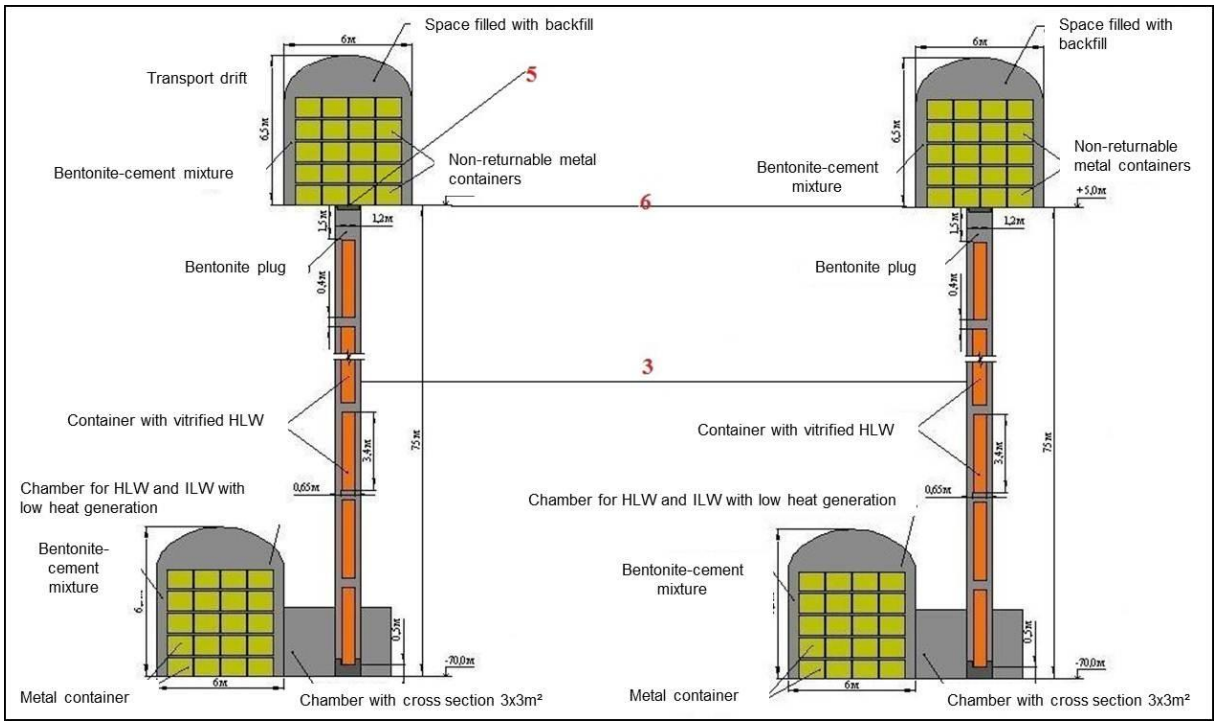

Fig. 5-3: Sketch of emplacement boreholes and drifts (modified after VNIPIPT, 2013b)

For the disposal of the non-returnable but removable parts of the returnable containers with radioactive wastes class 2 chambers will be created at the emplacement chambers of the lower horizon. Stacking the concrete containers and the thin-walled non-returnable transport containers (TNMK) class 2 in the emplacement chambers will be carried out with a crane and a forklift truck (Fig. 5-4).

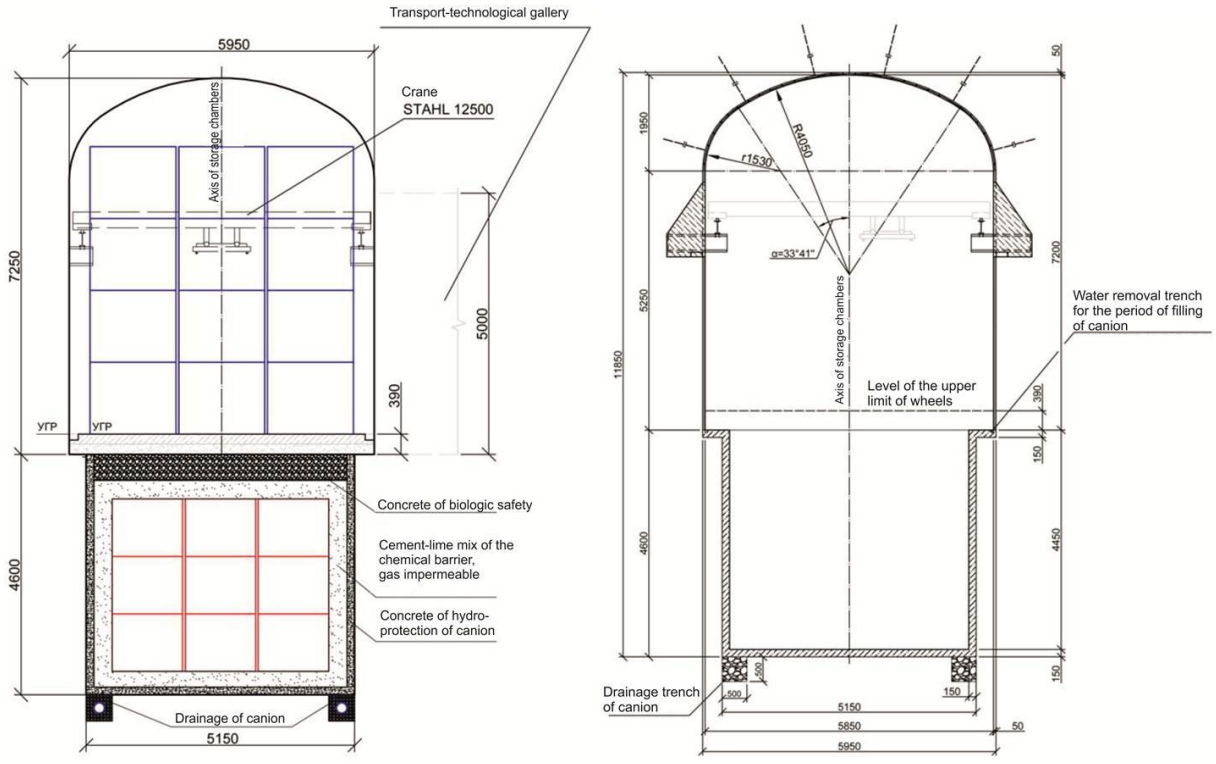

Fig. 5-4: Drift filling at the lower level (modified after VNIPIPT, 2013b)

5.2 Containers

The containers for delivery and disposal of the radioactive waste in the deep underground repository are divided into containers for radioactive waste management class 1 (category very high level waste) and class II (category long-lived high-level waste and long-lived intermediate level waste). Fig. 5-5 to Fig. 5-7 illustrate the different type (classes) of containers.

Radioactive waste of class 1 will be transported in a TUK-140/1 – a special transport cask for delivery of vitrified high-level radioactive waste with high heat generation – to the first horizon of the disposal facility. The transport cask will carry one container containing 3 canisters vitrified high-level waste (Fig. 5-7).

Each cask is placed in an additional cover to prevent leakage of radioactive waste due to corrosion. A cask with additional cover carries three canisters with vitrified heat-generating high-level radioactive waste, each weighing 500 kg. In the transfer hall, the casks will be removed from the transport container and reloaded into a small transport container for only one cask. For emplacement in a borehole, the container in the small transport container will be transported to the emplacement device already positioned over a borehole.

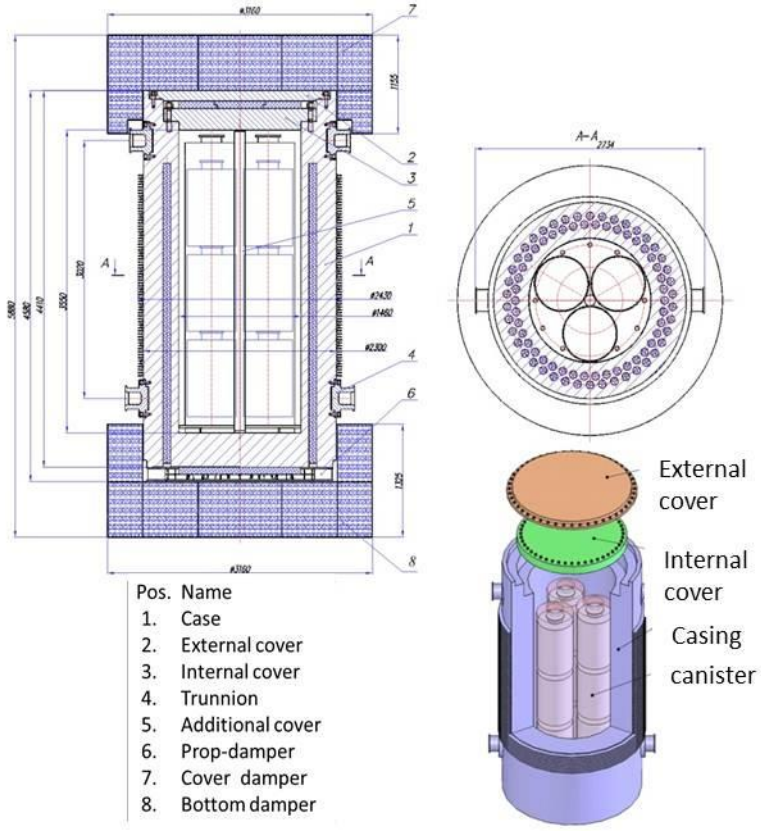

Fig. 5-5: Transport cask (TUK) and a container for delivery covers with canisters, enclosing vitrified high-level waste modified after VNIPIPT, 2013b)

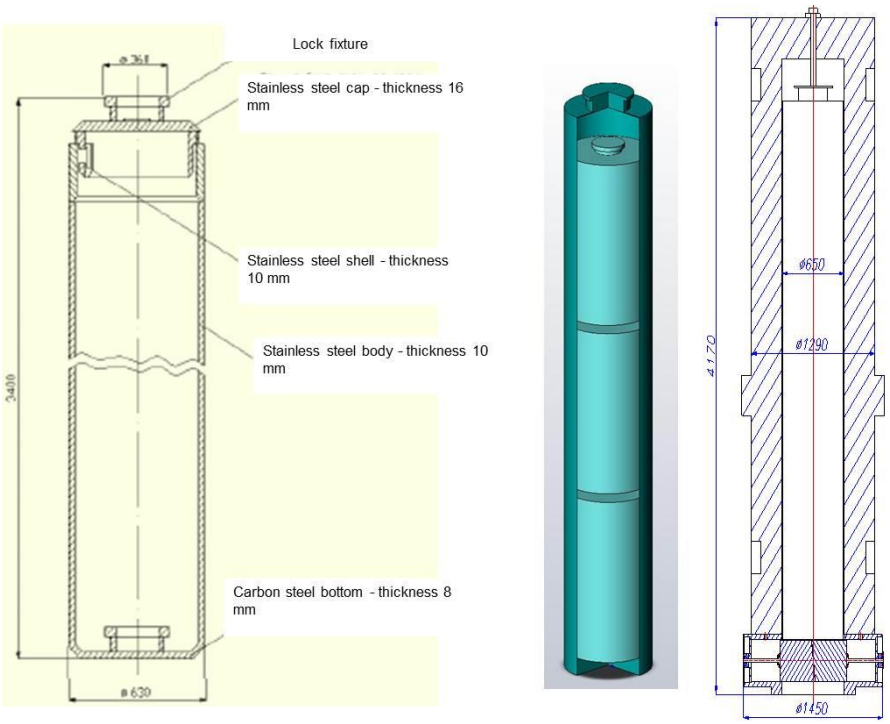

Fig. 5-6: Container for canisters of vitrified high-level waste (modified after VNIPIPT, 2013b)

For the disposal of radioactive waste class II, the following containers may be used (The containers shown in Fig. 5.7 are just existing examples for illustration):
Thin-walled non-returnable transport containers (TNMK)
In addition to the existing primary packaging (Fig. 5-7, top):
Package Type - PU-2, Material - Steel
External dimensions – 1.65 × 1.65 × 1.375 m, Wall thickness - 8 mm
Useful volume - 3.5 m^3, Container weight RW - 9 m

Non-returnable protective concrete container (NZHBK)
(Analogue container NCS-150-1,5P) (Fig. 5-7 bottom)
Package Type – A, Material - heavy concrete (density - 4 t / m^3)
External dimensions – 1.65 × 1.65 × 1.375 m, Wall Thickness - 110 mm
Useful volume - 1.9 m^3, Container weight RW - 12 t

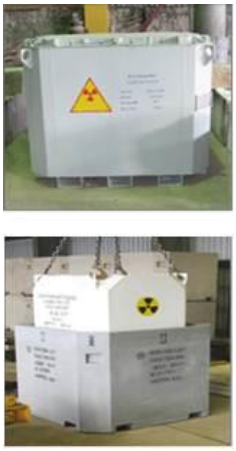

Fig. 5-7: Container types (VNIPIPT, 2013b)

Returnable metal container (VMC) with non-returnable removable part (NVCH) BMK:
Package Type - B (U), Material - Steel
External dimensions – 1.65 × 1.65 × 1.375 m, Wall Thickness - 150 mm
Useful volume - 1.5 m^3, Container weight RW - 20 t

Returnable metal container (BMK) with non-returnable removable part (NVCH) NVCH:
Package Type - for internal circulation on PGZRO, Material - Steel
External dimensions – 1.35 × 1.35 × 1.1 m, Wall Thickness - 6 mm
Useful volume - 1.5 m^3, Container weight RW - 5 m

These transport containers were checked for compliance with the NP-053-04 "Safety regulations for transportation of radioactive materials".

5.3 Conceptual design of the sealing system

The current repository concept considers a backfilling and sealing concept of the emplacement boreholes. A complete sealing system for the entire repository is still to be developed. Especially the five access shafts to the underground facilities represent the main pathway between the underground repository and the biosphere and therefore play an important role in the safety case. In the following the first conceptual approach of a complete sealing system for the current repository design is described.

5.3.1 Boundary conditions

The potential host rock at a depth of 200 to 700 m is characterized by an average hydraulic conductivity of 10^{-8} to 10^{-9} m/s. The hydraulic conductivity at the contact zones between veins and rock lies one decade higher. The exact hydraulic properties and the connection between the veins are not known. Significantly higher filtration coefficients and permeability cannot be excluded especially during far distant evolution. Therefore, the conceptual sealing design considers the veins as potential pathways and tries to separate them from other aquifers and the disposal areas.

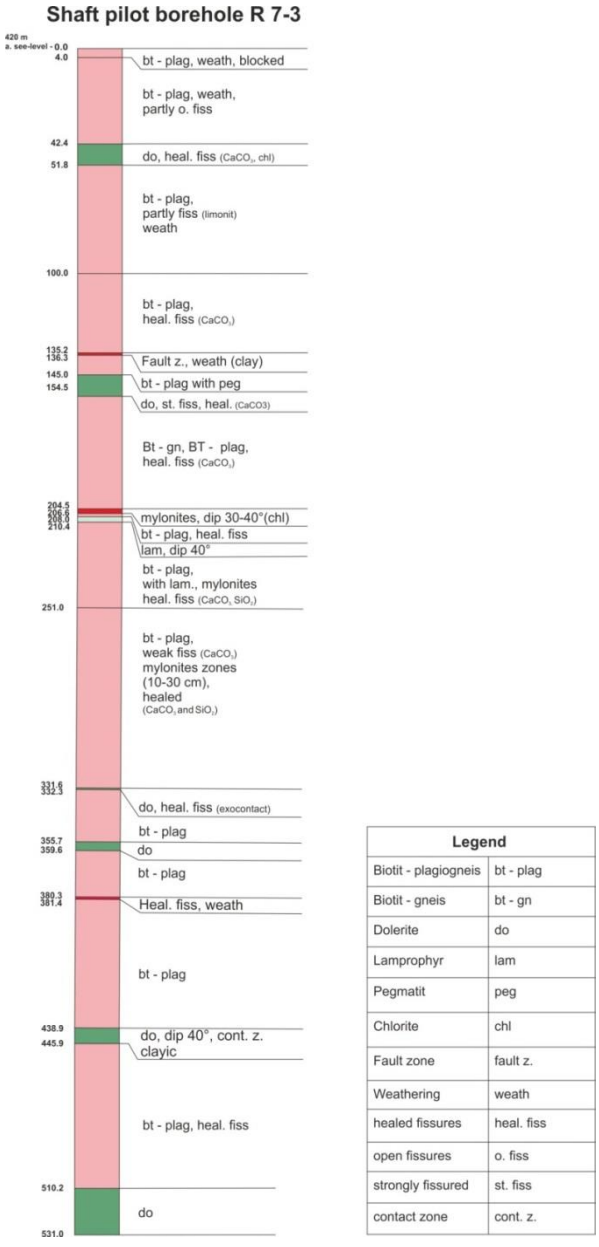

Fig. 5-8: Lithological profile of the pilot borehole R 7-3

For the design of the shaft seal the lithological profile of the pilot borehole R 7-3 was chosen as a reference profile (Fig. 5-8). It is expected that the general geological structure between the different shafts does not vary significantly. Differences are only assumed in the respective depth and thickness of the lithological units, which may influence the final location and the length of the sealing elements. The principle structure of the sealing system is assumed to be the same.

The general goal of the disposal of radioactive waste in deep geological formations is the separation of the waste from the biosphere. This enables the protection of nature from negative influences of radiation and toxic parts of the waste. This general requirement leads to special requirements for the technical components of the repository. The sealing system made as a multi barrier system of different (geo-) technical barriers has to limit the migration of fluids on potential pathways into or out of the repository significantly. The movement of fluids (gas or liquids) could lead to a migration of radionuclides

General requirements and recommendations can be stated as follows.

- all disposal drifts shall be separated from each other
- all underground openings shall be completely backfilled
- sealing components shall be stable during their functional period
- the sealing system shall minimize all fluid movements
- the design of the sealing system shall consider redundancy
- the design of the sealing system shall consider diversity
- the sealing system shall be maintenance free without any re-adjustments
- the sealing system shall be built as simple and robust constructions

The design of the sealing system and the individual sealing elements depends on the expected loads, the expected boundary conditions, and the future evolution of the repository system as will be explained in the following chapter.

5.3.2 Compliance assessment methodology

The strategy for demonstrating compliance of a seal design with the design basis or design requirements has recently been developed during the ISIBEL project (Krone et al., 2013) and the “Preliminary Safety Assessment for the Gorleben Site” (VSG) (Müller-Hoeppe et al., 2012). It is a semi-probabilistic, reliability-oriented concept that uses partial safety factors and is based on the internationally recognized Eurocodes (Eurocode 7, 2009; Eurocode 0, 2010). The Eurocodes are a series of 10 European standards. Each of these codes consists of several parts (JRC & DG-ENTR. 2008). In engineering, it can thus be considered as state of the art for demonstrating the load-bearing capacity of a structure, i.e. the ability of a structure to perform to the required standards under induced loads.

The safety case for the system as a whole and for the individual barriers consists of a number of individual safety assessments for various limit states that include, e.g., the mechanical properties of the construction material. As a first step, the requirements for the multi-barrier system as a whole and for the individual subsystems need to be derived from the safety goals. Whether specific requirements are met is demonstrated by means of “assessment cases“ (load cases). The term "assessment cases" was chosen analogous to the term used in long-term safety assessments as in addition to the load, other parameters need to be taken into account as well. The assessment cases are derived from the combinations of actions (impacts) and from the specific system characteristics. The respective states of the structure, e.g., the stress states, are to be determined by means of equilibrium considerations. The following individual assessments are essential for demonstrating compliance with the design basis according to the state of the art in technology:

- Demonstration of sufficient hydraulic resistance (demonstration of tightness)
- Demonstration of sufficient load bearing capacity (structural integrity)
  - Demonstration of structural stability
  - Demonstration of crack limitation
  - Demonstration of deformation limitation
  - Deformation of filter stability
  - Demonstration of long-term stability

These assessments are essential for demonstrating the effectiveness of a sealing construction. Furthermore, the *feasibility* needs to be assessed and demonstrated. Fig. 5-9 shows the individual assessments and their connections to the overall demonstration of functionality. More information about the individual assessments can be found in Herold & Jobmann (2015) which is stored on the enclosed CD as a pdf-file.

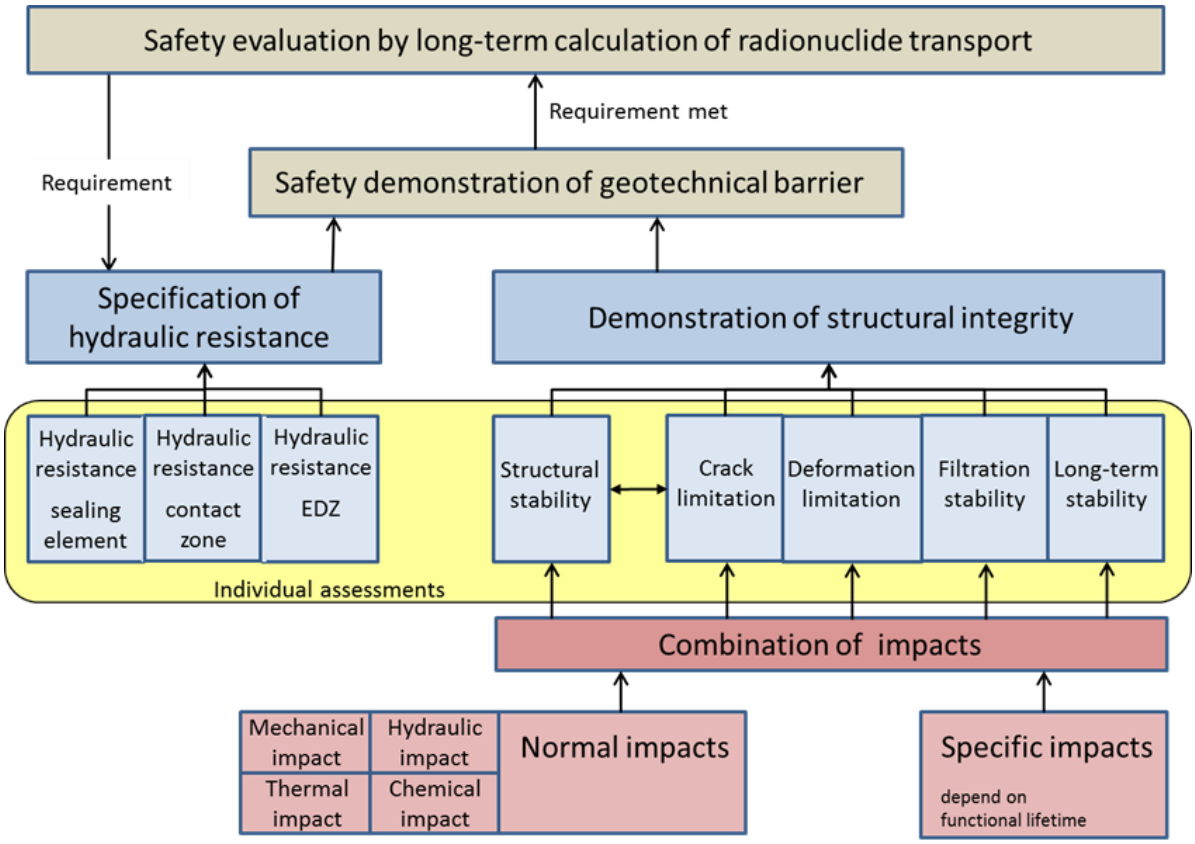

Fig. 5-9: Connection of hydraulic long-term calculations in a long-term safety assessment with the individual, function-related assessments using the example of a shaft seal (after Müller-Hoeppe et al., 2012).

The demonstration of compliance is carried out by conducting a limiting value evaluation of the loads on a structure and the resistance of the structure to those actions, e.g., the (existing) stresses are compared with the nominal design stresses which can be calculated from the material strength. The loads on the structure are compared with the resistances of the structure by means of limiting criteria. The reference to a limit state makes sense because both loads and resistances are determined from typical distribution functions. The limit state describes the state of the structure where it just barely meets the requirements. If this state is exceeded, then the structure no longer complies with the design requirements. Accordingly, in order to meet the design requirements, the resistances need to be higher than the actions on the structure.

The design values (also called “rated values”) for the individual assessments are derived from the characteristic values of the actions on and the properties of the barrier combined with the related partial factors. This approach is illustrated in Fig. 5-10. When applying the method of partial factors, actions and resistances, i.e. the parameters of the targeted relation, are allocated partial factors.

The effects of actions or impacts (S_d) are multiplied by partial safety factors and, thus, increased, whereas resistances (R_d) are divided by partial factors and, thus, decreased. This method and the application of partial factors generally account for uncertainties in the representative values of the actions and uncertainties in the properties of the structure. More information can be found in Herold & Jobmann (2015) stored on the enclosed CD.

The individual assessments of the limit states are to be carried out “at the level of ultimate limit state verifications”, i.e. they have to have the same reliability level as a verification of ultimate limit states. This safety concept is necessary in order to ensure that the design complies with the requirements. In the structures considered, the demonstration of tightness is thus to be considered at the level of a verification of ultimate limit states, because a loss of tightness would result in “danger to life and limb” (Kiefer, 1997).

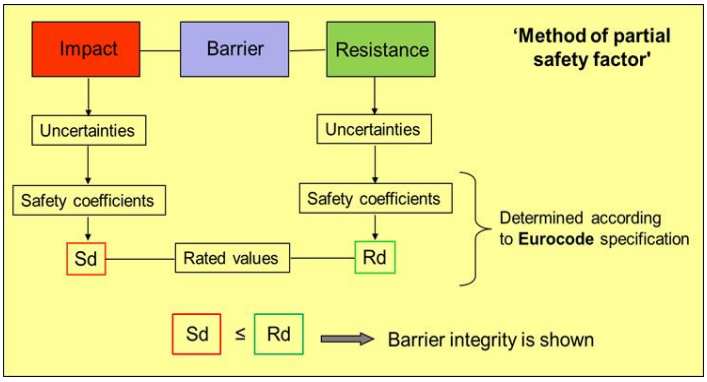

Fig. 5-10: General principle of the partial safety factor method

Unlike in the Eurocodes, the term “resistance” includes more than just mechanical stability. The term is used synonymous for the prevention of a danger to life and limb and can also be used, e.g., for the hydraulic resistance. Compliance with the reliability level for resistance in the corresponding assessment ensures the functional integrity of the structure. For the individual assessments four general design situations have to be considered:

- constant/steady/permanent design situation
- temporary design situation
- exceptional design situation
- earthquake

As mentioned above, the assessments give information on the reliability of a structure. To demonstrate reliability, a corresponding confidence level or failure probability needs to be met. In an ultimate limit state verification, a failure probability p_f of 10^{-4} for the intended lifetime of the structure is sufficient. Thus, the verification of the effectiveness of the safety function indicates that the probability that a barrier does not fail prematurely during its expected lifetime is $p_f = 10^{-4}$, i.e., the survival probability p_s of the barrier is $p_s = 1 - p_f$ (Müller-Hoeppe & Krone, 1999).

To actually perform the individual assessments the expected loads on the different sealing components have to be defined. To get a comprehensive overview of all the processes going on in and around a repository, the development of a site specific FEP-catalogue (FEP = Features, Events, and Processes) is a proper way of compiling these processes. Such a FEP-catalogue is a sound basis for the development of the probable repository evolution (**reference scenario**) as well as less probable repository evolutions (**alternative scenarios**). For both, the reference scenario and the alternative scenarios those FEP can be identified which have a significant impact on specific sealing components of the engineered barrier system. Based on these identified FEP the expected loads on the sealing components during their functional lifetime can be derived and the individual safety assessments can be done. More details and an assessment application example for specific shaft sealing components can be found in Herold & Müller-Hoeppe (2013).

5.3.3 Sealing materials and system elements

5.3.3.1 Sealing material

Materials used for the sealing of mine openings have to have a low permeability, be long-term stable, and be compatible as far as possible with the chemical properties of the host rocks and the pore water. The current sealing concept includes several different sealing con-

structions inside different mine openings. Each sealing element is adjusted to the hydraulic, mechanical, thermal and chemical requirements and the expected impacts at the sealing location. The use of different sealing elements and sealing materials takes into account the principle of redundancy and diversity. Generally, various different sealing materials are suitable for the closure of high-level radioactive waste repositories in crystalline rock formations. The materials used in the sealing concept are (Herold & Jobmann, 2015):

- Bentonite in form of pellets and powder to be compacted in-situ, in form of pre-compacted blocks or in sandwich construction including equipotential segments (Schuman et al., 2009)
- Bitumen and asphalt combinations. Both types are used as a redundant and diverse sealing material to bentonite. While bentonite needs water intake to develop full sealing properties, bitumen has full sealing properties directly after installation.
- Pure bitumen which can move into gaps and cracks, for example in an excavation damaged zone (EDZ). Because of the impermeability and the good adhesion of bitumen especially the contact zone between plugs and rock can be tightened.
- Bitumen filled gravel elements. Especially inside shafts, it is possible to combine bitumen and gravel (crushed rock) into one sealing element. Hard rock gravel creates a filling of the mine opening with low settling. The filling of the pores with bitumen yields an additional sealing effect.
- Mastic asphalt, the use of which as sealing material is known from the closure of common mine shafts.

5.3.3.2 Abutments

Abutment constructions made of concrete have a high resistance against mechanical loads. The high resistance allows the use of concrete as construction material for abutments. Abutments prevent uncontrolled movements of sealing elements and hold them in place. The properties of the fresh and hardened concrete are easily controllable by the four main components cement, aggregates, water and admixtures. To minimize the gas generation inside the repository, reinforcement inside the concrete should be avoided.

5.3.3.3 Backfilling

One basic requirement for the closure of the repository is the complete backfilling of all mine openings. Backfilling is a generic term for a wide range of technics and possibilities to refill mine openings. Backfill can be classified according to the kind of material, the kind of installation, and the function. Backfilling for mechanical stabilization can be realized by mechanical installation of gravel or crushed rock. The lose material will be dropped into the drift and – if necessary –compacted. Materials of small grain size can be backfilled using slinger trucks. If the backfill has a fine grain structure, pneumatic installation is also possible. Hydraulic installation (pumping) is used for the installation of concrete-based or slurry backfill. Backfill may also fulfil sealing functions.

5.3.4 Sealing concept

5.3.4.1 Emplacement boreholes

The long-lived high-level waste and the long-lived intermediate level waste is planned to be distributed over the emplacement levels in such a way that a uniform distribution of both levels will be achieved. The emplacement drifts in the emplacement horizons are isolated from each other by means of drift seals. Seals are also located between each emplacement borehole and the containers disposed of in the adjacent emplacement drifts. The gaps between the containers in the emplacement drifts are intended to be backfilled with a bentonite-cement mixture. A transverse niche is provided for maneuvering the emplacement device in the emplacement drifts. After the bentonite-cement mixture has been poured over the con-

tainers in the emplacement drifts, the space between the roof and the bentonite-cement mixture covering of the top containers remains empty. This remaining gap will be filled with backfill material (final material still to be determined). The remaining space between the container in the emplacement boreholes for HLW and the borehole wall will be filled with granular bentonite (Fig. 5-3).

Possible adaptations to the sealing concept

As an alternative, the following adaptation of the sealing concept is proposed. Backfilling by cast in place of concrete-bentonite mixtures should be extended to the whole drift. The already filled parts of the emplacement drifts can be backfilled in regular distances. The main functions of the backfill are the complete filling of all remaining open spaces inside the drift and the reduction of the hydraulic conductivity. The proposed cement-bentonite mixture will produce a fine grout with a high flowability. The bentonite inside the mixture reduces bleeding and decreases the strength of the grout. Designing a concrete with high flowability and low permeability is also possible by the admixture of several other materials. In this case, the use of bentonite is not required. The final backfilling mixture depends on the hydraulic conductivity requirements, the required functional period and the operational requirements. Chemical impacts from the host rocks and the pore water have a significant influence to the long-term stability of the concrete mixture.

Option 1

As a first option, the sealing between the emplacement boreholes and the emplacement drifts could be enhanced. At the top of each borehole the unavoidable excavation damaged zone (EDZ) will be smoothly taken out to an acceptable depth of approx. 0.5 m which covers the most disturbed part of the EDZ.

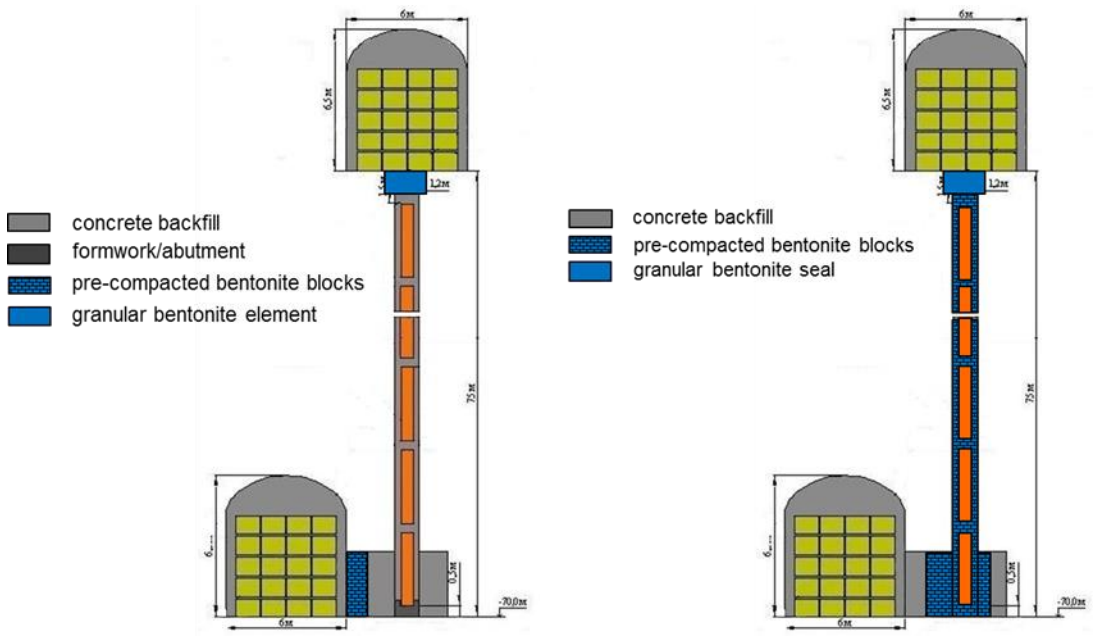

Fig. 5-11: Optional sealing concept of the emplacement boreholes to enhance the separation to the emplacement drifts (option 1 left and.option 2 right).

On a length of about 1.2 m this area will be filled with granular bentonite made of pellets and powder (Fig. 5-11). In-situ compaction of the bentonite is easily possible. This sealing element separates the borehole from the upper disposal drift and would enhance the sealing effect by minimizing any fluid migration through the EDZ around these sealing elements.

Option 2

Inside the boreholes a bentonite buffer made of pre-compacted blocks could be installed as an additional engineered barrier. However, an important requirement for the installation is a high drilling precision. The installation of the buffer will be realized in parallel to the canister emplacement. The first canister will be emplaced inside the blind ending niche. The borehole is extended to the floor by a steel liner, with the same inner diameter. Inside the niche a second barrier of bentonite blocks separate the borehole from the drift. The remaining space has to be backfilled. Inside the borehole pre-compacted rings made of bentonite can be used (Fig. 5-11). The rings fill the area between canister and borehole contour. To ensure a sufficient distance between the canisters, massive bentonite discs could be used. A sufficient tolerance for the installation of the rings has to be recognized during fabrication. The remaining annular gaps between bentonite and rock or canister will not be filled. The pre-compacted rings will provide a sufficient swelling capacity to close these remaining gaps. Hydraulic conductivity and swelling pressure of the bentonite blocks can be defined by the compaction density. As in option 1, at the top of each borehole a 1.2 m high sealing element covers the borehole.

5.3.4.2 Emplacement drifts

Both ends of the emplacement drifts will be closed by plugs. Each plug is separated into a sealing element and an abutment. The sealing element is designed as a bentonite elements made of pre-compacted blocks. At the side facing the emplacement drift the bentonite is directly connected to the backfill. The concrete abutment is located in the opposite next to the access drift (Fig. 5-12). The sealing has to provide a sufficient low hydraulic conductivity, shall provide a long-term stability with regard to the chemical composition of the pore water and shall provide a mechanical stability against the rock and pore water pressure. Prior to a quantitative plug design, process analyses should be performed to identify the thermo-hydro-mechanical (THM) loads on the individual plugs.

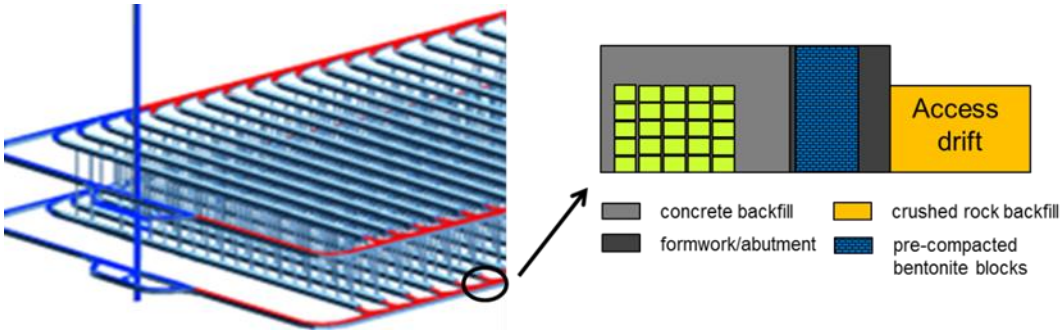

Fig. 5-12: Plug concept for sealing the emplacement drifts

5.3.4.3 Access drifts

The emplacement areas are framed by ventilation and transport drifts. Those access drifts are connected to the shafts and the infrastructure area. Sealing the access drifts creates an additional barrier between the shaft sealing and the near field sealing systems inside the emplacement drifts. Therefore, all access drifts are equipped with sealing plugs near the infrastructural area and the shafts (Fig. 5-13). The drift sealing has to provide a sufficient low hydraulic conductivity, shall provide a long-term stability with regard to the chemical composition of the pore water and shall provide a mechanical stability against the rock and pore water pressure. Requirements on the thermal properties of the sealing construction seem less important because of the large distance to the heat producing waste packages. Prior to a quantitative pug design process analyses should be performed to identify the THM-loads on the individual plugs.

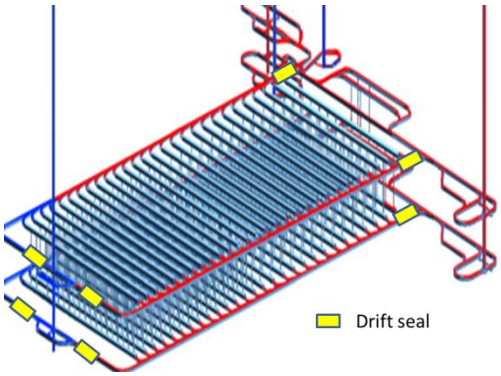

Fig. 5-13: Location of the access drift seals.

The plug is designed symmetrically (Fig. 5-14). In the centre a core made of bitumen and asphalt separates the two sides. In this area the EDZ is removed slightly deeper than at the remaining sealing area. The core is designed as a small slot and consists of pure bitumen and asphalt blocks. The installation starts with stacking the cold asphalt blocks of a predefined size. During stacking the contour at the bitumen/asphalt seal is coated with a bitumen undercoat to increase the adhesion between the rock and the bitumen/asphalt element.

In a second stage the remaining space between the blocks is filled with hot and thus liquid bitumen. The heat of the bitumen melts the inner part of the asphalt blocks. By this, a homogeneous bitumen-asphalt element will establish. At the same time the cold asphalt blocks protect the adjacent bentonite against the thermal input (Knoll et al., 2010).

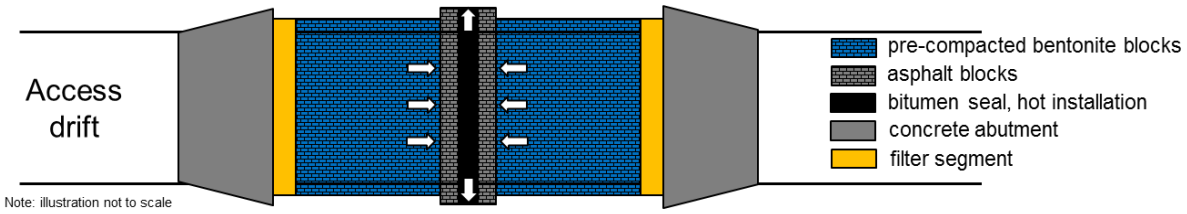

Fig. 5-14: Conceptual design of the plugs for sealing access drifts

At both sides of the bitumen core sealing elements made of pre-compacted bentonite blocks are installed. Due to the pre-compaction the bentonite blocks have a high dry-density minimizing possible settlements. During saturation of the bentonite the increasing swelling pressure acts on the abutments and the bitumen core. Displacements at the outer sides are limited by the abutments. The bitumen core instead will be influenced by the pressure build up. If pressure increases the bitumen will be squeezed yielding a better contact to the rock mass. In addition the bitumen will probable squeezed into gaps, dykes or fissures within the surrounding rock decreasing the hydraulic conductivity in those areas.

Equipotential segments (filter layers) are located between the bentonite and the abutment. If water reaches the construction the equipotential segments allow an evenly spread saturation of the bentonite at its outer faces.

The function of the concrete abutments is to keep the bentonite in place and to avoid a volume change of the bentonite to ensure an increase in swelling pressure. During saturation water will pass the abutments. It is one important task to select a suitable type of concrete material with less chemical interactions between the concrete, the pore water and the bentonite. Negative chemical interactions are e. g. the change of cations between pore water and bentonite. This reduces the swelling capacity of the bentonite. The use of low pH-value concrete avoids those negative chemical effects.

The crossing of dykes during underground excavations cannot be excluded. As already mentioned in a previous section, the interfaces between dykes and the host rock are possible fluid pathways. If one of those dykes crosses a drift and if the dyke is hydraulically active, this area should be sealed to avoid a direct connection between the emplacement area and

these potential pathways for fluid migration. The plug design for these locations is based on the conceptual design of the plug for access drifts (Fig. 5-14). To separate the dyke form the drift the length of the plug is extended. An additional bitumen element is added and both bitumen elements enclose the dyke. Between them a bentonite seal with equipotential segments is located (Fig. 5-15). The equipotential segments consisting of a material with a high hydraulic conductivity allow a homogeneous saturation even in case of a dipping dyke and an unregularly water inflow.

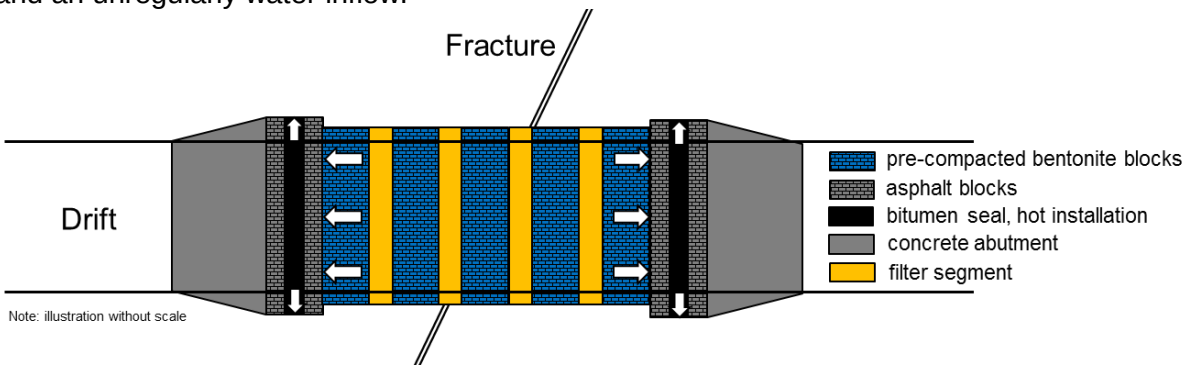

Fig. 5-15: Conceptual design for the hydraulic separation of fractures from drifts

Due to the possible water inflow from the fracture the different bentonite elements start to swell. As explained for the normal drift plug the swelling pressure will act on the bitumen elements by squeezing them against the concrete abutments and the rock mass in that area enhancing the sealing of the contact zone and the EDZ. Any water coming from the fracture is enclosed in this plug. Prior to a quantitative design process analyses should be performed to identify the THM loads on these kind of plugs.

5.3.4.4 Shafts

Shafts create a direct connection between the biosphere and the underground openings of the repository. The penetration of the host rock produces a high permeable pathway, which has to be closed in order to ensure a safe enclosure. This results in special technical requirements and measures. A shaft sealing should be designed in a way that any radionuclide release will be so small that no dose limits are exceeded during the radiological consequence analysis. This includes not just the free cross section. The contact zone between shaft filling and host rock and also the EDZ around the shaft have to be taken into consideration. The shaft closure has to provide a sealing function directly after its construction.

For preparation of the sealing element location all internals of the shaft have to be removed. Hydraulic active layers and potential pathways (dykes or fractures) shall be separated to avoid mixtures between different aquifers and thus different chemical compositions or fast inflows. Based on these considerations and the lithological profile different sealing elements are proposed for specific depth levels (Fig. 5-16). Starting at the lower part of the shaft, a separation of the two mine levels is required to avoid interactions between them. The shaft landings at both levels are located in or next to a dolerite layer. To avoid negative influences from the mining related stress redistribution around the shaft landings, possible plugs should be located in a sufficient distance to them. The biotite layer between both levels has a thickness of approximately 64 m and provides sufficient space for the sealing. Above the upper mine level a wide area of undisturbed gneiss is located in a depth between 360 and 439 m with only one healed fissured area included. This area was chosen to contain the main sealing element. Two series of dykes cross the shaft profile in a depth of 135 and 205 m which might act as potential pathways. To separate them from each other and to separate the different horizons, additional sealing are proposed to be located in these areas.

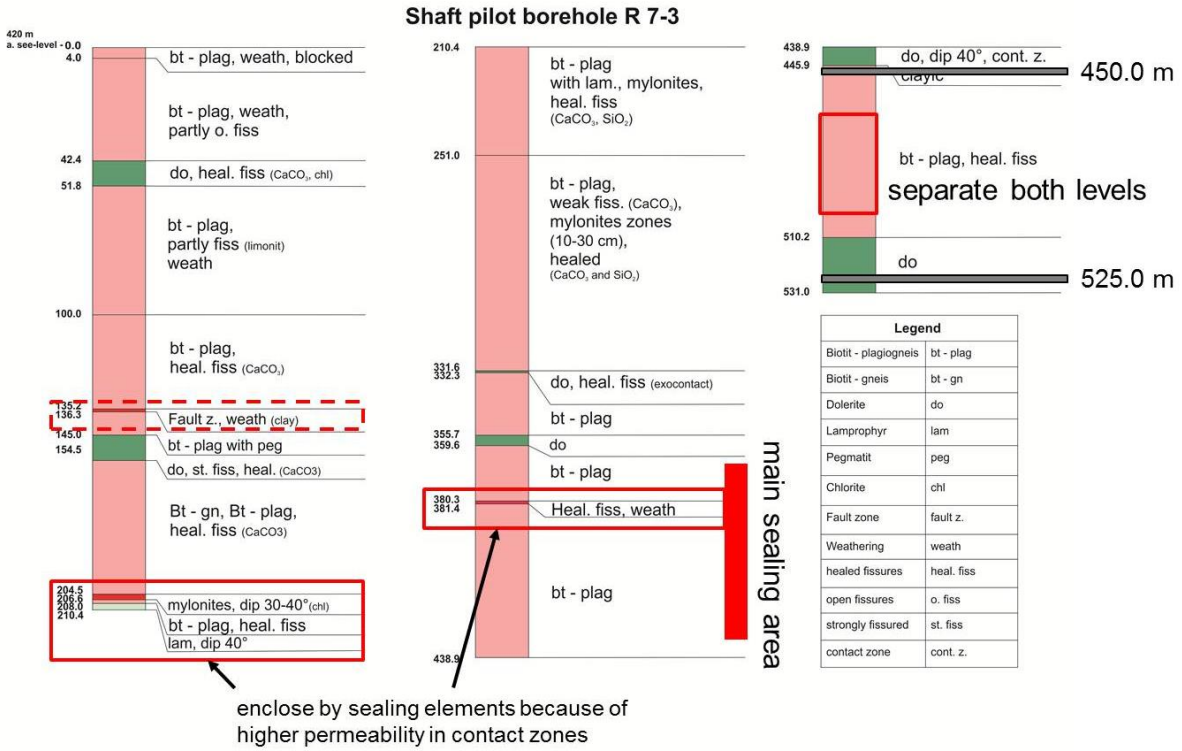

Fig. 5-16: Shaft profile and potential plug locations

The construction of the shaft sealing is one of the last actions of the repository closure. All five shafts are sealed in a similar way. Differences are just assumed in the respective depth and thickness of the lithological units which might influence the final location and the length of the sealing elements. The principle structure of the sealing system is assumed to be the same.

During the preparation of the sealing process, all internals have to be removed. Water proof liners will stay inside the shafts, except at the locations of the plugs. The filling starts with the backfilling of the shaft sump and the lower shaft landing (filling column 4 in Fig. 5-17). In general, the backfill inside the shaft has no sealing function. The backfill has to provide mechanical stability of the whole shaft column. Therefore the backfill material has to be stable against the mechanical loads and to avoid significant settling. Hard rock gravel is known as a good backfilling material for closure of common mining shafts. Gravel, as it is also used for railroad construction, has a high compressive strength. Common minerals are serpentinite or basalt. Hard rock can be used in all backfill areas of the shaft filling. This includes the filling column 1, 2, 3 and 4. In dependency of the size of the cross section and the grain size distribution during loading, the gravel column transfers the loads to the shaft wall. It might also be possible to process the broken rock from mine excavation for the use as backfill material. The backfill made of hard rock gravel is also located inside the horizontal part of the shaft landing. The area next to the shaft is also backfilled by gravel to create a stable filling and to avoid movements of the filling material. Sealing elements have to be located in an area which is not influenced by mining related stress redistributions or even damaged.

Shaft landing stations of example are not suitable for sealing. The lower sealing element (sealing element C in Fig. 5-17) has to be located at an undisturbed area between the two shaft landing stations. This requirement influences the length of the lower gravel filling. The length depends, to some extent, on the dimensions and the stress fields around the two shaft landings. The sealing element is designed as an in-situ compacted bentonite element, enclosed by two concrete based abutments. At the sealing location the shaft liner has to be

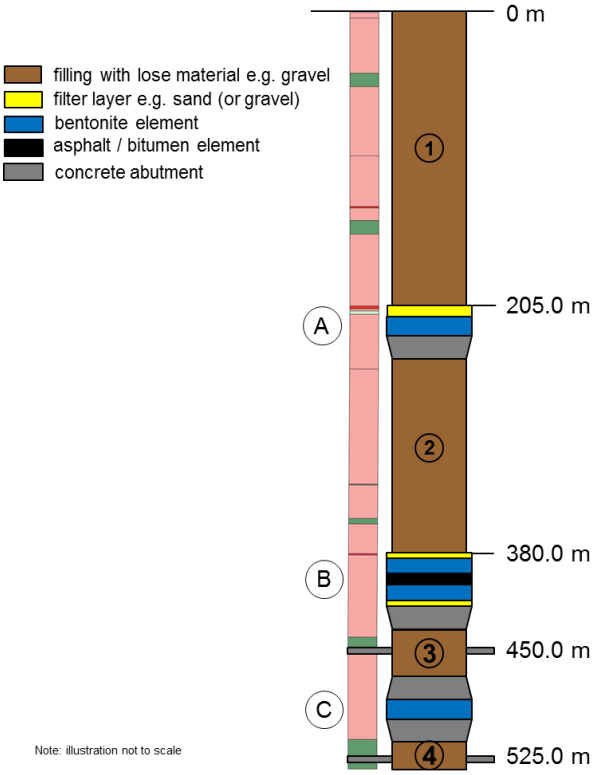

Fig. 5-17: Schematic design of the shaft sealing concept

removed. If the EDZ is characterized by a high permeability the part close to the contour has to be removed as well. To avoid additional bulking the installation of the sealing has to be realized close to the removal. For reasons of stability and operational safety an additional temporary liner could secure the contour of the shaft. The bentonite is assumed to be a binary mixture made of pellets and power. The mixture will be compacted in layers of up to 1 m thickness to achieve the necessary final dry density. A homogeneous compaction of the bentonite is significant for the swelling properties during saturation.

The two concrete abutments above and below the sealing element ensure a sufficient position stability of the bentonite element. At the same time displacements of the bentonite due to swelling are avoided since an increasing volume would lead to lower swelling pressures and thus to lower sealing abilities.

The abutments have to be interlocked with the host rock. Therefore, it is necessary to remove the liner. If the existing space is too small for simple cylindrical abutments, more complex structures, such as tapered or interlocked abutments could be used as well. The schematic illustration of the shaft sealing (Fig. 5-17) shows all abutments as trapeze (tapered in 3D). The final design and also the material selection depend on the boundary conditions given by the environmental conditions and the loads on the abutment.

The next section of the shaft is characterized by the second mine level. The backfilling at the second level is assumed to be realized in the same way as for the first level. The main sealing element is located in the large undisturbed area above the upper mine level. This sealing is defined as the main sealing because it separates the repository from the surface. The sealing module consists of two different elements, one bentonite element in which a bitumen element is enclosed. The idea is the same as for the drift seals. Due to the swelling pressure of the bentonite the bitumen core will be squeezed leading to an enhanced sealing of the contact zone to the rock and maybe parts of the EDZ as well. The dyke at about 380 m might be a hydraulically active. Therefore, a filter layer with a high hydraulic conductivity is foreseen at the depth. A possible water inflow through the dyke would fill the filter layer rapidly assuring a homogeneous saturation of the bentonite from its upper side, which at the same time is a protection of the bentonite against erosion from localized fluid inflows. The filter is assumed to consist of a graded layer of sand and gravel.

Sedimentation of the bentonite into the bitumen will be very small, because of the fine grain size. Using the sandwich principle for the bitumen layer reduces sedimentation, too. Soft bitumen can be packed between two layers of stiffer bitumen, e.g. oxidized bitumen (Kudla et al., 2009). The oxidized bitumen is connected to the bentonite and avoids high sedimentation rates. The softer core of pure bitumen provides a high adhesion to the rock and thus a good sealing function. Below the sealing module an additional concrete abutment provides the mechanical position stability. The abutment function on top of the sealing module is realized

by the filling column. The gravel column produces a sufficient resistance to avoid vertical movement of the bentonite.

The remaining shaft is filled with two gravel columns (column 1 and 2). Both are interrupted by a sealing element in a depth of approximately 205 m. At this level other dykes cross the shaft. The plug is needed to avoid water inflow into filling column 2 which would potentially lead to a mixture of water with different chemical compositions coming to the top of sealing module B. This would increase the uncertainties about the chemical long-term stability of the module B. The length of the seal depends of the height of the intersection between the dykes and the shaft. The intersection varies in dependency of the dipping angle and the shaft diameter. The bentonite plug is located below the depth of the dykes and a filter layer on top of the bentonite provides a homogeneous saturation when filled with water and avoids local erosion of the bentonite. Like the two others, this upper sealing element is made of a bentonite mixture of pellets and powder. Below the sealing element a concrete abutment provides mechanical stability whereas at the top, the stability is provided by the upper gravel column.

5.3.4.5 Overview of the complete sealing system

The complete sealing system consists of

- ***Shaft seals*** consisting of three different sealing modules
- ***Access drift seals*** of two types depending on whether fractures are present or not
- ***Emplacement drift seals*** designed as small modules and
- ***Borehole seals*** at the top and bottom of the emplacement boreholes

Fig. 5-18 gives an overview of the complete sealing system. For clarity the borehole plugs and the emplacement drift seals are shown exemplarily at one emplacement drift and one emplacement borehole only. In addition, some illustrations have been added showing the kind of sealing material and implementation procedures at the various sealing modules.

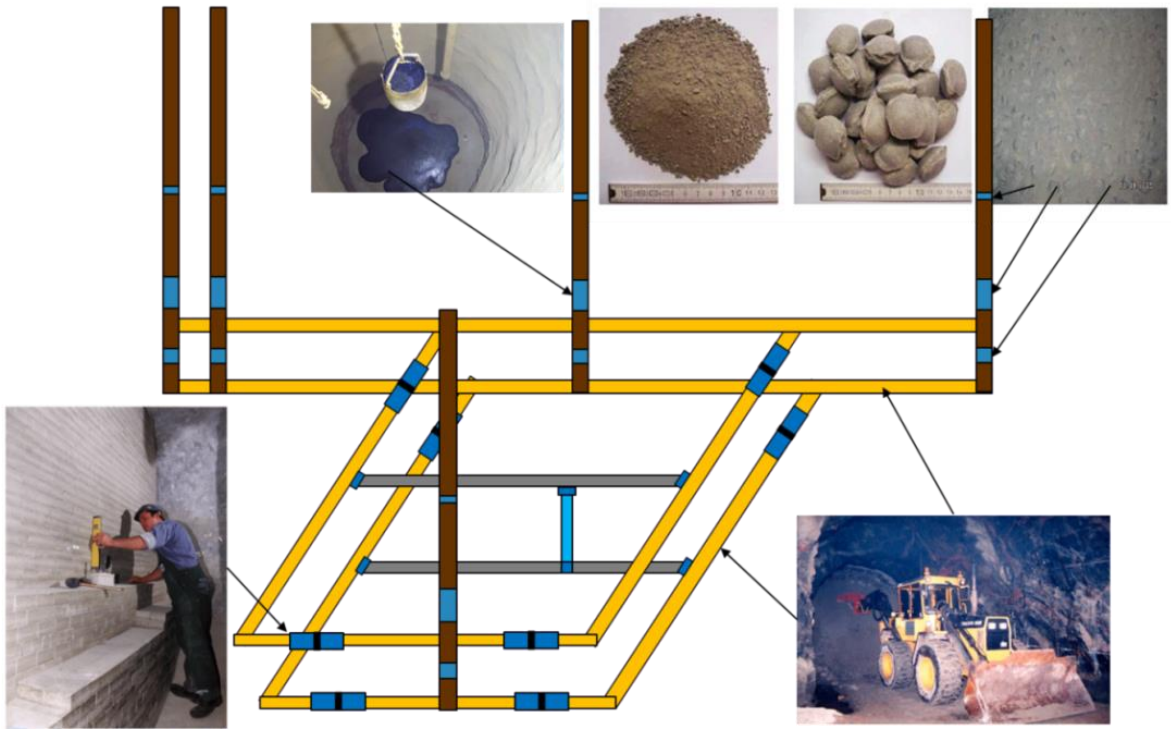

Fig. 5-18: Schematic illustration of individual sealing locations within the repository together with some figures of potential materials and implementation work. Legend: brown=gravel column, blue=bentonite, yellow=chrushed rock backfill, gray=concrete based backfill, back=bitumen/asphalt, pictures taken from (Wilsnack et al., 2008) (Gruner, 2008), (Gunnarsson et al., 2001), (Schachtbau Nordhausen, 2015)

5.4 Indications for URL research programme

In 2014/2015, DBE TECHNOLOGY GmbH sponsored a bachelor thesis at the Technical University of Clausthal dealing with the research programme for an underground research laboratory in crystalline rock (Middelhoff, 2015). The results of this thesis will be summarized in the following chapter:

As defined by NEA (2013), an underground research laboratory (URL) is an… *underground facility in which site characterization and testing activities are carried out along with technology development and demonstration activities in support of the development of deep geological repositories for radioactive waste*. The main objective of a URL is to support the repository development process by facilitating research activities in an environment similar to the repository. In this context the main issues are:

- to develop the technology and methodology required for underground experimentation
- to provide data to understand the behaviour and the performance of the repository system and their interactions
- to demonstrate the robustness of the design and to show potential areas for optimizing engineering components and processes
- to build confidence with stakeholders for their understanding of the important processes governing repository performance

There are two types of URLs:

Purpose built, generic URLs are facilities that are developed for generic research and testing purposes at a site that will ***not be used*** for waste disposal. But the results of this research work will provide information that may support disposal elsewhere. Worldwide, 10 URLs of this type have been operated in crystalline rock. Meanwhile 5 of these URLs have been decommissioned. Still in operation are: Grimsel Test site (Switzerland), ÄSPÖ Hard Rock Laboratory (Sweden), Olkiluoto Research Tunnel (adjacent to the Olkiluoto LLW repository, Finland), Mizunami URL (Japan) and KOREA URT (South Korea).

The only site-specific URL in crystalline rock that has been developed at a site that ***is considered*** as site for waste disposal is the ONKALO URL (Finland). This URL type is the initial stage of a repository at that site.

On the one hand, all relevant areas of the host rock can be analysed in a URL, and the results of the investigations help to develop an understanding of the mechanical, hydraulic, chemical and thermal boundary conditions at the site. On the other hand, specific problems concerning the operation and closure of a future repository can be analysed in detail, e.g. functionality, feasibility and compatibility of technical equipment or components of the sealing system. Furthermore, aspects of long-term safety, like radionuclide migration via fractures or sorption capacity of the rock, can be evaluated.

Detailed knowledge of the boundary conditions in the geosphere is a prerequisite for the development and optimization of a suitable disposal and repository concept. It is also necessary to demonstrate the suitability of repository components (e.g. the engineered barrier system, EBS). Safety assessments require a comprehensive database of all properties of the geologic environment.

Several safety-relevant geologic issues have been identified for the Yeniseysky site that need a comprehensive examination and evaluation, e.g. the characterization of fault zones and fractured rocks, the geomechanical properties of the host rock and fault zones, the hydrogeological situation, and the functionality and durability of the EBS, etc.

5.4.1 Selected projects

Because of the comprehensive data available, the Grimsel Test Site, the ÄSPÖ Hard Rock Laboratory and the ONKALO URL have been selected for this study. The advanced URL research programmes of these projects have been analysed in order to identify key issues and to identify criteria for the evaluation of the relevance and completeness of a scheduled R&D programme.

5.4.1.1 Grimsel Test Site (GTS, Switzerland)

The Grimsel Test Site is located in the Aar-Massif, which consists of crystalline rock, like gneisses, granite, schists, and amphibolites – with intrusions by dyke rocks. The URL is located at an altitude of 1730 m and consists of a branched tunnel system with a length of more than 1000 m, which has been excavated by a full-face tunnelling machine. The goal of implementing this URL was to increase the knowledge about the properties of the crystalline host rocks and to develop methods of host-rock characterization and disposal techniques that are not specific to the site. A future use of the Grimsel site as a repository site was not intended.

5.4.1.2 Äspö Hard Rock Laboratory (HRL, Sweden)

The Äspö HRL is located on the east coast of Sweden, near Oskarshamn, and consists of three shafts and a tunnel starting at Simpevarp peninsula and ending beneath Äspö Island. Here, the tunnel descends as a spiral ramp to a depth of -460 m. Different experimental areas are arranged along the ramp. The total length of the tunnel is 3.600 m. The host rocks consist of the finely porphyritic Äspö granite and an equigranular quartz monzodiorite – both with intrusions of diorite-gabbro dykes and granite dykes.

The objectives of the research programme for the Äspö HRL comprise an analysis of the potential host rock with regard to all issues that are relevant for the long-term safety of a future repository.

So – in addition to an extensive rock characterization programme – a demonstration programme has been initiated to test the concept (KBS-3) developed for the disposal of canisters with spent fuel in vertical or horizontal boreholes. The nearfield barriers of this concept consist of a copper canister and a surrounding bentonite buffer. The demonstration tests intend to demonstrate the effectiveness and applicability of the different components of this concept. All steps, from construction of barriers and emplacement of the canisters (technical feasibility and functionality), to the subsequent evolution of the barrier properties (swelling of buffer, corrosion of canister, chemical, hydraulic, mechanic and thermal interaction with host rock and circulation groundwater) have been analysed in the course of in-situ tests.

5.4.1.3 ONKALO (Finland)

The Finnish URL is located on the island of Olkiluoto (west coast of Finland) and consists of three shafts and a spiral access ramp with a length of 4.600 m that declines to a depth of 455 m. In the course of a site selection process, this site was selected as a site for the HLW repository. Then, the URL will become part of this repository. The geosphere at the Onkalo site is characterized by different kinds of gneisses in combination with pegmatitic granite and diabase. There are large homogeneous host rock areas restricted by large fracture zones. The KBS-3 concept is the common basis for the Swedish as well as for the Finnish repository concept. Therefore, most R&D work and demonstration tests for this concept have been concertedly performed by SKB and Posiva. Site-specific work focusses on obtaining information on the detailed characteristics of the host rock. To evaluate and demonstrate the compliance of the rock characteristics with the host rock requirements for the future repository, Posiva implemented a rock suitability classification system.

The demonstration tests for the engineered barrier system will mainly be done at the Äspö HRL. Because Posiva will use the KBS-3 concept as well, they participate in the demonstration tests in Äspö and transfer the results to the Onkalo site (POSIVA 2003).

5.4.2 URL research programme structure and summary list

An analysis of the research programmes of these URLs shows that all research programmes focus on investigations / experiments for the following objectives:

- ***host rock characterization, e.g.***
  - geology, mineralogy and geochemistry
  - hydrogeology and hydrochemistry
  - hydraulic properties, e.g. fluid conductivity
  - rock mechanics and tectonics
  - thermal properties
- ***interaction repository – host rock, e.g.***
  - disturbance of the host rock by excavation of the repository (EDZ)
  - mutual chemical impact (construction materials – host rock)
  - mechanical / hydraulic loads
  - thermal impact (by heat generating waste)
- ***development / verification of the repository concept, e.g.***
  - development of waste emplacement concept and corresponding technology
  - backfilling and sealing methods
  - refinement of excavation techniques
  - material specification and monitoring techniques

The defined URL programmes of Äspö and Onkalo as well as the research activities at the GTS in Switzerland have been compiled in a comprehensive R&D list of objectives of the investigations. To come to a common research list for URLs, a screening was carried out to avoid any duplicate issues. An evaluation of the specific objectives showed that many experiments of the different projects have very similar objectives and can, therefore, be subsumed. This underlines the site-independent relevance of these aspects for site / repository characterization. In this work the analysis, comparison and evaluation of the different studies / experiments remained an open point. The methodological approach has been considered at a very general level only. The only integrated criterion for consideration of investigations and experiments was whether they were successful or not. With regard to the transferability of investigations in a URL it is possible that the methodology / strategy is applicable elsewhere, but the results of the measurements rely on the site-specific boundary conditions and are therefore not transferable to other projects and sites. Finally, a summary list of 248 different objectives has been compiled: 92 objectives for host rock characterization, 39 objectives for interaction between host rock and repository, and 117 objectives for repository development.

5.4.3 Relevance test

To come to a site-independent list of key issues for a URL programme, the relevance test cancels all aspects that are unique (only relevant for a very specific geology or a unique repository concept) and therefore not relevant for other projects. Furthermore, all experiments that failed or that were not successful to reach the envisaged results were excluded. A check whether the investigations / experiments are applicable to the Yeniseysky project was beyond the scope of the project. Such an evaluation would require much site-specific information that is not yet available.

Moreover, a project-specific check was made to see whether all (known) aspects of the geology and repository concept of the Yeniseysky project can be integrated into the URL

programme structure. The screening of objectives differentiates between geosphere-relevant aspects and repository-specific aspects. The relevance test evaluated the objectives taking into account the geological boundary conditions and the planned repository concept for Yeniseysky.

As a result of the relevance test, five objectives were excluded from the host rock characterization, one from interaction between repository and host rock, and twenty-six from repository concept development (Middelhoff 2015).

5.4.4 Completeness test and final URL objectives list

The completeness test checks whether all (known) aspects of the geology and repository concept of the Yeniseysky project can be integrated into the URL programme structure. This included the safety-relevant points of special interest that were identified and described in this report:

- Geological characterization of fault zones and rocks
  - contact zone of gneisses with intrusive bodies
  - position and spatial orientation of the fault zones
- Tectonics: vertical + horizontal movements of existing geologic units, incl. seismicity
- Geomechanical properties of the host rocks and fault zones (mechanical / thermal loads)
- Hydrogeological characterization of the host rock
- Characterization of local and regional flow system
- Examination of sorption coefficients of the fault zones
- Performance and durability of the backfill (bentonite-cement mixture)

A comparison of these points with the draft list that resulted from the relevance test showed that all issues can easily be integrated into the structure of the draft research programme.

5.4.5 Catalogue of objectives of a URL programme

From the steps described above, a catalogue of objectives was compiled that identified 216 objectives that are site-independent and can be transferred to any URL project in crystalline rock. To optimize transferability and manageability, the three main issues of the programme have been subdivided into 59 objective subgroups (indications). The most relevant aspects are:

- **Host rock characterization**: rock mass, fractures, geomechanics and hydrogeology
- **Interaction repository – host rock**: EDZ, chemical interaction, mechanical, hydraulic and thermal impacts
- **Development / verification of repository concept**: Full-scale tests of repository components, construction of buffer and drift / shaft seal, interaction canister – buffer – lining, development of properties of clay-based buffer and seal materials, optimization of drift excavation techniques, validation and verification of computer codes

5.4.6 Results

Based on three URL projects, a catalogue of important objectives for R&D work in URLs in crystalline rocks has been developed systematically (Middelhoff 2015). This catalogue is applicable to different sites in crystalline rocks and also covers all safety-relevant points of special interest identified for the Yeniseysky site. To increase the clearness of a research programme structure, a list of important subgroups of objectives (indications) for URLs in crystalline rock has been prepared.

5.4.7 Proposals for future work

Generally, ONKALO can serve as a reference model for the Russian concept. In future, the complete investigations performed in ONKALO should be collected and assessed. The contents of the objectives catalogue can be specified in more detail to evaluate and clarify the aims. The different investigations and experiments should be analysed, evaluated, and integrated into a URL programme. The objectives of the different research groups can be specified / adapted due to project-specific requirements (site-specific geology and the Yeniseysky repository concept). Figure 5.19 illustrates the methodological approach for the development of a draft catalogue of the objectives of an URL programme

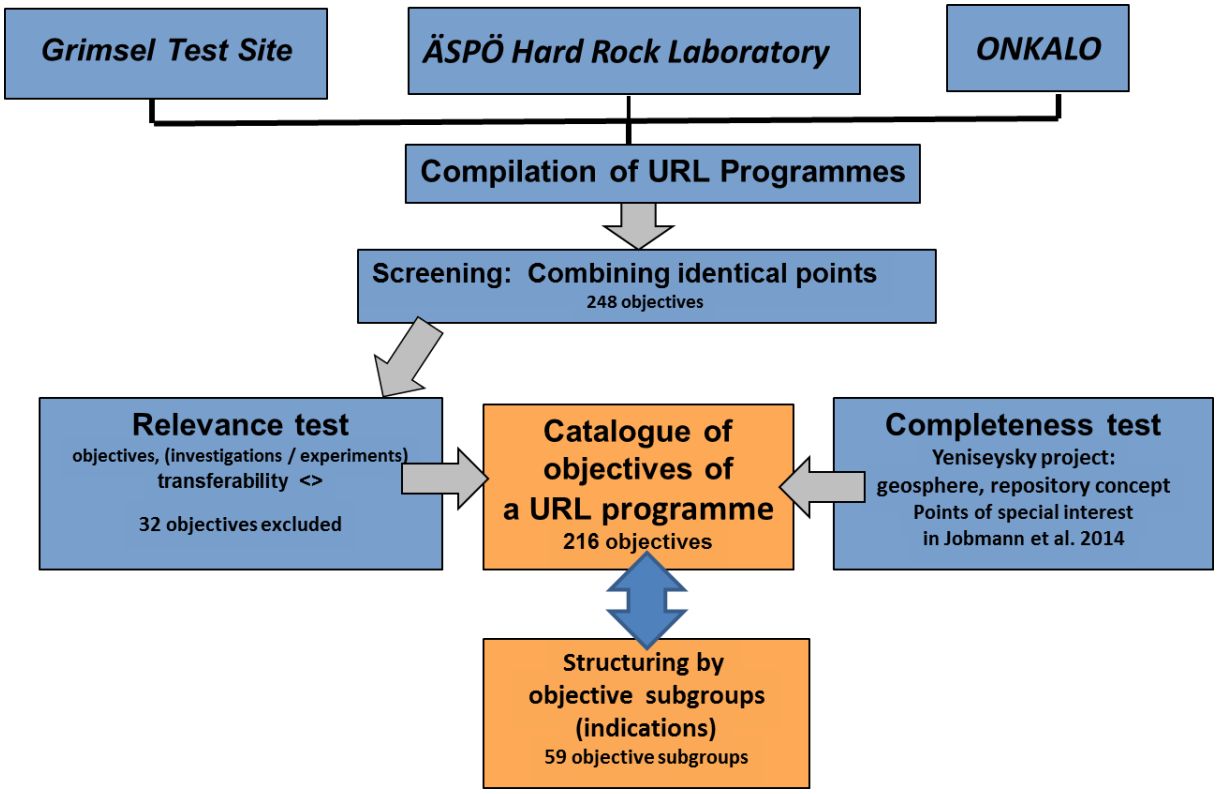

Fig. 5-19: Methodological approach for the development of a draft catalogue of the objectives of a URL programme

6 Evaluation of barrier performance

6.1 Geotechnical and technical barriers

This section describes the temperature evolution in one emplacement borehole as well as in the area between the different emplacement boreholes. Indications about gas pressure build-ups are given and possible seismic impacts are analysed. Finally, the radionuclide release and migration are analysed.

6.1.1 Thermal investigations

6.1.1.1 Thermal evolution next to HLW containers

The temperature evolution in the near-field of waste containers containing heat-generating, vitrified radioactive waste and in the host rocks was simulated based on the provided disposal concept and repository design (Beygul, 2013). The disposal concept is explained in chapter 5. Based on this concept, three geometric variants have been investigated that differ mainly in the distances between drifts and boreholes and initial heat output. The geometric data is shown in Tab. 6.1, and the principle configuration of the numerical model is shown in Fig. 6-1.

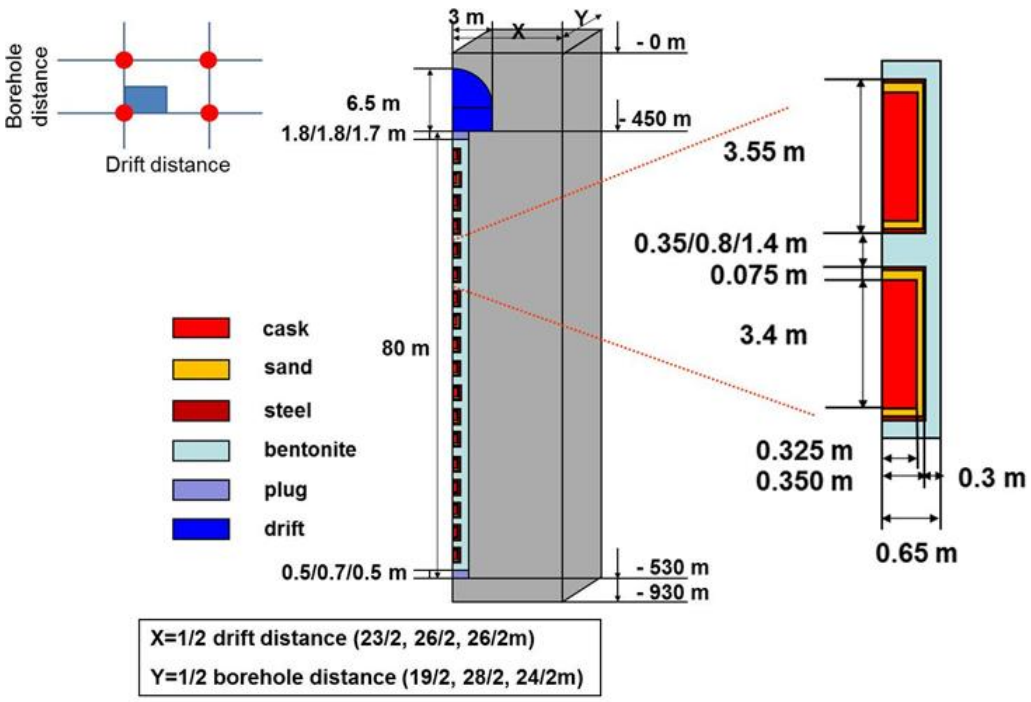

Fig. 6-1: Numerical model of the disposal configuration

Tab. 6.1: Disposal configurations

	Unit	Variant 1	Variant 2	Variant 3
Drift distance	m	23	26	26
Borehole distance	m	19	28	24
Containers per borehole	-	20	18	16
Container distance	m	0.35	0.8	1.4
Plug at borehole top	m	1.8	1.8	1.7
Plug at borehole bottom	m	0.5	0.7	0.5

The different drift and cask distances are related to the different emplacement fields described in chapter 5. The thermal parameters used in the simulations are given in Tab. 6.2, and the data used for the HLW provided by VNIPI PT are given in Tab. 6.3 (Beygul, 2013).

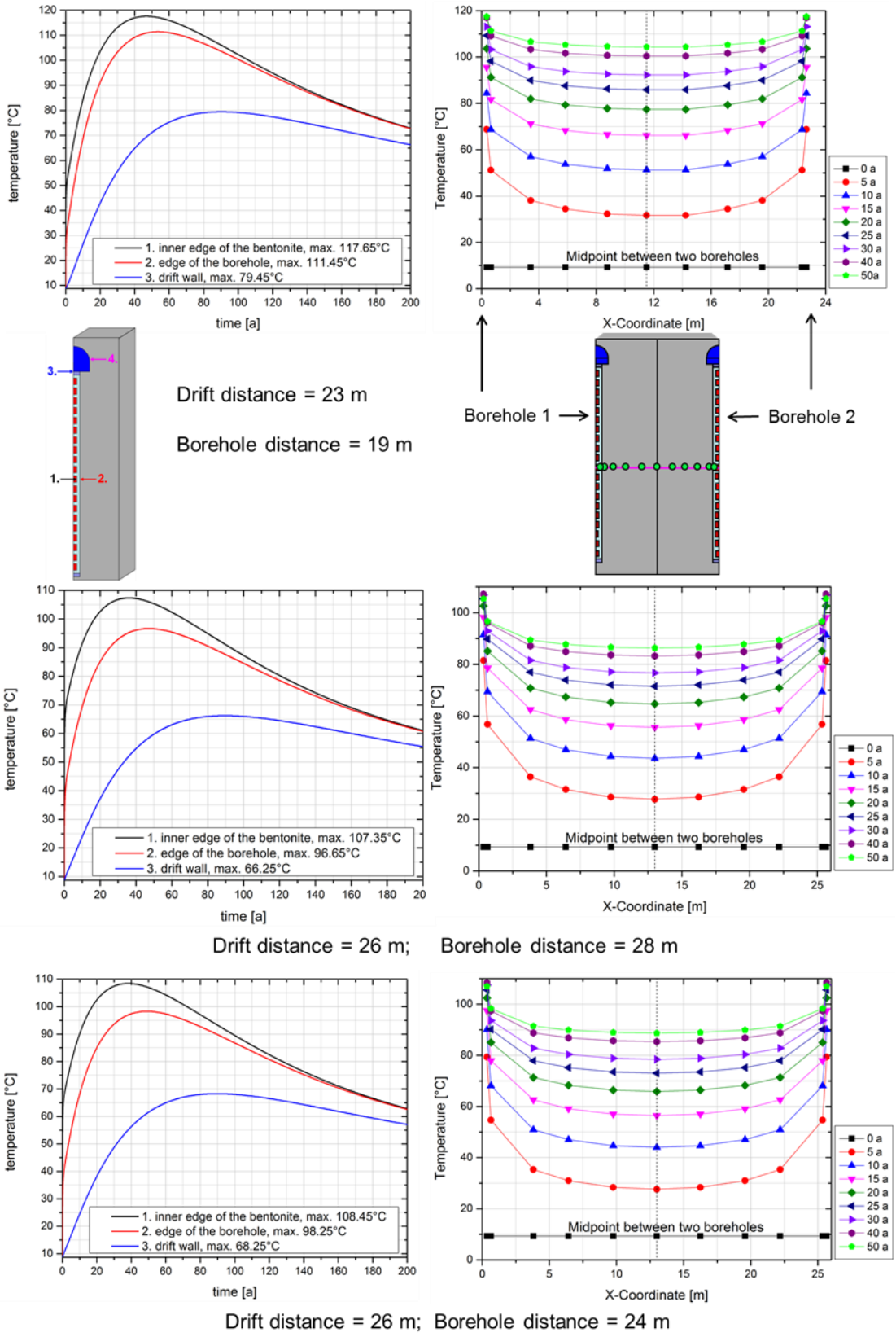

Fig. 6-2: Calculation results of the three variants. Temperature evolution at three observation points at the borehole (left) and at observation points between two boreholes (right)

Tab. 6.2: Thermal parameters

Parameter	Unit	Gneiss	Bentonite	Vitrified HLW
Material density	kg/m^3	2700	1800	2500
Thermal conductivity	W/(m·K)	2.7	0.86	2.4
Specific heat capacity	J/(m·K)	770	1313	800

Tab. 6.3: Parameters of HLW (Beygul, 2013)

Parameters	Unit	Value
Initial heat output	W/m^3	1000 (1) 1500 (2) 1500 (3)
Half-life period of HLW	years	30
HLW volume per container	m^3	0.6

During the numerical calculations, which have been performed using the FLAC3D computer code (Itasca 2005), the temperature evolution at specific points was recorded. The maximum temperature at the bentonite buffer, the host rocks, and at the drift bottom was observed at three points. Points 1 and 2 are located in the middle of a borehole at the inner and outer edge of the bentonite buffer and point 3 is located at the bottom of the drift. The temperature evolution at these points is plotted in Fig. 6-2 for all three variants (left graphs).

In addition, the temperature evolution between two adjacent boreholes is shown on the right graphs in Fig. 6-2. For all three variants the maximum temperature of the bentonite buffer is below 120°C. The temperature maximum is highest for variant 1 and even for this variant, the time period in which the temperature of the bentonite is higher than 100°C is only about 110 years. Neither the maximum value nor the time period with high temperatures gives rise to the assumption that the barrier integrity is jeopardized.

The temperature between two boreholes and thus of the host rocks for variant 1 exceeds 100°C (right graph). According to the vapour pressure curve and the depth level of more than 450 m of the emplaced containers, a significant vaporization of the water in the host rocks is not to be assumed. The original hydrostatic pressure in the rock next to the borehole will recover rather fast after the borehole has been filled leading to a boiling temperature of more than 250°C.

6.1.1.2 Influence of successive container emplacement

Due to simplification, previous temperature calculations were based on the assumption that all emplacement boreholes will be filled at the same time. Normally, 3D numerical simulations make use of symmetrical conditions to keep the numerical model as small as possible in order to reduce the computation time as much as possible. When all the boreholes are loaded successively, the assumed symmetric conditions are no longer valid, which means that the complete emplacement field has to be discretized in the numerical model. Due to the necessary fine discretization in the direct vicinity of the heat sources, this leads to substantial computation times. Therefore, the analytical computer code LINSOUR (Engelmann & Müller-Hoeppe, 1992) was used to analyse the difference between simultaneous and successive loading of the boreholes in terms of temperature development.

The computer code LINSOUR relies on the analytical solution of the heat transfer differential equation for a finite, line shape, instationary heat source emplaced in an infinite, homogenous and isotropic medium with constant material data. With respect to the linearity of the differential equation, LINSOUR uses superposition to model the temperature field of more than one heat source. Fig. 6-3 shows the borehole configuration of an emplacement field simulated with LINSOUR. The heat output of each line source (borehole) has been calibrated to cover the heat release of 18 containers as foreseen in the disposal concept.

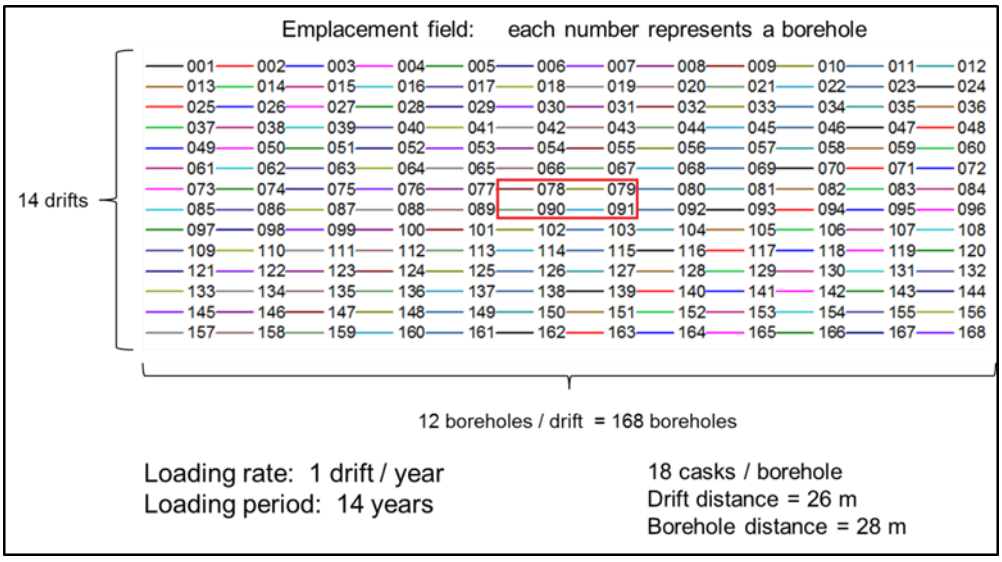

Fig. 6-3: Emplacement field used for analytical calculations

As loading rate, it was assumed that one drift (12 boreholes) will be filled in one year resulting in a total loading period of 14 years.

The highest temperature occurs in the four boreholes in the middle of the emplacement field at the depth of the tenth container (Fig. 6-4). To analyse the difference between simultaneous und successive loading this depth point was used to compare the calculation results. In Fig. 6-5 (left) the temperature development resulting from an instantaneous loading is plotted. The maximum temperature at the field boundary is about 40°C less than in the middle of the field. The calculation results assuming a successive loading of the boreholes are shown in Fig. 6-5 (right). No significant change of the maximum temperature can be seen. The only difference is the starting point of the temperature curve. For a more detailed comparison the temperature evolution of boreholes 91 (middle of the field) and 168 (field boundary) are plotted for both kinds of borehole loading in Fig. 6-6.

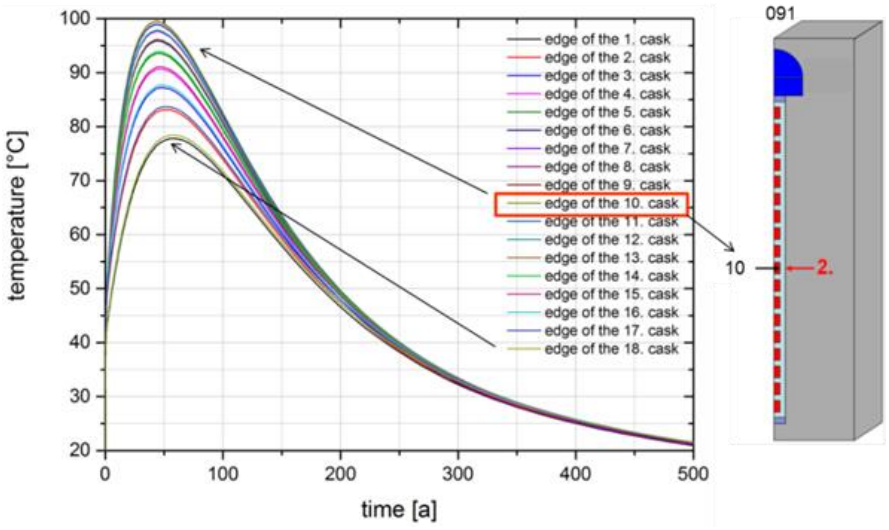

Fig. 6-4: Temperature development in one borehole at the depth of the containers

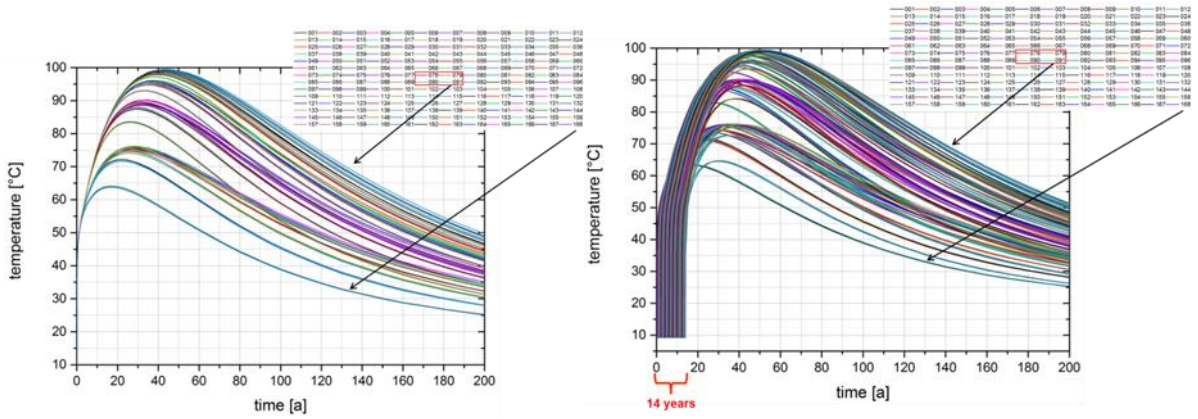

Fig. 6-5: Temperature developments at all observation points for instantaneous und successive borehole loading

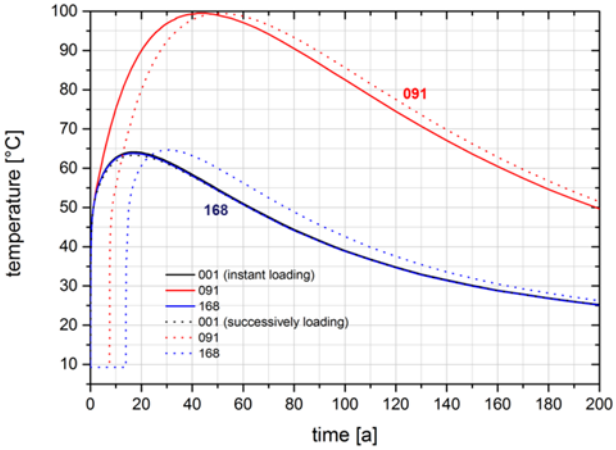

Fig. 6-6: Temperature evolution at two borehole locations in the middle of the field and at the field boundary for instantaneous and successive loading

The solid lines represent the results of the simultaneous loading and the dotted lines those of the successive loading. As can be seen, there is only a very small change in the maximum temperature. The main difference is the time when the maximum temperature is reached. This time is delayed in case of a successive loading, and the delay depends on the location of the borehole. The results are plausible as the total energy input as well as the locations of the heat input are identical for both kinds of loading. The maximum temperature would only change if the geometric shape of the emplacement field is changed, for example by using different drift distances. Besides delaying the maximum temperature occurrence, the successive loading leads to a shift of the starting points and to a slight change of the shape of the curves.

6.1.2 Influence of gas pressure build-up

Gas formation in the repository – if critical gas pressures are reached – can lead to crack formation in the engineered barriers and thus impair their safety function. The investigations focus on gas pressure evolution due to waste container erosion and thermal expansion.

The gas forming on the container surface is either present as flowing gas phase or – depending on the pressure conditions – it is dissolved in the pore water where it is transported by means of gas diffusion. These processes are significantly influenced by the temperature conditions existing at the site. However, the simulations do not take into account the mechanical behaviour of the host rocks or of the engineered barriers. Neither do they consider the influence of temperature and degree of saturation on petrophysical properties.

The modelling concept assumes that the waste containers are emplaced in 18-m-deep boreholes in crystalline host rocks. In the borehole, the containers are emplaced with a predefined distance from each other. The individual containers are surrounded by a bed of sand followed by a bentonite buffer. The sand acts as heat spreader. The section between the top of the uppermost container and the bottom of the lowermost container is the thermally active part of the borehole. The dimensions and settings relevant to the model are listed in Tab. 6.4.

In accordance with the configuration, the total borehole length is divided into an active borehole length of 15 m, a borehole plug of 2.0 m, and a bottom plate of 0.5 m. The container spacing is based on an equal distribution of 6 containers over the active borehole length, which results in a container spacing of 1.8 m. The borehole diameter of 1.75 m is determined by the container diameter as well as the thickness of the sand layer and of the bentonite. The model is based on the assumption that there are no gaps between container wall, sand, bentonite, and host rocks that would influence fluid flow and heat transfer. The depth of the upper boundary of the model area is assumed to be 650 m. The simulation takes into account a cylindrical symmetry of the model. Fig. 6-7 shows the section of the model area that illustrates the interfaces between container, heat spreader, buffer, and host rocks. The numbered cells at the interfaces between neighbouring media are reference points for comparing simulation results.

Tab. 6.4: Dimensions relevant to modelling

Borehole length	[m]	18.0
Length of thermally active section	[m]	15.0
Borehole spacing	[m]	30.0
Borehole diameter	[m]	0.45
Container length	[m]	1.0
Number of containers per borehole	[-]	6
Container wall thickness	[m]	0.007
Thickness of sand layer	[m]	0.25
Thickness of bentonite buffer	[m]	0.40

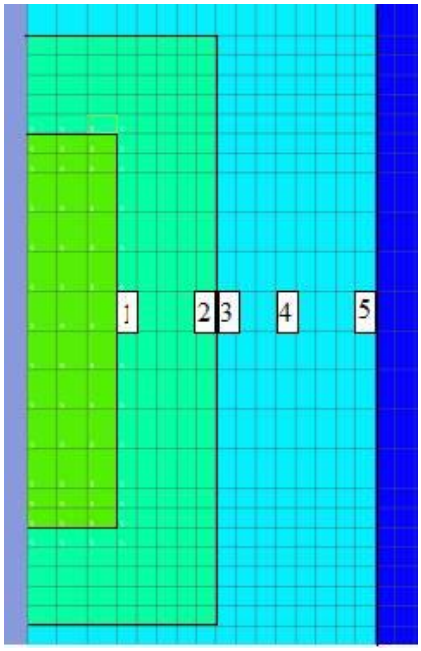

Fig. 6-7: Discretization mesh of the model area with container, heat spreader, buffer, and host rocks. The numbered cells are located at the fourth container

One half of the borehole modelled is filled with HLW containers, the other half with containers of the Cs/Sr fraction. In the reference case, the initial water saturation in the model area is 100%. The pressure build-up was calculated using TOUGH2 (Pruess et al., 1999), which had been extended by the EWASG module (**E**quation of State for **WA**er, **S**alt and **G**as).

The relative permeability of the liquid phase $k_{r,l}$ is modelled using the Genuchten-Mualem approach according to (Van Genuchten, 1980):

$$k_{r,l} = S_l^{*\frac{1}{2}} \left(1 - \left(1 - S_l^{*\frac{1}{m}} \right)^m \right)^2 \tag{6-1}$$

with:

$$S_l^* = \frac{S_l - S_{r,l}}{1 - S_{r,l}}$$

where S_l indicates the effective and $S_{r,l}$ the residual saturation of the liquid phase. The parameter m is set to 0.45 for the entire model area.

The corrosion rate q is modelled as a function of the temperature T using

$$q = a \exp\left(-\frac{\tau}{T} \right) \tag{6-2}$$

with a and τ as model parameters.

Fig. 6-8 compares data on corrosion behaviour found in various sources (Alkan & Müller, 2007). The corrosion models used in the simulation use the parameter τ = 1360.5 K. The reference case uses a parameter a of 50 µm a^{-1} (corrosion model 1) while the variation uses 100 µm a^{-1} (corrosion model 2).

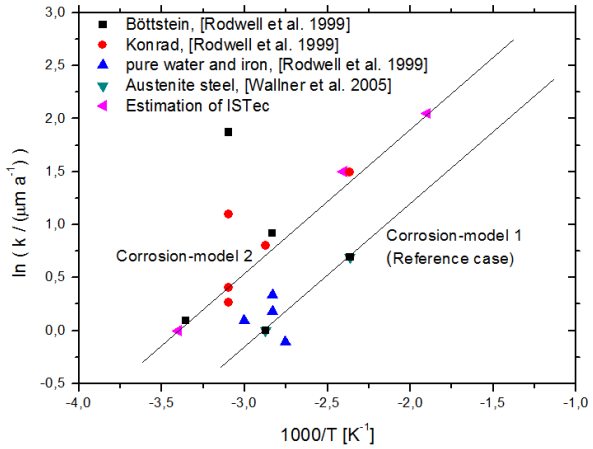

Fig. 6-8: Data on container corrosion and corrosion models applied

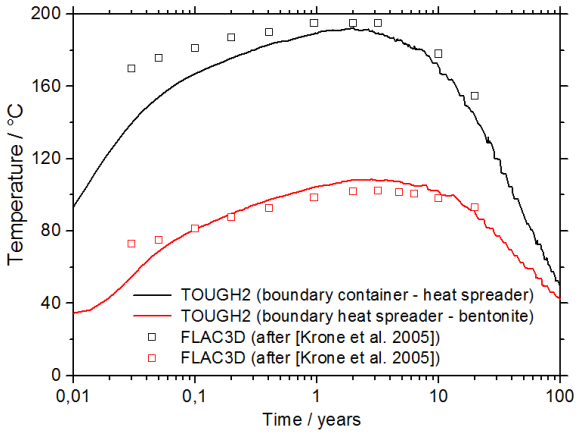

Fig. 6-9: Comparison of the temperature evolution with results from (Krone et al. 2005)

The heat output from the waste is assumed to be the arithmetic mean of the heat output of both types of waste considered. A comparison with the design calculations carried out with FLAC3D in (Krone et al., 2005) shows that for this purpose the thermal conditions can be modelled with adequate precision as shown in Fig. 6-9 for two comparison points. Initial conditions and the other model parameters are compiled in table 6-5 and table 6-6.

Tab. 6.5: Initial conditions

Reference depth	[m]	650.0	Water saturation	[-]	1.0
Temperature at reference depth	[°C]	29.5	Temperature gradient	[K m^{-1}]	0.037
Hydraulic pressure (reference depth)	[MPa]	7.8	Pressure gradient	[MPa m^{-1}]	0.011

Tab. 6.6: Model parameters

Parameter	Unit	Host rocks	Bentonite + admixture	Sand	Waste matrix
Density	[kg m^{-3}]	2180.0	2180.0	2000.0	8000.0
Heat conductivity	[W m^{-1} K^{-1}]	2.35	1.70	0.70	1,2
Specific heat capacity	[J kg^{-1} K^{-1}]	950.0	1050.0	1000.0	920.0
Porosity	[-]	0.01	0.05	0.20	-
Permeability	[m^2]	10^{-20}	10^{-18}	10^{-17}	10^{-21}
Gas entry pressure	[MPa]	1	5,9*	1	-
Maximum capillary pressure	[MPa]	10^2	10^4	10^2	-
m (van Genuchten)	[-]	0.45	0.45	0.45	-

Fig. 6-10 shows the pressure and temperature evolution in cell 3 (Fig. 6-7) of the model mesh for the reference case. The thermal expansion of the gas in the heat spreader and the bentonite is a major factor. It causes the pressure to increase to 15 MPa in the initial phase. Despite of the gas evolution due to corrosion, the pressure decreases to 3 MPa in the course of 2 years and stabilizes at this level in the long term. This means that gas evolution due to corrosion has hardly any influence on the pressure build-up.

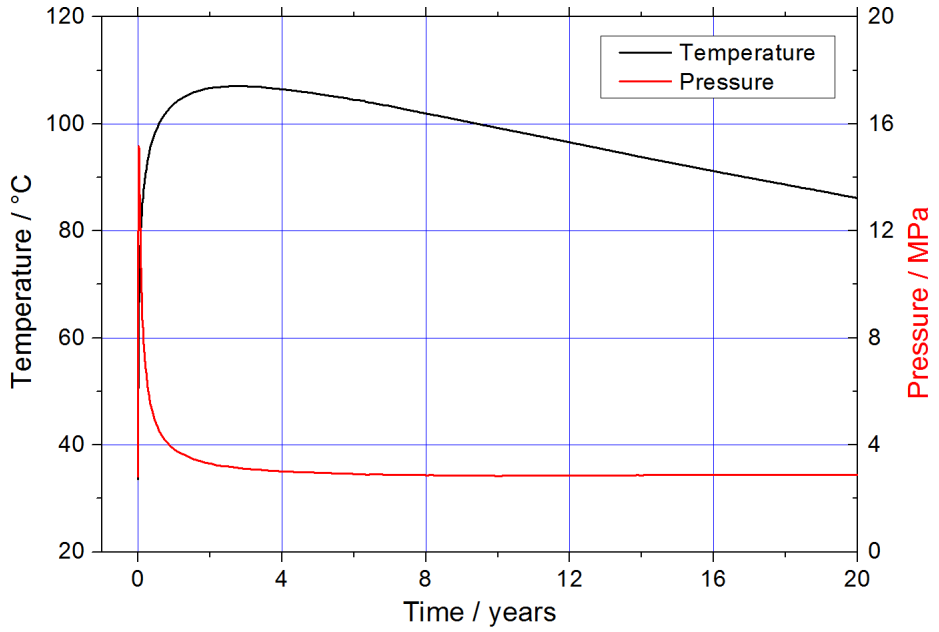

Fig. 6-10: Pressure and temperature evolution at the interface between heat spreader and buffer at the location of the fourth container (cell 3) for the reference case

Varying the gas diffusion has no significant effect on the pressure. Likewise, a simulation with an increased corrosion rate does not cause a significant pressure increase but causes an increase in gas saturation as shown in Fig. 6-11.

* The gas entry pressure into bentonite is determined as a function of permeability according to (Pusch, 1987).

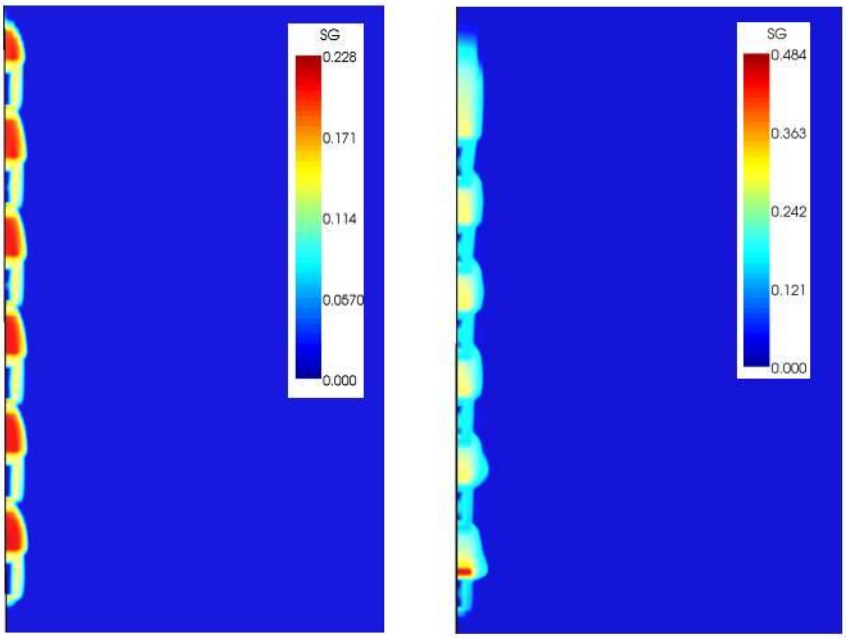

Fig. 6-11: Gas saturation after 100 years in the reference case (left) and with increased corrosion (corrosion model 2, right)

What is essential for the pressure maximum is the permeability of the formations the gas passes through, as Fig. 6-12 shows for the variation of the bentonite permeability and Fig. 6-13 for the variation of the rock permeability. Taking into account excavation damaged zones or fractures in the host rocks likewise leads to a significant decrease of the maximum pressure.

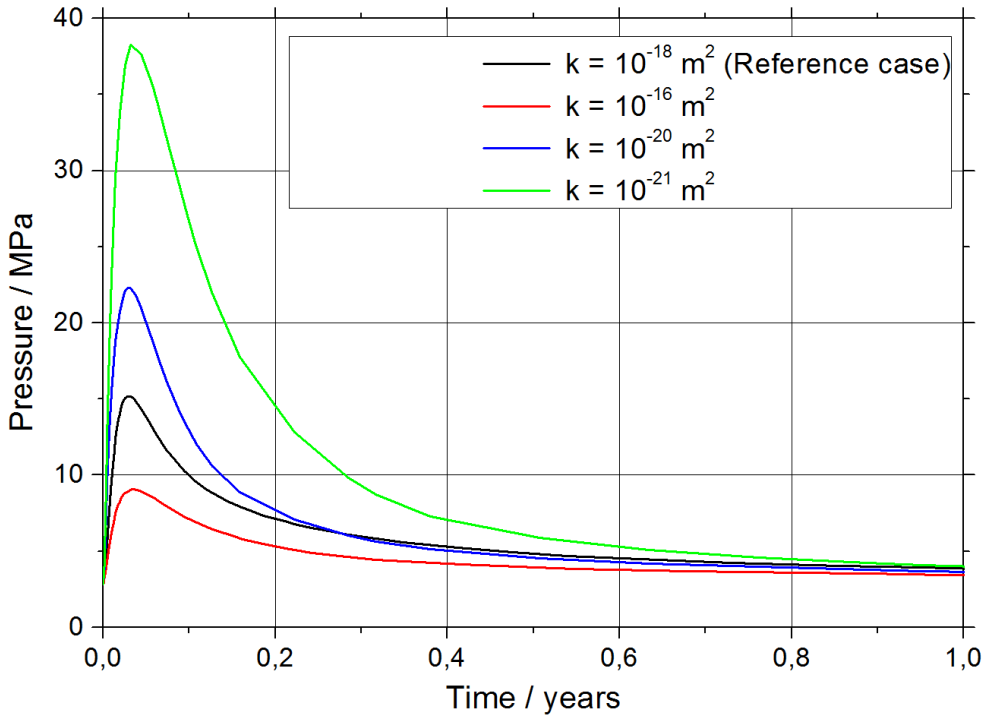

Fig. 6-12: Pressure evolution in cell 3 when varying the permeabilities of the bentonite

The initial pressure saturation is also essential to the pressure build-up in the initial phase. Compared with the initially gas-free reference case, the gas prevents an extreme increase in pressure in the initial phase due to its high compressibility, as can be seen in Fig. 6-14.

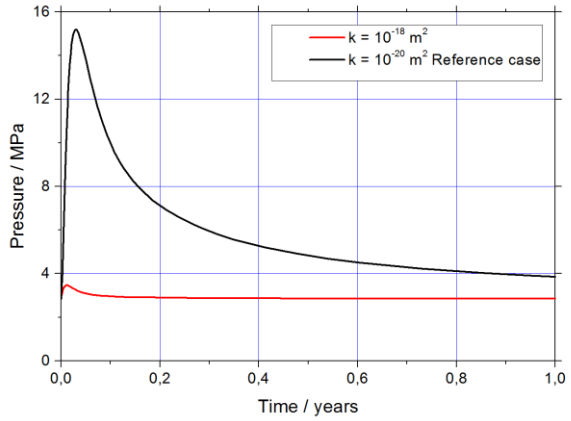

Fig. 6-13: Influence of the permeability of the host rocks on the pressure in cell 3

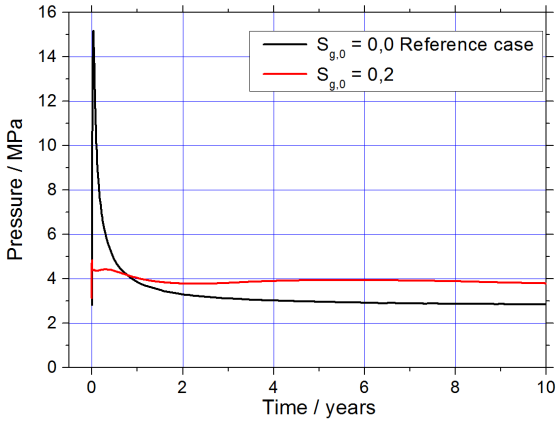

Fig. 6-14: Pressure evolution in cell 3 when varying the initial gas saturation

The main results of the calculations on gas pressure build-up and parameter variation are summarized and assessed below:

- In the initial phase, i.e. shortly after the waste containers have been emplaced, the gas pressure evolution is significantly influenced by the thermal expansion of the gas that is present in the vicinity of the containers. Within the course of the ensuing years, the pressure decreases to a stable level.
- The pressure decrease is mainly caused by diffusion. A decrease in gas diffusion by half an order of magnitude does not lead to significant changes in the pressure behaviour.
- A major factor in the pressure evolution is the permeability of the bentonite. If its permeability is very low, it is possible that pressure builds up, which in turn may lead to crack formation in the bentonite and may, thus, compromise its isolation properties.
- The permeability of the host rocks is likewise significant for the pressure evolution. The pressure build-up is lower at increased permeabilities. The same applies for the increased permeability of the excavation damaged zone. Fractures in the host rocks lead to a further decrease in pressure.
- Gas pressure build-up due to corrosion does not become effective for many years when the pressure evolution due to thermal expansion has already stabilized. Due to the low gas production rate, however, it does not have any significant influence on the pressure evolution. An increase in the gas production rate (by half an order of magnitude) leads to a higher gas saturation but not to significantly higher pressures.

In summary, it should be noted that the permeability and the initial degree of saturation of the bentonite have the strongest influence on the gas pressure evolution and that these properties – contrary to the permeabilities of the host rocks, incl. excavation damaged zone and fractures – are projectable when designing a repository. In view of the gas pressure evolution, these aspects should be taken into account when designing the bentonite barrier; e.g. when planning the degree of compaction, in order to avoid impairments of the barrier functions. This is to be demonstrated when building a safety case.

6.1.3 Investigation of earthquake impact on canisters

When designing a repository site in crystalline rocks, one has to assume that fractures may exist in the areas where emplacement boreholes are to be located and that these fractures may evolve into fault ruptures due to seismic impacts. It is thus possible that displacements of blocks of host rocks occur along these fractures. It also has to be assumed that widespread fractures along which displacements may occur already exist throughout the host rocks (cf. Fig. 6-15, left). However, it is also possible that such fractures evolve in virgin host rocks. The genesis of a fault rupture along a fracture that crosses an emplacement borehole with a waste container leads to shear stresses that may cause the container to break. The right side of Fig. 6-15 illustrates the impact of a rupture along a fracture that crosses a waste container.

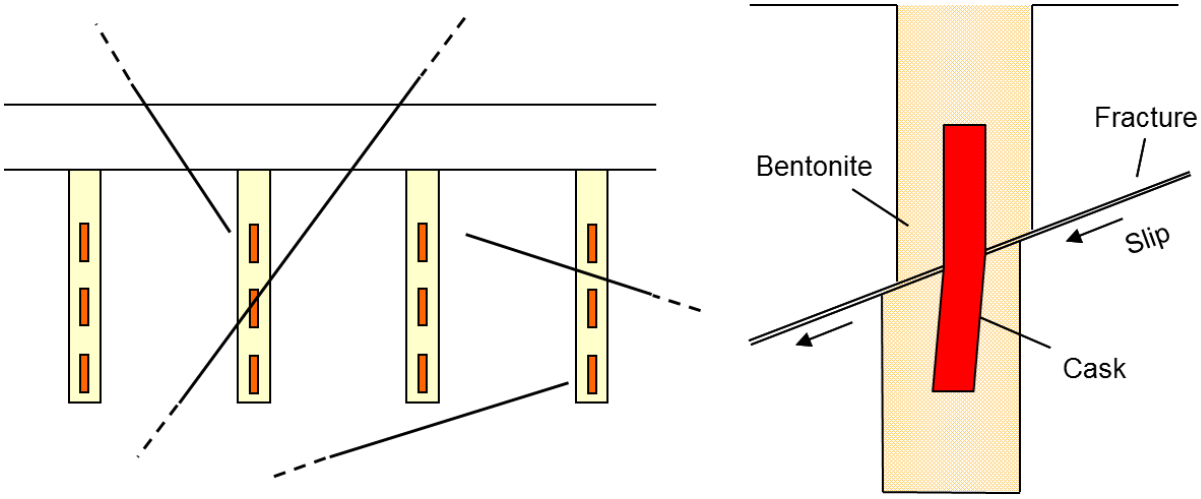

Fig. 6-15: Possible fractures in the emplacement area and impact of a rupture on a waste container

6.1.3.1 Simulation of the impact of seismically induced fault ruptures

The calculations carried out with FLAC3D (Itasca, 2005) to simulate the genesis and impacts of a seismically induced fault rupture are based on a fracture that crosses the emplacement location of a waste container. The orientation of the fracture influences the impacts on the container. To estimate these impacts, scenarios with a horizontally crossing fracture, a fracture crossing at an angle of 30°, and with a vertically crossing fracture are considered (Fig. 6-16). In addition to this, the filling level of the container was assumed to be either 100% or 80% as this determines the stiffness of the container and, thus, the degree of deformation caused by the shear stress. Due to technical reasons, it is indeed possible that containers are not completely filled with waste.

The model includes the following material components:

- the host rock, consisting of two blocks that are movable against each other and that – like a shear box – generate the shear stress
- the bentonite buffer
- the container wall
- the waste matrix

For reasons of conservatism, the “heat spreader“ sand, originally planned between container and bentonite, was not taken into account. In the undisturbed state, the components are embedded into each other in a cylindrically symmetric way.

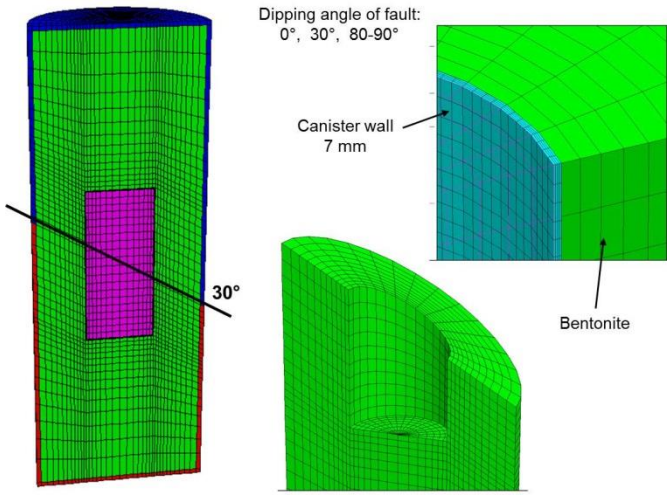

Fig. 6-16: Discretisation mesh (cross section) of the undisturbed geometry for simulating the scenarios with a fracture that crosses at an angle of 30° with host rock (red, blue), bentonite buffer (green), and waste matrix (magenta)

The simulation of the stress on a container is based on the following assumptions:

- The fracture crosses the container at its centre.
- The rock is assumed to be an incompressible solid body; i.e. there will be no mechanical deformation of the host rocks.
- The deformation velocity is so high that no pore pressure dissipation due to hydraulic effects occurs.
- The fracture aperture is negligible compared with the container dimensions and is set to 0.
- The isotropic compressive stress acting on the system is 10 MPa, which corresponds to an approximate depth of 400 m to 500 m.

The assumption that no pressure dissipation occurs is conservative as pressure dissipation would lead to a decreased stiffness of the saturated bentonite-water-system and, thus, to higher forces acting on the container.

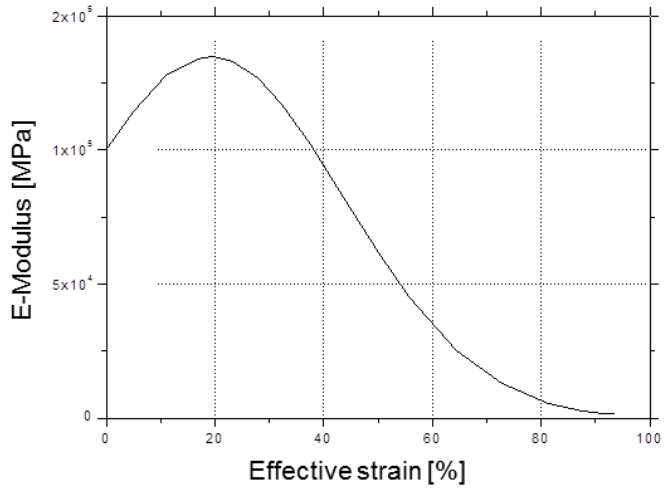

For the austenitic steel of the container wall, a nonlinear elastic constitutive law as a function of the effective distortion is used (Fig. 6-17). For the bentonite and the waste matrix, behaviour in accordance with the Mohr-Coulomb constitutive law is assumed. The same applies to the three contact zones between host rock, bentonite, container wall, and waste matrix. Furthermore, the bentonite is modelled as hardening material due to the dependence of cohesion on the plastic shear deformation.

Fig. 6-17: Young's Modulus of the container steel as a function of the effective distortion

The model parameters in and surrounding the waste container are summarized in table 6-7 and table 6-8.

Tab. 6.7: Model parameters of the materials surrounding the waste container (Krone et al., 2005; Billaux, 2007)

Parameter	Unit	Contact zone host rock-bentonite	Bentonite	Contact zone bentonite – waste container
Outer radius	[m]	1.05	1.05	0.437
Inner radius	[m]	1.05	0.437	0.437
Height	[m]	3.00	3.00	1.00
Density	[kg m^{-3}]	-	$1.95 \cdot 10^{3}$	-
Cohesion	[Pa]	$5.0 \cdot 10^{5}$	$4.325 \cdot 10^{6*}$	$2.5 \cdot 10^{4}$
Friction angle	[°]	25	0	25
Dilatancy angle	[°]	0	0	0
Normal stiffness	[N m^{-1}]	$1.8 \cdot 10^{12}$	$8.33 \cdot 10^{9}$	$1.8 \cdot 10^{15}$
Parameter	Unit	Contact zone host rock - bentonite	Bentonite	Contact zone bentonite - waste container
Modulus of elasticity (Young's modulus)	[Pa]	-	$5 \cdot 10^{9}$	-
Poisson's ratio	[-]	-	0.4	-
Tension cut-off	[Pa]	$6.0 \cdot 10^{5}$	$7.5 \cdot 10^{6}$	$7.5 \cdot 10^{6}$

* Initial value of the bentonite cohesion, which changes in accordance with the strain state

Tab. 6.8: Model parameters of the materials in the waste container

Parameter	Unit	Container wall	Contact zone container wall – waste matrix	Waste matrix
Outer radius	[m]	0.437	0.430	0.430
Inner radius	[m]	0.430	0.430	0.000
Height	[m]	1.00	1.00	0.986
Density	[kg m^{-3}]	$7.85 \cdot 10^{3}$	-	$2.00 \cdot 10^{4}$
Cohesion	[Pa]	$4.325 \cdot 10^{6}$	$2.5 \cdot 10^{4}$	$2.5 \cdot 10^{6}$
Friction angle	[°]	0	25	0
Dilatancy angle	[°]	0	0	0
Normal stiffness	[N m^{-1}]	$8.33 \cdot 10^{10}$	$1.8 \cdot 10^{15}$	$3.55 \cdot 10^{9}$
Shear stiffness	[N m^{-1}]	$1.79 \cdot 10^{9}$	$9.84 \cdot 10^{15}$	$2.66 \cdot 10^{9}$
Modulus of elasticity (Young's modulus)	[Pa]	$3.85 \cdot 10^{10}$	-	$6.4 \cdot 10^{10}$
Poisson's ratio	[-]	0.4	-	0.2
Tension cut-off	[Pa]	$7.5 \cdot 10^{6}$	$6.0 \cdot 10^{5}$	$5.0 \cdot 10^{6}$

During the implementation with FLAC3D, two approaches were used:

- The easier to manage *small-strain-mode* of FLAC3D, which does not allow a deformation of the discretization mesh. This mode can be used if a high stiffness of the container is assumed to lead to only small deformations and if the impacts of the distortions on the stress state compared with the stress redistribution in the container caused by the shear force are assumed to be negligible.

- The *large-strain-mode*, which requires that the meshes are adjusted to the occurring distortion so that the meshes do not become numerically irregular due to a shifting of the knots.

The generation of the deformable meshes of the *large-strain mode* is very time consuming and is only possible taking into account the geometry and the impacting forces.

The simulations show that the distortions in *small-strain-mode* are slightly smaller than in *large-strain-mode* and are probably smaller than the actual distortions to be expected. The horizontally crossing fracture and the fracture crossing at an angle of 30° resulted in distortions of up to 4.4% with a fracture displacement of 16 cm maximum (Fig. 6-18 and Fig. 6-20), where the fracture crossing at an angle caused slightly larger distortions than the horizontally crossing fracture. While the displacement is the same, the vertically crossing fracture resulted in distortions of less than 1% (Fig. 6-21). The filling level of the container only slightly influences the results, as a comparison between Fig. 6-19 and Fig. 6-18 shows. The limit value for the distortion is 5%. Taking into account a safety margin, the calculations were carried out for distortions of up to 4.4% which resulted in a maximum fracture displacement of 16 cm. This value was used as maximum permissible displacement value in order to not exceed the distortion limit of 5% anywhere.

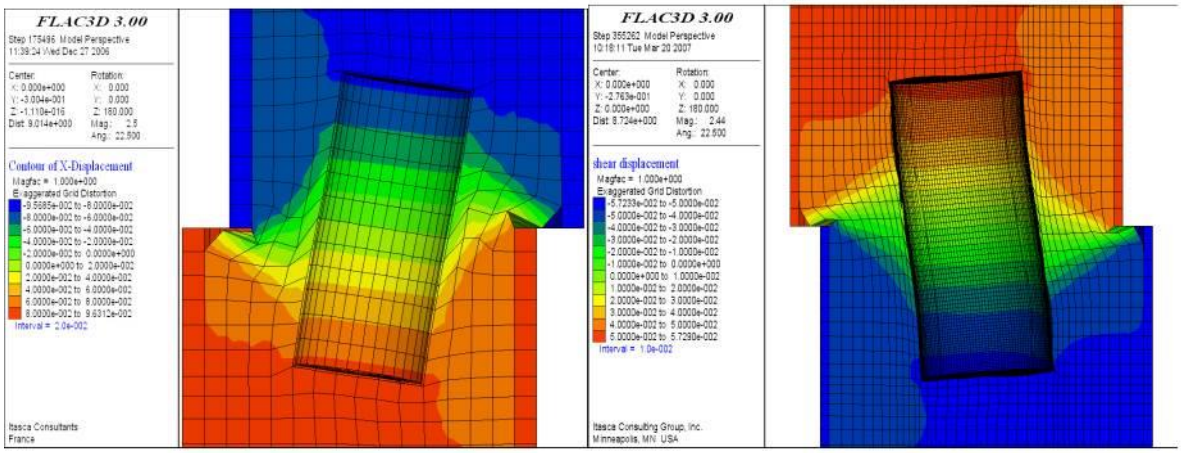

Fig. 6-18: Displacement field of the container in small-strain-mode (left) and large-strain-mode when the fracture crosses horizontally

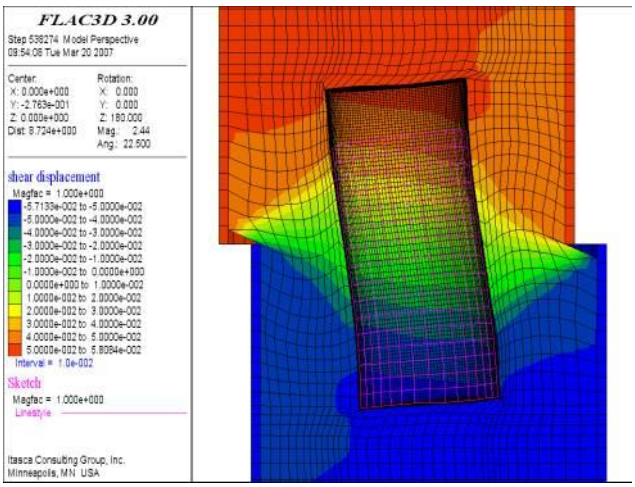

Fig. 6-19: Displacement field of a container filled to 80% of its capacity in large-strain-mode when the fracture crosses horizontally

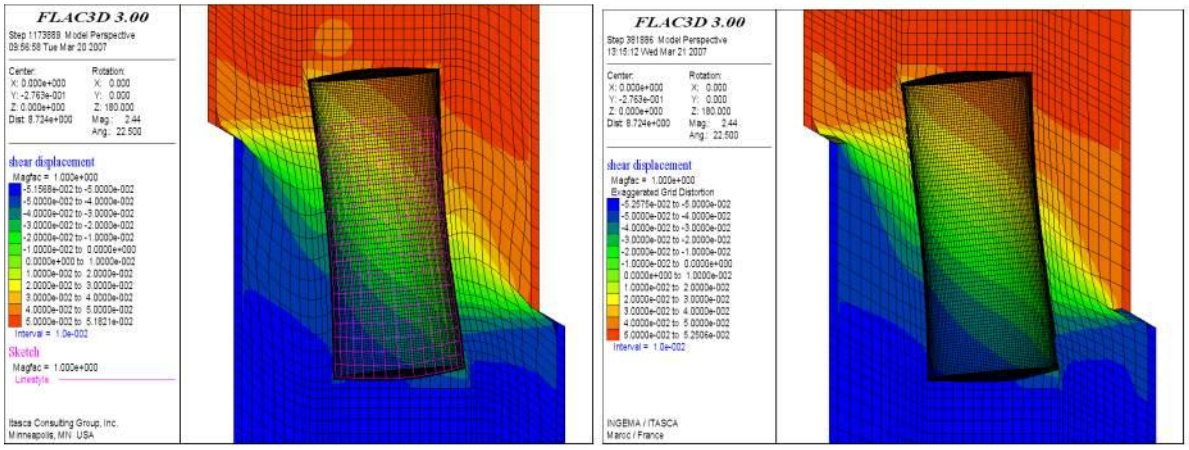

Fig. 6-20: Displacement field of a container filled to 100% (left) and filled to 80% of its capacity when the fracture crosses at an angle of 30°

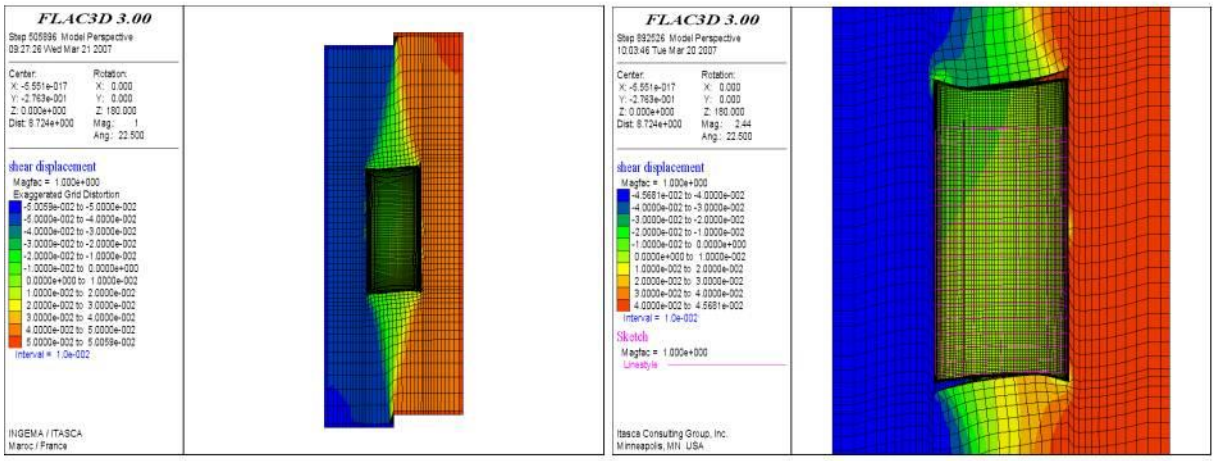

Fig. 6-21: Displacement field of a container filled to 100% (left) and filled to 80% of its capacity when the fracure crosses vertically

6.1.3.2 Risk assessment

If and to what extent the maximum permissible fracture displacement calculated above will place a risk when taking into account the seismic conditions given in the area to be studied will be discussed in the following.

From literature, a number of studies are known that link seismic parameters; e.g. the magnitude of an earthquake, with geologic structures visible on the surface; e.g., fault zones or displacements. Detailed studies on this issue can be found in the work of (Coppersmith & Youngs, 2000) and (Wells & Coppersmith, 1994). The latter compiled a data basis from more than 420 well-documented earthquakes all over the world with a magnitude >4.5 that they used to derive mathematically describable relations between e.g. magnitude, length, and depth of surface and subsurface rock displacements or ruptures. The following figures are taken from the work of (Wells & Coppersmith, 1994) and illustrate these relations together with the regression equations (Fig. 6-22 and Fig. 6-23). The left sides of the figures show the regression of all measuring values, while the right sides show specific regressions for various types of ruptures.

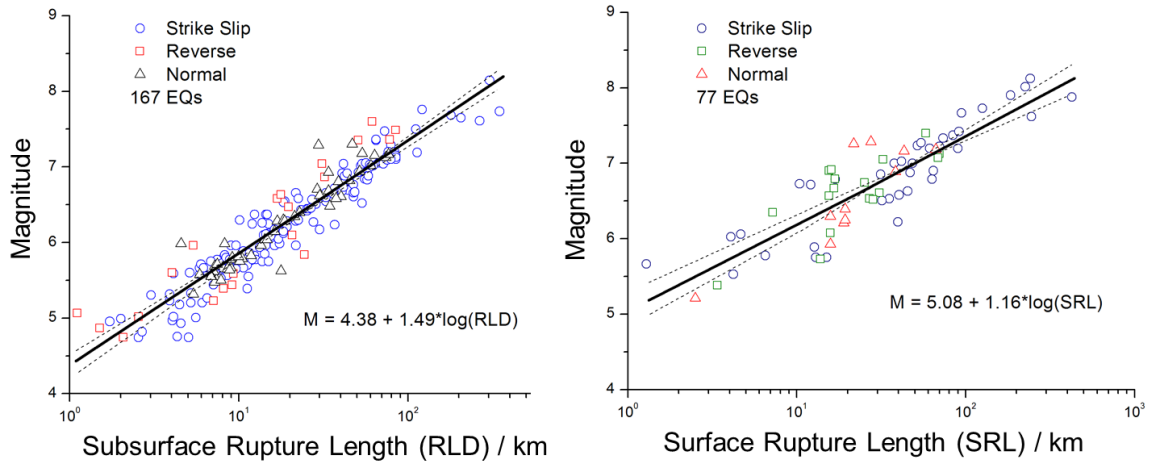

Fig. 6-22: Relation between magnitude and subsurface as well as surface rupture length (modified after Wells & Coppersmith, 1994)

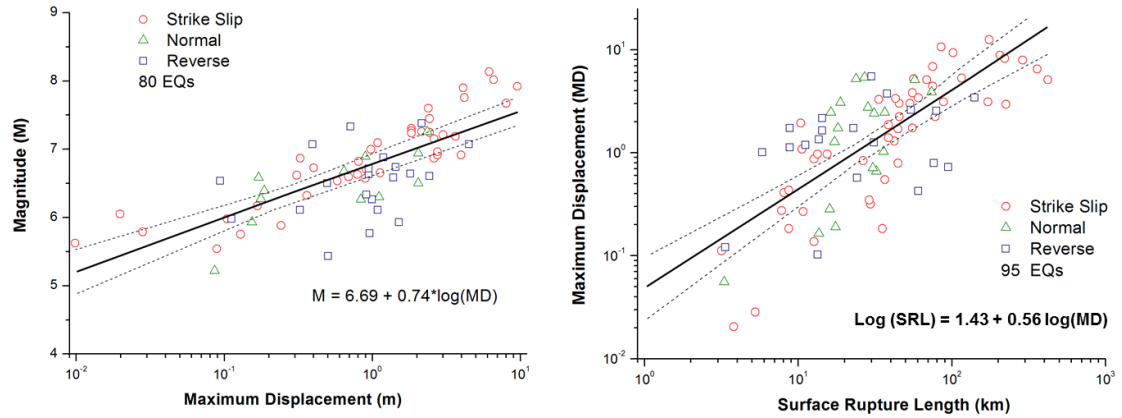

Fig. 6-23: Relation between magnitude and maximum rock displacement as well as relation between maximum rock displacement and surface rupture length (modified after Wells & Coppersmith, 1994)

The regression relations can be used to determine with a confidence level of 95% the magnitude as well as the surface and subsurface rupture lengths that are related to a maximum rock displacement of 16 cm (eq. (6-4) and (6-5)).

$$M = 6.69 + 0.74 \log(MD) \quad (6\text{-}3)$$

$$M = 4.38 + 1.49 \log(RLD) \quad (6\text{-}4)$$

$$\text{Log } (SRL) = 1.43 + 0.56 \log(MD) \quad (6\text{-}5)$$

where:

M	Moment magnitude
MD	Maximum permissible rock displacement / m
SRL	Length of surface rock displacement / km
RLD	Length of subsurface rock displacement / km

Equations (6-3) to (6-5) result in a magnitude of 6.1, which is a relatively high value, a subsurface length of the rock displacement of approximately 14 km, and a surface length of the visible displacement of approximately 4 km.

Considering the dimensions of such fault ruptures, it becomes clear that they can hardly remain undetected during exploration. It also means that mapping and surveying of fault ruptures should be carried out with utmost care in order to be able to avoid such fault zones when designing a repository.

As to the necessary magnitude of 6.1, a seismologic map covering data of the past 200 years (Fig. 6-24) shows that in the vicinity of the planned repository only one single earthquake of this magnitude has been measured and that was just less than 200 km south of the survey area.

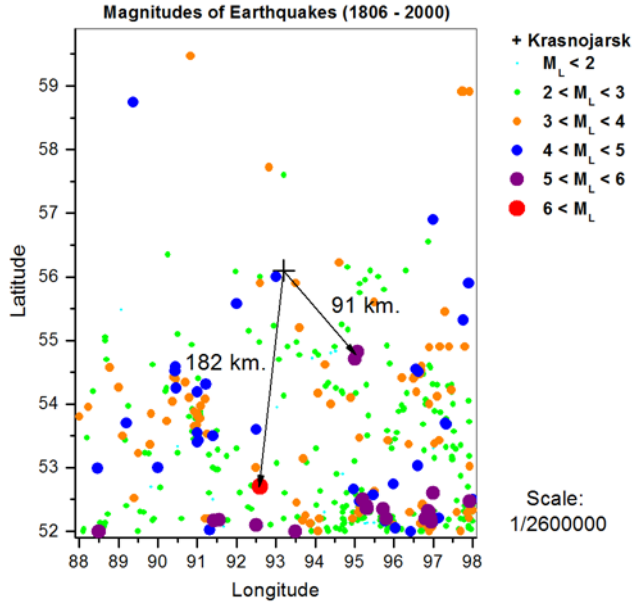

Fig. 6-24: Distribution and magnitudes of the earthquakes in the greater Krasnojarsk area in the past 200 years ((Shebalin & Leydecker, 1997) in SSR catalogue, ISC catalogue in (ISC-Bulletin, 2001)). See chapter 2.3.

Distances of primary fault ruptures to fractures in the survey area

For energetic reasons (an overview of empirical data can be found in La Pointe et al., (1997), only primary fault ruptures with a length of >3 km can be dislocated by more than 0.1 m. At a length of 3 km (assumed width 10-50 m) it is probable but not guaranteed that all these fault zone are detected in a surface exploration. Zones with a width of <5 m are definitely hard to detect in a surface exploration. It has to be assumed, however, that during the underground exploration and the construction of the repository, further fracture zones will be detected and that the primary fault ruptures run sub-horizontally.

It is possible to estimate the distance to a repository that needs to be explored in order to identify fault ruptures that are longer than 3 km and could cause problems. (Coppersmith & Youngs, 2000) have compiled results of field studies on the dislocation of secondary fault ruptures as a function of displacement along primary fault ruptures after heavy earthquakes in the *Basin and Range Province* in western USA. They found out that the link between the relation between primary and secondary dislocation and the distance between primary and secondary fault rupture can be analysed using a gamma distribution. Whether this model can be transferred to the seismicity in Krasnoyarsk is unknown. If the latter is assumed to be possible, however, it is possible to estimate the minimum dimensions of the areas that need to be explored in order to detect and describe primary fault ruptures. If a threshold value for the secondary displacement is defined; e.g. 0.16 m as determined in the calculations above, the model presents the secondary displacement – as a function of the distance – that would be necessary to reach the threshold value. (Wells & Coppersmith, 1994) also published tables that list statistically significant relations between the length of a visible surface fault line, the magnitude, and the maximum displacement. The second table can be used to relate the

primary displacement to the length of the surface fault line and to the earthquake magnitude (Fig. 6-23). When these two tables are combined, the minimum exploration radius that is necessary to characterize primary fault ruptures can be identified. If the most severe earthquake possible is assumed, the table can be used to determine the maximum exploration radius. Maximum radii for the magnitudes 7.0, 7.5, 8.0, 8.5, and 9.0 are listed in Tab. 6.9 (Bäckblom et al., 2004).

Tab. 6.9: Maximum exploration radii estimated based on data from field studies (modified after Bäckblom et al., (2004))

SF = Strike-slip fault, R = Reverse (thrust) fault, N = Normal fault, M = Mean for all types of faults

Earthquake magnitude				Expected maximum movement (m)				Expected surface length (km)			
SF	R	N	M	SF	R	N	M	SF	R	N	M
7.0	7.0	7.0	7.0	1.51	1.55	2.14	1.91	42.7	35.5	30.9	40.7
7.5	7.5	7.5	7.5	4.95	2.16	5.96	4.90	100.0	73.3	55.0	90.2
8.0	8.0	8.0	8.0	16.22	3.02	16.60	12.59	234.4	151.4	97.7	199.5
8.5	8.5	8.5	8.5	53.09	4.22	46.24	32.36	549.5	312.6	173.8	441.6
9.0	9.0	9.0	9.0	173.78	5.89	126.82	83.18	1288.2	645.7	309.0	977.2

Ratio secondary to primary movement for threshold value 0.16 m				Necessary exploration radius (km)			
SF	R	N	M	SF	R	N	M
0.10596026	0.10322581	0.07476636	0.08376963	7.70	7.83	8.47	8.30
0.03232323	0.07407407	0.02684564	0.03265306	10.41	8.49	10.71	10.24
0.00986436	0.05298013	0.00963855	0.0127085	12.80	9.28	12.80	12.16
0.00301375	0.03791469	0.00346021	0.00494438	15.04	9.91	14.72	14.08
0.0009207	0.02716469	0.00124204	0.00192354	17.29	10.72	16.65	15.84

This table can be calculated using the regression equations published by (Wells & Coppersmith, 1994) that relate the earthquake magnitude to the maximum primary movement and surface length depending on the type of rupture. An earthquake with a magnitude of 7.0 and strike-slip fault for example would cause a primary displacement of 4.95 m and a surface rupture length of 100 km. The bottom part of the table is calculated from (Coppersmith & Youngs, 2000). The ratio is calculated by dividing the threshold value of the secondary movement (0.16 m) by the expected maximum primary movement, e.g., 0.16/4.95 = 0.032. Using the gamma distribution published by (Coppersmith & Youngs, 2000) that relates the secondary to the primary movement depending on the distance, the maximum necessary exploration radius can be determined. The table shows that even at a magnitude of 9.0, the maximum exploration radius would not be larger than approximately 18 km. Thus, according to these relations, a site is sufficiently characterized with regard to secondary faults due to earthquakes, if all large fault ruptures; i.e.; with lengths of more than 30 km, within a radius of 20 km of a repository have been detected (Fig. 6-25).

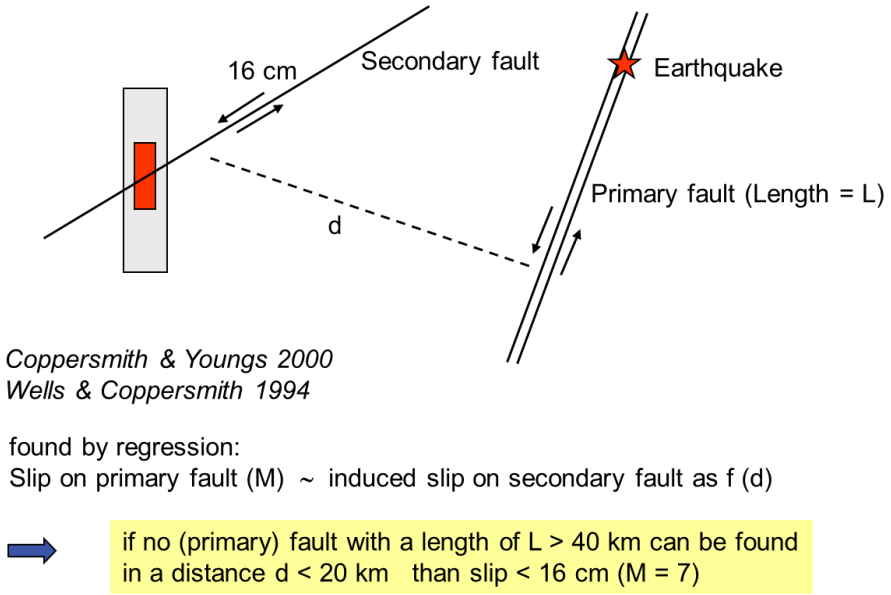

Fig. 6-25: Sketch illustrating the distance dependence between primary and secondary faults and movements along the latter

Consequently, if no fault ruptures with surface lines of more than 30 km length can be found within a radius of 20 km of the site, the probability that secondary displacements exit or occur along faults or fractures that cross the boreholes is extremely low.

6.1.4 Investigation of earthquake impact on EDZ

The mechanical stability of the planned underground opening has been investigated by numerical calculations considering the anisotropic stress state in the Krasnoyarsk region (Beygul et al., 2011). The results of these calculations show that the mechanical stability of the drift configuration can be assured. The mechanical parameters of the rocks in that region have been investigated by Gupalo et al. (1999) providing information about the change of the parameters with increasing fracture density in the rocks.

One topic that has not yet been investigated is the extension of an excavated damaged zone (EDZ) around the underground openings. An EDZ might act as a preferential pathway for radionuclides and should be considered in the safety assessment. Based on the mechanical parameters provided by Gupalo et al. (1999) and the stress state provided by Beygul et al. (2011) the potential extension of an EDZ due to excavation was calculated. Since earthquakes are quite usual in the Krasnoyarsk region, the question arose, whether an earthquake could have a significant impact on the extension of the EDZ around the underground emplacement drifts. To answer this question, dynamic mechanical calculations have been performed using a standardized synthetic seismic acceleration curve which is typical for this region.

6.1.5 Calculation of EDZ extension

In order to get an impression about the rock damage around the underground openings, drift excavation in the area of the planned repository was simulated, and the extent of the (EDZ) was determined taking into account the site specific mechanical rock parameters.

6.1.5.1 Geometry of the model

A 3D-model has been developed consisting of one borehole and one emplacement drift above. The model has a width of 23 m in X direction (drift spacing in the emplacement field) and a width of 19 m in Y direction (borehole spacing in the emplacement field). In the vertical Z direction, the model extends to a depth of -580 m. A drift is located in the middle of the XY plane at a depth of -450 m and runs in Y direction. A borehole is located in the middle of the model and extends in Z direction to a depth of -530 m. Fig. 6-26 shows one section of the model in the XZ plane and one section in the XY plane.

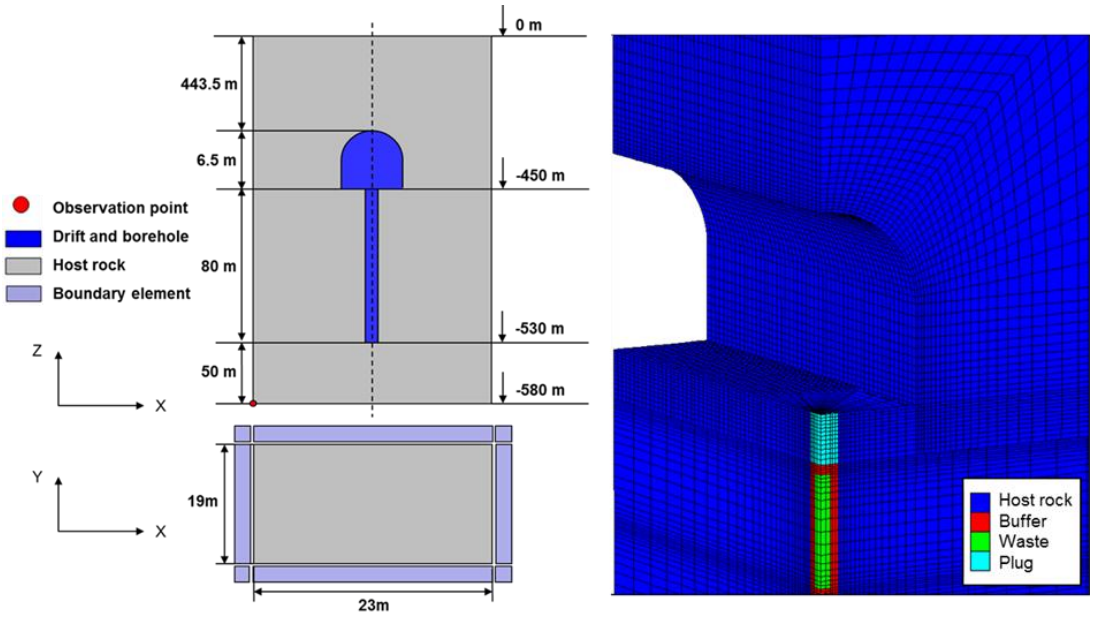

Fig. 6-26: Geometric dimensions and discretisation of the 3D model

6.1.5.2 Constitutive laws and mechanical rock parameters

The elastoplastic behaviour of the host rock can be simulated using the Hoek-Brown constitutive model. The advantage of this constitutive model is that a rock mass with different fracture densities can be handled. Different fracture densities yield different mechanical rock properties of the rock mass. A brief history of the development of the Hoek-Brown failure criterion was compiled by Hoek & Marinos (2006). The Hoek-Brown failure criterion can be described using the following equation (Hoek & Brown, 1997; Hoek et al., 2002; Eberhardt, 2012):

$$\sigma_1^{'} = \sigma_3^{'} + \sigma_{ci}\left(m_b \cdot \frac{\sigma_3^{'}}{\sigma_{ci}} + s\right)^a \qquad (6\text{-}6)$$

With:

$\sigma_1^{'}$ = maximum effective principal stress at failure

$\sigma_3^{'}$ = minimum effective principal stress at failure

σ_{ci} = uniaxial compressive strength of the intact rock material

The Hoek-Brown parameters m_b, s, and a are material constants that are related to the Geological Strength Index (GSI), the rock damage D and the constant m_i.

$$m_b = m_i \cdot \exp\left(\frac{GSI - 100}{28 - 14D}\right) \quad (6\text{-}7)$$

$$s = \exp\left(\frac{GSI - 100}{9 - 3D}\right) \quad (6\text{-}8)$$

$$a = \frac{1}{2} + \frac{1}{6}\left(e^{-GSI/15} - e^{-20/3}\right) \quad (6\text{-}9)$$

The Hoek-Brown failure criterion is an empirical relationship but recently a theoretical derivation has been proposed by Zuo et al. (2015). A discussion on the range of application and the limitations of GSI as well as general guidelines for the use of GSI are given in Marinos et al. (2005). An introduction of the rock damage parameter D to cover e.g. blast damage effects can be found in Hoek et al. (2002). As discussed with VNIPI PT, the GSI should have a value range between 55 and 75 for the host rock in the location Krasnoyarsk. Three GSI variants within this value range were used in the calculations. The parameters used are shown in Tab. 6.10. The higher the GSI, the better the quality of the host rock.

Tab. 6.10: Parameter variations of the GSI used during the calculations

Variant	GSI [-]	D [-]	m_i [-]	σ_{ci} [MPa]	σ_c [MPa]	m_b [-]	s [-]	a [-]
a-1	55	0.5	28	130	6.317	3.285	0.0025	0.504
a-2	65				12.491	5.289	0.0094	0.502
a-3	75				24.479	8.514	0.0357	0.501

The rock damage D has a value range from 0.0 to 1.0. The zero value represents undamaged or slightly damaged, high-quality rock while 1 represents very badly damaged and poor-quality rock. Three variants of D were used in the calculations. The higher D, the lower the quality of the rock, i.e. the larger the extent of the EDZ after excavation. The parameters used are shown in Tab. 6.11. The last parameter set c1 covers the anisotropic stress state in the Krasnoyarsk region given in Beygul et al. (2011). The anisotropy coefficient is defined by $\sigma_h/\sigma_v = 0.75$.

Tab. 6.11: Used parameter variations of D during the calculations

Variant	D [-]	GSI [-]	m_i [-]	σ_{ci} [MPa]	σ_c [MPa]	m_b [-]	s [-]	a [-]
b-1	0	65	28	130	18.456	8.022	0.0205	0.502
b-2	0.5				12.491	5.289	0.0094	0.502
b-3	1.0				6.954	2.298	0.0029	0.502
c-1	0,5				12.491	5.289	0.0094	0.502

6.1.5.3 EDZ extension

The results of the parameter variations described in chapter 2.2 with regard to the EDZ extension are given in Tab. 6.12. An illustration of the damaged area is exemplarily shown in

Fig. 6-27 for the parameter set c1. For the parameter set that represents the most weak assumed host rock, which is a very conservative assumption, the EDZ in the drift does not exceed an extension of 1.6 m. The EDZ extension around the borehole is about 0.1 m which is quite reasonable for crystalline rocks. Nevertheless, the EDZ extension in the drift is important when drift seals are to be planned and installed. Knowing the depth of the EDZ will

help to decide, whether parts of the EDZ should be carefully excavated or sealed by injection measures, especially at the position of plugs.

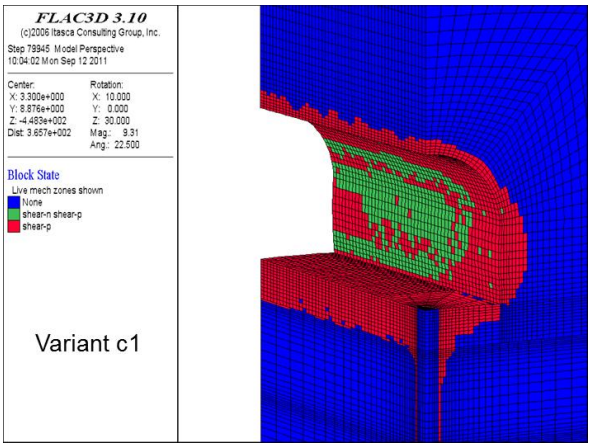

Fig. 6-27: Illustration of EDZ extension for the parameter set c1.

Tab. 6.12: Extention of the EDZ at different locations

Set	EDZ drift wall [m]	EDZ floor [m]	EDZ roof [m]	EDZ borehole [m]
a1	0.8	1.6	0.6	0.08
a2	0.65	1.6	0.4	0.08
a3	0.28	1	0.3	0.08
b1	0.4	1.2	0.4	0.08
b2	0.65	1.6	0.4	0.08
b3	0.8	1.6	0.7	0.08
c1	0.9	1.6	0.7	0.08

With regard to the anisotropic stress state it can be said, that the depth of the EDZ is not affected much. The main difference to the isotropic results is that the failure mechanism is different as illustrated in Fig. 6-27. In addition, a calculation taking into account the thermal effect from the radioactive waste was performed. The extent of the EDZ does not change during the temperature evolution. The thermal expansion and thus, the thermal induced stress have no significant influence on the EDZ extension contrary to the mechanical rock properties.

6.1.5.4 Comparison of Hoek-Brown and Mohr-Coulomb failure criteria

Prior to the application of earthquake induced dynamic mechanical loads, the plausibility of the achieved results with the Hoek-Brown failure criterion was checked via a comparison with the results obtained by using the Mohr-Coulomb failure criterion. Using the following equations, the Hoek-Brown parameters can be converted into corresponding Mohr-Coulomb parameters. The conversion has been performed by using the RockLab software (Rocscience, 2007). RocLab is a software program for determining rock mass strength parameters, based on the generalized Hoek-Brown failure criterion (Hoek et al., 2002).

$$\phi' = \sin^{-1}\left[\frac{6am_b\left(s+m_b\sigma'_{3n}\right)^{a-1}}{2(1+a)(2+a)+6am_b\left(s+m_b\sigma'_{3n}\right)^{a-1}}\right] \quad (6\text{-}10)$$

$$c' = \frac{\sigma_{ci}\left[(1+2a)s+(1-a)m_b\sigma'_{3n}\right]\left(s+m_b\sigma'_{3n}\right)^{a-1}}{(1+a)(2+a)\sqrt{1+\left[6am_b\left(s+m_b\sigma'_{3n}\right)\right]^{a-1}/\left[(1+a)(2+a)\right]}} \quad (6\text{-}11)$$

The Hoek-Brown parameter set a2 was used as a reference parameter set for the conversion. The converted friction angle and the converted cohesion are:

ϕ' = 40.36° and

c' = 9.396 MPa

The Mohr-Coulomb failure criterion can be described by a linear equation using c and Φ:

$$\sigma_1' = \frac{2c'\cos\phi'}{1-\sin\phi'} + \frac{1+\sin\phi'}{1-\sin\phi'}\sigma_3' \qquad (6\text{-}12)$$

Fig. 6-28 shows the Hoek-Brown and Mohr-Coulomb failure criteria and the corresponding plasticity states using the parameter set a2 (Tab. 6.10). The plasticity states are very different in this case under the two constitutive models.

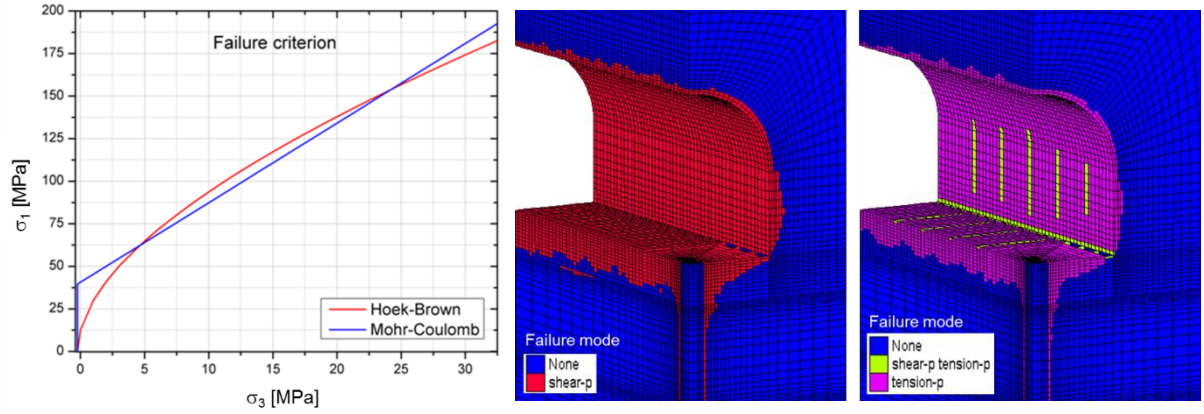

Fig. 6-28: Illustration of the Hoek-Brown and Mohr-Coulomb failure criteria (left) and a comparison between Hoek-Brown and Mohr-Coulomb simulation results regarding plasticity states (right).

The zones near the drift meet the shear failure criterion when using the Hoek-Brown constitutive law while the same zones under the Mohr-Coulomb model do not meet the failure criterion but the tension failure criterion.

The reason is the relatively large difference between the two failure criteria at small minimum principal stresses (Fig. 6-28 left). The Mohr-Coulomb line is above the Hoek-Brown curve with a minimum principal stress from 0 MPa to 3 MPa. Therefore, the zones near the drift exceed the shear failure conditions when using Hoek-Brown but do not reach the shear failure conditions when using Mohr-Coulomb.

Due to the relatively large difference between the two failure criteria at small minimum principal stresses, a bi-linear Mohr-Coulomb failure criterion has been introduced. Such a criterion has been successfully applied by NAGRA for simulating the failure behaviour of Opalinus clay (NAGRA, 2002). Fig. 6-29 shows the Hoek-Brown failure criterion and the converted Mohr-Coulomb criterion. The corresponding Mohr-Coulomb parameters are listed in table 6.13.

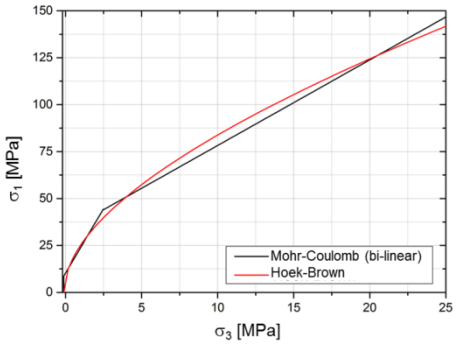

Fig. 6-29: Hoek-Brown and Mohr-Coulomb (bi-linear) failure criteria.

Tab. 6.13: Parameters of the converted Mohr-Coulomb criterion used in Fig. 6-29.

Range of bi-linear criterion [MPa]	Cohesion [MPa]	Friction angle [°]	Tensile strength [MPa]	σ_3 max [MPa]
0 – 2.5	1.391	59.79	0.116	2.0
2.5 - end	7.647	39.82	0.116	27.5

The first parameter set covers the range σ_3< 2.5 MPa, the second set covers the range MPa< σ_3< 25 MPa. As can be seen from Fig. 6-29 both failure criteria now have a quite similar characteristic. Since the results for both criteria a quite similar with regard to the extension of the EDZ (Li & Jobmann, 2015), the Hoek-Brown criterion was used for the following dynamic analysis in the 3D-model.

6.1.6 Earthquake impact on EDZ

6.1.6.1 Boundary conditions and mechanical parameters

As static boundary conditions, the grid points at the bottom and on the sides of the model boundaries were fixed to avoid any displacements. These boundary conditions have been used to simulate the excavation of the borehole and the drift. The used rock parameters are given in Tab. 6.14 for the elastic rock parameters and in Tab. 6.15 for two Hoek-Brown parameter sets.

Tab. 6.14: Elastic rock parameters

Density [kg/m^3]	Young's modulus [GPa]	Poisson's ratio [-]
2700	15000	0.27

Tab. 6.15: Hoek-Brown parameter sets

Set	GSI* [-]	D [-]	m_i [-]	σ_{ci} [MPa]	m_b [-]	s [-]	a [-]	σ_c [MPa]
1	55	0,15	28	110	4.927	0.0052	0.504	27.5
2	75	0.15	28	110	11.521	0.0679	0.501	27.5

*GSI = Geological Strength Index

After excavation and thus breakout of the borehole and drift elements, the dynamic boundary conditions were added. To this reason additional boundary elements have been added which allow for management of dynamic boundary conditions. Two S-waves and one P-wave enter the model from the bottom model boundary. The waves propagate in Z direction to the top of the model. When the waves reach the top of the model, they are reflected by the upper model boundary and propagate back towards the bottom. The lower additional boundary elements were defined as a so-called *quiet boundary* (Itasca, 2005) in order to absorb the reflected waves and to prevent a second reflection (Lysmer & Kuhlemeyer, 1969). After starting the use of the dynamic boundary conditions, the static boundary conditions at the lower model boundary were deleted. The lateral additional model boundary elements were defined as so-called *free field boundaries* (Itasca, 2005). These kinds of boundaries retain their non-reflecting properties (Cundall et al., 1980).

In summary, six additional boundary elements around the original model were created. The zones of the boundary elements have the same dimensions, properties and stress states as the corresponding zones at the model boundaries and the movements of these elements are exactly the same as for the original boundary elements. A standardized synthetic seismic acceleration curve with a force that occurs once in every 5000 years and is typical for this region is simulated in the calculation. It is a synthetic seismogram of a 7-degree earthquake of the second category (Russian scale) and has been provided by VNIPI PT (Beygul, 2014). This synthetic acceleration curve is divided into 3 components in X, Y, and Z direction shown as blue lines in Fig. 6-30. By integrating the acceleration curves once or twice, the corresponding velocity and displacement can be determined. If these waves are established as boundary conditions directly at the lower model boundary, the model reflects – after the

seismic wave has passed – an unchanged wave velocity and undesired residual displacement. In order to avoid this effect, a so-called ‘baseline correction' has been performed (Li & Jobmann 2014).

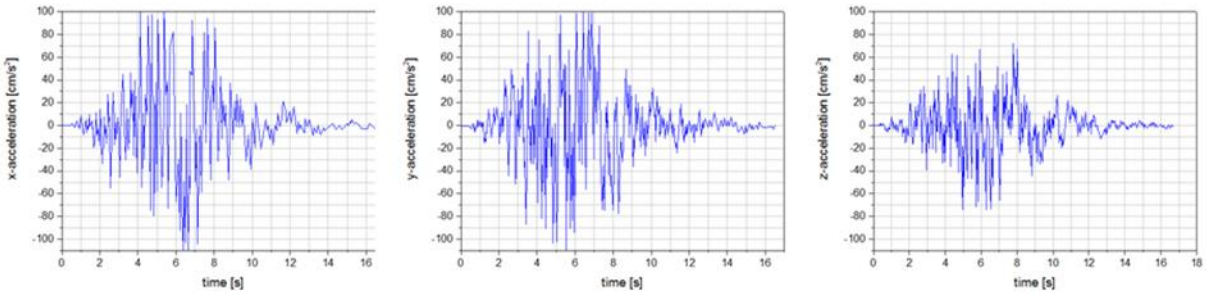

Fig. 6-30: Acceleration in X, Y, and Z direction (left) and velocity and displacement (right) before and after baseline correction.

For the dynamic calculation, the three baseline-corrected waves were entered at the lower model boundary and propagate in vertical direction towards the upper model boundary. Two of these waves are S-waves that oscillate perpendicular to the direction of propagation (X and Y direction) while the P-wave oscillates in direction of propagation (Z direction). The propagation velocity depends on the type of wave and the mechanical rock properties.

$$C_p = \sqrt{\frac{K + 4G/3}{\rho}} \tag{6-13}$$

$$C_s = \sqrt{G/\rho} \tag{6-14}$$

With:
C_p = velocity of the P-wave [m/s]
C_s = velocity of the S-wave [m/s]
ρ = rock density [kg/m^3]
K = modulus of compressibility [Pa]
G = shear modulus [Pa]

The change in stress state in the rock mass caused by the waves can be calculated by means of the following equations:

$$\sigma_n = 2(\rho C_p)v_n \tag{6-15}$$

$$\sigma_s = 2(\rho C_s)v_s \tag{6-16}$$

With:
σ_n = normal stress [Pa]
σ_s = shear stress [Pa]
v_n = particle velocity in normal direction [m/s]
v_s = particle velocity in shear direction [m/s]

During the propagation of the dynamic waves, there is a loss of energy in the dynamic system, which is due to so-called mechanical damping. Frequently used types of damping are Rayleigh damping, hysteretic damping, and local damping. This calculation uses Rayleigh damping, a description of which can be found for example in Wilson (2004). The parameters describing the Rayleigh damping are the critical damping ratio ξ_{min} [-] and the central frequency f_{min} [Hz]. Guidelines for determination of Rayleigh damping parameters can be found in Chowdhury & Dasgupta (2003) and Spears & Jensen (2009). The calculation uses empirical values of 5% for the critical damping (Biggs, 1964) and a natural frequency of 192.3 Hz for the central frequency.

6.1.6.2 Calculation results

The simulation comprises the following steps:

- Establishment of a primary static stress state
- Drift excavation
- Borehole drilling
- Simulation of two S-waves with a particle movement in X/Y direction and wave propagation in Z direction, and simulation of a P-wave with a particle movement in Z direction and wave propagation in Z direction.

Fig. 6-31 shows the particle velocities and displacements in the respective directions at the observation point at the lower model boundary (cf. Fig. 6-26). According to equations 6-13 and 6-14, the S-waves in X and Y direction have a vertical propagation velocity of 1478.93 m/s while the P-wave in Z direction has a vertical propagation velocity of 2634.78 m/s. With a depth of 580 m, the S-waves reach the upper model boundary in 0.22 s, while the P-wave reaches it in 0.785 s. The waves are then reflected by the upper model boundary and reach the lower model boundary in 0.784 s (S-wave) and 0.44 s (P-wave). In the end, the reflected waves are absorbed by the *quiet boundary*. The entire process is influenced by Rayleigh damping. For this reason, the particle velocity and displacement (superposition of original and reflected wave due to Rayleigh damping) are significantly lower/smaller than the input values. On the right of Fig. 6-31 the displacements in the respective directions at three points at the drift contour (floor, roof, and wall) are plotted. The points at the drift contour already have an initial displacement due to excavation prior to the seismic impact. Over time, the points move due to the seismic acceleration. As can be seen, the movements of the observation points are very similar in all three directions. This indicates that an earthquake would shake the underground construction as a whole by moving all points in the same way.

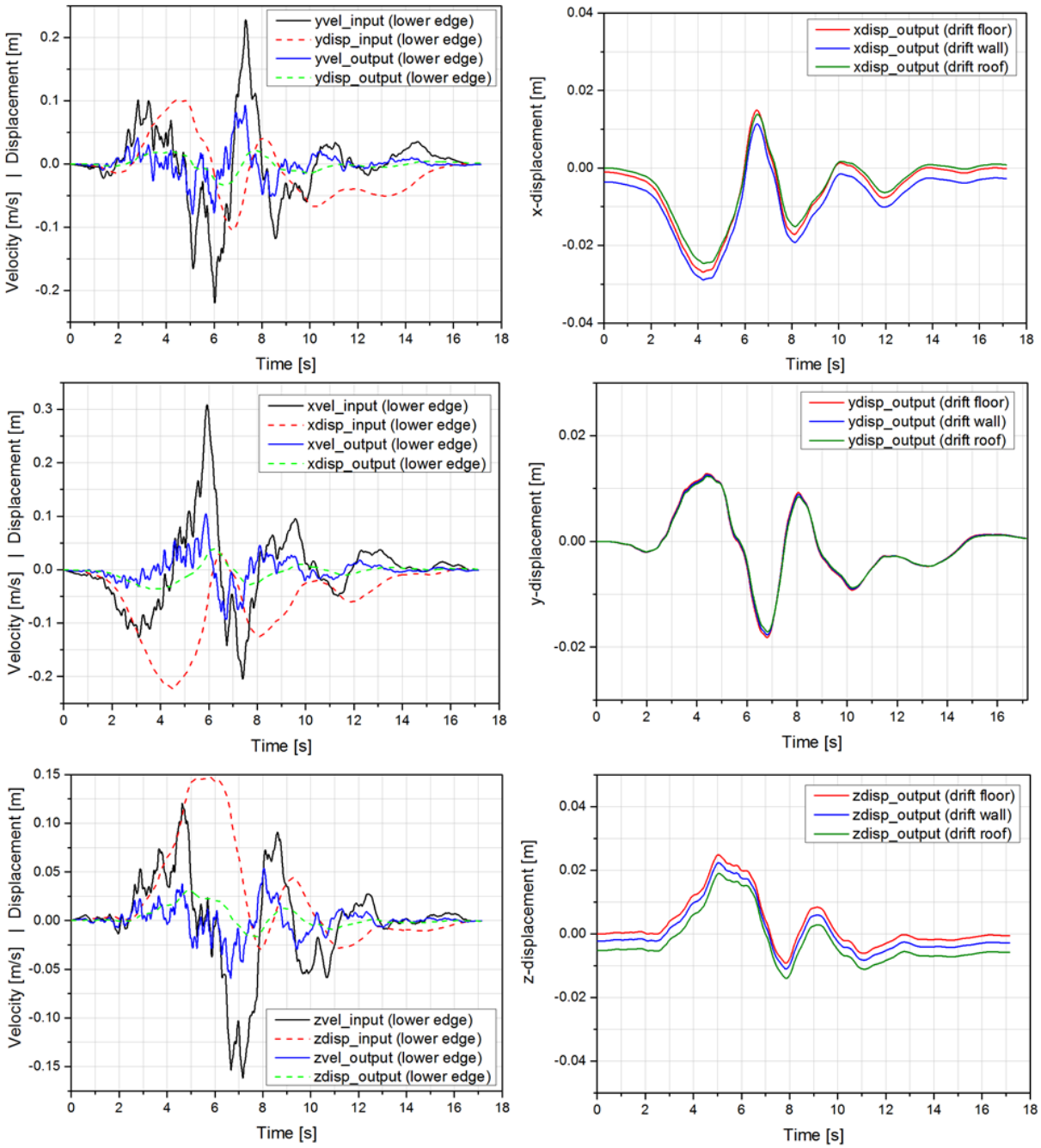

Fig. 6-31: Particle velocity and displacements in all three direction over time for different points.

To identify whether any different movements occur, the displacements of the three points have been subtracted from each other. The resulting curves represent the differences in movement of the three observation points. These curves are plotted in Fig. 6-32. The displacements due to excavation have been corrected by an offset. The highest differences are observed between the floor and the roof of the drift indicated by the red curve in the three plots of Fig. 6-32.

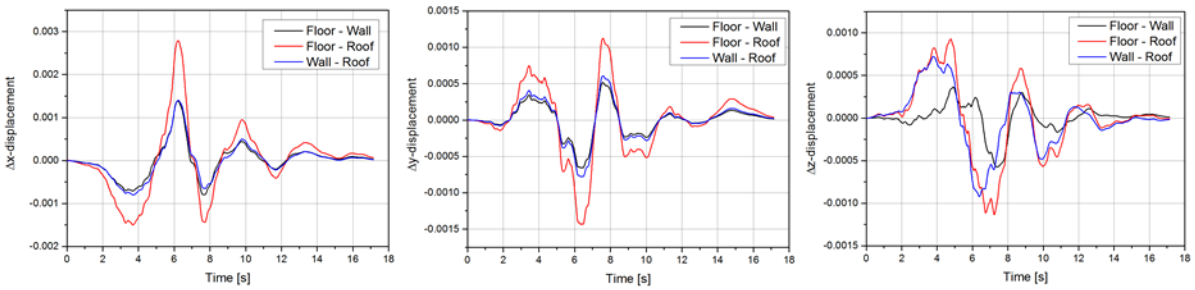

Fig. 6-32: Differences in movement of the three observation points.

Looking at the vertical displacement differences (Δz-displacements) in the last plot it is noticeable that there is a small phase shift for the displacement differences between the drift floor and the drift wall (black curve) during the first eight seconds. This indicates that there are similar movements but at different times which could be a reason for (small) shear displacements at the drift contour.

For both parameter sets given in Tab. 6.15 calculations have been performed. In both cases the seismic movement causes stress redistribution, although it is not high. The extension of the excavation damaged zone does not change significantly not even for the parameter set representing the most weak rock conditions (GSI = 55).

As an example, Fig. 6-33 illustrates the excavation damaged zone in the near field of the drifts prior to and after the seismic movement for parameter set 2. The changes are marked with black arrows and red circles. These small changes clearly indicate that it is not to be expected that the EDZ will increase as a result of an earthquake. That means that no precautions have to be planned when positioning a plug in order to avoid any bypass of the plug through an extended EDZ.

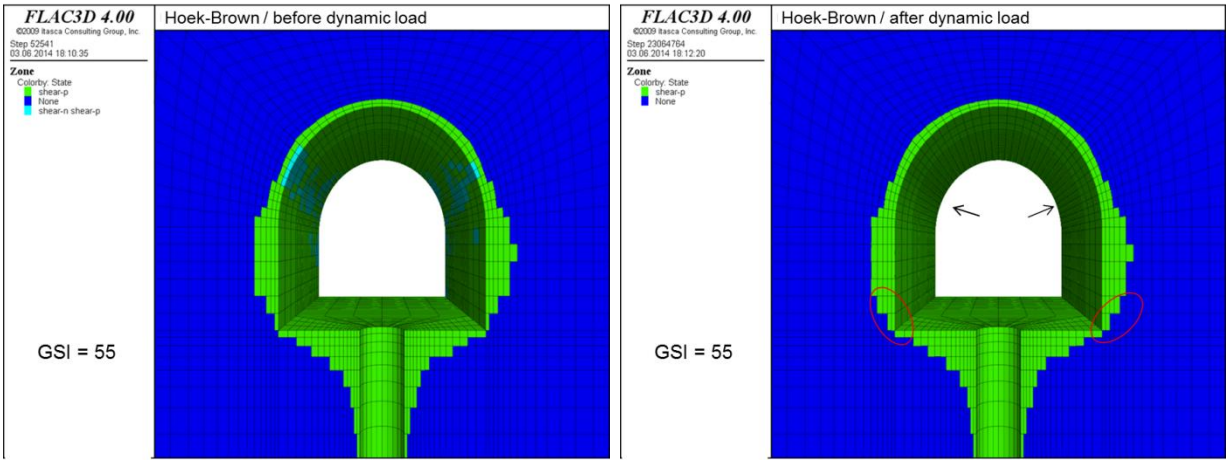

Fig. 6-33: Excavation damaged zone before and after seismic movement.

6.1.7 Radionuclide release and migration

The analysis of the radionuclide release and migration was carried out for the vitrified HLW. A release of radionuclides from the ILW is not considered.

6.1.7.1 Basic assumptions

A possible influence of the disposed ILW on the geochemical environment in the mine (e.g. pH, E_h-values) and thus on the release and migration of the HLW is not considered, since there are no sufficient data and models to analyse such an influence. For the calculations of release and migration of radionuclides from the HLW, it is assumed that appropriate technical barriers guarantee that there is no influence from the ILW on the HLW.

Furthermore it is assumed that the disposal areas (boreholes) are efficiently sealed from the access drifts. Therefore, the access drifts and the EDZ around the drifts do not provide a pathway for radionuclides along the drifts and shafts. Instead, the EDZ connects the buffer/boreholes with the potential fractures in the host rocks representing the preferred pathway for the migration of radionuclides.

Taking into account these assumptions, the release of radionuclides is calculated considering the following scenario (Fig. 6-34):

1. Failure of all containers after 500 years
2. radionuclides are dissolved according to geochemical conditions in the water-filled void volume in the containers
3. dependent on the concentration gradient, the released radionuclides migrate by diffusion through the bentonite

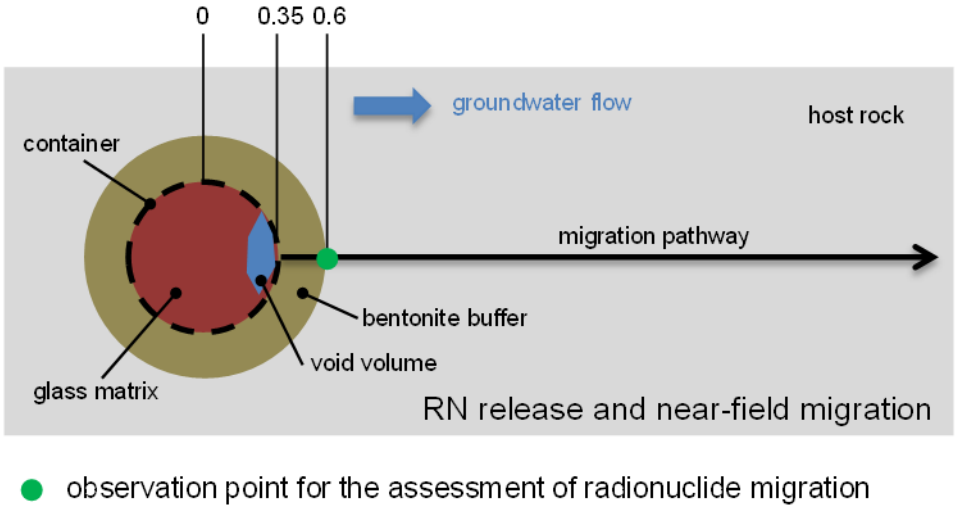

Fig. 6-34: Processes in near-field modelling

6.1.7.2 Input data

This chapter describes the input data required for the deterministic calculation in the analysis of the radionuclide release and migration through the bentonite buffer. The input data for the near-field modelling is arranged in the following categories:

- geometry
- source-term
- buffer and boundary conditions.

6.1.7.3 Geometry

The schematic repository layout is illustrated in chapter 5 and is taken from the repository concept developed by VNIPI PT. The disposal sections are designed as a horizontal system of drifts and comprise an area of about $2.5 \cdot 10^5$ m^2. The repository consists of two sections:

section one comprises 14 drifts with a distance of 23 m, section 2 comprises 14 drifts with a distance of 26 m. The containers are disposed of in 75-m-deep vertical boreholes drilled from the floor of the drifts. The distance between the boreholes along a single drift is 15 m (section 1) and 23 m (section 2). Every borehole contains 18 containers with a length of 3.4 m each. The containers are surrounded by a buffer of bentonite blocks (see chapter 5.1).
The transport distances through the bentonite and through the host rocks can be taken from Fig. 6-34. The geometry parameters are summarized in Tab. 6.16.

Tab. 6.16: Geometry input data for the near-field model

Parameter	Value
Repository area	$2.5 \cdot 10^{5}$
Number of Boreholes	462
Borehole length	75
Numbers of containers per borehole	18
Transport length through the bentonite	0.25

6.1.7.4 Source Term

The data for the radionuclide inventory is based on the data provided in chapter 4. For the calculations, the six containers of each borehole are regarded as one container. Therefore, the inventory of one container in the simulations has six times the inventory of a container as given in Tab. 6.17.

Tab. 6.17: Radionuclide inventory

Nuclide	Half-life [a]	Container [Bq]	Repository [Bq]
Se-79*	$3.270 \cdot 10^{5}$	$1.005 \cdot 10^{10}$	$8.358 \cdot 10^{13}$
Tc-99	$2.100 \cdot 10^{5}$	$4.477 \cdot 10^{11}$	$3.723 \cdot 10^{15}$
Cs-135	$2.000 \cdot 10^{6}$	$1.681 \cdot 10^{10}$	$1.398 \cdot 10^{13}$
Np-237	$2.144 \cdot 10^{6}$	$2.348 \cdot 10^{08}$	$1.953 \cdot 10^{12}$
U-238	$4.468 \cdot 10^{9}$	$2.426 \cdot 10^{07}$	$2.017 \cdot 10^{11}$
Pu-239	$2.411 \cdot 10^{4}$	$3.450 \cdot 10^{10}$	$2.869 \cdot 10^{14}$
Am-241	$4.322 \cdot 10^{2}$	$3.239 \cdot 10^{13}$	$2.693 \cdot 10^{17}$
Am-243	$7.370 \cdot 10^{3}$	$5.089 \cdot 10^{11}$	$4.232 \cdot 10^{15}$

* The half-life of Se-79 has been revised several times. Initially, a value of 65 000 years was given in the nuclide charts.
A value of $1.1 \cdot 10^{6}$ had been used in PA calculations since 1997, but was revised to be 327,000 years (Jörg et al., 2010).

Data for the container geometry is given in Tab. 6.18. The containers are made of steel. Due to the corrosion of the steel, the container fails after a certain time. It is assumed that the container will collapse under the bentonite swelling pressure in case the container wall is partly corroded. A container life-time of 500 years is used in this work. Conservatively, it is assumed that all containers would fail at the same time. Thereafter they offer no physical resistance to radionuclide migration.

After a container has failed, water will come into contact with the glass matrix. The glass matrix begins to dissolve and the radionuclides are released from the glass matrix. In reprocessed waste there is no instantaneous release because all radionuclides are homogeneously immobilised in the matrix and no volatile radionuclides exist. It is assumed that the release rate is a constant rate for all radionuclides and is set to $5.0 \cdot 10^{-4}$ per year with a corresponding life-time of 2,000 years for a glass block. This rate is in the same order of

magnitude as the mobilisation rates derived for vitrified HLW from the French nuclear fuel reprocessing plant of AREVA in La Hague (Noseck et al., 2008) and mobilisation rates derived in (Krone et al., 2005). In the uncertainty analysis a higher mobilisation rate is assumed due to the fact that phosphate glass can have a higher mobilisation rate than borosilicate glass (see chapter 4). Conservatively, no account is taken of sorption and co-precipitation of radionuclides with products of the glass and metal corrosion.

Tab. 6.18: HLW container data

Parameter	Value
Length [m]	3.40
Diameter [m]	0.70
Void volume [m^3]	0.60
Mass of waste [kg]	1,500
Matrix density [kg/m^3]	2,500
Life-time [a]	500

After the radionuclide release from the matrix the radionuclides are dissolved in the water volume within the container. Some radionuclides may precipitate when they reach their solubility limits within the container water volume. As 18 containers are virtually merged for the calculations, the water volume equals 18 times the void volume of a single container. The dissolved radionuclides are available for the diffusion in the bentonite buffer.

The data for the solubility limit for each element are given in Tab. 6.19. These values correspond to the realistic value in NAGRA (1994a). Given the lack of stable Cs solid phases, the “high” solubility limit of Cs-135 denotes a solubility limit that is high enough not to be reached under the regarded geochemical conditions.

The element-specific sorption coefficients for bentonite and crystalline rocks are listed in Tab. 6.20. The values applied are realistic values proposed in Stenhouse (1993).

Tab. 6.19: Solubility limits in [mol/m^3]

Element	Solubility limit
Se	$1 \cdot 10^{-5}$
Tc	$1 \cdot 10^{-4}$
Cs	high
Ra	$1 \cdot 10^{-7}$
Th	$5 \cdot 10^{-6}$
Pa	$1 \cdot 10^{-7}$
U	$1 \cdot 10^{-4}$
Np	$1 \cdot 10^{-7}$
Pu	$1 \cdot 10^{-5}$
Am	$1 \cdot 10^{-2}$

Tab. 6.20: Sorption coefficients Kd for bentonite and crystalline rocks in [m^3/kg]

Element	K_d bentonite	K_d crystalline
Se	0.005	0.01
Tc	0.1	0.5
Cs	0.01	0.1
Ra	0.01	0.5
Th	5	1
Pa	1	1
U	5	1
Np	5	1
Pu	5	5
Am	5	5

6.1.7.5 Buffer and near-field

In the near-field, radial diffusion transport through the bentonite buffer is considered. Sorption on the bentonite is taken into account. These processes were modelled with the computer code CLAYPOS. The near-field geometry was already described in Fig. 6-34. The transport length through the bentonite is 0.25 m. It is assumed that the boreholes are filled with bentonite blocks with a density of 2800 kg/m^3. The pore diffusion coefficient is set to $5 \cdot 10^{-10}$ m^2/s. The data for the element-specific transport parameters was taken from the sorption database developed for the NAGRA Kristallin-I study (Stenhouse, 1993) and listed in Tab. 6.20.

The groundwater flow through the host rocks and the excavation damaged zone (EDZ) is an important boundary condition for the diffusion through the bentonite buffer as well as for the transport of radionuclides through the host rocks. The groundwater flow was determined by field investigations. According to these investigations, the groundwater flow through the area of the repository via the fractured zones is assumed to be 152 m^3/a (see chapter 6.2.2).

6.1.7.6 Modelling results

In order to understand the migration behaviour of the important dose relevant radionuclides, the modelled period is 10^8 years. It is obvious that the assumptions and conditions made for the modelling in the near-field become increasingly uncertain in the future and that the integrity of the barrier system cannot be guaranteed for such a long time. This period can only be applied for analysing trends of radionuclide migration.

Fig. 6-35 illustrates the radionuclide fluxes from the bentonite buffer. The combination of high solubility and relatively low sorption value makes Cs-135 the radionuclide with the highest mobility. The release of other dose-relevant radionuclides such as Se-79, Tc-99 and Np-237 is limited due to their low solubility limit. This is illustrated in Fig. 6-35 with the horizontal curves for these radionuclides (the peak between 34,000 and 20,000 years in the Np-237 curve is a result of Np-237 build-up caused by the decay of Am-241.

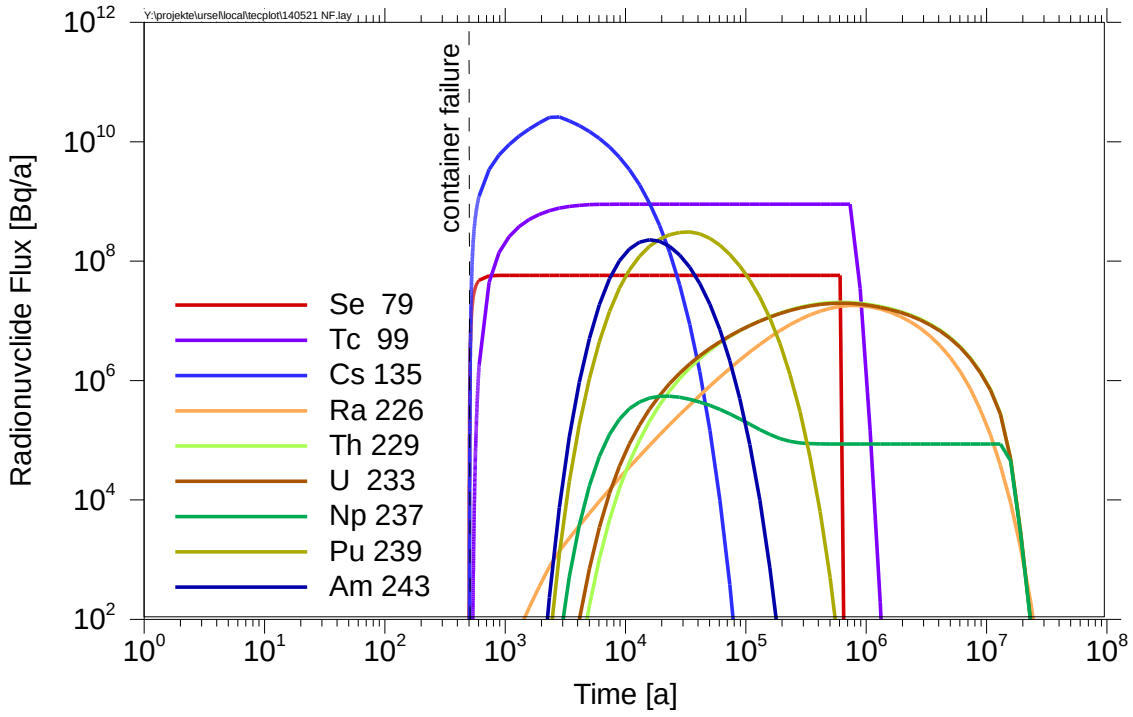

Fig. 6-35: Radionuclide fluxes from the bentonite buffer

6.2 Geological barrier

Based on past investigations for the Yeniseysky site numerical models for groundwater flow and tracer transport as well as for the radionuclide migration were updated and further developed. The main goal is to evaluate the barrier performance of a potential repository in crystalline rocks. Hydrogeological simulations are performed using the code d^{3}f (chapter 6.2.1).

Considering the groundwater flow velocity calculated with the computer code d^{3}f and the projected repository layout, the long term evolution of the repository system and the radionuclide transport is simulated using the computer code RepoTREND (chapter 6.2.2). The influence of uncertainties is being evaluated probabilistically (chapter 6.3).

6.2.1 Groundwater flow and tracer transport

Groundwater flow and transport simulations were performed based on data provided by VNIPI PT during the years 2010 to 2012. Geological and hydrogeological data as described in chapter 2 (more specifically chapter 2.6) and chapter 3 was available only at a later stage of the hydrogeological modelling work. Therefore these data were not considered in the simulations presented here. They will be evaluated and necessary data will be included in future simulations. This mainly concerns the direction of groundwater flow, which is assumed to be oriented to the northeast in this report. Newer investigation results indicate a groundwater flow to the west. Model variations concerning the groundwater flow direction will be performed in the future. Regarding the transport simulations, the volume of contaminated groundwater that may be released into the geosphere was updated and will be considered in future transport simulations.

However, conducted simulations presented in this report are based on a schematic cross section in accordance with model assumptions presented in Figure 2-18. Hydrogeological parameters were set in agreement with VNIPI PT.

To perform groundwater flow and transport simulations the given geological cross section (Fig. 6-36) had to be digitized first. This was done using the geographic information system ArcMap 10.0, a component of the software package ArcGIS by ESRI (ESRI, 2010). The resulting shapefiles were exported to the Drawing Interchange File Format (DXF) by Autodesk (Autodesk, 2011). Using the code GISLab (Jungblut, 2011), the dxf-files were merged and simplified in order to be exported to the grid generator ProMesh (Reiter & Wittum, in prep.). Groundwater flow and transport simulations were performed using the code d^{3}f (distributed, density-driven flow), which was developed under the auspices of GRS (Fein & Schneider, 1999). The data were visualised with the program grape (Grape, 2011).

One of the main characteristics of d³f is the possibility to simulate the groundwater flow and tracer transport in large, heterogeneous model areas over long periods in time. d^{3}f is able to take the density-driven flow into account, which is of particular importance when regarding the groundwater flow in the vicinity of salt formations. Newest developments allow the explicit consideration of fractures, heat transport and free groundwater tables.

6.2.1.1 Model set-up

The groundwater flow and transport model is based on a schematic cross section through the investigation area (Fig. 6-36). The cross section strikes southwest to northeast. It has an approximate length of 1600 m and depth of 650 m. In the study area, the Baikal stream and the Shumikha river are the gaining streams. Here, these two rivers serve as surface water divides. In order to align the two-dimensional hydrogeological model with the water divides, the model was setup for the central region of the cross section, i. e. the area between the two rivers “Basin Baikal stream” and “Basin Shumikha river”. Surface water flow is directed to-

wards the rivers and streams. Subsurface water flow in the near-surface hydrogeological units is directed to the northwest in the southern parts of the investigation area, and to the northeast in the central, eastern and northern part of the investigation area, according to the hydraulic gradient (VNIPI PT, 2012b).

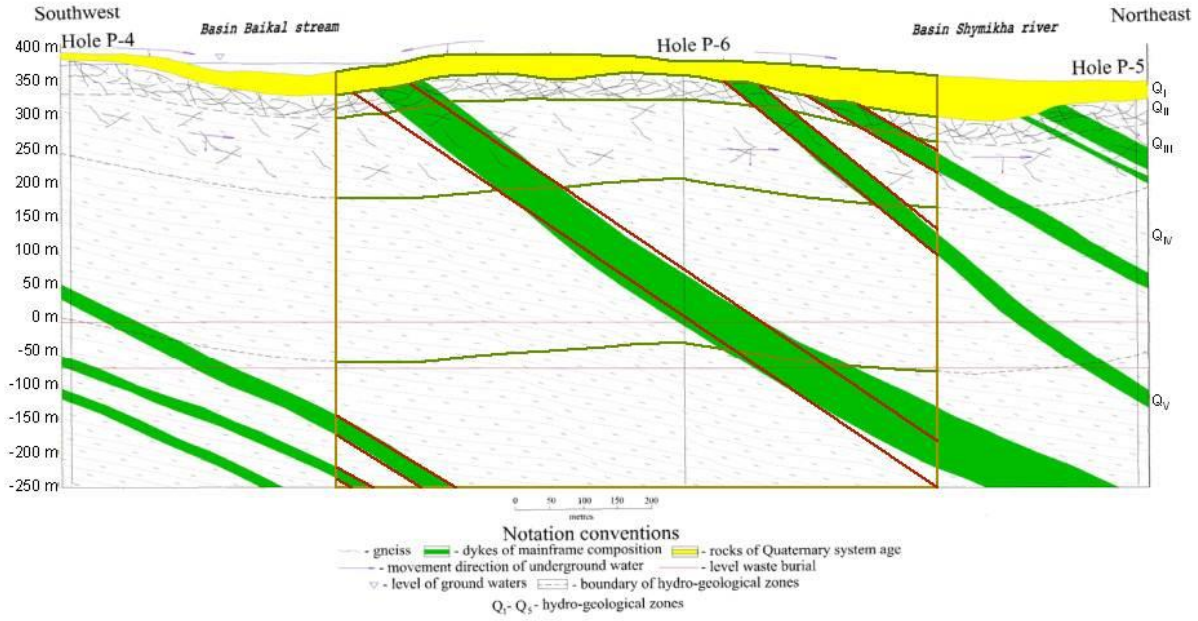

Fig. 6-36: (Hydro-) Geological cross section through the investigation area (VNIPI PT, 2012b) and model geometry

In the study area, the Baikal stream and the Shumikha river are the gaining streams. Here, these two rivers serve as surface water divides. In order to align the two-dimensional hydrogeological model with the water divides, the model was setup for the central region of the cross section, i. e. the area between the two rivers “Basin Baikal stream” and “Basin Shumikha river”. Surface water flow is directed towards the rivers and streams. Subsurface water flow in the near-surface hydrogeological units is directed to the northwest in the southern parts of the investigation area, and to the northeast in the central, eastern and northern part of the investigation area, according to the hydraulic gradient (VNIPI PT, 2012a).

The different hydrogeological zones in the underground can be identified in Fig. 6-36. The topmost unit Q_I consists of Quarternary sediments with a thickness between ca. 10 m to approx. 65 m (yellow in Fig. 6-36). The lower four units Q_{II} – Q_V consist of gneiss in different stages of weathering with a decreasing permeability and porosity with depth. The thickness of the units is increasing with depth and ranges from ca. 50 m in the upper gneiss unit Q_{II} to more than 200 m in the lower units Q_{IV} and Q_V.

The gneiss units contain a series of dykes (green in Fig. 6-36) dipping steeply to the east (90/65[2]). These dykes show similar hydraulic parameters as the gneiss and thus do not need to be regarded explicitly in the model. However, contact zones between the gneiss and the dykes show a higher permeability and are regarded as discrete elements in model simulations. Based on these data, a two-dimensional numerical model was setup simplifying the geological setting as depicted in Fig 6-36. Green lines indicate the interface of the different hydrogeological units Q_I to Q_V, while red lines indicate the location of contact zones between the gneiss and the dykes. Brown lines symbolise the bottom and side limits of the model.

The course grid, generated with ProMesh, is given in Fig. 6-37. The model has a length of 910 m and a height of ca. 656 m. It consists of five geological units, which are:

[2] Notation: Dip direction / dip angle

- Q_I: A thin, intensively weathered zone near the surface with a thickness between 10 m and approx. 65 m,
- Q_{II}: A lesser weathered transition zone with an average thickness of ca. 50 m, and
- Q_{III} – Q_V: The almost unweathered gneiss as the lowest and thickest layer reaching down to a depth of more ca. 700 m.

Q_{III} shows a higher permeability and porosity than the lower units Q_{IV} and Q_V, which feature identical hydraulic parameters. These lower two units only differ from each other regarding the hydraulic characteristics of the contact zones to the dykes and thus have to be regarded as separate units for reasons of grid generation. The dip angle of the contact zones was set according to the geological cross section and ranges between ca. 30° and 40°.

The abstracted model geometry is derived as shown in Fig. 6-37. The resulting coarse grid contains 513 vertices, 1,289 edges and 778 elements. For flow simulations with the code d^3f, this coarse grid is refined four times. The fine grid, used for the groundwater flow and transport simulations, contains 62488 vertices, 84287 nodes, 249374 edges, and 165088 elements.

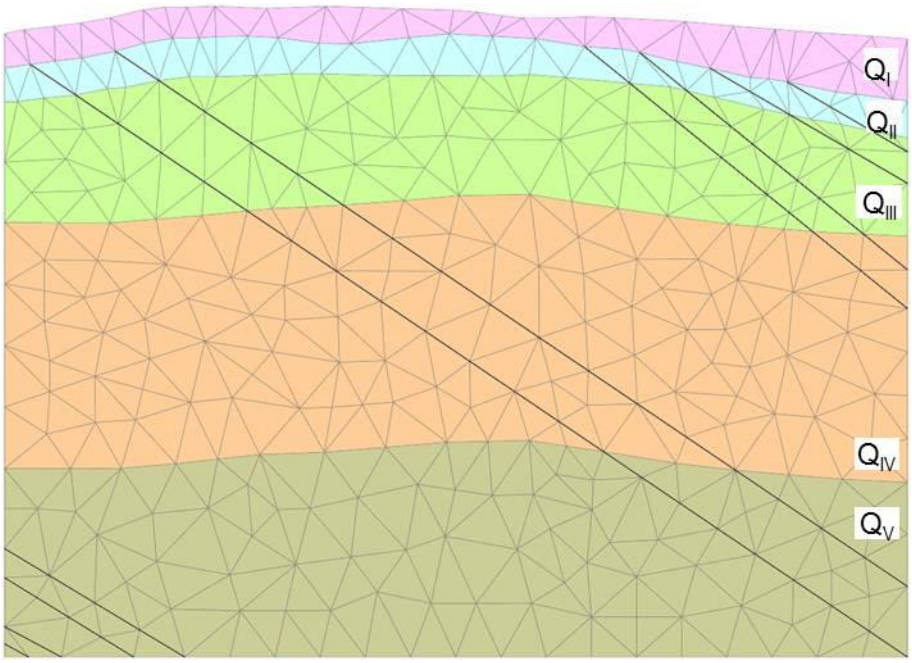

Fig. 6-37: Geometry and course grid for the hydrogeological model with names of hydrogeological units and location of considered contact zones (black lines)

6.2.1.2 Flow simulations

The hydraulic parameters (VNIPI PT, 2012a) for the five hydrogeological units and for the contact zones between the gneiss and the dykes are given in Tab. 6.21 and Tab. 6.22.

The hydrogeological properties of the dykes are comparable to those of the un-weathered gneiss. Therefore, they do not need to be regarded as separate hydrogeological units. The contact zones between the dykes and the gneiss show a higher permeability and porosity than the dykes themselves. In contrast to the dykes with a thickness of 5 - 15 m, the contact zones are thinner and show an aperture of 0.5 m only. As a consequence, the lowly permeable dykes are neglected in the model, and only the higher permeable contact zones are modelled explicitly.

Tab. 6.21: Hydraulic parameters for the five hydrogeological units Q_I to Q_V (VNIPI PT, 2012a)

Parameter	Q_I	Q_{II}	Q_{III}	Q_{IV}/Q_V
Thickness [m]	10 – 65	50	90	> 200
Filtration coefficient K_f [m/day]	0.31	0.15	0.001	0.0003 – 0.0005
Hydraulic gradient *i* [-]	0.06	0.08	0.07	0.02
Porosity *n* [-]	0.4	0.05	0.012	0.002 – 0.004

Tab. 6.22: Hydraulic parameters for the contact zones in the lower two hydrogeological units Q_{IV} and Q_V (VNIPI PT, 2012a)

Parameter	Contact Zones in Q_{IV}	Contact Zones in Q_V
Thickness [m]	0.5	0.5
Filtration coefficient K_f [m/day]	0.005	0.001
Hydraulic gradient *i* [-]	0.08	0.08
Porosity *n* [-]	0.02	0.006

Where ranges instead of explicit values are given, the arithmetic mean is used in the model. Since data for the contact zones in Q_{II} and Q_{III} were not available (Tab. 6.22), it is assumed that the aperture doesn't change along the different units. Thus, it is set to 0.5 m. The porosity and permeability of the contact zones within the units Q_{II} and Q_{III} are extrapolated (elevated) in the same ratio as in the unit Q_{IV} compared to the surrounding gneiss. Data for the contact zones in Q_{II} and Q_{III} should be updated for further flow and transport simulations.

The intrinsic permeability *k* is used in the code d^{3}f instead of the filtration coefficient K_f. The intrinsic permeability can be derived from the filtration coefficient by the following relationship (Busch et al., 1993):

$$k = K_f \cdot \frac{\upsilon}{g} \tag{6-17}$$

with

$k = intrinsic\ \ permeability\ [m^2]$

$K_f = \ filtration\ \ \ coefficien\ t\ [ms^{-1}]$

$\upsilon = kinematic\ \ viscosity\ \ [m^2 s]$

$g = gravitation\ vector\ [ms^{-2}].$

For pure water at a temperature of 20 °C the kinematic viscosity equals $1.0068 \cdot 10^{-6}$ m^2 s^{-1}. Using a gravitation vector of 9.81 m s^{-2} this relation can be approximated by:

$$k \approx K_f \cdot 10^{-7}. \tag{6-18}$$

Tab. 6.23 and Tab. 6.24 summarise the applied hydraulic values for the five hydrogeological units and for the contact zones in the lower four units.

Tab. 6.23: Hydrogeological parameters for the three geological units according to VNIPI PT (2012a)

Hydrogeological unit	Q_I	Q_{II}	Q_{III}	Q_{IV}/Q_V
Porosity *n* [-]	0.4	0.05	0.012	0.003
Permeability *k* [m²]	$3.59 \cdot 10^{-13}$	$1.74 \cdot 10^{-13}$	$1.16 \cdot 10^{-15}$	$4.63 \cdot 10^{-16}$

Tab. 6.24: Hydrogeological parameters for the contact between the dykes and gneiss in the units Q_{II} to Q_V according to VNIPI PT (2012a).

Contact zone in hydro-geological unit	Contact zones in Q_{II}	Contact zones in Q_{III}	Contact zones in Q_{IV}	Contact zones in Q_V
Thickness [m]	0.5*	0.5*	0.5	0.5
Porosity *n* [-]	0.33*	0.08*	0.02	0.006
Permeability *k* [m²]	$2.18 \cdot 10^{-12}$*	$1.45 \cdot 10^{-14}$*	$5.79 \cdot 10^{-15}$	$1.16 \cdot 10^{-15}$

* Values are derived as stated in the text

Initial conditions have to be set for the salt concentration of the groundwater and the temperature. The code d³f is able to take the density-driven flow into account. The mineralisation of the groundwater ranges from ca. 90 mg l^{-1} in the near-surface formations, to ca. 600 mg l^{-1} in a depth of about 100 m and ca. 980 mg l^{-1} in the depth of about 300 m (Gupalo et al., 2004b). With regard to the convective flow of the groundwater, this very low salt concentration is negligible, thus the initial concentration of salt in the groundwater is set to zero. The mean temperature is assumed to be 5.2°C at the ground surface in the Yeniseysky area (VNIPI PT, 2011). According to the geothermal gradient of 0.8°C/100 m (VNIPI PT, 2011), the temperature rises linearly to 10.4°C in 656 m depth. As investigated in previous model simulations, the temperature field has no significant influence on the flow field and the flow velocity. Therefore a constant temperature field is defined in d³f. Heat transport is not regarded in the groundwater flow simulations.

At the model surface, groundwater recharge is assumed to take place. The groundwater recharge amounts to 485 mm (VNIPI PT, 2012a). This is realised in the model as a Neumann boundary condition with the inflow velocity of $1.54 \cdot 10^{-8}$ m s^{-1}. The basis of the model is impermeable to flow and transport.

Generally, the groundwater flow is directed to the Shumikha River northeast of the potential repository site (VNIPI PT, 2012a). Boundary conditions are given in form of hydraulic gradients for each of the hydrogeological units. For the upper Quaternary unit Q_I a gradient of 0.06 is given, while for the intensively weathered underlying unit Q_{II} the gradient is 0.08. The lower gneiss units show reduced gradients of 0.07 for Q_{III} and 0.02 for Q_{IV} and Q_V. The contact zones to the dykes show a gradient of 0.08 in Q_{IV} and Q_V. Contact zones in the unit Q_{III} are crossing the north-eastern limit of the model. A hydraulic gradient is not given in VNIPI PT (2012a) but needs to be defined for the simulations. The same approach as described above for defining the permeability and porosity for the contact zones in the unit Q_{III} is applied. The resulting hydraulic gradient is comparably high with a value of 0.28.

This hydraulic gradient is considered in the model by defining the appropriate velocity boundary conditions for each side line section of the model geometry. The boundary conditions can be defined as follows:

1. At the southwestern (left) side of the model, the pressure is set to the hydrostatic pressure, while for the north-eastern (right) side of the model the outflow velocity is calculated according to the given hydraulic gradient.
2. At the north-eastern (right) side of the model, the pressure is set to the hydrostatic pressure, while for the southwestern (left) side of the model the inflow velocity is calculated according to the given hydraulic gradient.

Both options are realised in the model and simulation results of the two different implementations are compared to each other in the following. The flow velocity can be calculated by

$$q = \frac{Q}{A} = \frac{K_f \cdot i \cdot A}{A} = K_f \cdot i \tag{6-19}$$

with

$q = Darcy\ velocity\ \ [ms^{-1}]$

$Q = transfluent\ water\ volume\ \ [m^3 s^{-1}]$

$A = area\ \ [m^2]$

$K_f = filtration\ coefficien\ t\ \ [ms^{-1}]$

$i = hydraulic\ gradient\ \ [-]$.

The hydraulic gradients and filtration coefficients are given by VNIPI PT (2012a). Calculated flow velocities are given in Tab. 6.25.

Tab. 6.25: Calculated flow velocity, to be used as a boundary condition.

	$K_f\ [ms^{-1}]$	$i\ [-]$	$q\ [ms^{-1}]$
Q_I	$3.59 \cdot 10^{-6}$	0.06	$2.15 \cdot 10^{-7}$
Q_{II}	$1.74 \cdot 10^{-6}$	0.08	$1.39 \cdot 10^{-7}$
Q_{III}	$1.16 \cdot 10^{-8}$	0.07	$8.10 \cdot 10^{-10}$
Q_{IV}	$4.63 \cdot 10^{-9}$	0.02	$9.26 \cdot 10^{-11}$
Q_V	$4.63 \cdot 10^{-9}$	0.02	$9.26 \cdot 10^{-11}$
Contact zones in Q_{III}	$1.45 \cdot 10^{-7}$*	0.28*	$4.06 \cdot 10^{-8}$*
Contact zones in Q_{IV}	$5.79 \cdot 10^{-8}$	0.08	$4.63 \cdot 10^{-9}$
Contact zones in Q_V	$1.16 \cdot 10^{-8}$	0.08	$9.26 \cdot 10^{-10}$

* Values marked with an asterisk are derived as explained in the text

The steady-state flow field and the hydrostatic pressure were calculated for the given model assumptions. The hydrostatic pressure distribution is given in Fig. 6-38 for model variation 1 and 2.

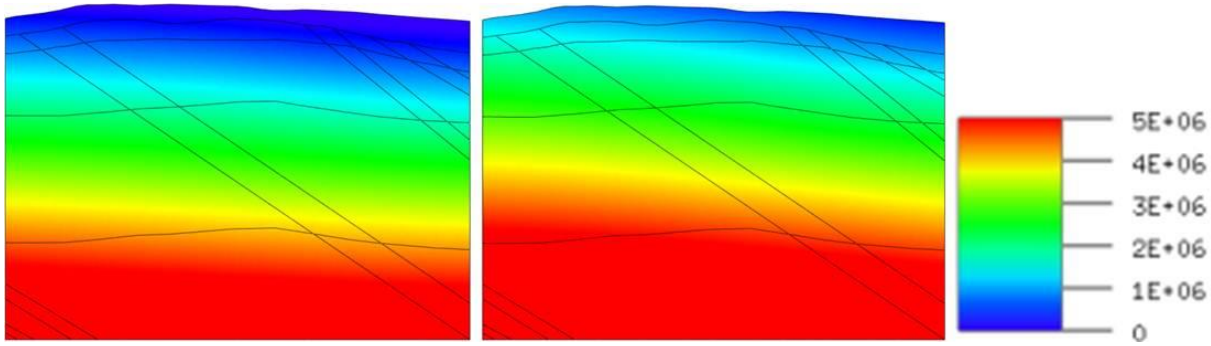

Fig. 6-38: Hydrostatic pressure [Pa] distribution in the Yeniseysky model area for a steady-state flow simulation for both model variations 1 (left) and 2 (right); Scale from 0 to $5 \cdot 10^6$ Pa

The given hydraulic gradient from the southwest to the northeast, which is implemented in the models as a velocity boundary condition, results in a decreasing pressure from the southwest to the northeast in both model variations. The pressure distributions in the two model variations differ considerably from each other. In model variation 2, the pressure is generally higher than in model variation 1 and shows a steeper gradient.

Ranges of the groundwater flow velocities for both model variations are given in Tab. 6.26. Groundwater velocity distributions and flow directions are depicted in Fig. 6-39 for model variation 1 and in Fig. 6-40 for model variation 2.

Tab. 6.26: Darcy velocity [m s^{-1}] in the hydrogeological units Q_I to Q_V for a steady-state flow simulation for both model variations

Hydrogeological unit	Groundwater flow velocity [m s^{-1}]	
	Model variation 1	Model variation 2
Q_I	$8 \cdot 10^{-8}$ - $3 \cdot 10^{-7}$	$2 \cdot 10^{-7}$ - $6 \cdot 10^{-7}$
Q_{II}	$3 \cdot 10^{-8}$ - $2 \cdot 10^{-7}$	$9 \cdot 10^{-8}$ - $2 \cdot 10^{-7}$
Q_{III}	$3 \cdot 10^{-10}$ - $1 \cdot 10^{-9}$	$1 \cdot 10^{-9}$ - $8 \cdot 10^{-10}$
Q_{IV}	$1 \cdot 10^{-10}$ - $5 \cdot 10^{-10}$	$2 \cdot 10^{-10}$ - $7 \cdot 10^{-10}$
Q_V	$1 \cdot 10^{-10}$ - $3 \cdot 10^{-10}$	$1 \cdot 10^{-10}$ - $5 \cdot 10^{-10}$

For both model variations, highest flow velocities can be observed in the upper hydrogeological units Q_I and Q_{II} with values in the range of 10^{-8} to 10^{-7} m s^{-1} as well as in Q_{III} with values in the range of 10^{-10} to 10^{-9} m s^{-1}. The lower units Q_{IV} and Q_V show the lowest flow velocities with values of less than $1 \cdot 10^{-9}$ m s^{-1}. Generally, higher flow velocities can be observed for model variation 2, exceeding the velocities in model variation 1 by a factor of two to three.

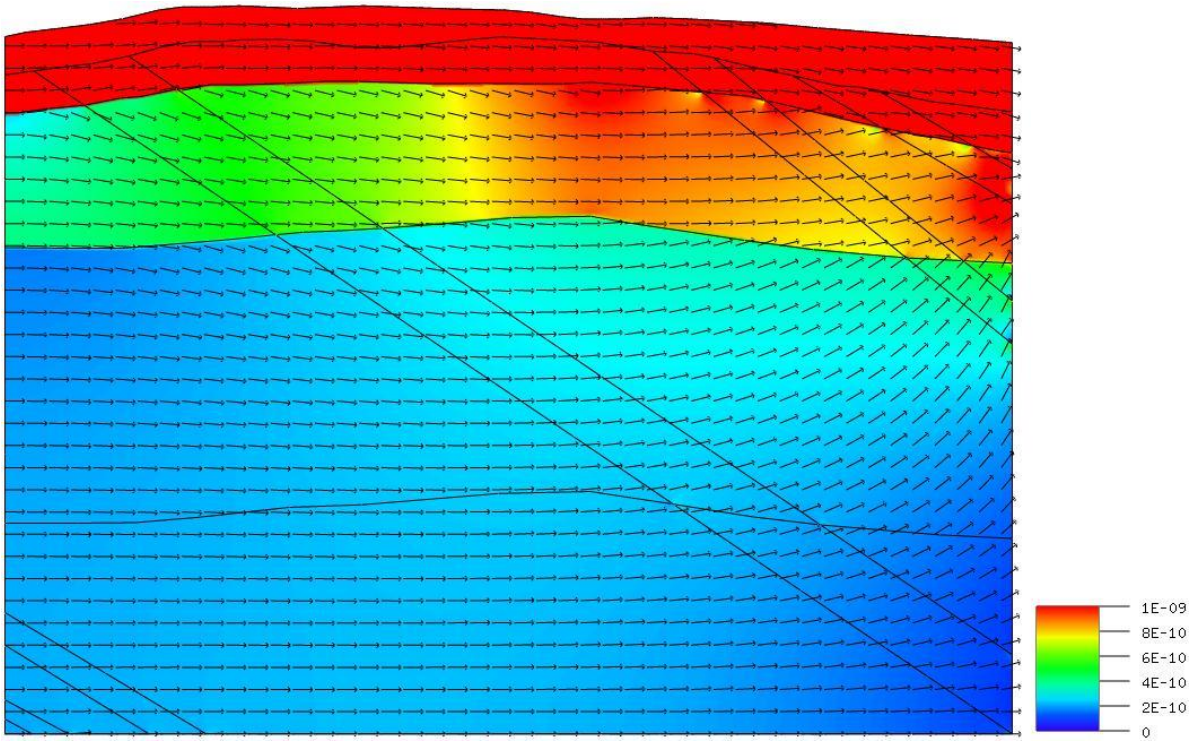

Fig. 6-39: Darcy velocity ([m s^{-1}], colours) and flow direction (vectors) in the hydrogeological units Q_I to Q_V for a steady-state flow simulation for model variation 1

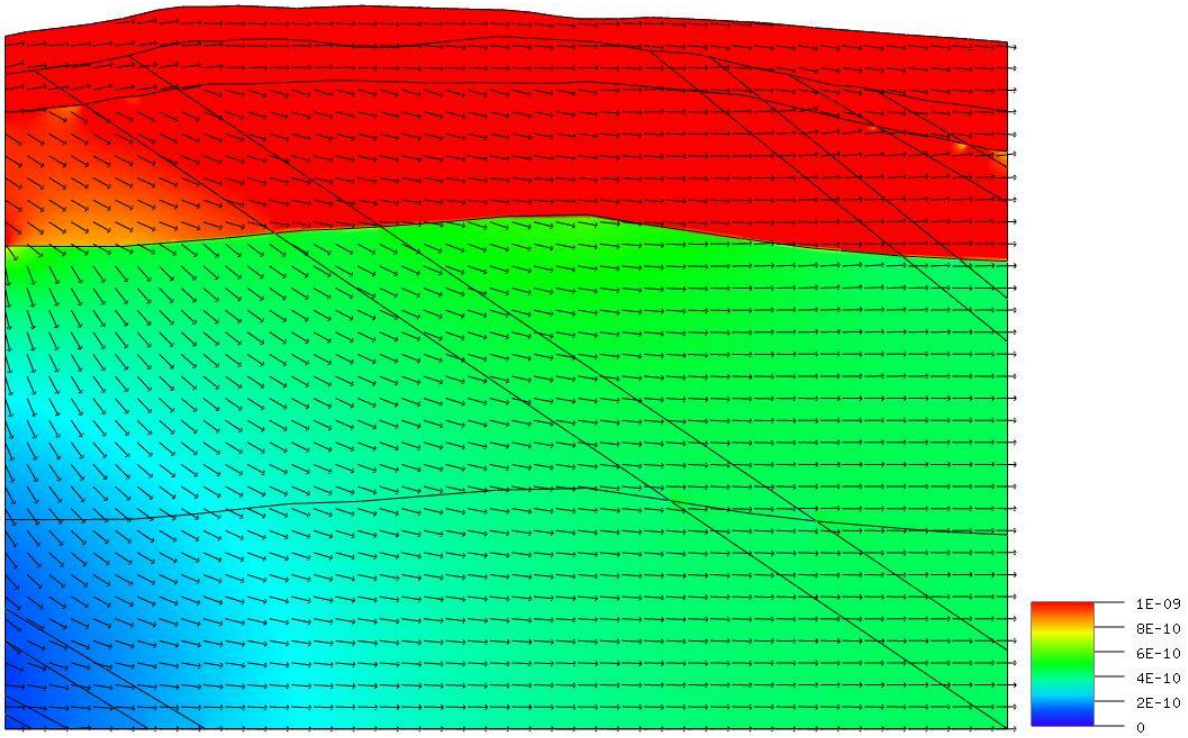

Fig. 6-40: Darcy velocity ([m s^{-1}], colours) and flow direction (vectors) in the hydrogeological units Q_I to Q_V for a steady-state flow simulation for model variation 2

From the southwest to the northeast, the flow velocity is increasing in both model variations. Model variation 1 shows lowest flow velocities in the north-eastern part of Q_V and highest flow velocities in the central and north-eastern part of Q_I and Q_{II}. In contrast to that, model variation 2 shows lowest flow velocities in the southwestern part of Q_V and highest flow velocities the central part of Q_I and Q_{II}.

In both model variations, the groundwater flow is generally directed from the southwest to the northeast due to the inflow of groundwater from the southwest. In Q_I and Q_{II}, the inflowing groundwater as well as the recharge water is discharged to the northeast, which is facilitated by the high permeability of those two units. Within Q_{III} the differences between the two model variations become visible. In the southwestern part, the groundwater flow is directed to the northeast and the bottom of the model for both model variations. However, in the north-eastern part of Q_{III}, there is an upward flow component in model variation 1, while the horizontal component of the groundwater flow is dominant in model variation 2.

The most obvious differences between the two model variations can be observed in the units Q_{IV} and Q_V. In model variation 1 the flow is generally directed from the southwest to the northeast with a dominant horizontal component until approximately the centre of the model domain. In the north-eastern part, the vertical component of the groundwater flow gains influence resulting in an upward flow mainly in Q_{IV}. Model variation 2 shows a downward groundwater flow in the southwestern part of Q_{IV} and Q_V, changing over to a horizontal flow in the central and north-eastern part of Q_{IV} and Q_V.

These differences in the groundwater flow direction in Q_{IV} and Q_V are caused by the definition of the boundary conditions at the southwestern and north-eastern model boundaries. In model variation 1 a hydrostatic pressure is defined for the southwestern boundary of the model domain, while for the north-eastern boundary an outflow is given in form of a velocity boundary condition. Groundwater, which is discharged over the eastern model boundary of Q_{III}, does not only originate from the inflow over the southwestern boundary of Q_{III} but to a fair extent is drawn from the over- and underlying units. This results in an upward flow in Q_{IV}

and Q_V. For model variation 2 an inflow of groundwater is defined for the southwestern boundary, while a hydrostatic pressure is defined for the north-eastern boundary. Here again, the boundary condition for Q_{III} has a strong impact on the flow field. Groundwater that enters the model area over the southwestern boundary of Q_{III} is not only discharged over the north-eastern boundary of Q_{III}. Part of the inflow is directed downwards into Q_{IV} and Q_V and discharged over their north-eastern boundaries. Thus no upward flow component is observed for units Q_{IV} and Q_V.

Evaluating the flow field for the two models variations, it is obvious that the boundary conditions have to be specified according to field measurements. Instead of giving the hydrostatic pressure for one of the model boundaries, it is advisable to define the pressure distribution (hydraulic head) for the side boundaries of the model and for each of the hydrogeological units separately. Hence, a realistic and resilient simulation of the groundwater flow would be possible.

The flow velocity in the contact zones between the gneiss and the dykes for both model variations is directed downwards to the northeast of the model (Fig. 6-41 and Fig. 6-42). Ranges for the flow velocity are given in Tab. 6.27. The flow velocity within the contact zones is higher than in the hydrogeological units (Tab. 6-28). The permeability of the contact zones is higher than that of the gneiss itself, causing a higher flow velocity in the contact zones than in the gneiss with a difference of up to one order of magnitude (Tab. 6-28). In general, the flow velocity in the contact zones is higher in model variation 2 than in model variation 1.

In Tab. 6-28 the simulated flow velocities are compared to the flow velocities derived from the data given by VNIPI PT (2012a). Model simulations and given values are in fairly good agreement with each other. In Q_{III} to Q_V simulated flow velocities are higher than the velocities given by VNIPI PT (2012a). This results from the additional inflow of groundwater into the lower units from the overlying units. Again, this is due to the different definition of the boundary conditions in the two model variations. A better accordance of the given values and the model results would be achieved based on a more realistic description of the given hydraulic situation in the model.

A revision of the input parameters and boundary conditions will help assessing the realistic flow velocity and flow direction for each of the units and contact zones.

Tab. 6.27: Darcy velocity [m s^{1}] in the contact zones in hydrogeological units Q_{II} to Q_V for a steady-state flow simulation for both model variations

Contact zone in hydrogeological zone	**Darcy flow velocity [m s^{-1}]**	
	Model variation 1	**Model variation 2**
Q_{II}	$3 \cdot 10^{-7}$ - $2 \cdot 10^{-6}$	$9 \cdot 10^{-7}$ - $3 \cdot 10^{-6}$
Q_{III}	$4 \cdot 10^{-9}$ - $3 \cdot 10^{-8}$	$9 \cdot 10^{-9}$ - $5 \cdot 10^{-8}$
Q_{IV}	$1 \cdot 10^{-10}$ - $4 \cdot 10^{-9}$	$4 \cdot 10^{-9}$ - $7 \cdot 10^{-9}$
Q_V	$1 \cdot 10^{-10}$ - $6 \cdot 10^{-10}$	$2 \cdot 10^{-10}$ - $2 \cdot 10^{-9}$

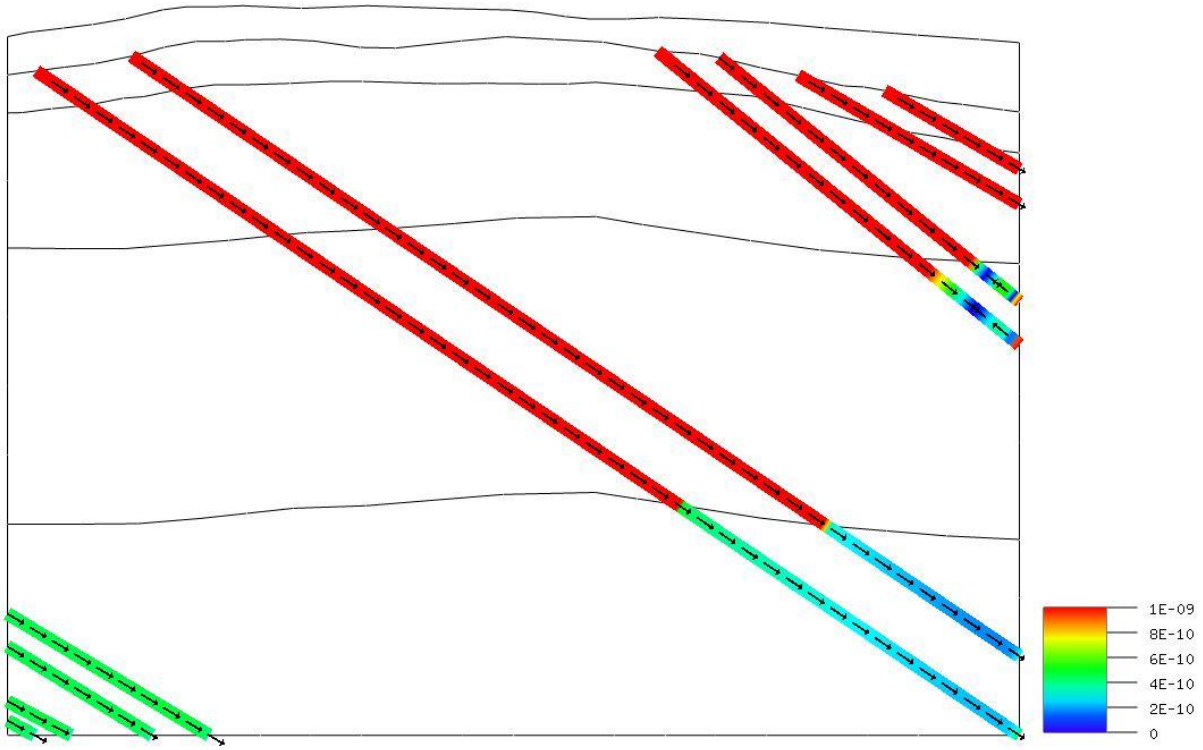

Fig. 6-41: Darcy velocity ([m s^{-1}], colours) and flow direction (vectors) in the contact zones between the dykes and the gneiss for a steady-state flow simulation for model variation 1

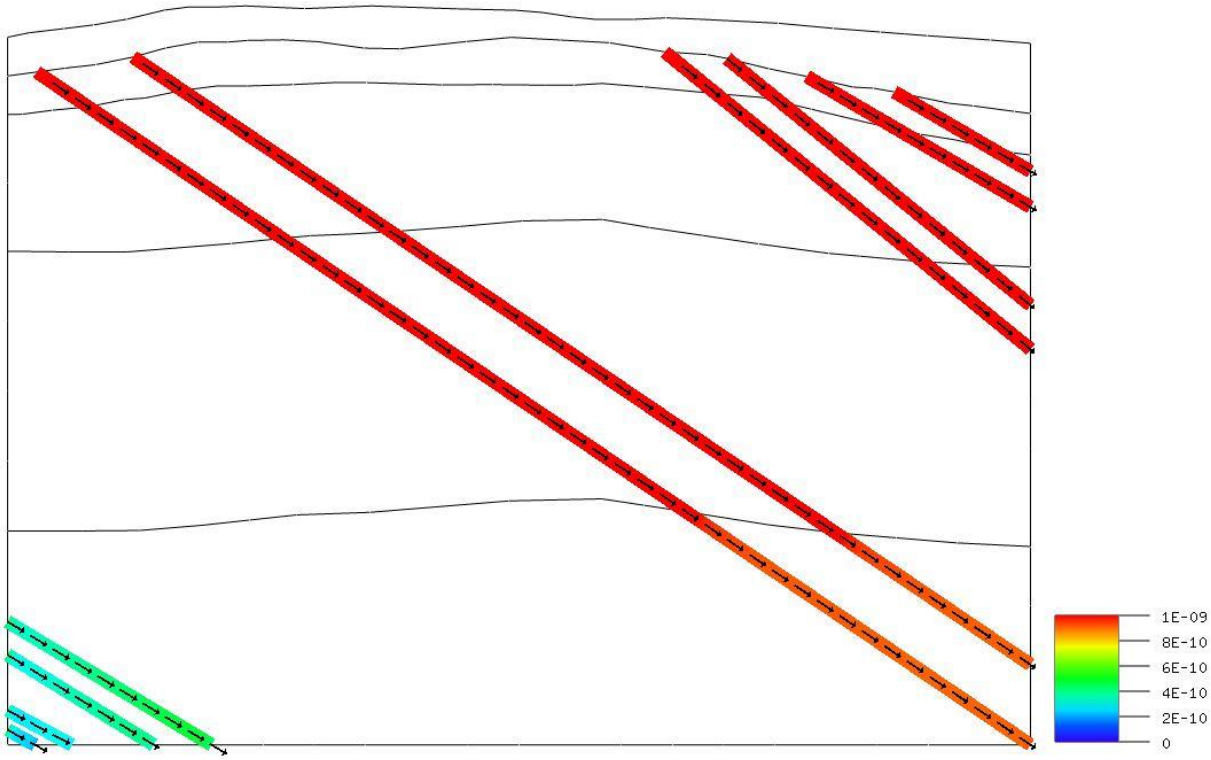

Fig. 6-42: Darcy velocity ([m s^{-1}], colours) and flow direction (vectors) in the contact zones between the dykes and the gneiss for a steady-state flow simulation for model variation 2

Tab. 6.28: Darcy velocity [m s^{-1}] in the hydrogeological units Q_I to Q_V and in the contact zones in Q_{II} to Q_V for a steady-state flow simulation for both model variations

Hydrogeological unit	Darcy flow velocity [m s^{-1}]		
	Model variation 1	Model variation 2	(VNIPI PT, 2012a)
Q_I	$8 \cdot 10^{-8}$ - $3 \cdot 10^{-7}$	$2 \cdot 10^{-7}$ - $6 \cdot 10^{-7}$	$2.15 \cdot 10^{-7}$
Q_{II}	$3 \cdot 10^{-8}$ - $2 \cdot 10^{-7}$	$9 \cdot 10^{-8}$ - $2 \cdot 10^{-7}$	$1.39 \cdot 10^{-7}$
Q_{III}	$3 \cdot 10^{-10}$ - $1 \cdot 10^{-9}$	$1 \cdot 10^{-9}$ - $8 \cdot 10^{-10}$	$8.10 \cdot 10^{-10}$
Q_{IV}	$1 \cdot 10^{-10}$ - $5 \cdot 10^{-10}$	$2 \cdot 10^{-10}$ - $7 \cdot 10^{-10}$	$9.26 \cdot 10^{-11}$
Q_V	$1 \cdot 10^{-10}$ - $3 \cdot 10^{-10}$	$1 \cdot 10^{-10}$ - $5 \cdot 10^{-10}$	$9.26 \cdot 10^{-11}$
Contact zones in Q_{II}	$3 \cdot 10^{-7}$ - $2 \cdot 10^{-6}$	$9 \cdot 10^{-7}$ - $3 \cdot 10^{-6}$	$6.85 \cdot 10^{-6}$*
Contact zones in Q_{III}	$4 \cdot 10^{-9}$ - $3 \cdot 10^{-8}$	$9 \cdot 10^{-9}$ - $5 \cdot 10^{-8}$	$4.06 \cdot 10^{-8}$*
Contact zones in Q_{IV}	$1 \cdot 10^{-10}$ - $4 \cdot 10^{-9}$	$4 \cdot 10^{-9}$ - $7 \cdot 10^{-9}$	$4.63 \cdot 10^{-9}$
Contact zones in Q_V	$1 \cdot 10^{-10}$ - $6 \cdot 10^{-10}$	$2 \cdot 10^{-10}$ - $2 \cdot 10^{-9}$	$9.26 \cdot 10^{-10}$

* Values are derived as stated in the text
Simulated flow velocities, that are considerably higher than the given values, are marked bold

In summary, the investigated area shows good prerequisites to be considered as a potential repository site. This concerns the low flow velocity in the lower units of the gneiss and the downwards groundwater flow. Further investigations are necessary to characterize the flow system in more detail and to identify the main transport paths from the location of the potential repository to the surface. According to Tóth (1963), intermediate and regional flow systems have to be regarded if the depth-to-width ratio of a basin exceeds the ratio of one-to-twenty (Fig. 6-43). In this case, tracers and pollutants may be transported downwards in the first place, but will eventually reach the surface after transiting the intermediate or regional flow system. Thus, a detailed investigation of the hydrogeological situation of the regional flow system is crucial for a reliable safety assessment of a potential repository site. Further model simulations should then be performed considering the specified hydraulic data and the hydrogeological setting of the investigation area.

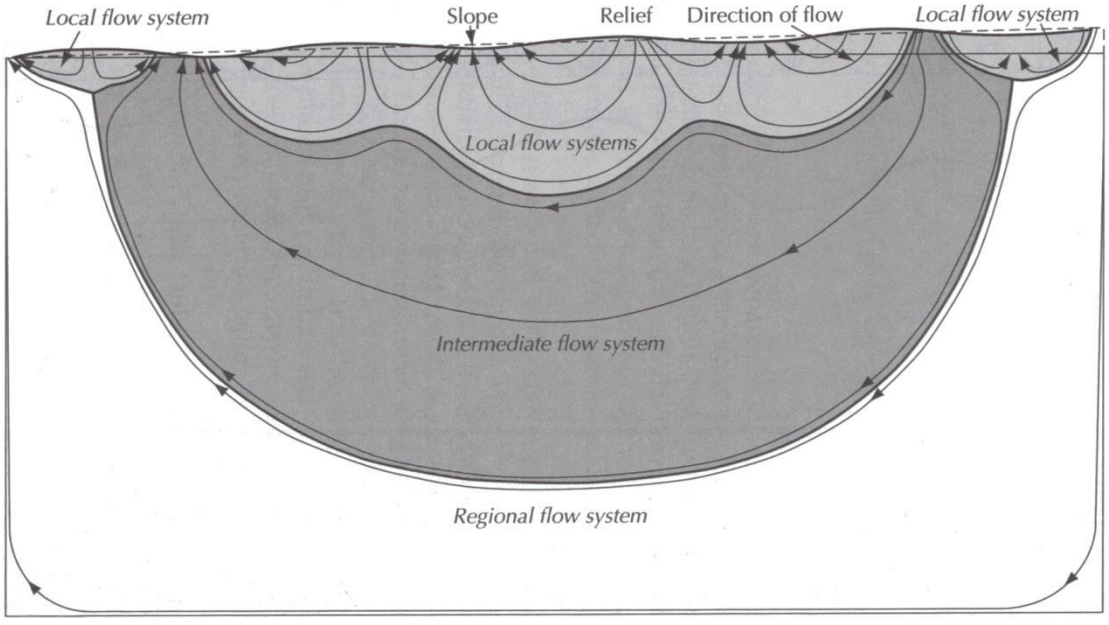

Fig. 6-43: Groundwater flow systems according to Tóth (1963)

6.2.1.3 Transport simulations

Tracer transport can be simulated using the code d³f, in case an inert tracer is regarded. More complex transport simulations using the code r³t (radionuclides, reaction, retardation, and transport (Fein, 2004)) taking the sorption and the radioactive decay into account, will be performed in the future. Based on the groundwater flow simulations described in chapter 6.2.1.2, first basic transport simulations were conducted regarding an inert tracer and simplified transport parameters. For these simulations, the concentration of the tracer in the model area needs to be stated in form of a relative concentration:

$$c_{rel} = \frac{c_{abs}}{c_{abs,\max}} \tag{6-20}$$

with:

$$c_{abs} = \frac{m_{tracer}}{m_{tracer} + m_{H_2O}} \tag{6-21}$$

and

$c_{abs} = relative\ \ tracer\ concentration = relative\ \ tracer\ mass\ \ fraction\ [-]$

$c_{abs} = absolute\ \ tracer\ mass\ \ fraction\ [-]$

$c_{abs,\max} = \ maximum\ absolute\ \ tracer\ mass\ \ fraction\ [-]$

$m_{tracer} = mass\ of\ \ tracer\ [kg]$

$m_{H_2O} = mass\ of\ \ water\ [kg]$

The tracer in solution is assumed to have no influence on the density and viscosity of the groundwater. The maximum mass fraction is set to 0.264 according to the solubility of sodium chloride in pure water. The inflow of the tracer is defined as a constant point source of $3.17 \cdot 10^{-11}$ $m^3\ s^{-1}$, which equals $1.0 \cdot 10^{-3}$ $m^3 a^{-1}$. Assuming a saturation of the inflowing solution with sodium chloride, this equates to an inflow of 0.359 kg tracer substance per year. Two different locations of the point source were realised for these orienting calculations. The first location is at the interface of Q_{IV} and Q_V in the southwestern part of the model (S1), and the second location is at an intersection of a contact zone with the interface of the units Q_{IV} and Q_V in the north-eastern part of the model (S2, Fig. 6-44).

A longitudinal dispersion length of 10 m, a transversal dispersion length of 0 m and a diffusion coefficient of $1 \cdot 10^{-9}$ $m^2\ s^{-1}$ was assumed for the entire model domain including the fractures and contact zones. No sorption or interaction processes of the inert tracer with the minerals of the geological units are assumed to take place. Radioactive decay is also not regarded in the model simulations.

The initial concentration of the tracer in the model area was set to 0. At the surface and the western and eastern boundary of the model, a Neumann type boundary condition was defined. For an inflow of groundwater the tracer concentration is set to 0, while for an outflow of groundwater the tracer concentration equals the actual concentration of the tracer in the outflowing groundwater.

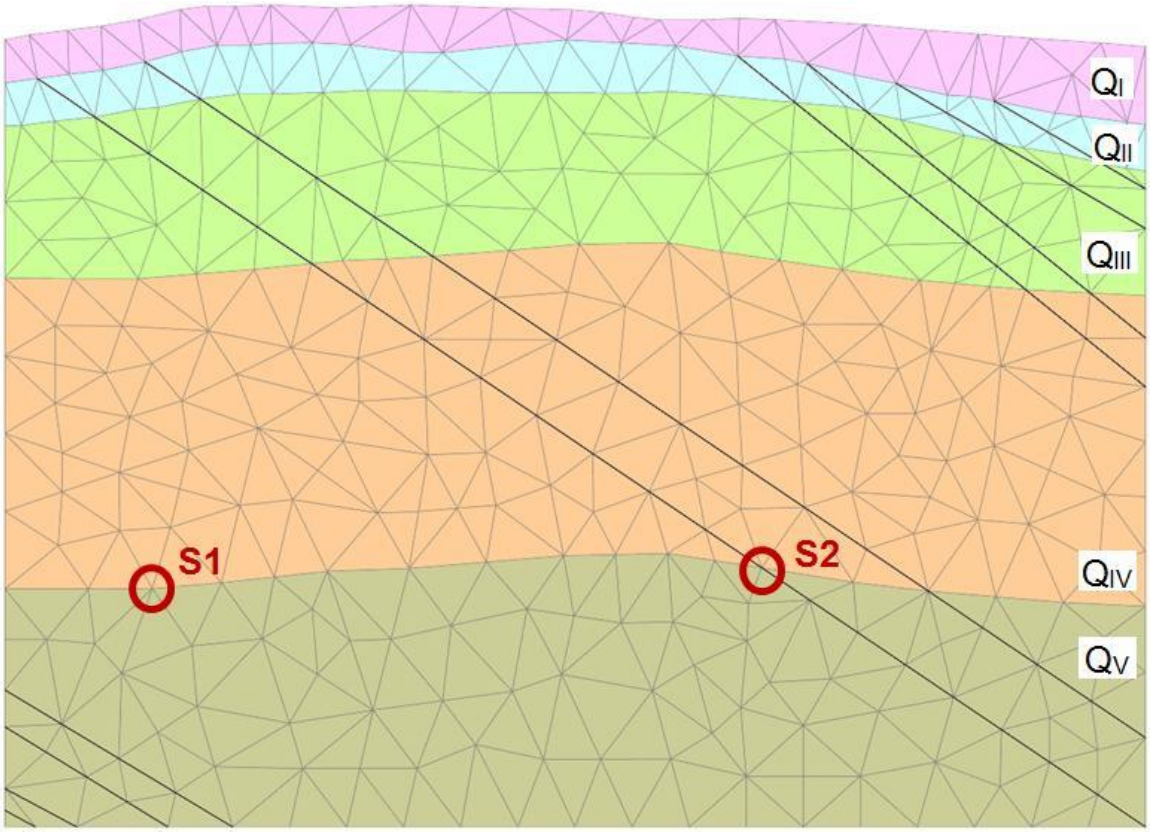

Fig. 6-44: Geometry and course grid for the hydrogeological model with names of hydrogeological units and location of considered contact zones. Red circles indicate the location of tracer sources.

For each of the two model variations 1 and 2, both locations of the source point S1 and S2 were simulated and are discussed here. All four model variations were run for a model time of 1000 years with a time step of 10 years. The following figures indicate the tracer concentration as a relative concentration ranging from 0 to $2.64 \cdot 10^{-3}$, which equals about 11 $kg \cdot m^{-3}$ tracer.

Model variation 1 shows a tracer transport according to the flow velocity in the northeastern direction (Fig. 6-45 and Fig. 6-46). For the source location S1 (Fig. 6-45), the tracer distribution is more or less horizontal in the vicinity of the source. Where the tracer reaches the two contact zones in the center of the model, the tracer plume is broadened slightly, which can clearly be observed when choosing a smaller resolution of the scale. In the northeastern part of the model area, the upwards groundwater flow gains influence. Thus the tracer is also transported upwards and even reaches the unit Q_{III} in this simulation. Mainly within the unit Q_{IV}, but to a certain amount also in Q_{III}, the tracer is transported over the model boundary to the northeast. The contact zones have low influence of the tracer transport, because the advective flow through the units is the dominant transport process. The flow velocity in the contact zones is higher than in the hydrogeological units and the flow within the contact zones is directed downwards. Therefore tracer concentration distributions are shifted slightly downwards compared to the tracer concentration distributions in the neighboring units. The steady-state of the tracer transport is reached after approximately 500 - 600 a.

In case the tracer source is located further northeast (S2, Fig. 6-46), the tracer follows the same pathways and is influenced by the same dominant transport process (advection). Due to the fact, that this time, the source is located in an area, where the vertical component of the groundwater flow has already gained influence, the tracer reaches the upper model unit Q_{III} in a higher concentration than in case its source is located further southwest. The tracer plume is less broad than for source location S1. In Fig. 6-46, the influence of the contact

zones can clearly be observed. As stated above, the tracer concentration plume shows an offset where it crosses one of the contact zones. The steady-state distribution of the tracer is reached after approximately 200 – 300 a.

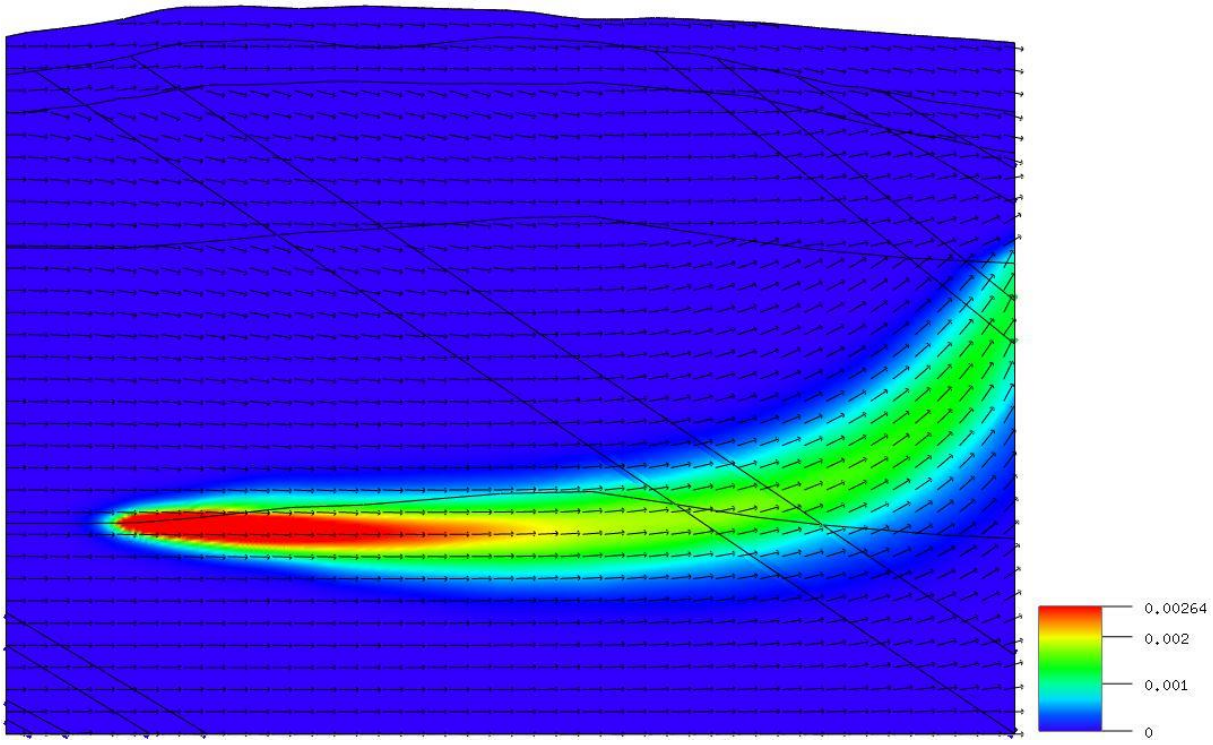

Fig. 6-45: Relative tracer concentration after 1,000 a model time, source point S1, model variation 1
Colours indicate the relative tracer concentration ranging from 0 to $2.64 \cdot 10^{-3}$, which equals ca. 11 kg m^{-3}.

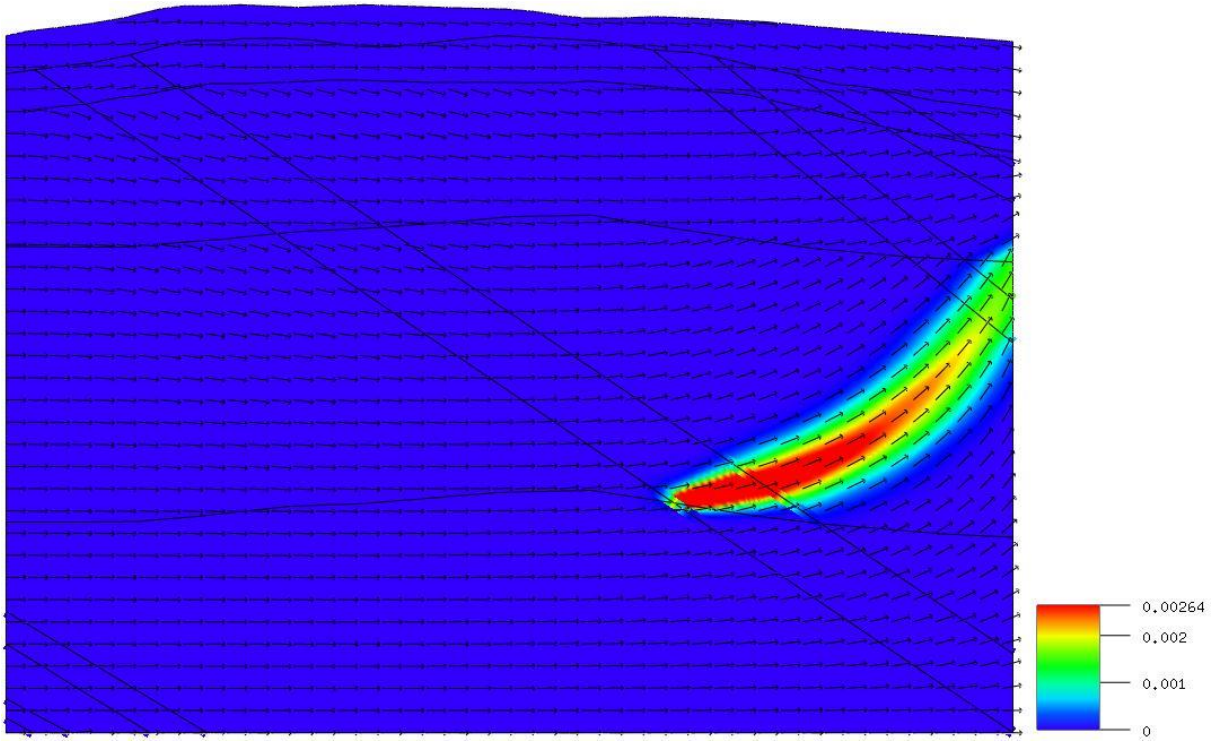

Fig. 6-46: Relative tracer concentration after 1,000 a model time, source point S2, model variation 1
Colours indicate the relative tracer concentration ranging from 0 to $2.64 \cdot 10^{-3}$, which equals ca. 11 kg m^{-3}.

Model variation 2 features the same dominant transport processes as model variation 1, but the transport directions strongly differ from each other. Here again, the tracer is transported according to the flow direction (Fig. 6-47 and Fig. 6-48). When a source location in the southwestern part (S1) is assumed, the tracer plume mainly extends through the lowest hydrogeological unit Q_V (Fig. 6-47). When the steady-state tracer distribution is reached, the plume has reached the north-eastern model boundary. The tracer only leaves the model via the model boundary of Q_V. As discussed above, intermediate and regional flow systems can extend over a larger width than the local flow systems, so the tracer could eventually reach the upper hydrogeological units in a greater distance than covered by this model area. This simulation shows the importance of a more detailed investigation of the local, intermediate and regional flow systems of the area.

Also for model variation 2 the consequence of a different location of the source (S2) was investigated (Fig. 6-48). In this case, the vertical tracer transport has less influence than in all other transport simulations presented here. Where the tracer plume reaches the contact zone, the offset of the tracer concentration within the fracture can clearly be observed (Fig. 6-48) as for model variation 1, source location S2 (Fig. 6-46). The tracer leaves the model area in the lower part of Q_{IV} and at the interface of Q_{IV} and Q_V in the north-eastern direction. The steady-state tracer distribution in the model area is reached after less than 200 a model time.

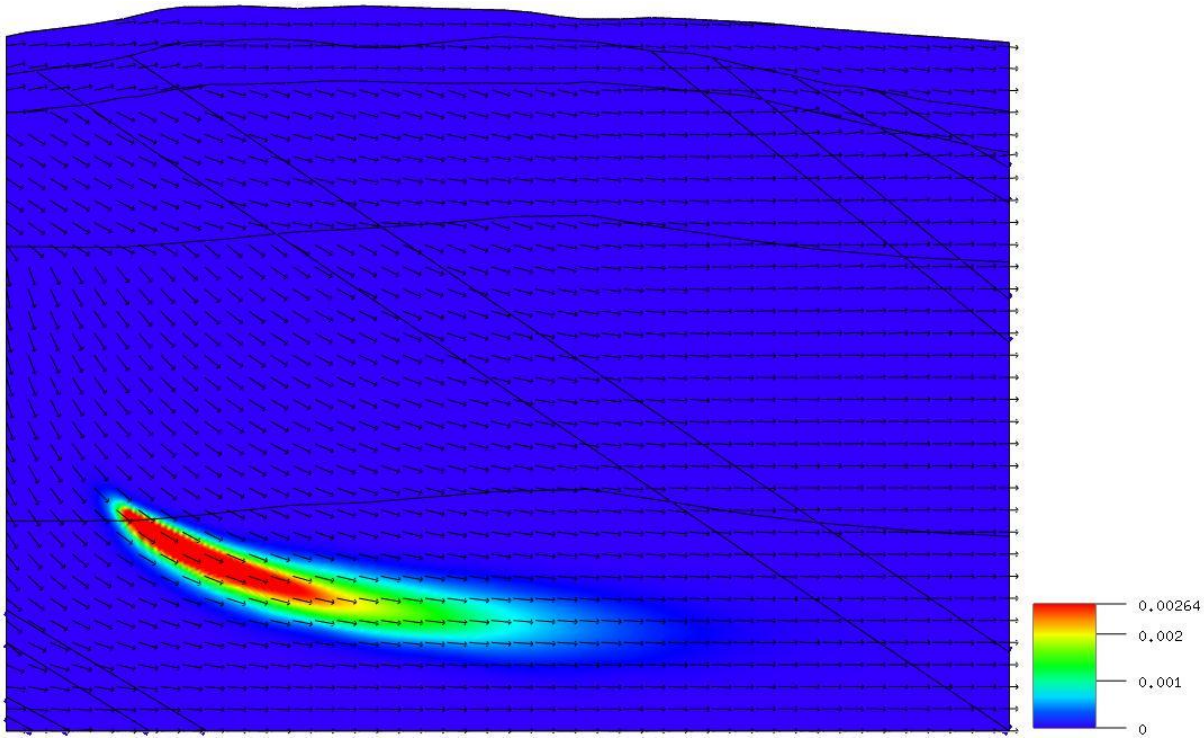

Fig. 6-47: Relative tracer concentration after 116 a model time, source point S1, model variation 2
Colours indicate the relative tracer concentration ranging from 0 to $2.64 \cdot 10^{-3}$, which equals ca. 11 kg m^{-3}.

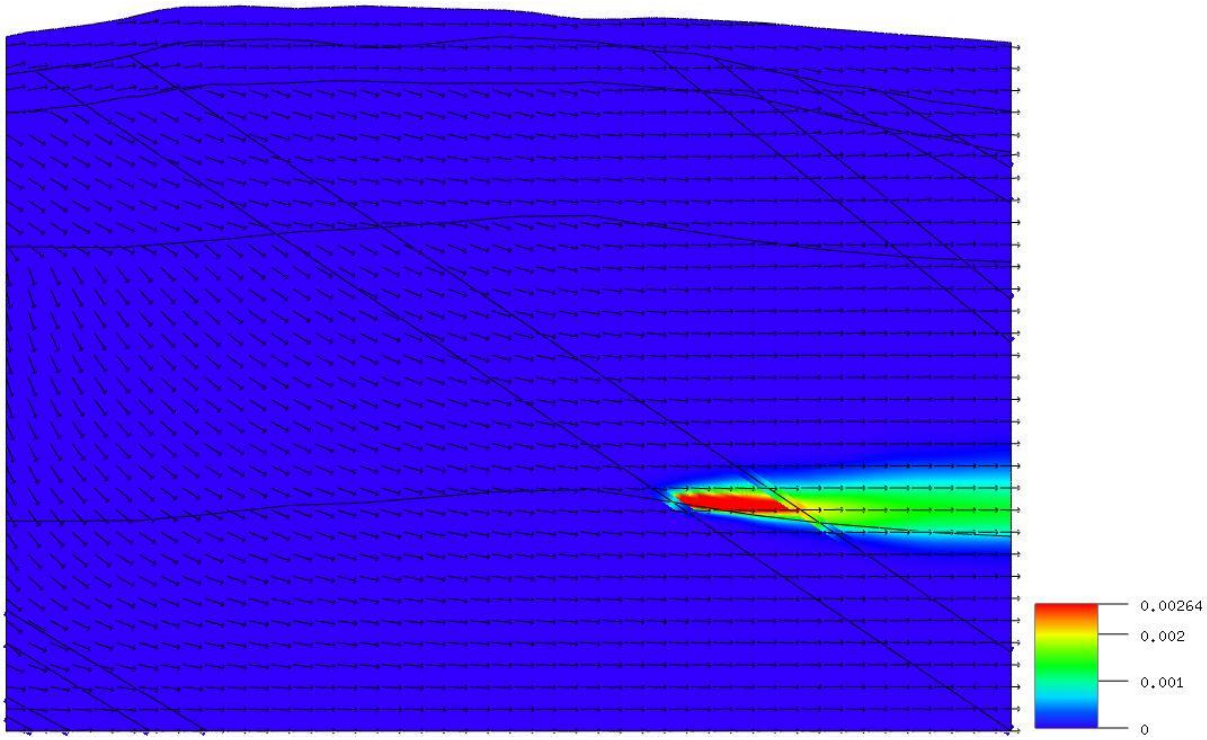

Fig. 6-48: Relative tracer concentration after 1,000 a model time, source point S2, model variation 2
Colours indicate the relative tracer concentration ranging from 0 to $2.64 \cdot 10^{-3}$, which equals ca. 11 kg m^{-3}.

Summarizing the results of the transport simulations, it can be stated that the results are strongly dependent on the defined boundary conditions and thus on the detailed characterization of the hydrogeological and hydraulic setting. Based on the assumptions, the tracer is either transported within the lower units of the model or can reach the upper units as well. The tracer leaves the model domain in the same range of concentration in all four model variations. Advection is the dominant transport process for the tracer in these simulations, but other processes, such as the diffusion and transversal dispersion, can gain influence when the model parameters are defined according to field or laboratory experimental data.

The fracture system should be investigated in more detail (distribution of fractures and porosity of the infill material, as stated above), because of its impact on the flow velocity and the sorption capacity. And finally, the values for the sorption coefficient of the most important radionuclides to be considered for the gneiss are necessary. Laboratory experiments should be performed to determine the sorption characteristics of the rocks, where data is missing. Information on realistic radionuclide release rates as well as a list of radionuclides to be considered in transport simulations can be derived from the near-field simulations.

6.2.2 Radionuclide migration

6.2.2.1 Model description

Advection through fracture networks dominates transport in most crystalline-basement environments. Because waste is emplaced in low-permeability domains of the disposal site, the first part of the migration path is expected to have the highest transport resistance (Mazurek, 2010). Conservatively it is assumed here that the EDZ can provide a long-term effective connection between the waste and the fracture system in the host rocks (Fig. 6-49). The following pathway lengths in the host rocks are considered: 100 m, 200 m and 500 m. The radionuclide migration through the host rocks is modelled with GeoTrend-Frame (Reiche et al., 2014) and takes into account the advective radionuclide transport through a fractured medium and the matrix diffusion (parameters in Tab. 6.19). Sorption coefficients for the crys-

talline rocks are given in Tab. 6.20. Sorption coefficients on the fracture surface K_{Df} are calculated from the sorption coefficients for the crystalline rocks K_{Dr} using

$$K_{Df} \approx b \frac{1 - n_f}{n_f} \rho_r K_{Dr} \qquad (6\text{-}22)$$

The other parameters b, n_f and ρ_r are given in Tab. 6.29.

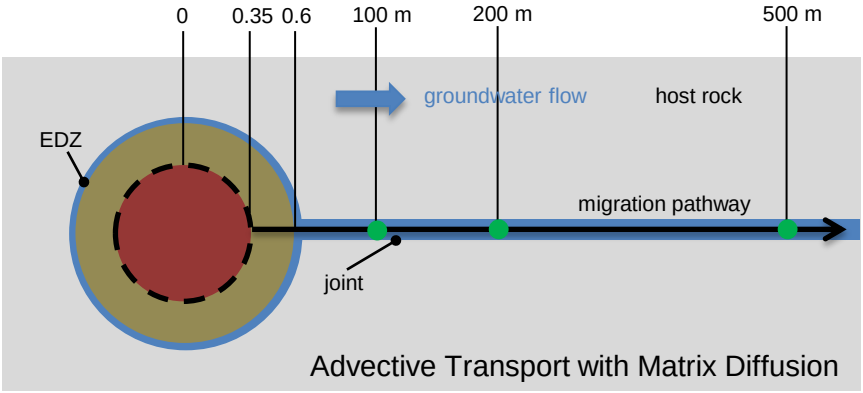

Fig. 6-49: Schematic representation of the investigated transport mechanisms in the host rocks

The data applied for the far-field model is taken from the project WIBASTA (Jobmann et al., 2008) or is derived by new exploration results in the Yeniseysky area carried out by VNIPI PT.

In the calculations it is assumed that the transport of radionuclides occurs within a network of water conducting fractures. In the transport model a representative element volume is considered and the different transport characteristics are reduced to single model parameters. The transport of the radionuclides through the gneissic rock is described by an advective-dispersion based equation coupled to an equation describing the diffusion in the rock matrix (Reiche et al., 2014).

The Darcy velocity q in the host rocks is the ratio of the groundwater flow to the cross section of the repository system in flow direction. The advective velocity within the fracture zones is then calculated from the Darcy velocity by:

$$v_a = \frac{q}{2bWn_f} \qquad (6\text{-}23)$$

The fracture density W determines the total trace length in a plane perpendicular to the flow direction. The porosity of the filling material n_f describes the volume fraction of the water-bearing zones available for advective flow, $2b$ is the aperture width of the fractures.

Field investigations of the gneissic host rocks yield a hydraulic permeability of $4 \cdot 10^{-4}$ m/d and a hydraulic gradient of 0.02. The Darcy velocity q is thus $8 \cdot 10^{-6}$ m/d or $2.9 \cdot 10^{-3}$ m/a. Taking into account a repository area in flow direction of about 52250 m^2 (700 m times 75 m) the groundwater flow is 152 m^3/a. Using

$$v_a = \frac{q}{n} \tag{6-24}$$

with an estimated effective porosity *n* of 0,01 the advective velocity v_a is 0.3 m/a. Applying (6-24) in (6-23) *W* can be calculated by

$$W = \frac{n}{2bn_f} \tag{6-25}$$

With a measured aperture width of 0.05 m and a porosity n_f of 0.4 the fracture density is 0.5 m/m^2. The parameter values chosen for the deterministic calculations are given in Tab. 6.29.

Tab. 6.29: Input data for the far-field model

Parameter		Value
Repository area (flow direction)	[m^2]	52250
Darcy velocity	[m/a]	$2.9 \cdot 10^{-3}$
Rock density	[kg/m^3]	2,670
Porosity (filling material)	[-]	0.4
Diffusion coefficient	[m^2/a]	0.005
Effective porosity	[-]	0.01
Penetration depth	[m]	0.20
Aperture width	[m]	0.05
Fracture density	[m/m^2]	0.5
Groundwater flow	[m^3/a]	152
Dispersion length	[m]	1.0

6.2.2.2 Exposure calculations

The radionuclide migration is modelled as a diffusion process through the bentonite buffer. Then advective transport through host rocks is calculated. The radionuclide flux and the corresponding radionuclide concentration are calculated after a transport through the host rocks of 100 m, 200 m and 500 m. According to the results of the exploration of the host rocks the groundwater flow in the vicinity of the repository is directed downwards and there is no obvious migration path to the biosphere. In order to calculate an indicator for the radiological consequences of the calculated radionuclide concentrations in the host rocks, it is conservatively assumed that the observed radionuclide concentrations are instantaneously transported to the upper aquifer, which represents the water source for the biosphere. For the calculations a groundwater flow in the upper aquifer of about $1.5 \cdot 10^5$ m^3/a is estimated (Fig. 6-50).

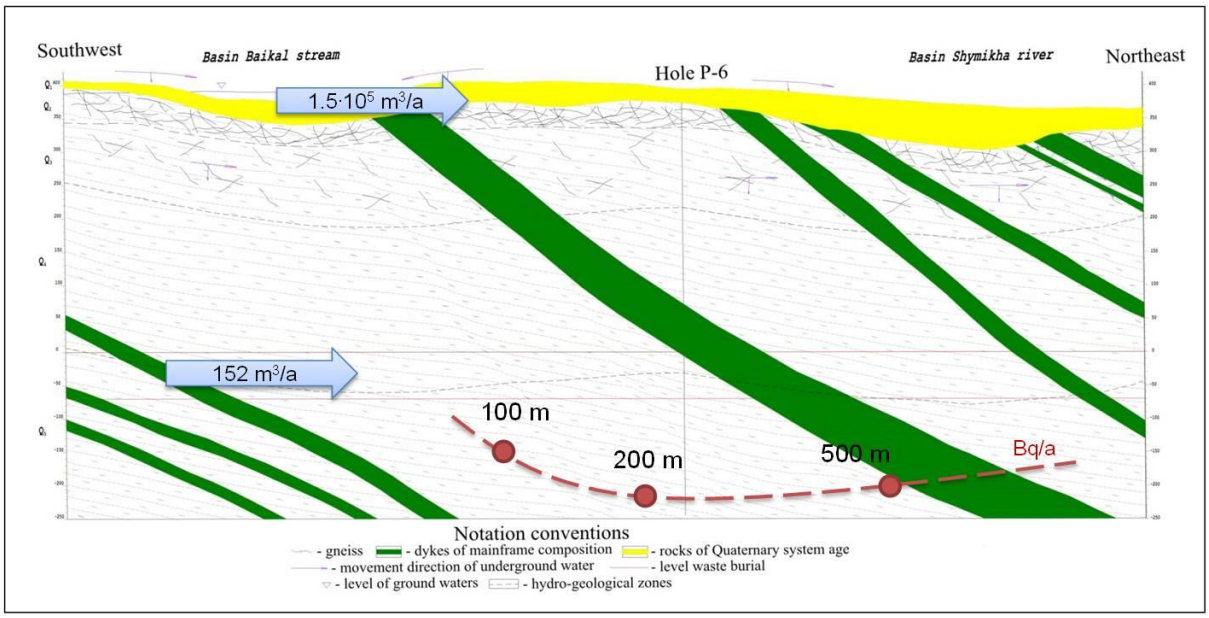

Fig. 6-50: Potential radionuclide migration pathway (dashed line) and observation points to calculate radiation exposure

Tab. 6.30 summarizes the dose conversion factors (DCF) applied for the conversion of radionuclide concentrations to an annual exposure.

Tab. 6.30: Dose conversion factors (DCF) in [(Sv/a)/(Bq/m^3)] (Keesmann et al., 2005)

Activation and fission products and Np- series		U- and Ac-series	
Nuclide	**DCF**	**Nuclide**	**DCF**
Se-79	$3.4 \cdot 10^{-7}$	**U-238**	$7.1 \cdot 10^{-7}$
Tc-99	$8.8 \cdot 10^{-9}$	**Th-234**	$4.8 \cdot 10^{-9}$
Cs-135	$5.7 \cdot 10^{-8}$	**U-234**	$1.4 \cdot 10^{-6}$
Am-241	$8.0 \cdot 10^{-7}$	**Th-230**	$3.7 \cdot 10^{-5}$
Np-237	$4.7 \cdot 10^{-6}$	**Ra-226**	$3.0 \cdot 10^{-5}$
U-233	$3.9 \cdot 10^{-6}$	**Pb-210**	$2.3 \cdot 10^{-6}$
Pa-233	$8.8 \cdot 10^{-9}$	**Po-210**	$4.9 \cdot 10^{-6}$
Th-229	$1.7 \cdot 10^{-5}$	**Am-243**	$2.0 \cdot 10^{-6}$
Ra-225	$1.1 \cdot 10^{-7}$	**Pu-239**	$9.8 \cdot 10^{-7}$
Ac-225	$3.7 \cdot 10^{-8}$	**U-235**	$3.3 \cdot 10^{-6}$
		Pa-231	$4.0 \cdot 10^{-5}$
		Ac-227	$1.0 \cdot 10^{-5}$
		Th-227	$1.9 \cdot 10^{-8}$
		Ra-223	$1.1 \cdot 10^{-7}$

6.2.2.3 Modelling results

Because of the preliminary character of the applied parameters, the necessary assumption on the radionuclide migration pathway and the missing scenario analysis, it is not possible to give a statement regarding the safety for a repository at the site Yeniseysky with the calculations of radionuclide migration through the host rocks. Instead the results of the calculation give an orientation, which features and processes are important for the calculation of radiological consequences of a HLW repository under the given conditions and assumptions. The

calculation of a radiation exposure is considered to be an indicator used for comparing the results of different calculations.

In order to understand the migration behaviour of the important dose relevant radionuclides and for analysing trends of radionuclide migration, the modelled period is 10^8 years in order to cover all radiation exposures. It is obvious that the basic geological assumptions and conditions become increasingly uncertain in the future and that the integrity of the barrier system cannot be guaranteed for such a long time. Fig. 6-51 to Fig. 6-53 show the results of the radionuclide migration through the host rocks after 100, 200 and 500 m. After 100 meters the peak occurs between $5 \cdot 10^5$ and $1 \cdot 10^6$ years. Se-79 and Cs-135 dominate the calculated radiation exposure up to $3 \cdot 10^6$ years. After about $3 \cdot 10^6$ years the actinide chains (mainly by Th-230 and Ra-226) are the main contributors to the exposure.

After an advective transport of 200 m through the fractures of the host rocks the same radionuclides are relevant. The peak of the migration front occurs between 10^5 and 10^6 years. At this time Cs-135 and Se-79 are the dominant contributors to the radiation exposure. The peak of the actinides occurs around 10^7 years.

After 500 m the peak of the Cs-135 and Se-79 contribution is shifted to about 200,000 years, the peak of the actinide contribution to $2 \cdot 10^{-7}$ years. Due to the logarithmic scale Fig. 6-52 and Fig. 6-53 look quite similar.

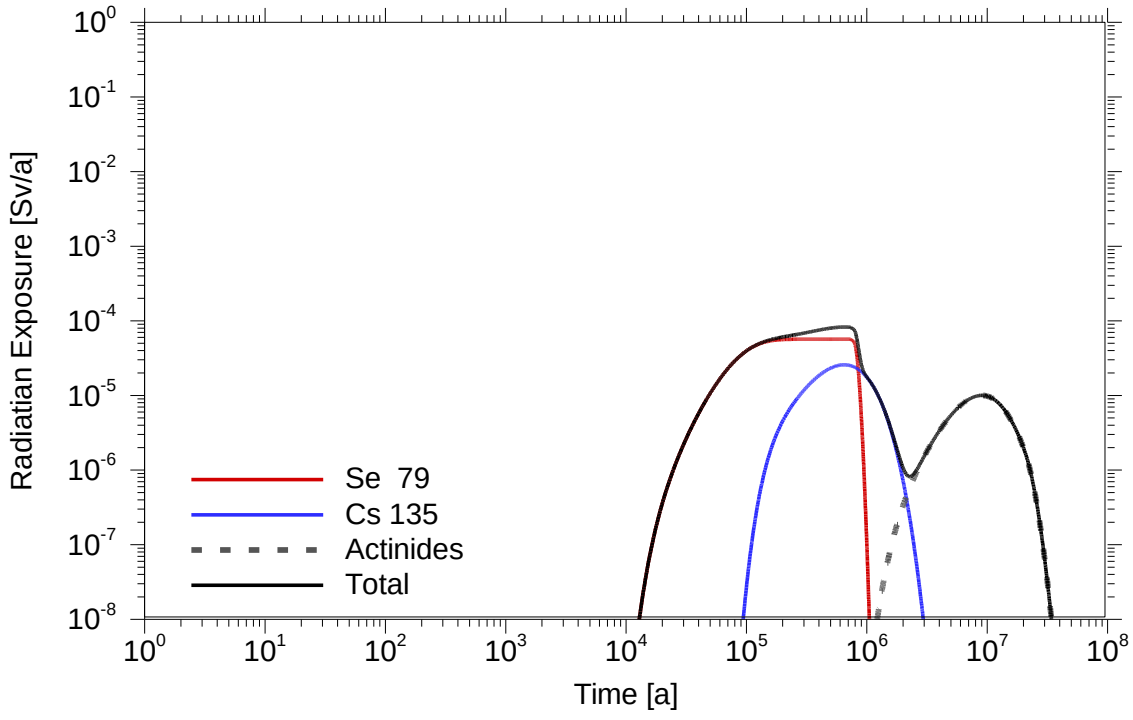

Fig. 6-51: The indicator “Annual radiation exposure” after an advective transport of 100 m through the host rocks

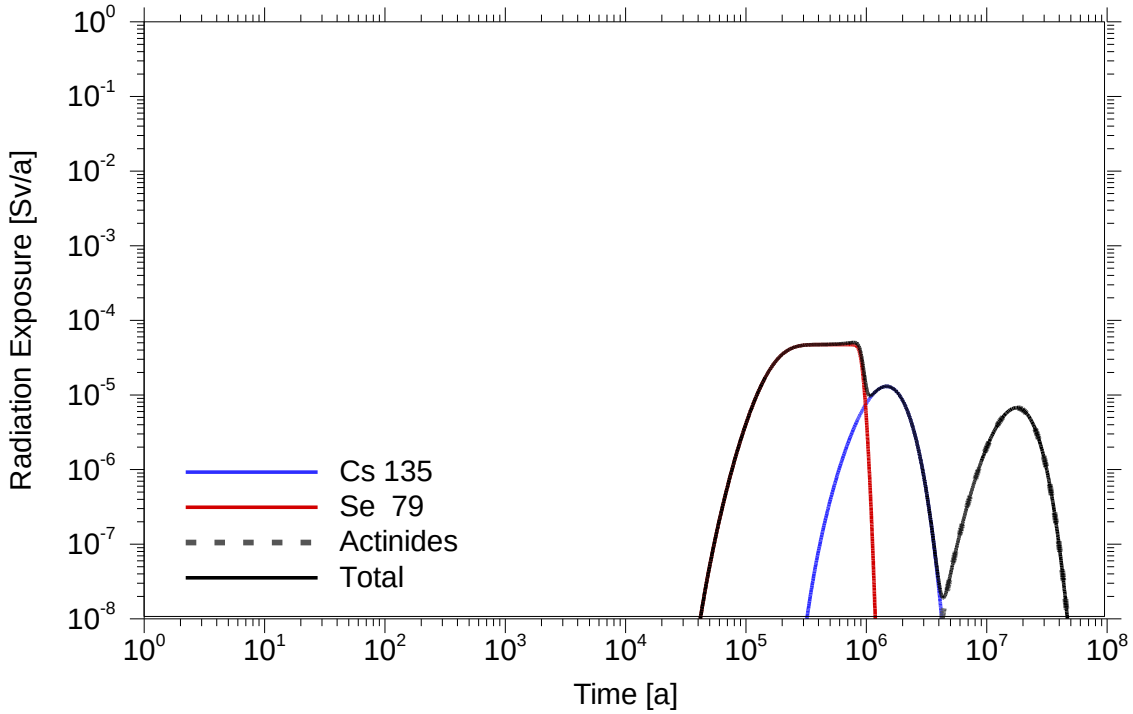

Fig. 6-52: The indicator “Annual radiation exposure” after an advective transport of 200 m through the host rocks

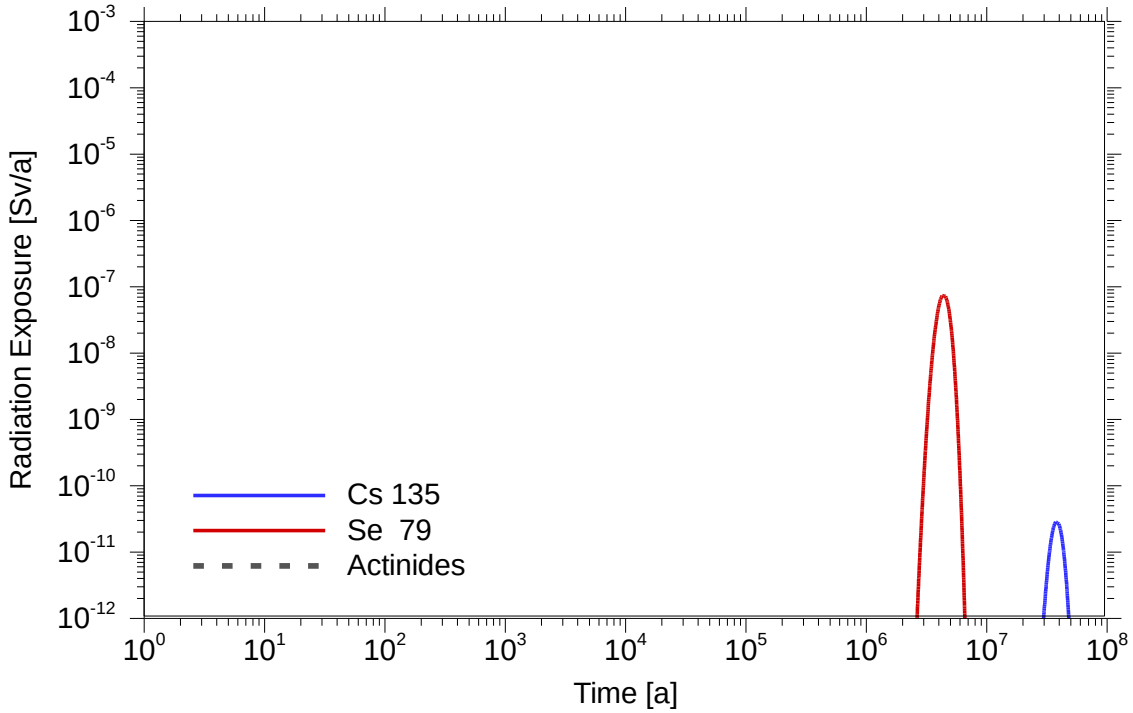

Fig. 6-53: The indicator “Annual radiation exposure” after an advective transport of 500 m through the host rocks

6.3 Sensitivity analysis

For the assessment of the long-term safety of a geological repository for radioactive waste, adequate handling of the various uncertainties within the system and the available data is essential. Performance Assessment includes a number of interacting physical and chemical effects, which leads to a non-linear, non-monotonic and sometimes even virtually non-continuous behaviour. A robust and reliable global sensitivity analysis of such models can be

a demanding task, which requires a sufficiently high number of runs with a good coverage of the parameter space. For the sensitivity analysis the following methods are used (Spießl & Becker, 2014):

- CSM (Contribution to Sample Mean) plots are obtained by sorting the model output values according to increasing values of the considered input parameter and then plotting the total contribution to the mean of the output versus the proportional size of increasing subsets. The more the curve deviates from the diagonal the higher is the sensitivity of the model against the respective parameter. A left-curved progression, normally below the diagonal, means a positive influence (parameter increase → output increase); a right-curved progression, normally above the diagonal, represents a negative influence (parameter increase → output decrease).

- SRRC (Standardized Rank Regression Coefficients) are calculated as the coefficients of a multilinear regression between the input and the output ranks. By the rank transformation the nonlinear, but largely monotonic model is better adapted to linear regression. Positive SRRC values mean a positive influence, negative values a negative influence.

- EASI stands for an effective algorithm for estimating sensitivity indices of first order. In contrast to the FAST/EFAST methods, which require specific frequency data for the input parameters, EASI can introduce these into existing sample sets. This is accomplished by sorting and shuffling the values of the different input parameters. The output is arranged according to the input data. The arranged data are then analysed using the power spectrum of the output as it is done in FAST/EFAST. A big advantage of EASI is that any sampling scheme can be applied, existing samples can be extended and model evaluations can be re-used.

6.3.1 Parameter distribution

The distributions of the random variables applied are uniform distribution functions, if no information about preferential values of the parameters is available, so each of the values within the bandwidth has the same likelihood to be applied in the calculation. For the porosity of the filling material and the aperture width of the fractures triangular distributions are chosen, since the values used in the deterministic calculations are already supported by site investigations.

All distributions of parameter values that are varying by significantly more than one order of magnitude logarithmic distributions are chosen.

To obtain the range for the distribution function the following assessment reports have been evaluated:

- SR-Can / SR-Site: Long-term safety for the final repository for spent nuclear fuel at Forsmark (SKB, 2011a-c)
- Kristallin-I: Safety Assessment Report (NAGRA, 1994a-c)
- Swiss Sorption Data Bases (Bradbury et al., 2010)
- H12: Project to establish the scientific and technical basis for HLW disposal in Japan (JNC, 2000)
- SPA: Spent Fuel Performance Assessment for a hypothetical repository in crystal-line formations in Germany (Lührmann et al., 2000)

6.3.1.1 Near-field

Container lifetime: The mean container lifetime is varied between 1 and 5000 years. In the model an instantaneous failure of all containers is conservatively assumed. A more advanced failure function is currently not implemented in the near-field model CLAYPOS.

Mobilisation rate: A higher mobilisation rate of a factor 10 is assumed due to the fact that phosphate glass can have a higher mobilisation rate than borosilicate glass (Anderson et al., 2000).

Solubility limit Se: Limiting phase depends on the geochemical conditions. Range varied from 10^{-6} to 10^{-4} mol/m^3 for granitic rock under reducing conditions (Duro et al., 2006). The conservative value of $6 \cdot 10^{-4}$ applied in SPA is used as upper limit.

Solubility limit U: UO_2 is the limiting phase. Range from $3 \cdot 10^{-7}$ to 10^{-1} mol/m^3 (Duro et al., 2006). This range covers the values used in other investigations.

Solubility limit Th: ThO_2 is the limiting phase. Range from $4 \cdot 10^{-6}$ to $5 \cdot 10^{-3}$ mol/m^3 (Duro et al., 2006). This range covers the values used in other investigations.

Solubility limit Ra: $RaSO_4$ is the limiting phase. Range from 10^{-6} to 100 mol/m^3 in (Duro et al., 2006). In Kristallin-I a value of 10^{-7} mol/m^3 proposed, this is applied as lower limit. For H12 a lower value of 10^{-9} mol/m3 is proposed for the reference case. Here it is argued that the values in observed concentrations in groundwater are not higher than 10^{9} mol/m^3 and that this value is conservative.

Solubility limit Np: $Np(OH)_4$ is the limiting phase. Duro et al., (2006) propose a range from 10^{6} to 10^{-5} mol/m^3. In Kristallin-I and SPA the value of 10^{-7} is proposed. This value is used as lower limit.

Sorption coefficient Cs: SR-Site proposes a range from 0.015 - 0.56 m^3/kg. The conservative value (0,001 m^3/kg) proposed by Stenhouse (1993) is used as lower limit.

Sorption coefficient U(VI): SR-Site proposes a range from 0.5 - 18 m^3/kg. For U(IV) the range is 3.6 to 1113 m^3/kg. In order to be conservative the range for U(VI) is used.

Sorption coefficient Th: SR-Site proposes a range from 6 - 700 m^3/kg. The conservative value proposed by Stenhouse (1993) is 0.5 and is used as lower limit.

Sorption coefficient Ra: SR-Site proposes a range from 0.0007 – 0.027 m^3/kg. This range covers the values used in other investigations and is used for the probabilistic calculations.

6.3.1.2 Near-field and far-field

Groundwater Flow: The groundwater flow is site-specific and is not transferable from other repository sites in granitic rock. The value is preliminary varied over two orders of magnitude. Results from the groundwater modelling with d^{3}f will be applied.

6.3.1.3 Far-field

Fracture Density: The fracture density is not transferable from other repository sites in granitic rock. The value is varied over three orders of magnitude for the probabilistic calculations.

Porosity (filling material): The average porosity of the filling material due to site investigations is about 40%. This value is used as peak value of a triangular distribution. The lower and the upper limit illustrate a range of possible values.

Matrix porosity: The average porosity of the rock matrix due to site investigations is about 1%. This value is used as peak value of a triangular distribution. The lower and the upper limit illustrate a range of possible values (e.g. JNC (2000) uses a range of 1 - 3%)

Penetration depth: JNC (2000) proposes a range of 0.03 to 1 m. The maximum value given by SR-Site (12.5 m) is used as upper limit. The lower limit is estimated to 0.1 m.

Aperture width: The average aperture width due to site investigations is about 0.05 m. This value is used as peak value of a triangular distribution. The lower and the upper limit illustrate a range of possible values.

Sorption coefficient Cs: SR-Site proposes a range from 0.000035 - 0.0035 m^3/kg. The realistic value proposed by Stenhouse (1993) is 0.1. The value 0.05 proposed by JNC (2000) with a range of 0.001 to 10 m^3/kg. The sorption coefficient for Cs for crystalline rocks and intermediate groundwater conditions (pH, ionic strength) is 0.26 m^3/kg (Bradbury et al. 2010). This value is used as upper limit. (For high ionic strength the sorption coefficient is 1.4 m^3/kg).

Sorption coefficient U(VI): SR-Site proposes a range from $5 \cdot 10^{-6}$ – 0.002 m^3/kg. For U(IV) the range is 0.0284 – 0.98 m^3/kg. The realistic value proposed by Stenhouse (1993) is 1 m^3/kg and is used as upper limit (10 in H12).

Sorption coefficient Th: SR-Site proposes a range from 0.00284 - 0.984 m^3/kg. The conservative value proposed by Stenhouse (1993) is 1 m^3/kg and is used as upper limit (A value of 10 m^3/kg is used in H12).

Sorption coefficient Ra: SR-Site proposes a range from $3.9 \cdot 10^{-5}$ - 0.0015 m^3/kg. The realistic value proposed by Stenhouse (1993) is 0.5 m^3/kg and is used as upper limit. This value is also used by H12 as upper limit.

The parameter distributions are summarized in Tab. 6.31. The solubility limits and sorption coefficients of the actinides are dependent parameters due to their similar chemical behaviour.

Tab. 6.31: Parameter distributions for the probabilistic calculations

Parameter		Bandwidth		Distribution function
		lower limit	upper limit	
Near-field	**Container lifetime [a]** TLifeCont	1	5,000	log. uniform
	Mobilisation rate MobRate	$5.0 \cdot 10^{-4}$	$5.0 \cdot 10^{-3}$	uniform
	Solubility limit Se [mol/m³] SolLimSe	10^{-6}	$6 \cdot 10^{-4}$	log. uniform
	Solubility limits U, Th, Ra, Np [mol/m³] SolLimU	U: $3 \cdot 10^{-7}$ Th: $4 \cdot 10^{-6}$ Ra: 10^{-7} NP: 10^{-7}	U: 10^{-1} Th: $5 \cdot 10^{-3}$ Ra: 100 NP: 10^{-5}	log. uniform
	Sorption coefficient Cs [m³/kg] SorpCsBen	0.001	0.56	log. uniform
	Sorption coefficients U, Th, Ra [m³/kg] SorpUBen	U: 0.5 Th: 0.5 Ra: 0.0007	U: 18 Th: 700 Ra: 0.027	log. uniform
	Groundwater flow [m³/a] FlowGw	0.1	10	log. uniform
Far-field	**Fracture density [m/m²]** DensFrac	0.01	10	log. uniform
	Porosity (filling material) [-] PorFM	0.05	0.5	triangular
	Matrix porosity [-] PorMat	0.001	0.05	uniform
	Penetration depth [m] PenDep	0.1	12.5	log. uniform
	Aperture width [m] Apert	0.01	0.2	triangular
	Sorption coefficient Cs [m³/kg] SorpCsG	0.000035	0.26	log. uniform
	Sorption coefficients U, Th, Ra [m³/kg] SorpCsU	U: $5 \cdot 10^{-6}$ Th: 0.003 Ra: 0.00004	U: 1 Th: 1 Ra: 0.5	log. uniform

6.3.2 Results

The three applied sensitivity methods show similar results giving confidence that the identified parameters are of high importance for further investigations. According to these methods the most important parameters are (Fig. 6-54 to Fig. 5-56):

- CSM: Groundwater flow (FlowGW), sorption coefficient of Cs for the gneissic rock (SorpCsG) and bentonite (SorpCsBent) and the penetration depth (PenDep)
- SRRC: Groundwater flow (FlowGW), sorption coefficient of Cs for the gneissic rock (SorpCsGand the penetration depth (PenDep)
- EASI: Groundwater flow (FlowGW), sorption coefficient of Cs for the gneissic rock (SorpCsG) and bentonite (SorpCsBent)

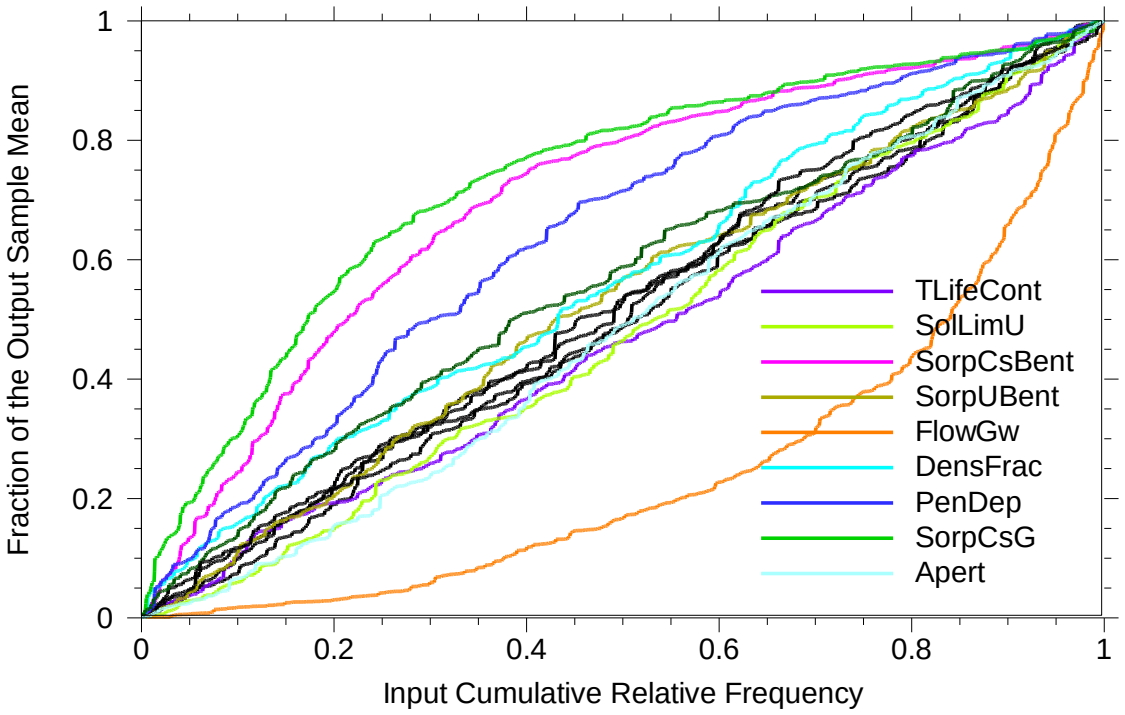

Fig. 6-54: Parameter sensitivity: CSM plot, parameter names are explained in Tab. 6-31

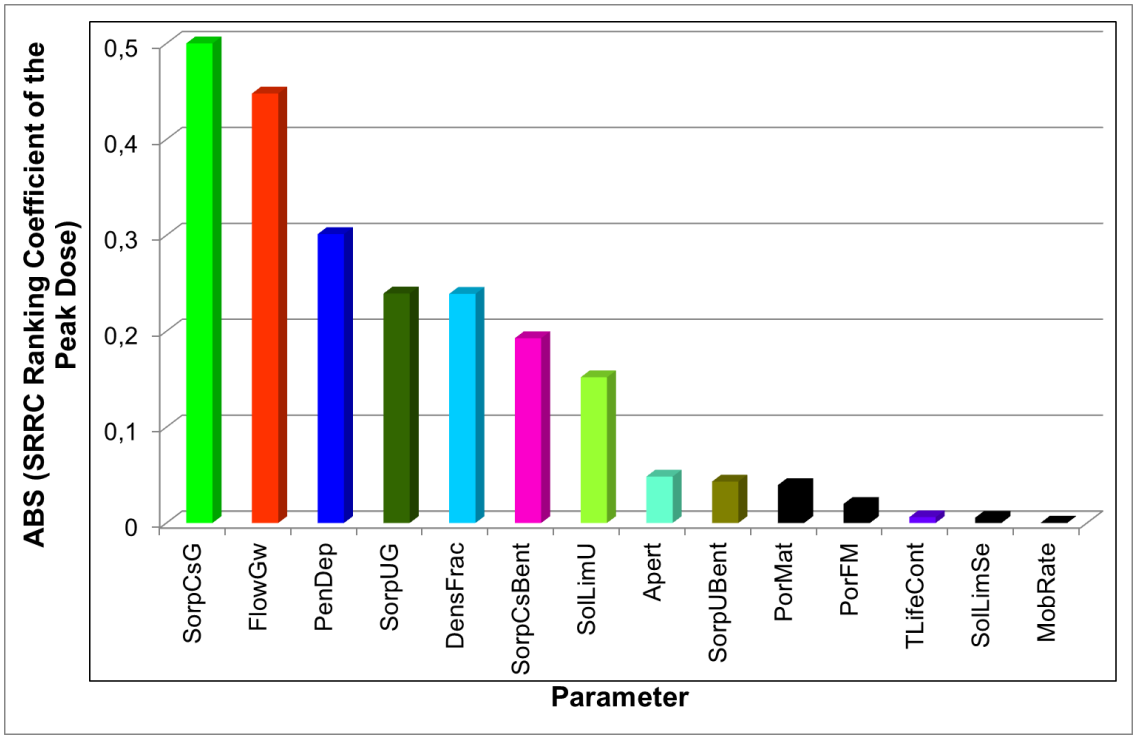

Fig. 6-55: Parameter Sensitivity: SRRC Ranking coefficients, parameter names are explained in Tab. 6-31

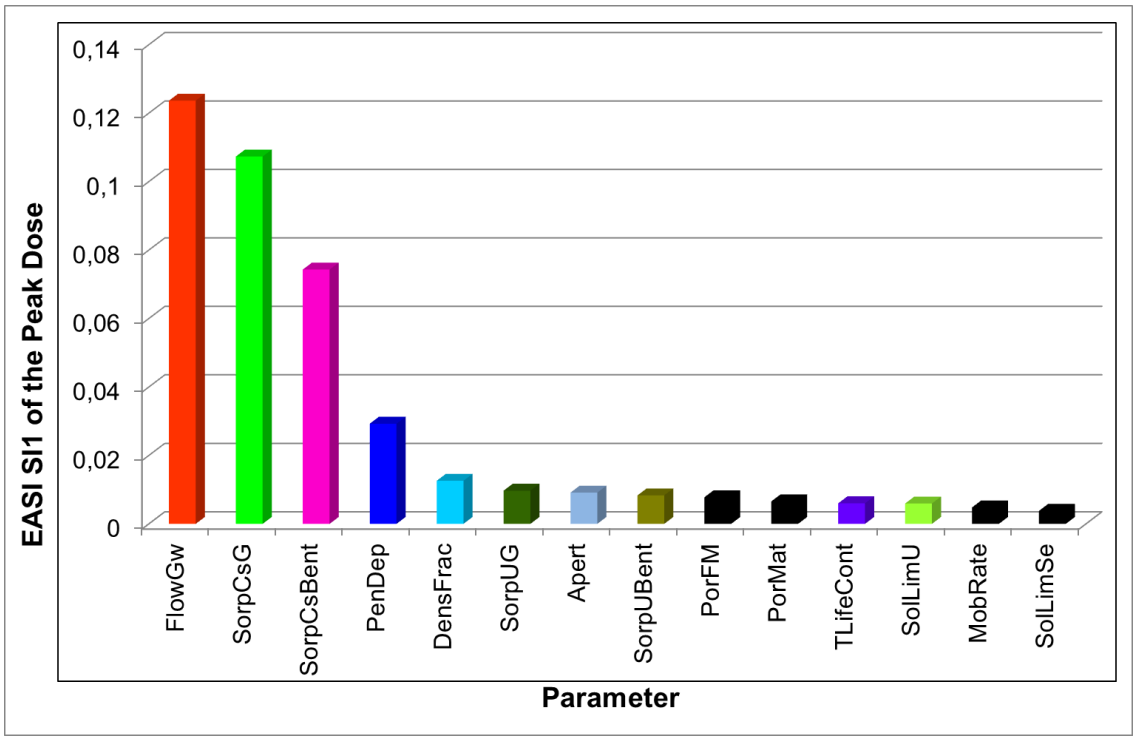

Fig. 6-56: Parameter Sensitivity: EASI, parameter names are explained in Tab. 6-31

7 Summary and recommendations

This report provides a condensed overview of the manifold site-specific safety investigations regarding HLW disposal in crystalline host rocks. The investigations were performed by BGR, GRS, and DBE TECHNOLOGY GmbH in the past years in close cooperation with VNIPI PT and other Russian organizations involved in the investigation of the Yeniseysky site near Zheleznogorsk in the Krasnoyarsk region.

The investigations focused mainly on major long-term safety aspects of HLW disposal in crystalline rocks, in particular on the performance of the geologic and engineered barrier system. It was not intended to perform a comprehensive preliminary safety analysis; however, these investigations address a wide range of issues that need to be considered in a safety analysis, and the results can be used as guidance for necessary future investigations. Although uncertainties remain, they did not indicate any obstacles regarding the feasibility of safe HLW disposal at the considered site but offered several favourable site features.

Corresponding recommendations for future investigations are outlined below in more detail.

Repository concept

From the perspective of the repository concept, which in principle provides a useful structure, the performance and durability of the bentonite-cement mixture that is proposed as a novel material for sealing drifts and other underground cavities in order to prevent radionuclide transport from the HLW repository to the biosphere remains to be demonstrated. The negligibility of undue influences, which may be caused by the proposed co-disposal of ILW in access drifts above and below the emplacement boreholes for HLW disposal, remains to be demonstrated as well. Alternatively, sufficient isolation of ILW disposal in separate drifts and/or a separate part of the repository can be considered.

Geology

In the course of the geological exploration of the Yeniseysky site during the last years, comprehensive new site-specific data concerning the geological structure and the hydrogeological conditions as well as the barrier properties of the potential host rocks have been gathered. Already in earlier phases of collaboration, a geological 3D model of the Yeniseysky site was prepared by BGR in close cooperation with VNIPI PT based on the geological-geophysical exploration data (especially on seismic and gravimetric data). Integration of recently obtained new data into the geological 3D model will refine the knowledge about the geologic-tectonic structure of the Yeniseysky site.

The long-term safety assessment for a HLW repository requires extensive knowledge about the tectonic structure of the region. Thus, exploration of fault zones and fractured rocks as well as modelling of the vertical and horizontal movements of the geologic units where the construction of the repository is planned is essential. Several regional fault zones were identified in the study area from aerial photographs and from seismic, gravimetric and geoelectric data. However, the precise position and spatial orientation of fault zones is mostly uncertain due to an inconsistent data base. The regional investigations have shown that the rates of relative movement of the blocks on either side of faults in the Yeniseysky area vary between 0.077 and 0.3 mm/a. Radon and helium measurements do not indicate recent tectonic activity. It is assumed that the majority of faults was filled by dykes and shows no recent tectonic activity.

The long-term monitoring of seismic activity and the geomorphological studies in the region verify that the potential repository site lies in a stable platform region with low seismic and neotectonic activity and a low tendency of uplift. Uplift will occur very slowly and will have only a minimal effect on the stability and hydraulic properties of the rock massif. The systematic records of seismic activity in the region from 1963 to the present show a complete absence of earthquakes with a Richter-scale magnitude greater than 5 in the Krasnoyarsk region. In-situ studies in excavations of the MCC Zheleznogorsk confirm the assignment of the study area to a stable, seismically inactive platform region.

The rocks of the Yeniseysky site are heterogeneous (frequently alternating lithologies) and usually exhibit multi-phase metasomatism. The contacts of gneisses with intrusive bodies in the Yeniseysky area show an especially strong metasomatism. Microscopic analyses were conducted to determine the degree of metasomatism and to assess the influence of alteration on the petrophysical properties. Weathering has formed smectite, illite-smectite, kaolinite, and sometimes vermiculite in most of the samples collected near the ground surface. The occurrence of these clay minerals in the altered samples increases the sorption capacity of sorption of radionuclides on the geologic barrier. Altered samples from greater depths contain secondary sericite, chlorite, and carbonate. Talc was identified by radiography in the gabbro-diabase.

Textures and properties of rocks of the Yeniseysky site are typically associated with elevated anisotropies. The microstructural and ultrasonic data show that the rocks are mostly heterogeneous, besides relatively homogenous, low-fractured gneissic rocks. The gneisses of the region Yeniseysky belong to relatively hard rocks and the metadolerite to the category of hard to very hard rocks.

The rocks of the gneiss complex generally have a good thermal conductivity due to the relatively high contents of good heat-conducting minerals such as quartz, feldspar, and amphibole (in the basic rocks). Those parts of the complex with high mica content have a significantly lower thermal conductivity, which can lead to heat accumulation if these parts are large enough. For this reason, the spatial distribution of gneissic rocks with high mica content must be well-mapped during the geological exploration of the repository site.

The host rocks represent a heterogeneously composed gneissic complex that is penetrated by numerous steeply dipping basic dykes. The fissure zones that were identified during the geological exploration of the region have a thickness of 1 to 4 cm and a dip angle of 15 to 35°. In all cases the fissures are filled with carbonate and feldspars and rarely with quartz.

Lithology and hydraulic parameters of contact zones of gneisses with intrusive bodies (dykes) are of particular interest. At present, a detailed lithological and hydraulic characterization of the contacts, fault zones and fractures is missing. Measurements of the hydraulic permeability of the individual fault zones or of the contact zones between different types of rocks (e.g., gneisses in contact with basic veins) have not been conducted due to a lack of suitable instruments. Owing to missing systematic and detailed data from boreholes, especially from fault zones and from lithological contacts, nothing can be said about the distribution and frequency of these rocks and alteration types, or about age relationships. For the safety analysis of the potential repository site, these zones (the contact of gneisses with intrusive bodies and dykes) should be specifically looked for and characterized in detail.

Temperature and displacement analyses

Preliminary repository layout variants have been provided by VNIPI PT that were to be evaluated with regard to the temperature evolution. For three main variants, 3D numerical simulations have been performed that focused on the evaluation of the buffer temperature.

Based on the data provided by VNIPI PT on the heat release from the containers, the maximum temperature in the bentonite buffer in all variants was below 120°C. The time period during which the temperature in the bentonite is higher than 100°C is only about 110 years. Neither the maximum value nor the time period with high temperatures gives rise to the assumption that the barrier integrity is jeopardized.

It should be pointed out that new research results concerning microbial corrosion activities on waste containers have become available. These investigations show that a temperature increase in the bentonite buffer leads to a significant reduction of the corrosion activities of microbes because microbes become inactive or die at temperatures of more than 122°C. At the same time, earlier research results on the mineralogical alteration of swellable clay minerals recommend not to exceed a maximum temperature of 150°C – at least not for decades.

Assuming a successive instead of a simultaneous loading of the emplacement boreholes, the maximum temperature in the entire field will be more or less identical. The main difference is the point in time when the maximum temperature is reached at a specific borehole. This time is delayed in case of a successive loading, and the delay depends on the location of the borehole in the emplacement field. In addition to delaying the maximum temperature occurrence, the successive loading leads to a shift of the starting points of the temperature increase and to a slight change in the shape of the temperature curves.

Prior to the thermal investigations of the recently provided disposal concept, an indicative analysis had been performed regarding the integrity of a bentonite buffer. Due to the thermal expansion of the gas and water in and around the buffer, the gas pressure may increase significantly. A careful design of the compacted buffer can avoid gas pressures that may jeopardize the buffer integrity by creating artificial pathways.

An earthquake may be strong enough to cause displacements on secondary faults at certain distances to the fault initiating the earthquake. In case these secondary faults are next to an emplacement borehole, a shear deformation of container and buffer cannot be excluded. Indicative calculations of earthquake-induced shear deformation show that observed and recorded earthquakes in the vicinity of the investigated site were not strong enough or much too far away to induce shear deformations that could jeopardize the container integrity.

Groundwater flow and radionuclide migration

The new exploration data concerning the permeability of the rocks in the Yeniseysky site show that from the earth surface to depths of 700 m impermeable rocks with filtration coefficients smaller than 0.005 m/d are dominant. Very low water content and very low permeability of the rocks are typical for the rock massif. All values of the filtration coefficient K_f obtained in situ for the studied rocks allow the attribution of these rocks to water impermeable rocks according to GOST (2011). According to exploration data, the massif has no permeable, water conducting layers or zones and also no “underground water lenses” and fracture zones along which surface water can reach the underground excavations. The zones of tectonic fracturing are substantially filled with dykes of intrusive rocks or with secondary minerals. These zones do not have any increased filtration coefficients and cannot serve as hydraulic pathways connecting the disposal level for HLW with the earth surface. Weak water conducting intervals are present only locally and only higher than the local drainage basis, approx. 150 m above the level of the planned repository. But hydraulically active fractures were observed even down to the bottom of the 100- and 600m-deep boreholes.

A detailed investigation of the hydrogeological situation of the local and regional flow systems is crucial for a reliable safety assessment of a potential repository site. The investigations show very low porosities and permeabilities. Laboratory tests of the open porosity show that the average porosity is 0.33 % and never more than 1 %.

The low porosity of the gneisses and the groundwater flow direction, which is directed downwards and to the northeast according to the dip direction of the dykes, are advantageous properties of the system regarding the construction of a repository for radioactive waste. The flow velocity decreases with depth. Despite the advantageous properties of the flow system, transported substances will eventually reach the surface after transiting the intermediate or regional flow system. To know the transport distances and travel times, it is important to know the appropriate flow system, especially the regional discharge and recharge system.

Some hydrogeological parameters specific for the region should be refined. The amounts of precipitation and groundwater recharge should be determined for the specific location and should not be derived from similar locations, because they are site-specific and highly variable parameters. For a more realistic simulation of the groundwater flow, the pressure distribution (hydraulic heads) within the different hydrogeological units and within the contact zones should be known in order to define the model boundaries.

Reliable values for the travel times of radionuclides can only be determined based on reliable data for the different hydrogeological units. The groundwater velocity measured at the site seems to be very high, if Darcy flow is assumed only through a porous medium with a porosity of 0.0035. The resulting advective velocity would be 0.8 m/year. The comparison of in-situ test and laboratory test show that the contribution of the matrix permeability to the overall permeability of the rock mass is quite low. A groundwater flow through a system of fractures is probable but such a system has not been detected so far. The approach chosen here to estimate the effective porosity to 0.01 is probably quite conservative. A more detailed investigation of the fracture system at repository depth, e.g. in the planned URL, will help to characterize the fracture system and to reduce conservative assumptions in the calculations.

Due to the lack of some relevant information, many calculations and prognoses must be carried out based on conservative assumptions. In this case, the geologic barrier will not be able to fully implement its protective functions, so that the importance of the geotechnical and technical barriers increases. Consequently, the repository concept should be adapted. For a comprehensive evaluation of the potential suitability of the investigated area, further investigations are necessary. The underground laboratory within the study area will help to obtain some of the relevant data mentioned above.

Radionuclide release

The calculations considering radionuclide release and migration reveal that the inventory and sorption of radionuclides are of major importance for the safety analysis of the HLW repository. Comparing the spectrum of radionuclides considered in these calculations with the spectrum of vitrified waste from La Hague, it can be concluded that more radionuclides can be expected, among them activation and fission products that could be relevant for the long-term safety, such as Cl-36 or I-129. Of the radionuclides considered so far, the following play a dominant role in the long-term safety considerations: Cs-135, Se-79, Ra-226 and Np-237 (Am-241). Of minor importance are Tc-99 and isotopes of Pu, Th and U. Additional information about the sorption coefficients of the host rocks for the dominant radionuclides will help to improve the safety analysis.

Outlook

Due to the incomplete geological exploration and lack of some data needed for a complete safety analysis, some beneficial statements and assumptions have been made. Additional studies will help to analyse the robustness of the repository system and to improve the repository concept. In this regard, information about the fault zones and fracturing of the rocks is of particular significance. The knowledge about the position and spatial orientation of the fault zones and also studies on fractures in the host rocks are important for the hydraulic characterization of the rocks, the characterization of the groundwater flow and the evaluation of radionuclide transport.

Only limited information is available about the distribution and hydraulic properties of the fault zones and the connections between them in the area of the planned repository. There is no permeability and porosity data for fault zones themselves. Nevertheless, the presence of zones with significantly higher permeability cannot be excluded. Most probably, large parts of the groundwater do not flow through the porous rock medium but through a system of fractures. Knowledge about the distribution of fractures and porosity of the filling material are also important because of its impact on the flow velocity and the sorption capacity. For this reason further investigations to this issue are recommended.

Even though all investigations were specific to the site, the majority of the results obtained regarding the applicability of the safety assessment approaches and tools used can be transferred to other HLW disposal projects in magmatic host rocks. This also applies to the lessons learned regarding an appropriate improvement of the required database with data on the waste and on the geologic structure.

8 References

Alkan, H., & Müller, W. (2007). Investigations on canister corrosion, resulting gas production and impact on surrounding bentonite buffer (in Germ.). Untersuchungsbericht, ISTec GmbH, Köln.

Anderson, E. B., Aloy, A. S., Burakov, B. E., & Jardine, L. J. (2000). Immobilization of Pu-containing wastes into glass and ceramics: results of US-Russia collaboration. In Plutonium Futures - The Science, Conference Transactions, American Institute of Physics. Pillay, K. K. S. and Kim, K. C.

Anderson, E. B., Dazenko, V. M., & Kedrovskij, O. L. (1993). Geological investigations on the territory of the southern part of Yeniseysky Ridge, as a justification for the option for secure final disposal of solidified high-level-waste (HLW) from the plant RT-2 in the deep geological formations (Generalization and analysis of the literature from the archive material and from the results of field-geological investigation works) (in Russ.). unpublished.

Anderson, E. B., Shabalev, S. I., & Savonenkov, V. G. (1998). Investigations of Nizhnekanskiy granitoid massif (Middle Siberia, Russia) as a promising site for deep geological disposal of HLW. Proc. of Internat. Conf. on Rad. Waste Disp., DisTec 98, Hamburg, 105-110, (S. 105-110).

Anderson, E., Belov, S., Kamnev, E., Kolesnikov, I., Lobanov, N., Morozov, V., et al. (2011). Underground isolation of the radioactive waste (in Russ.). Moscow.

Artjushkov, E.V. (1969): Quaternary Glaciations and transgressions in the West Siberia (in Russ.). In: Izvestiya (Messages) of Academy of Sciences of UdSSR. Geological series Nr. 7. pp. 98-114

Arzhannikov, S. G., Gavrilyk, T., & Semenov, R. M. (2004). Late Quaternary geodynamic and impulse tectonic movements within the influence zone of Kansky fault system (S-W Sebirischer platform) (russ.). Geology and Geophysics, 45(4), 430-442.

Astakhov, V. (2003): Middle Pleistocene glaciations of the Russian North. In: Quaternary Science Reviews. Volume 23, Issues 11-13, pp. 1285-1311.

Autodesk. (2011). Autodesk, Drawing Interchange File Format (DXF), release 2010, 2011.

Bäckblom, G., La Pointe, P., & Tullborg, E.-L. (2004). Preliminary study for developing a practical, stepwise field methodology for determining the acceptable proximity of canisters to fracture zones in consideration of future earthquakes. Tech. rep., SKB.

Bates, J., Bradley, C., Buck, E., Cunnane, J., Ebert, W., Feng, X., et al. (1994). High-level waste borosilicate glass: a compendium of corrosion characteristics, Volume II. Tech. rep., United States Department of Energy, Office of Waste Management, USA.

Belov, S. M. (2007). Investigation of the structure and geodynamical evolution of the Nizhekansky massif with regard to disposal of the radioactive high- level-waste (HLW) (in Russ.). Geoekologija, Moskau, 3, 248-266.

Beygul, V. (2013). Initial data for modelling of real conditions of hot HLW burial, unpublished.

Beygul, V. (2014). Notice in writing about synthetic seismograms valid for the Krasnoyarsk region. unpublished.

Beygul, V., A.A., M., & V.V., O. (2011). Mathematical modeling and substantiation of a long stability of the underground horizontal workings of the RE underground disposal (in Russ.). unpublished.

Biggs, J. M. (1964). Introduction to structural dynamics. New York: McGraw-Hill.

Billaux, D. (2007). Evaluation of seismic-induced shear ddeformation around a canister. Tech. rep., DBETEC and Itasca.

Bradbury, M., Baeyens, B., & Thoenen, T. (2010). Sorption Data Bases for Generic Swiss Argillaceous, Crystalline and Calcareous Rock Systems. Tech. rep., Paul Scherrer Institut PSI, Villingen, Schweiz.

Burmistrov, A., Starostin, V., Dergachev, A., & Petrov, V. (2009). Structural petro-physical analysis of natural resources deposits (in Russ.).

Busch, K.-F., Luckner, L., & Tiemer, K. (1993). Geohydraulik, Lehrbuch der Hydrogeologie, Band 3. Gebrüder Bornträger, Berlin/Stuttgart (in Germ.).

Cedercreutz, J. (2004). Future climate scenarios for Olkiluoto with emphasis on permafrost. Posiva 2004 – 06. Posiva report Olkiluoto, Finland.

Chowdhury, I., & Dasgupta, S. (2003). Computation of Rayleigh Damping Coefficients for Large Systems. The Electronic Journal of Geotechnical Engineering, 8.

Coppersmith, K., & Youngs, R. (2000). Data needs for probabilistic fault displacement hazard analysis. Journal of Geodynamics, 29, 329-343.

Cundall, P., Hansteen, H., Lacasse, S., & Selnes, P. (1980). NESSI – Soil Structure Interaction Program for Dynamic and Static Problems. Technical Report, Norwegian Geotechnical Institute.

Duro, L., Grivé, M., Cera, E., Gaona, X., Domènech, C., & Bruno, J. (2006). Determination and assessment of the concentration limits to be used in SR-Can. Tech. rep., SKB.

Eberhardt, E. (2012). The Hoek–Brown Failure Criterion. Rock Mech. Rock Eng., 45, 981-988.

Engelmann, H. J., & Müller-Hoeppe, N. (1992). Linsourprepost - Verification, validation and error estimation. Technical Report, DBE, Peine.

ESRI (2010). ArcMap, version 10.0.

Eurocode 7 (2009): Entwurf, Berechnung und Bemessung in der Geotechnik – Teil 1: Allgemeine Regeln. Deutsche Fassung DIN EN 1997-1:2004 + AC:2009.

Eurocode 0 (2010): Grundlagen der Tragwerksplanung. Deutsche Fassung DIN EN 1990:2002 + A1:2005 + A1:2005/AC:2010.

Fein, E. (2004). Software Package r3t. Model for Transport and Retention in Porous Media, (in Germ.), GRS-192, BMWA-FKZ 02E9148/2. Gesellschaft für Anlagen- und Reaktorsicherheit (GRS) mbH, Braunschweig, 319 p.

Fein, E., & Schneider, A. (1999). d³f – A program package for modelling density-driven flow (in Germ.) GRS-139, BMBF-FKZ 02C04650, Gesellschaft für Anlagen- und Reaktorsicherheit (GRS) mbH, Braunschweig, 245 p.

GOST (2011). GOST 25100-2011 Soils Classification; Russian National Standards.

Grape (2011). Grape Software 2011, University of Bonn and University of Freiburg.

Gruner, M., Rumphorst, K., & Sitz, P. (2008). Design and Emplacement of Bentonite Barriers. International Conference Underground Disposal Unit Design \& Emplacement Processes for a Deep Geological Repository. 16-18 June 2008, Prague.

Gunnarsson, D.; Börgesson, L.; Hökmark, H.; Johannesson, L.-E.; Sandén, T. Äspö Hard Rock Laboratory - Report on the installation ofthe Backfill and Plug Test, IPR-01-17, SKB, Stockholm, 2001

Gupalo, T., Seleznev, N., Gupalo, V., Zhidkov, V., & Zuikov, A. (1999). Behaviour of natural and engineered barriers under continuous thermal effects in storage and final disposal of radioactive wastes in geologic formations. Radioactive Waste Management and Environmental Remediation - ASME.

Gupalo, T. (2003). Evaluation of the thermo-mechanical impacts to the rocks in the underground constructions of the mining-chemical combine (in Russ.), unpubl. scientific report, VNIPI Promtechnologii. Tech. rep., VNIPIPT.

Gupalo, T., Milovidov, V., Prokopova, O., Shvez, S., Moskalischin, V., Sibgatulin, V., et al. (2004). Results of the geological geophysical and engineer-geological investigations in the region „Yeniseysky“ within the Nizhnekansky granitoid massif (in Russ.). Safety of nuclear technologies: Radioactive waste management, Proceed., PRoAtom, St. Petersburg, (S. 184-187).

Gupalo, T., Milovidov, V., Romanov, V., Lind, E., Besprozvannjh, A., Hudoberdin, I., et al. (2007). Evaluation of hard rock isolating properties for long-lived RW final isolation. II. Internat. Atomkern-Forum, GROZ, St. Petersburg, (S. 126-132).

Gupalo, T., Sokolovskij, L., Poljakov, V., & Milovidov, V. (2004). Hydrogeology of the Nizhnekansky massif (in Russ.). Exploration and protect of the natural resources, 10, 53-58.

Gvishiani, A. D., Belov, S. V., Agayan, S. M., Rodkin, M. V., Morozov, V. N., Tatarinov, V. N., et al. (2008). Methods of artificial intellect in assessment of tectonic stability of Nizhnekansky massif (in Russ.). Moscow.

Herold, P. & Jobmann, M. (2015). Conceptual design of a sealing system for a HLW repository in crystalline rocks, Technical Report, DBE TECHNOLOGY GmbH, Peine.

Herold, P., & Müller-Höppe, N. (2013). Safety demonstration and verification concept - Principle and application examples -. Technical Report, DBE TECHNOLOGY GmbH.

Hoek, E., & Brown, E. (1997). Practical estimates of rock mass strength. International Journal of Rock Mechanics and Mining Sciences, 34(8), 1165-1186.

Hoek, E., & Marinos, P. (2007). A brief history of the development of the Hoek-Brown failure criterion. Soils and Rocks, 2, 1-13.

Hoek, E., Carranza-Torres, C., & Corkum, B. (2002). Hoek-Brown failure criterium - 2002 edition. Proc. NARMS-TAC Conference, 1, S. 267-273. Toronto.

ISC-Bulletin 2001 ISC-On-line Bulletin. International Seismological Centre, Thatcham, United Kingdom (2001), (see at: HTUwww.isc.ac.uk/BullUTH)

Itasca (2005). FLAC3D Manuals.

Jain, V. (1998). Survey of solidification process technologies. Tech. rep., Center for Nuclear Waste Regulatory Analyses, San Antonio, Texas.

JNC (2000). Project to establish the scientific and technical basis for HLW disposal in Japan - Supporting report 3: Safety Assessment of the geological disposal system. Supporting Report, JNC.

Jobmann, M., Brewitz, W., Fahrenholz, C., Fein, E., Hammer, J., Keesmann, S., et al. (2008). Studies on the effectiveness of geological and geotechnical barrier systems with respect to the site selection in magmatic rocks (in Russ., in Germ.). BMWi-FKZ 02E9965 and 02E9975. Tech. rep., DBETEC, BGR, GRS.

JRC & DG-ENTR. (2008). The Eurocodes: Implementation and use, Booklet B1. The Eurocodes: Implementation and use, Booklet B1.

Jungblut, D. (2011). GISLab, version 0.01.

Keesmann, S., Noseck, U., Buhmann, D., Fein, E., & Schneider, A. (2005). Model calculations regregard long-term safety for repositories in salt and granite (in Germ.). GRS-206, BMWA-FKZ 02E9239. Gesellschaft für Anlagen- und Reaktorsicherheit (GRS) mbH, Braunschweig, 75 p.

Khaperskaya, A. V., & Kudryavtsev, E. G. (2008). Spent nuclear fuel management system in the Russian Federation, SNF stockpile and plans for reprocessing In: Spent fuel reprocessing options. IAEA. IAEA.

Kiefer, D. (10 1997). Sicherheitskonzept für Bauten des Umweltschutzes, DAfStb-Heft 481. Sicherheitskonzept für Bauten des Umweltschutzes, DAfStb-Heft 481. Berlin.

Knoll, P., Finder, M., & Kudla, W. (2010). Entwicklung eines Grundkonzeptes für langzeitstabile Streckendämme im leichtlöslichen Salzgestein (Carnallitit) für UTD/UTV, Teil 2 Errichtung von Funktionselementen, Teilbericht 7, Teutschenthal. Tech. rep.

Kolmogorova, P. P., & Kolmogorov, V. G. (2002). Recent vertical crustal movements in the Altai-Sayan province in relation to neotectonics and seismicity. Russian Geology and Geophysics, 43(6), 531-542.

Kolmogorova, P. P., & Kolmogorov, V. G. (2004). Recent vertical crustal movements in the region of Yenisei Ridge. Russian Geology and Geophysics, 45(4), 455-464.

Krone, J., Bollingerfehr, W., Filbert, W., Keller, S., Lommerzheim, A., Mönig, J., et al. (2013). Status of the safety concept and safety demonstration for an HLW repository in salt. Summary Report, DBE TECHNOLOGY GmbH, BGR, GRS.

Krone, J., Brewitz, W., Fahrenholz, C., Fein, E., Filbert, W., Gupalo, T., et al. (2005). Requirements for site exploration fpr HLW repositories in hard rock (in Germ., in Russ.). BMWA FKZ 02E9612 and FKZ 02E9622Abschlussbericht, DBETEC, BGR, GRS.

Kudla, W.; Dahlhaus, F.; Glaubach, U.; Gruner, M.; Haucke, J. (2009): Diversitäre und redundante Dichtelemente für langzeitstabile Verschlussbauwerke - Abschlussbericht, TU Bergakademie Freiberg, Freiberg,.

La Pointe, P., Wallmann, P., Thomas, A., & Follin, S. (1997). A methodology to estimate earth-quake effects on fractures intersecting canister holes. Tech. rep., SKB.

Laverov, N. P., Petrov, V. A., Velitschkin, V. I., & Poluektov, V. V. (2002). Petrophysical properties of granitoids of the Nizhnekansky massive: Toward the issue of the selection of the regions for the disposal of LAW and spent fuel (russ.). Geoecology, 4, 293-310.

Leydecker, G. (2005). Earthquake catalogue for Germany and adjacent areas for the years 800–2004, data file. Earthquake catalogue for Germany and adjacent areas for the years 800–2004, data file.

Li, S, & Jobmann, M. (2015). Potential EDZ extension at the planned repository site in the Krasnoyarsk region including seismic impact, Technical Report, DBE TECHNOLOGY GmbH, Peine.

Lührmann, L., Noseck, U., & Storck, R. (2000). Spent Fuel Performance Assessment (SPA) for a hypothetical repository in crystalline formations in Germany. GRS-154, BMWi-FKZ 02E8855, Gesellschaft für Anlagen- und Reaktorsicherheit (GRS) mbH, Braunschweig, 180 p.

Lukina, N. (2001). Justification of the tectonic stability of the northern part of NIzhnekansky granitoid massif (in Russ.), unpublished.

Lukina, N. V. (1996). Prognosis of the tectonic and geomorphological development of the northern part of Nizhnekansky granitoid massif for 10 000 years to 130 000 years in advance (in Russ.), unpublished.

Lukishov, B. G., Shwedow, N.P., Kuznetsov, N.V. & Ivanshenko, G.N. (2014): Thermomechanical aspects of the safety by the underground final HAW disposal in the geological formations. Speech, VNIPI Promtechnologii.

Lysmer, J., & Kuhlemeyer, R. L. (1969). Finite Dynamic Model for Infinite Media. J. Eng. Mech., 95(EM4), 859-877.

Makarchuk, T. F., Kurnosov, V. A., Dubrovsky, V. M., Tikhonov, N. S., Serov, A. V., & Samohotov, S. A. (1999). WWER reactor spent fuel treatment at the final stage of the fuel cycle. In: Status and trends in spent fuel reprocessing. Tech. rep., IAEA.

Makarchuk, T., & Kudryavtsev, E. (2005). Spent fuel treatment in the Russian Federation. In: Status and trends in spent fuel reprocessing. Tech. rep., IAEA.

Mangerud, J., Jakobsson, M., Alexanderson, H., Astakhov, V., Clarke, G.K.C., Henriksen, M., Hjort, C., Krinnerf, G., Lunkka J.-P., Moeller, P., Murray, A., Nikolskayai, O., Saarnisto, M. & Svendsen, J.I. (2004): Ice-dammed lakes and rerouting of the drainage of northern Eurasia during the Last Glaciation. In: Quaternary Science Reviews. Volume 23, pp. 1313-1332.

Marinos, V., Marinos, P., & Hoek, E. (2005). The geological strength index: applications and limitations. Bull. Eng. Geol. Environ., 64, 55-65.

Mazurek, M. (2010). Far-field process analysis and radionuclide transport modeling in geological repository systems. In Geological repository systems for safe disposal of spent nuclear fuels and radioactive waste. Ahn, J., Apted, M.J. (Ed.), Woodhead Publishing Series in Energy: Number 9, CRC Press, Boca Raton.

Meleshyn, A., & Noseck, U. (2012). Radionuclide inventory of vitrified waste after spent nuclear fuel reprocessing at La Hague. GRS-294, BMWi-FKZ 02E10548, Gesellschaft für Anlagen- und Reaktorsicherheit (GRS) mbH, Braunschweig, 149 p.

Middelhoff, M. (2015): Research program for a HLW-disposal site in crystalline rock: Collection of indications for the host rock characterization and the EBS demonstration - Bachelor thesis, TU Clausthal

Morozov, V. N., Rodkin, M. V., & Tatarinov, V. N. (2001). Consideration of the geodynamical safety of the objects of the nuclear fuel cycle (in Russ.). Geoecology, 3, 227-238.

Morozov, V., Kolesnikov, I., Belov, S., & Tatarinov, V. (2007). Stress and strain state of Nizhnekansky massif as a territory for potential disposal for radioactive waste (russ.) Geoecologica 6, Moskau.

Müller-Hoeppe, N., Buhmann, D., Czaikowski, O., Engelhardt, J., Herbert, H.-J., Lerch, C., et al. (2012). Integrität geotechnischer Barrieren - Teil 1 Vorbemessung. Technischer Bericht, GRS-287, DBE TECHNOLOGY GMbH, GRS, Peine, Braunschweig.

Müller-Hoeppe, N., & Krone, J. (1999). Ein neuer Ansatz zur Bewertung der Wirksamkeit von Barrieren im Endlager. Tech. rep., DBE TECHNOLOGY GmbH.

Nagra (1994a). Kristallin-I, Conclusions from the regional investigation programme for siting a HLW repository in the crystalline basement of Northern Switzerland. Tech. rep., Nagra.

Nagra (1994b). Kristallin-I, Results in Perspective. Tech. rep., Nagra.

Nagra (1994c). Kristallin-I, Safety Assessment Report. Tech. rep., Nagra.

Nagra. (2002). Projekt Opalinuston, Synthese der geowissenschaftlichen Untersuchungsergebnisse. Technical Report, NAGRA.

NEA (2013). Underground Research Laboratories (URL).- Nuclear Energy Agency, Organisation for Economic Co-operation and Development (OECD), Rad.Waste Management NEA/RWM/R (2013) 2

Noseck, U., Becker, D., Fahrenholz, C., Fein, E., Flügge, J., Kröhn, K.-P., et al. (2008). Assessment of the long-term safety of repositories. GRS-237, BMWi-FKZ 02E9954, Gesellschaft für Anlagen- und Reaktorsicherheit (GRS) mbH, Braunschweig, 191 p.

Obruchev, W.A. (1930). Distribution of the ice age tracks in the north of Europe and Central Asia. In: Geological review, Volume 21, Issue 4, pp. 243-283.

Ozerskiy, A. Y. (2012). Geochemical specialties of lower Archean rocks in the region of potential underground building in southern part of Yeniseysky Ridge (in Russ.). Exploration and protection of the natural resources, 39-44.

Ozerskiy, A. Y., & Karaulov, V. (2012). Hydrogeological investigations for engineering surveys for underground construction within a crystalline rock massif in the southern part of the Yeniseysky Ridge (in Russ.). Engineering research, 11, 52-59.

Ozerskiy (2013). Personal communication.

Petrov, V. (2008). Report about the scientific research toward investigation of underground isolation of radioactive waste on behalf of DBE TECHNOLOGY. Tech. rep.

POSIVA (2003): ONKALO – Underground Characterisation and Research Programme (UCRP).- Posiva Report 2003-03, ISBN 951-652-117-7, Olkiluoto (Fin.)

Pruess, K., C., O., & G., M. (1999). TOUGH2 USER'S GUIDE, VERSION 2.0. University of California, Berkeley, California, USA.

Reiter, S., & Wittum, G. (in prep.). ProMesh - a Flexible Interactive Meshing Software for Unstructured Hybrid Grids in 1, 2 and 3 Dimensions.

Reiche, T., Noseck, U., Wolf, J. (2014): Modeling pollutant transport in fractured porous media under consideration of colloids with the transport codes FRAME and COFRAME, (in Germ.). GRS-333, BMWi-FKZ 02E10367, Gesellschaft für Anlagen- und Reaktorsicherheit (GRS) mbH, Braunschweig, 237 p.

Rocscience. (2007). RocLab: Rock mass strength analysis using the Hoek-Brown failure criterion, User's Guide.

Rundkvist, D., & Mitrofanov, F. (1988). Precambrium geology of the USSR (in Russ.). Science, 439.

Schachtbau Nordhausen, 2015: Verwahrung des Altkalischachtes »Ludwigshall«, online citation: http://www.schachtbau.de/export/sites/www.schachtbau.de/pdf/projektblaetter_bergbau/SBN_2013_Verwahrung_Schacht_Ludwigshall.pdf, 2015

Schuhmann, R., Emmerich, K., Kemper, G., Königer, F., Kudla, W., Gruner, M., et al. (2009). Verschluss mit Äquipotenzialsegmenten für die untertägige Entsorgung (UTD und ELA) gefährlicher Abfälle zur Sicherstellung der homogenen Befeuchtung der Dichtelemente und zur Verbesserung der Langzeitstabilität. Tech. rep., Kompetenzzentrum für Materialfeuchte CMM, Karlsruher Institut für Technologie.

Shabalev (2009). Personal communication.

Shebalin, N. V., & Leydecker, G. (1997). Earthquake cataloguefor the former Soviet Union and borders up to 1988. European Commission, Report No. EUR 17245 EN, Nuclear Science and Technology Series (1997), 135 pp., 13 fig., ISSN 1018-5593, Office for official publications of the European Communities, Luxembourg, European Commission.

SKB (2011a). Long-term safety for the final repositpory for spent nuclear fuel at Forsmark. Main report of the SR-Site project, Volume 1. Tech. rep., SKB.

SKB (2011b). Long-term safety for the final repositpory for spent nuclear fuel at Forsmark. Main report of the SR-Site project, Volume 2. Tech. rep., SKB.

SKB (2011c). Long-term safety for the final repositpory for spent nuclear fuel at Forsmark. Main report of the SR-Site project, Volume 3. Tech. rep., SKB.

Skupin, K., Speetzen, S. & Zandstra, J.G. (2003): The ice ages in the Nord-East Westfalen and adjacent areas of the Lower Saxony (germ.). Geological survey of the Nordrhein-Westfalen. Krefeld.

Spears, R. E., & Jensen, S. R. (2012). Approach for Selection of Rayleigh Damping Parameters Used for Time History Analysis. 2009 ASME Pressure Vessels and Piping Division Conference. 134. Prague, Czech Republic: ASME.

Spiessl, S., Becker, D. (2014): Investigation of Different Sampling and Sensitivity Analysis Methods Applied to a Complex Model for a Final Repository for Radioactive Waste. Probabilistic Safety Assessment and Management PSAM 12, June 2014, Honolulu, Hawaii.

Stenhouse, M. (1993). Sorption Database for Crystalline, Marl and Bentonite for Performance Assessment. Tech. rep., Nagra.

Svendsen, J.I., Alexanderson, H., Astakhov, V.I., Demidov, I., Dowdeswell, J.A., Funder, S., Gataullin, V., Henriksen, M., Hjort, Ch., Houmark-Nielsen, M., Hubberten, H.W., Ifssonl, O.I., Jakobsson, M., Kjær, K.H., Larsen, E., Lokrantz, H., Lunkka, J.P., Lys, A., Mangerud, J., Matiouchkov, A., Murray, A., Moeller, P., Niessen, F., Nikolskaya, O., Polyak, L., Saarnisto, M., Siegert, C., Siegert, M.J., Spielhagen, R.F. & Stein, R. (2004): Late Quaternary ice sheet history of northern Eurasia. Quaternary Science Reviews, Volume 23, Issue 11-13, pp. 1229-1271.

Thiel, E. (1951). The Ice age in Siberia (in Germ.). In: Erdkunde, Band V, Publisher Boss, Kleve.

Tóth, J. A. (1963). A theoretical analysis of ground-water flow in small drainage basins. Cited in: Fetter, C. W. (2001). Applied Hydrogeology. Upper Saddle River, New Jersey (Prentice Hall), p. 598 (241). Journal of Geophysical Research, 68(16), 4795-4811.

Van Genuchten, M. (1980). A closed-form equation for predicting the hydraulic conductivity of unsaturated soils. Soil Science Society, 44, 892-898.

Velichko, A.A. (1987). Quaternary Glaciations at the USSR Territory. For the XII Congress of INQUA (Canada, 1987) (in Russ). Moscow “Nauka”.

Vernikovsky, V. A., & Vernikovskaya, A. E. (2006). Tectonics and evolution of granitoid magmatism in the Yenisey Ridge (russ.). Russian geology and geophysics, 47(1), 35-52.

VNIPIPT (2011). Personal communication, DBETEC, BGR, GRS, St. Petersburg, April, 13th – 15th, 2011. unpublished.

VNIPIPT (2012a). Presentation during project workshop, July 2012, Peine, Germany, unpublished.

VNIPIPT (2012b). Schematic cross section, provided by VNIPI PT, unpublished.

VNIPIPT (2013a). Presentation during project workshop, June 2013, Peine, Germany, unpublished.

VNIPIPT (2013b). Presentation during project workshop, October 2013, Moscow, Russia, unpublished.

Wells, D. L., & Coppersmith, K. J. (1994). New empirical relationships among Magnitude, Rupture Length, Rupture Width, Rupture Area, and Surface Displacement. Bulletin of the Seismological Soc. of Amerika, 84, 974-1002.

Wilsnack, T., Sitz, P., Heinemann, k., Rumphorst, K., & Hunstock, F. (2008). Flüssigkeitsdichte Verwahrung von Schächten. Kali und Steinsalz, 3, 24-35.

Wilson, E. L. (2004). Static and Dynamic Analysis of Structures (4th Ausg.). Berkeley, CA.

Zuo, J., Liu, H. & Li, H. (2015). A theoretical derivation of the Hoek-Brown failure criterion for rock materials, Journal of Rock Mechanics and Geotechnical Engineering, 7, pp. 361-366.

ANNEX

9 Laboratory investigations

9.1 Samples and preparation

In June 2013, eight drill core samples from the deep exploration borehole R-12 were obtained from NO.RAO and Krasnoyarskgeologiya. R-12 is located at the north-western corner of the investigated area, where the borehole R-7 was already drilled (Fig. 9-1). These samples stem from different depths between 166 m and 477 m below ground surface (bgs), including the targeted emplacement depth of ca. 400 m to 470 m bgs. The rock samples consist of biotite plagiogneisses, (meta)dolerites and migmatites. Fig. 9-2 shows the core samples obtained from Krasnoyarskgeologiya.

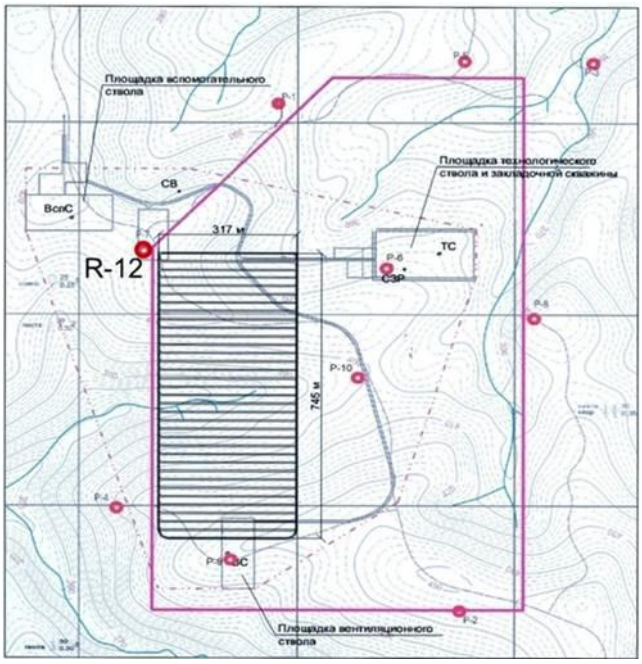

Fig. 9-1: Loocation of the borehole R-12

Fig. 9-2: Drill core samples from the deep exploration borehole R-12, obtained from NO.RAO and Krasnoyarskgeologiya

Different laboratory experiments were conducted at the laboratories of GRS, BGR, Moscow University (MGU) and IGEM RAN (Moscow). Tab. 9.1 gives an overview of the analyses performed and parameters determined. Detailed information and results are given in the following sections.

Tab. 9.1: Performed laboratory analyses and determined parameters, including lead-managing instituion

Analysis	Parameter	Category	Sample	Institution
Petrophysical analyses	Bulk Density	Petrophysical properties	Rock discs	GRS
	Effective Porosity			
	Water content			
	Water content (sat)			
	Grain density		Powders	
	Total porosity			
Hot Disk Basic System	Specific heat capacity (dry)	Thermo-physical properties	Rock discs	
	Thermal conductivity (dry)			
	Thermal diffusivity (dry)			
	Specific heat capacity (sat)			
	Thermal conductivity (sat)			
	Thermal diffusivity (sat)			
Permeability cell	Gas permeability	Geohydraulic properties		
	Water permeability			
Ultrasonics	Dynamic elastic parameters: Young‘s modulus	Geomechanic properties	Cores	
	Dynamic elastic parameters: Poisson‘s ratio			
Triaxial test	Static elastic parameters: Permeability			
	Static elastic parameters: Deviatoric stress			
	Static elastic parameters: Axial deformation			
	Static elastic parameters: Young‘s modulus			
Petrographic analyses and computer-tomography	Alteration and deformation / metamorphosis of rocks Open pores and fractures	Petrographic description Geohydraulic properties	Thin sections Cores	BGR IGEM RAS
Sorption experiments	Time-dependence of radionuclide sorption Distribution coefficients Digital radiography images	Sorption of radionuclides	Powders Rock discs	MGU, IGEM RAS

The core samples were documented and prepared for further analysis at BGR. Disc slices of the drill cores were needed to determine some of the geomechanical properties as well as petrophysical, thermo-physical, sorption and hydraulic properties. Therefore, two slices of ca. 1 cm thickness were cut off from every core sample. Tab. 9.2 lists the depths of the sample discs with the respective petrological sample denotation.

During sample preparation rest pieces of preparation and saw dust were collected and used for further analysis of petrophysical properties. Fig. 9-3 shows some of the rock discs and the rest pieces of preparation that were used for further analyses.

Tab. 9.2: Drill core samples: Depths and petrological denotation of the sample slices

Depth [m bgs]	Petrological denotation
166.12	Biotite plagiogneiss
166.34	Biotite plagiogneiss
201.13	Biotite plagiogneiss with cordierite, enriched with biotite
201.23	Biotite plagiogneiss with cordierite, enriched with biotite
347.62	Biotite plagiogneiss, kali-metasomatosis
347.63	Biotite plagiogneiss, kali-metasomatosis
417.75	Biotite plagiogneiss, banded
417.85	Biotite plagiogneiss, banded
443.29	Dolerite
443.39	Dolerite
444.82	Contact dolerite with lamprophyre
444.91	Contact dolerite with lamprophyre
459.33	Migmatite
459.34	Migmatite
476.48	Biotite plagiogneiss, migmatised
476.58	Biotite plagiogneiss, migmatised

Fig. 9-3: Drill core samples from the deep exploration borehole R-12, obtained from NO.RAO and Krasnojarskgeologiya

9.2 Microfabrics and deformation of rocks

Six samples of crystalline rocks (gneisses, migmatite and metadolerite) drilled in the Krasnoyarsk area in 2013 (exploration borehole R-12) were investigated by using a petrographic microscope and a medical computertomograph. The aim of the study was to reveal the deformation microstructures, deformation mechanisms and conditions. Particular attention was paid to possible open pores and veins or fractures, which could serve as pathways for fluid phases.

9.2.1 Methods

All samples were studied using a standard petrographic microscope. The microscopic studies were focusing on (i) the metamorphic index minerals, (ii) the deformation microfabrics, (iii) the deformation mechanisms of constituent minerals, (iv) the shape-preferred orientation of minerals and (v) the mineralization of tension gashes.

To reveal the three-dimensional distribution of dense and less-dense phases, all six samples have been analysed using computer tomography (CT) (for details, see Zulauf et al., 2003). CT studies were performed at the clinic of Frankfurt University in the Neuroradiologie Department using a multislice spiral CT scanner (Phillips CT Brilliance with 6 lines). Conditions for analyzing the samples were as follows: slice thickness = 0.8 mm, spacing = 0.6 mm, standard voxel resolution. The resolution of the CT images is ca. 0.5 mm. As a sufficient contrast in density is present in almost all samples, there is no problem to visualize the different phases using grey values. Thus, the light minerals, such as quartz or feldspar (ρ = 2.5 – 2.7 g cm^{-3}) can be separated from the mafic minerals, such as pyroxene, hornblende or biotite (ρ

≥ 3.0 g cm^{-3}). Light (felsic) minerals appear in dark colour, whereas heavy (mafic) minerals appear in light colour in the CT images.

Geometrical parameters have been determined from CT images using the software Smooth, which supports production, visualisation, and analyses of DICOM volumetric data. Smooth can be used for 3D reconstructions based on histological sections even if the latter are free from external landmarks. The presentation of data by polygons and voxels allows the combination of polygon models with arbitrary number of sections, the latter with any orientation when cutting through the volumetric data set. These sections can be processed interactively in real time. Complex polygon models can be produced from several less complex polygon models. The models shown on the screen are either transparent or opaque. The visualisation and interpretation of 3D models is significantly improved using a special pseudo-colour mode. Apart from central projection, there is a possibility to present the 3D models in parallel projection.

The CT data can also be used to reveal open pore space, which should appear as black domains in the CT images. To reveal even very low amounts of open pore space, the diagrams voxel frequency vs. grey-scale values have been plotted also in a logarithmic mode. The CT data are available in 2D and 3D. Parts of it are presented in the present report.

9.2.2 Results

9.2.2.1 Biotite Plagiogneiss (sample 1319721, 166.14 m depth)

The core with biotite plagiogneiss consists of two foliated parts, which are different in composition (Fig. 9-4 and Fig. 9-5, central part). The lower part is more coarse-grained and contains larger amounts of (dense) mafic minerals compared to the upper part. This is particularly visible in the 3D-CT reconstruction Fig. 9-5, right part). The boundary between more mafic and more felsic rock is parallel to the dominant foliation. This foliation results from both a shape-preferred orientation of the constituent minerals and a compositional layering, the latter based on an alternation of more mafic and more felsic layers (Fig. 9-5, left part).

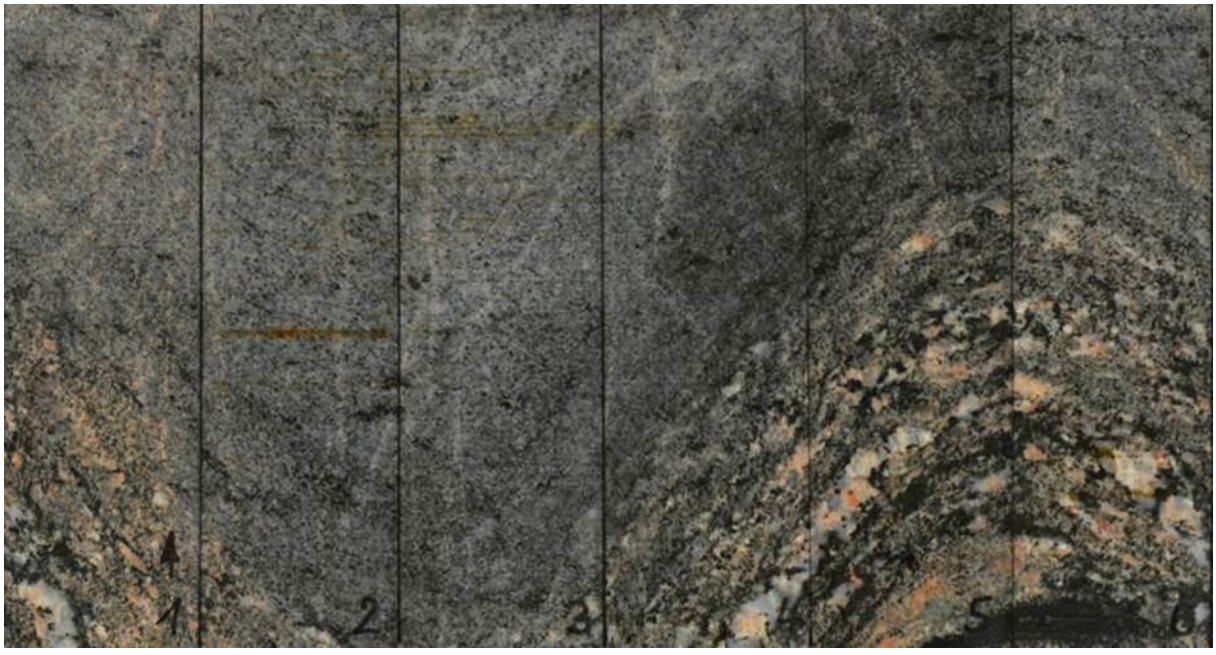

Fig. 9-4: Unwound surface of core sample 166.14 m (length of the core – 100 mm)

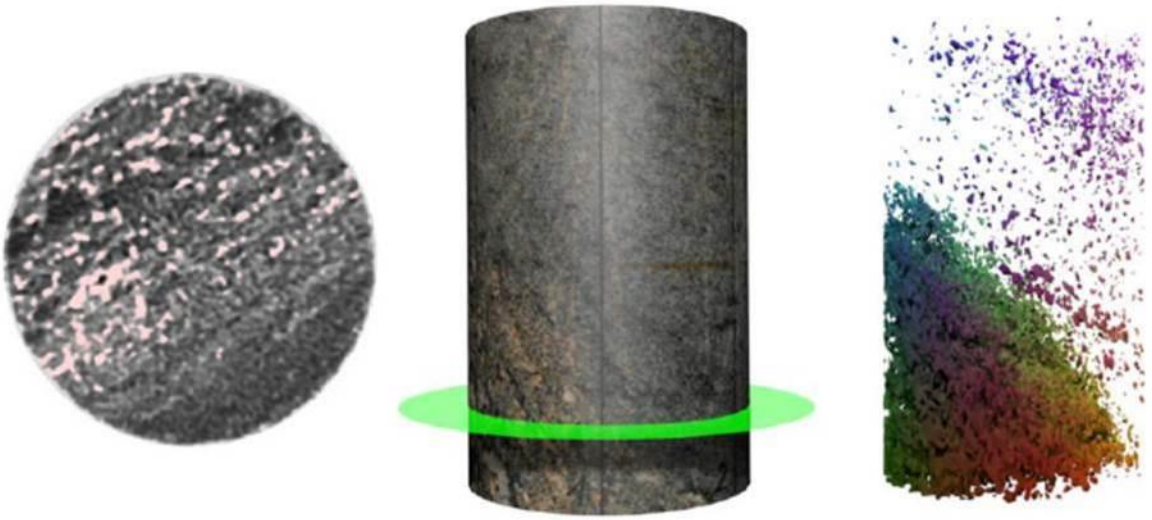

Fig. 9-5 Drilling core (central part), 3D-CT model (right part) and CT image of section shown by the green band surrounding the drilling core (left part). Note that light domains in the CT image reflect dense (mafic) phases, whereas the dark domains reflect less dense (felsic) phases.

Investigations of thin sections show the rock to consist of plagioclase, K-feldspar, quartz, biotite, and orthopyroxene. White mica is present, but only as a secondary retrograde phase. Accessory minerals are zircon, chlorite, and opaque phases. The grain size of quartz and feldspars differs significantly (Fig. 9-6a). Quartz shows high-temperature deformation fabrics, such as serrated grain boundaries, and perpendicular sets of subgrains (Fig. 9-6d). The phase boundaries between quartz and K-feldspar and between quartz and plagioclase are frequently strongly serrated. Plagioclase shows deformation twins according to both the albite and pericline laws (Fig. 9-6f) and is partly affected by sericitization and fracturing. K-feldspar shows perthitic exsolution lamellae and is partly present in form of flame perthite. Replacement by myrmekite is common (Fig. 9-6b). Some of the K-feldspars are fractured and bent. Biotite shows exsolved rutile needles and is partly replaced by chlorite. Small biotite also forms striking coronas surrounding the opaque phases (Fig. 9-6c). Orthopyroxene is present as lath-shaped mineral that was growing statically across the minerals and fabrics mentioned above (Fig. 9-6e).

The CT analyses show that the light minerals (quartz, feldspar) are most dominant. The plot voxel frequency vs. grey-scale value (not shown here) shows that very light phases, such as fluids or air bubbles, do not occur in the investigated core. Thus, open fractures or pore space, which are larger than ca. 0.5 mm (the resolution of the medical computer tomograph) are not present in this rock.

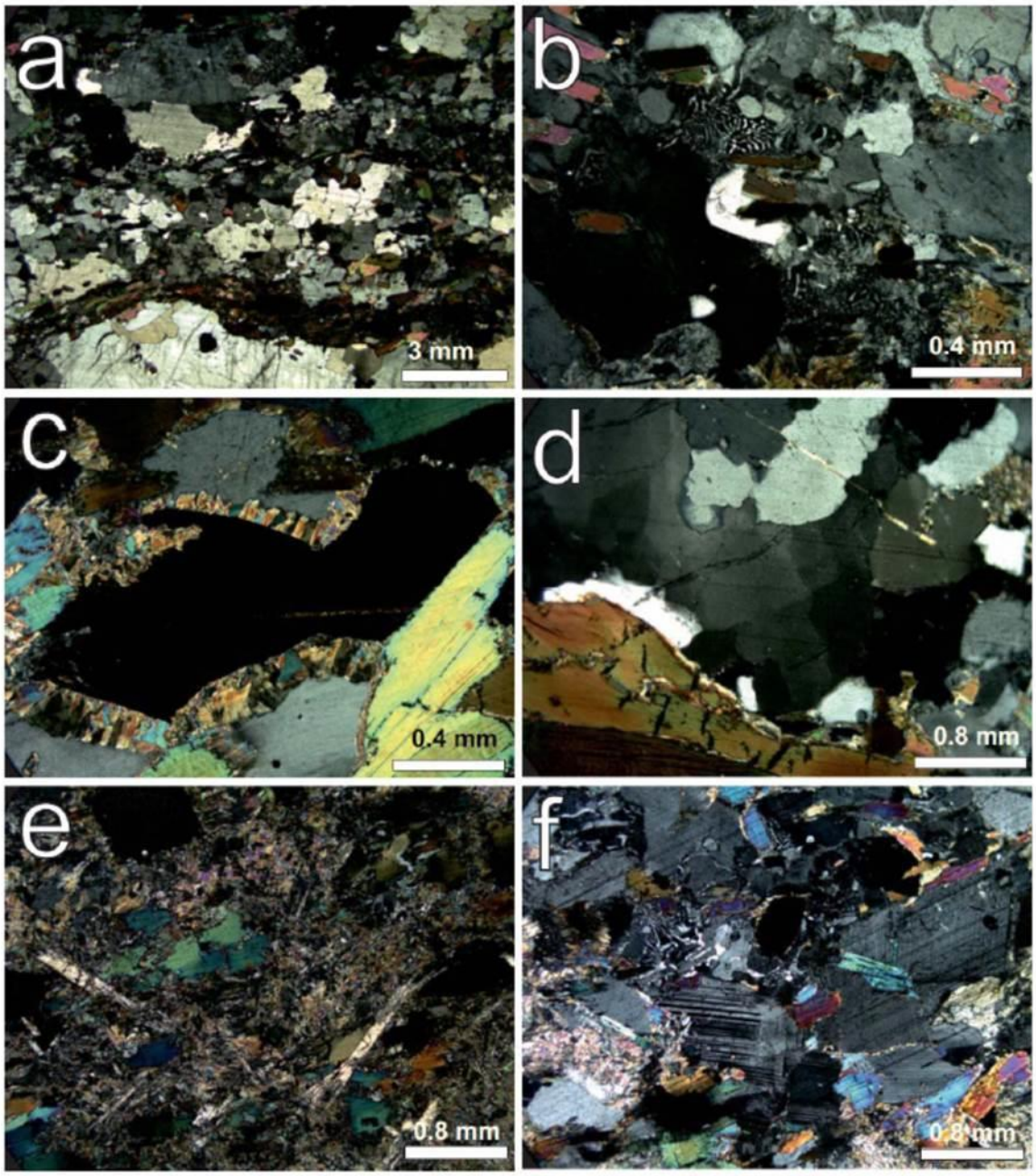

Fig. 9-6: Microphotographs of biotite plagiogneiss (sample 1319721) under crossed polarizers. (a) Overview showing the general fabric and strikingly different grain size of quartz and feldspar of biotite plagiogneiss. (b) Myrmekite replacing K-feldspar. (c) Opaque phase showing a corona of biotite; biotite is situated between the opaque phase and K-feldspar. (d) Lobate grain boundaries and perpendicular sets of subgrain boundaries (chessboard pattern) in quartz. (e) Orthopyroxene laths with random orientation developed postkinematically. (f) Deformation twins in plagioclase according to albite and perikline laws.

9.2.2.2 Banded Biotite Plagiogneiss (sample 1319722, 417.75 m depth)

The banded biotite plagiogneiss is very inhomogeneous in composition. The upper part is rich in mafic minerals and shows a striking foliation (Fig. 9-7). The foliation is based on alternating layers, which show different amounts of felsic and mafic minerals (Fig. 9-7 and Fig. 9-8, central part). This alternation is also obvious in the 3D-CT model (Fig. 9-8, right part). The lower part of the drilling core is particularly inhomogeneous and is dominated by felsic minerals (Fig. 9-8 right part). However, there are also large batches of mafic minerals (Fig. 9-8, left part). Thus, compared to the biotite plagiogneiss described above, the distribution of felsic and mafic components is much more heterogeneous.

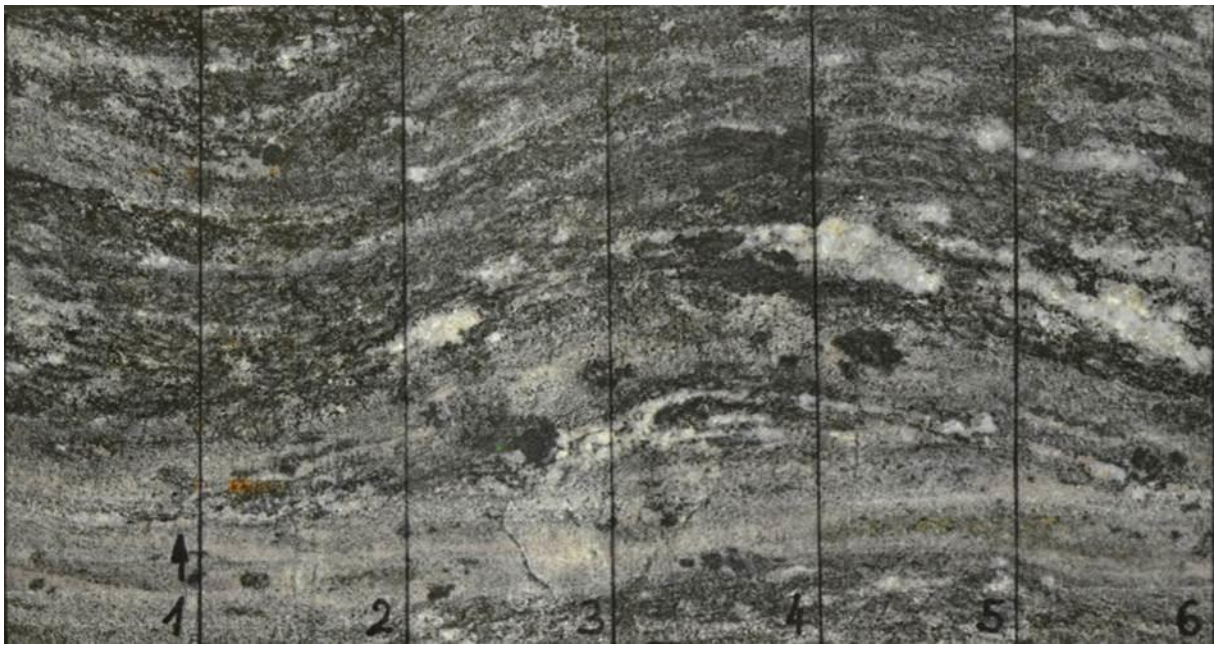

Fig. 9-7: Unwound surface of core sample 417.75 m (length of the core – 100 mm)

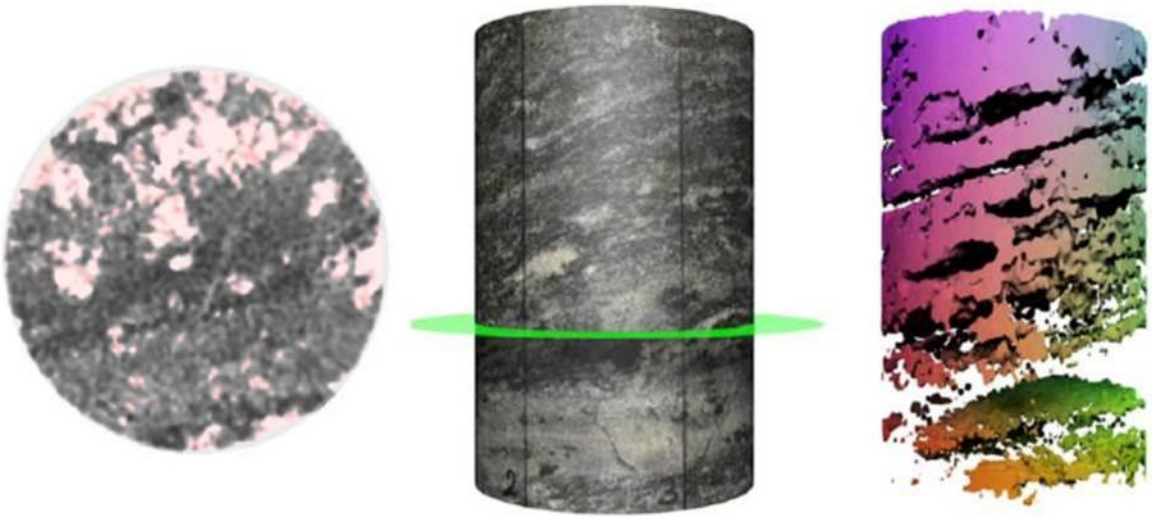

Fig. 9-8: Drilling core (central part), 3D-CT model (right part) and CT image of section shown by the green band surrounding the drilling core (left part). Note that light domains in the CT image reflect dense (mafic) phases, whereas the dark domains reflect less dense (felsic) phases.

Microscopic analyses revealed that the constituent minerals of the banded biotite plagiogneiss are plagioclase, biotite, and quartz. Less frequent are K-feldspar, garnet, orthopyroxene, and white mica. The very heterogeneous fabric and the strikingly different grain size of the constituent minerals of the banded biotite plagiogneiss are obvious from Fig. 9-9a,b. Quartz displays serrated grain boundaries and perpendicular sets of subgrain boundaries. Plagioclase is partly zoned due to a change in composition from core to rim, and shows deformation twinning according to the albite and pericline laws. Sericitization of plagioclase is also common. In contrast to the biotite plagiogneiss, describe above, the biotite of the banded version shows a random orientation of its long axis. There are striking exsolution lamellae inside biotite consisting of opaque phase, probably ilmenite. This exsolution is most-

ly restricted to the marginal parts of the biotite (Fig. 9-9f). K-felspar is present only in a few cases and is affected by myrmekitization. Garnet is present as relict inside biotite-rich domains. It is affected by boudinage and fracturing. The margins of garnet are replaced by green biotite (Fig. 9-9e). Orthopyroxene is present in form of lath-shaped minerals, which partly show exsolution lamellae. The content of these lamellae is difficult to determine under the microscope. Similar to the sample described above, orthopyroxene developed under static conditions, as is shown by the almost random orientation of the long side of the laths (Fig. 9-9c,d). Deformation of orthopyroxene is restricted to weak bending. White mica is present only as secondary phase, which has not been deformed.

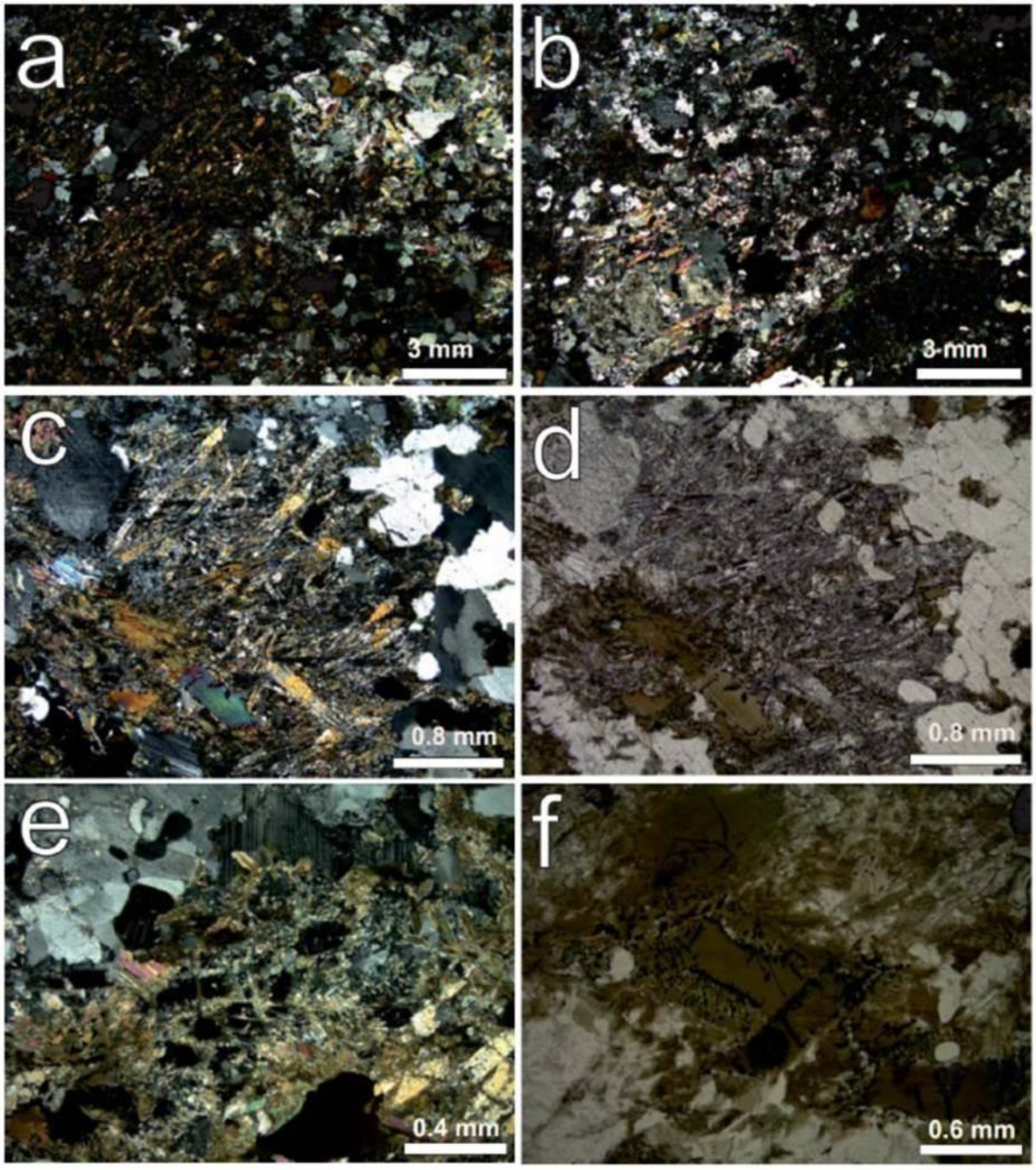

Fig. 9-9: Microphotographs of banded biotite plagiogneiss (sample 1319722). (a) and (b) Overview of banded biotite plagiogneiss; crossed polarizers. (c) Randomly oriented lath-shaped orthopyroxene replacing pre-existing unknown phase in a static environment; crossed polarizers. (d) Same like (c) but with parallel polarizers. (e) Garnet boudins (dark fragments in central part) are replaced by green biotite; crossed polarizers. (f) Oriented exsolution lamellae of opaque phase (?ilmenite) in biotite; parallel polarizers.

Similar to the sample described in the previous section, the CT analyses show that the light minerals (quartz, feldspar) are most frequent. The plot voxel frequency vs. grey-scale value shows that very light phases, such as fluids or air bubbles, do not occur in the investigated core. Thus, open fractures or pore spaces that are larger than ca. 0.5 mm (the resolution of the medical computer tomograph) are not present in the investigated banded biotite plagio-gneiss.

9.2.2.3 Metadolerite (samples 1319723 and 1319724, 443.29 m depth)

The metadolerite is the most homogeneous sample (Fig. 9-10) investigated in the present study. This is the reason why the 3D-CT model does not show any significant structure. The distribution of felsic and mafic minerals is also very homogenous as is shown in the CT section presented in Fig. 9-11 (left part).

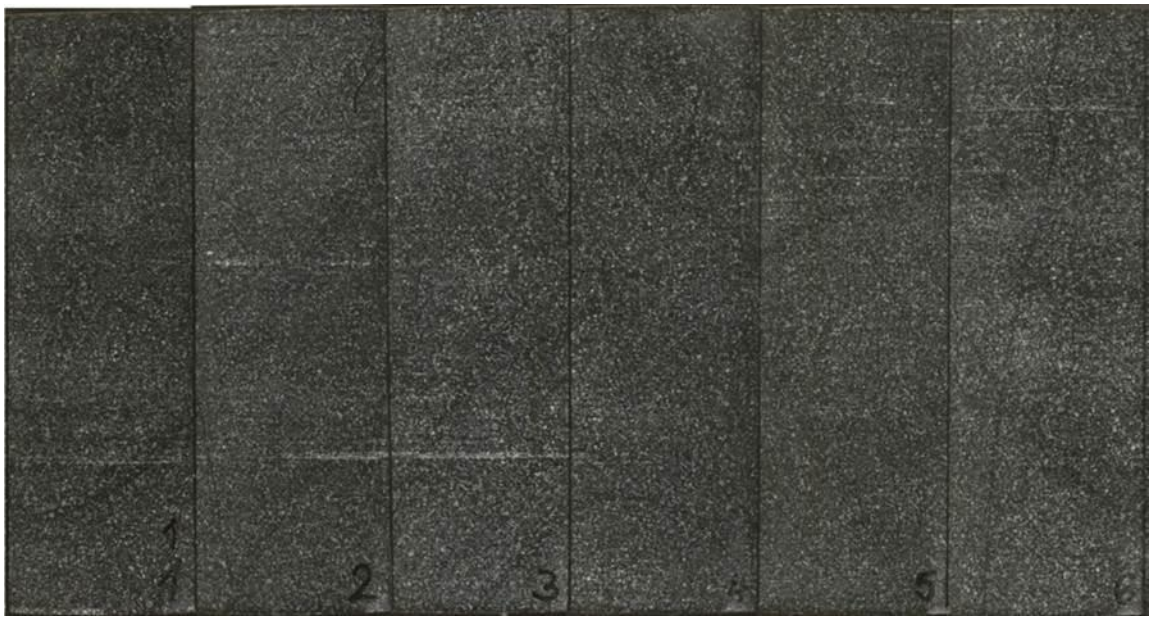

Fig. 9-10: Unwound surface of core sample 443.29 m (length of the core – 100 mm)

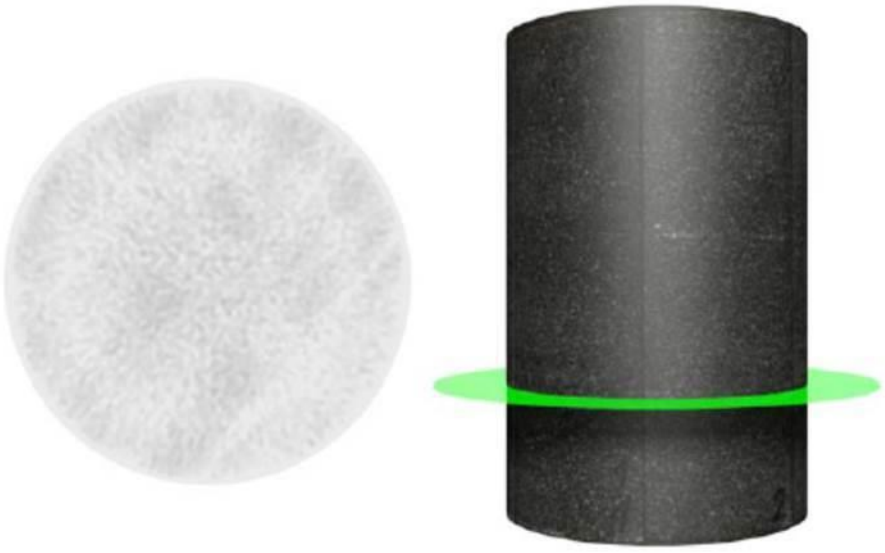

Fig. 9-11: Drilling core (right part) and CT image of section shown by the green band surrounding the drilling core (left part). Note that light domains in the CT image reflect dense (mafic) phases, whereas the dark domains reflect less dense (felsic) phases.

The investigated metadolerite consists of plagioclase and pyroxene, as the most constituent minerals, and of biotite, actinolite, prehnite, and opaque phases as less important components. The primary magmatic fabric is characterized by intergrowths of plagioclase and pyroxene both of which do not show a shape-preferred orientation (Fig. 9-12a). Plagioclase shows striking deformation twins according to both the albite and pericline law (Fig. 9-12d). In contrast to plagioclase, pyroxene shows intragranular fractures (Fig. 9-12b). Moreover, pyroxene is largely altered and replaced by secondary phases, such as prehnite and actinolite (Fig. 9-12f). Biotite is present as a corona-forming phase surrounding opaque phases (Fig. 9-12e).

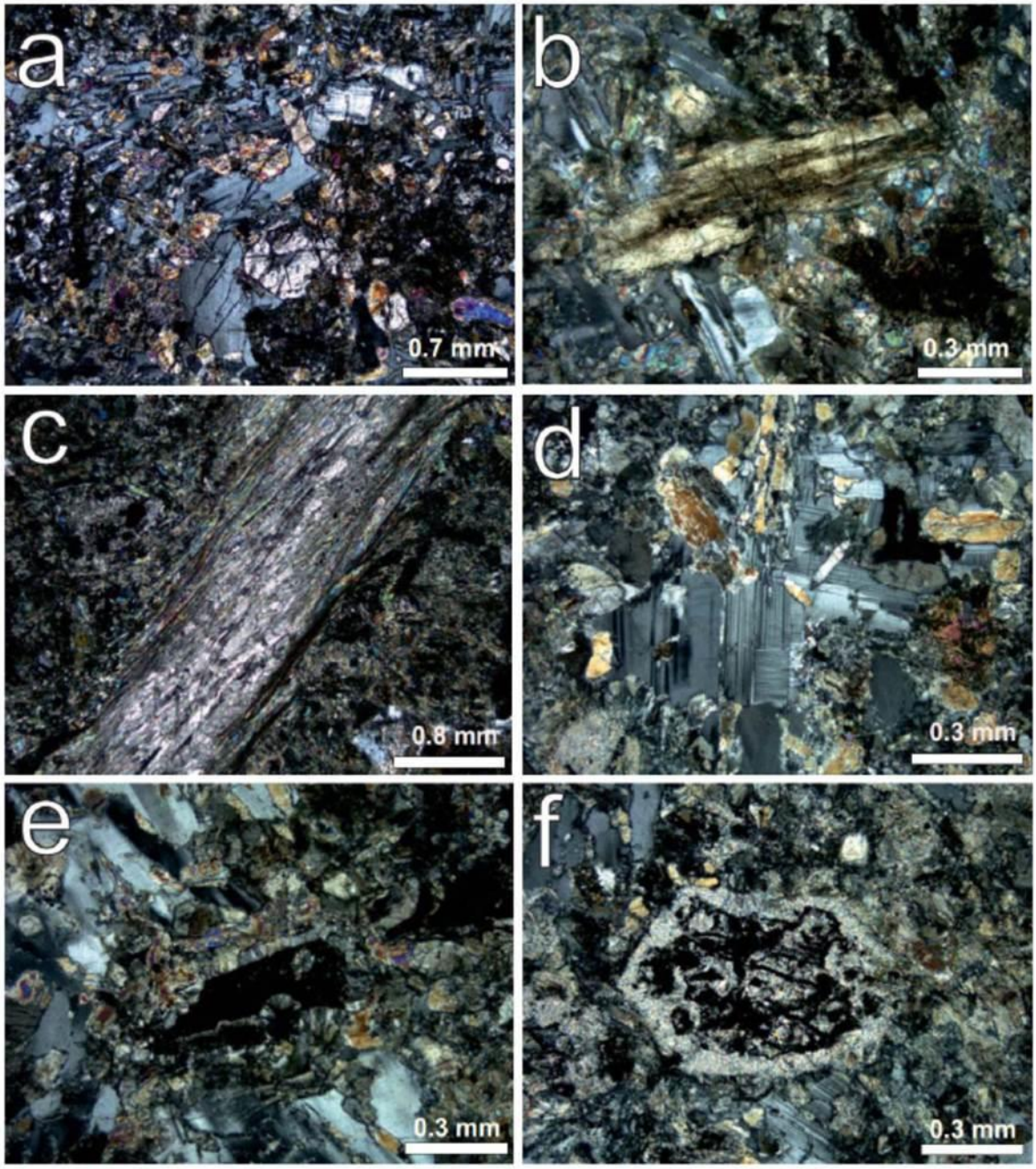

Fig. 9-12: Microphotographs of metadolerite (samples 1319723, 1319724) under crossed polarizers. (a) Partly altered plagioclase and pyroxene are cut by mineralized tension gashes. (b) Healed fractures are restricted to pyroxene, whereas plagioclase is free from fracturing. (c) Mineralized shear fracture filled with actinolite, chlorite and prehnite (at the margins) and with calcite (in the central part). (d) Deformation twins after both albite and pericline laws in plagioclase. (e) Corona of chlorite surrounding opaque phase. (f) Pseudomorphic replacement of former euhedral mineral (probably pyroxene) by actinolite, prehnite and opaque phase.

As a consequence of its rigid behaviour (in contrast to the quartz-bearing mechanically weaker gneisses), the metadolerite is affected by tension gashes and by semi-brittle shear zones, the latter showing some amount of dilation. The amount of displacement of the shear zones is low, and the open space along the shear zones if frequently filled with actinolite, prehnite, and chlorite (along the margins), and with calcite (in the central part) (Fig. 9-12c).

As the calcite of the shear fracture is entirely free from deformation twins, deformation after the formation and mineralization of these shear fractures did not occur. The tension gashes are filled with plagioclase or with chlorite and actinolite (Fig. 9-12a). It has to be emphasized that all of the tension gashes and dilationary shear fractures are mineralized, meaning that open space filled with air or fluid has not been observed under the microscope. This observation is confirmed by the CT analyses. Compared with the sample described above, the CT analyses show that the light minerals (in the present case: plagioclase) are much more frequent than pyroxene. The plot voxel frequency vs. grey-scale value confirms that very light phases, such as fluids or air bubbles, are lacking in the investigated metadolerite. Thus, open fractures or pore space, which are larger than ca. 0.5 mm are not present.

9.2.2.4 Migmatite (sample 1319725, 459.35 m depth)

The migmatite is the most heterogeneous sample of all samples analyzed (Fig. 9-13). It consists of light and dark domains, which reflect leucosome and melanosme. As both are strikingly different in density, they are well documented in the 3D-CT model and in the CT image (Fig. 9-14, right and left part, respectively).

Fig. 9-13: Unwound surface of core sample 459.35 m (length of the core – 100 mm)

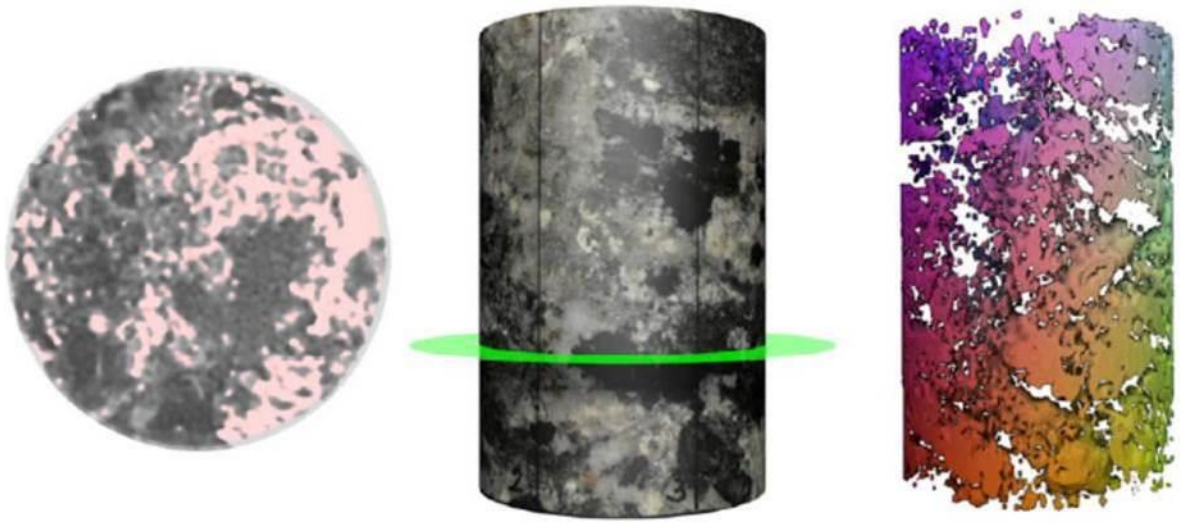

Fig. 9-14: Drilling core (central part), 3D-CT model (right part) and CT image of section shown by the green band surrounding the drilling core (left part). Note that light domains in the CT image reflect dense (mafic) phases, whereas the dark domains reflect less dense (felsic) phases.

The old (metamorphic) and new (‘melt’) domains are also well visible under the microscope (Fig. 9-15a,b). Relics of the pre-migmatic fabric consist of quartz, K-feldspar and plagioclase. Of particular interest are relics of plagioclase, which are up to 1 cm in dimension and show evidence for chemical zonation. These large plagioclases are partly altered and replaced by zoisite and sericite. The central part of the plagioclase also includes calcite, which reflects an An-rich core of the unaltered zoned plagioclase (Fig. 9-15f).

The large plagioclase crystals are commonly surrounded by a corona consisting of chlorite and a few amounts of calcite. In some cases vermicular quartz is embedded in the chlorite +/-calcite matrix resembling the fabric of myrmekite (Fig. 9-15d). It seems that the plagioclase between the vermicular quartz was replaced by chlorite and calcite. Relics of biotite inside these coronas suggest that we are dealing with pseudomorphs of chlorite after biotite. Former intragranular fractures in plagioclase are filled with opaque phases. K-feldspar is also present as large crystals, which are strongly sericitized. Quartz is present as roundish or drop-shaped crystals surrounded by leucosome (‘melt’, Fig. 9-15b). All of these quartz domains show evidence for high-temperature grain boundary migration in the form of serrated grain boundaries. Some of these boundaries are stepped. Moreover, most of the old quartz shows perpendicular sets of subgrain boundaries (Fig. 9-15a) and reaction fabrics. A common feature is the marginal replacement of quartz by white mica, the latter forming a corona (Fig. 9-15c).

The leucosome consists of quartz, plagioclase, chlorite, white mica and calcite. In contrast to quartz described from the paleosome, this quartz is undeformed and shows inclusions of relictic feldspar. White mica of the leucosome is also undeformed and in a few cases displays inclusions of tiny needle shaped minerals, probably sillimanite, which show a strong shape-preferred orientation. The preferred orientation of the needle shaped minerals, however, is oblique to the cleavage planes of the white mica (Fig. 9-15e). Chlorite, which is also undeformed, is present as pseudomorph after biotite. Some of the chlorite crystals include relics of fibrolitic sillimanite. Calcite of the leucosome is undeformed. Deformation twins are entirely lacking.

The CT analyses show that the light minerals (quartz, feldspar) are less dominant than the dense minerals (biotite, chlorite). The plot voxel frequency vs. grey-scale value suggests that open pore space with fluids or air bubbles does not occur in the investigated core. Thus,

even low amounts of open fractures or pore spaces that are larger than ca. 0.5 mm (the resolution of the medical computer tomograph) are not present in the migmatite sample.

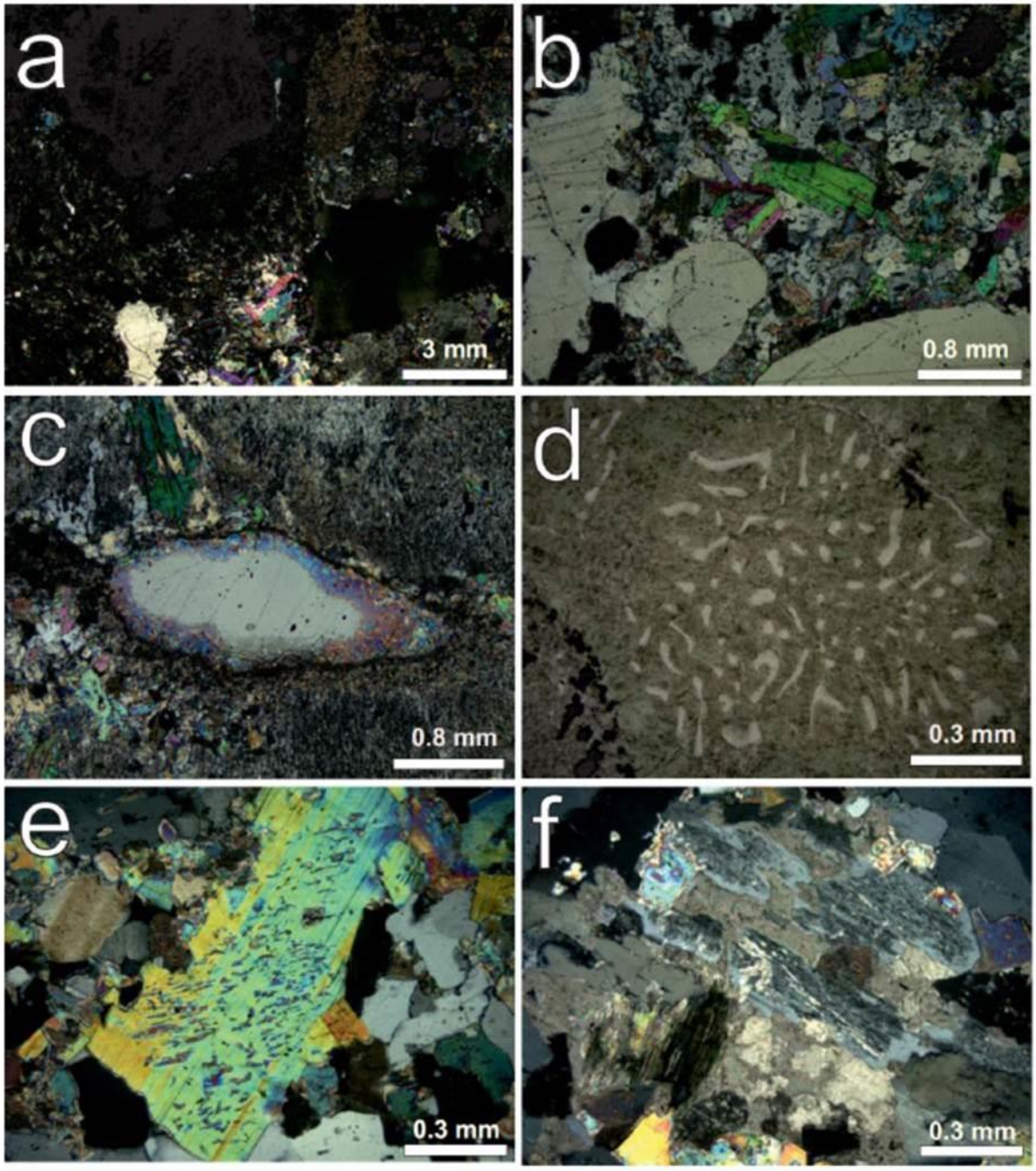

Fig. 9-15: Microphotographs of migmatite (sample 1319725) under crossed polarizers, apart from (d). (a) Overview of migmatite showing perpendicular sets of subgrain boundaries (chessboard pattern) in quartz in the lower right-hand side. (b) Relics of large old quartz (with fluid inclusion trails) is surrounded by new melt from which plagioclase, quartz and white mica have been grown. (c) Quartz inside K-feldspar shows a corona of white mica. (d) Exsolution lamellae of quartz inside a matrix of chlorite and sericite at the contact to large feldspar phenocryst. (e) Tiny inclusions (?sillimanite) in magmatic white mica show a strong shape-preferred orientation. They probably represent a former S-fabric that is largely erased outside of the mica. (f) Relics of plagioclase inside migmatitic 'melt'; younger phases, such as chlorite, white mica, and calcite result from greenschist facies overprint.

9.2.2.5 Migmatic biotite plagiogneiss (sample 1319726, 476.58 m depth)

The magmatic biotite plagiogneiss is also inhomogeneous concerning the distribution of felsic and mafic phases (Fig. 9-16). As the rock is fine grained, the heterogeneous distribution of mafic and felsic phases is not or is only hardly visible macroscopically (Fig. 9-17, central part). The heterogeneous distribution, however, is well documented in the 3D-CT model (Fig. 9-17 right part) and in the CT images (Fig. 9-17, left part). The migmatic biotite plagiogneiss is cut by a thin tension gash that is visible macroscopically because of its light color (Fig. 9-17, central part). When applying a special separation technique, it was also possible to visualize the mineralized vein in the 3D-CT model (Fig. 9-17, right part, grey color) and in the CT images (Fig. 9-17, left part, green color).

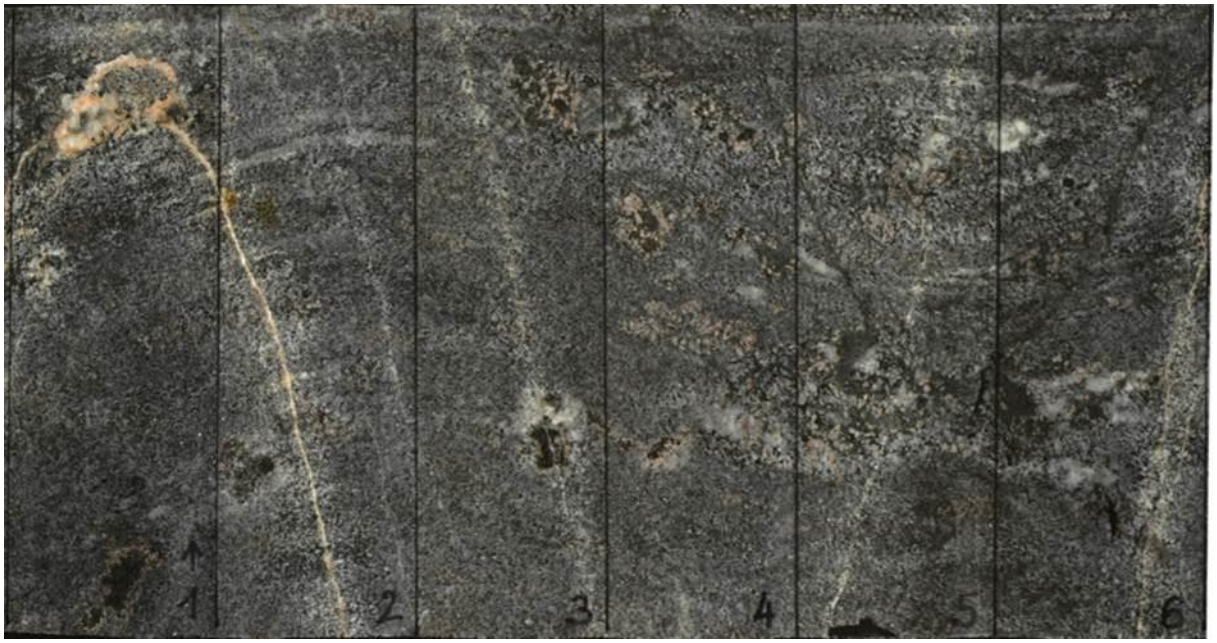

Fig. 9-16: Unwound surface of core sample 476.58 m (length of the core – 100 mm)

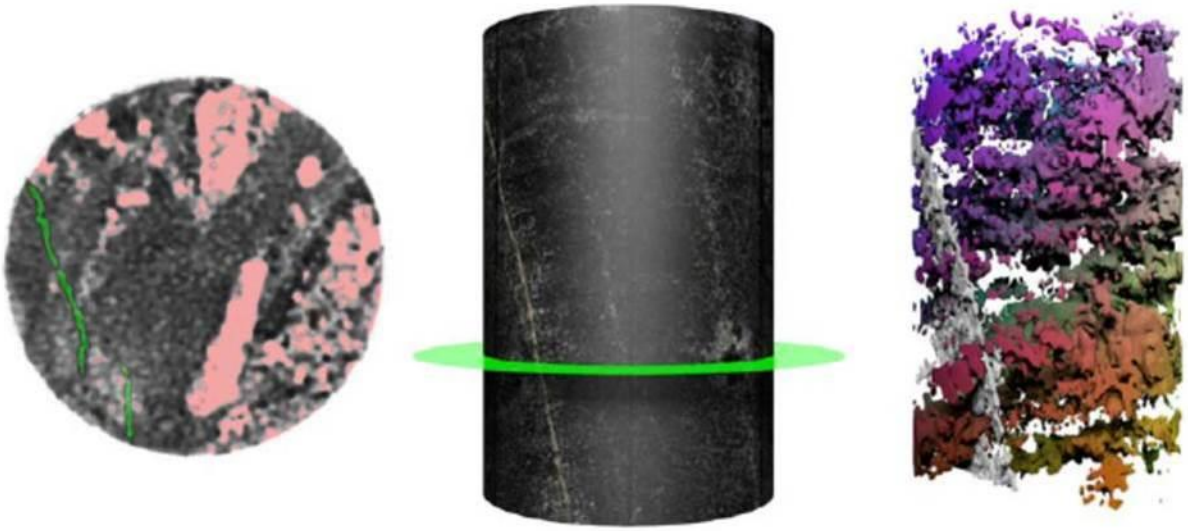

Fig. 9-17: Drilling core (central part), 3D-CT model (right part) and CT image of section shown by the green band surrounding the drilling core (left part). Note that light-pink domains in the CT image reflect dense (mafic) phases, whereas the dark domains reflect less dense (felsic) phases. The mineralized extensional vein is shown in grey in the 3D-CT model and in green in the CT image. For further details see text.

Microscopic analyses revealed that the magmatic biotite plagiogneiss consists of quartz, plagioclase, and biotite as the most important minerals. K-feldspar, Garnet, chlorite, sericite and opaque phases are present with minor amounts, and zircon occurs as an accessory mineral. The roundish shape of the zircons suggests a sedimentary origin of the protolith and thus a paragneiss. The central part of the core is cut by a thin sheet, which is finer-grained compared with the rest of the core. This fine-grained part might reflect a shear zone that underwent post-kinematic static annealing and recrystallization, or it results form a primary sedimentary layering. Quartz is largely isometric (Fig. 9-18a) and shows high-temperature deformation fabrics, such as serrated grain boundaries and perpendicular sets of subgrain boundaries (Fig. 9-18b).

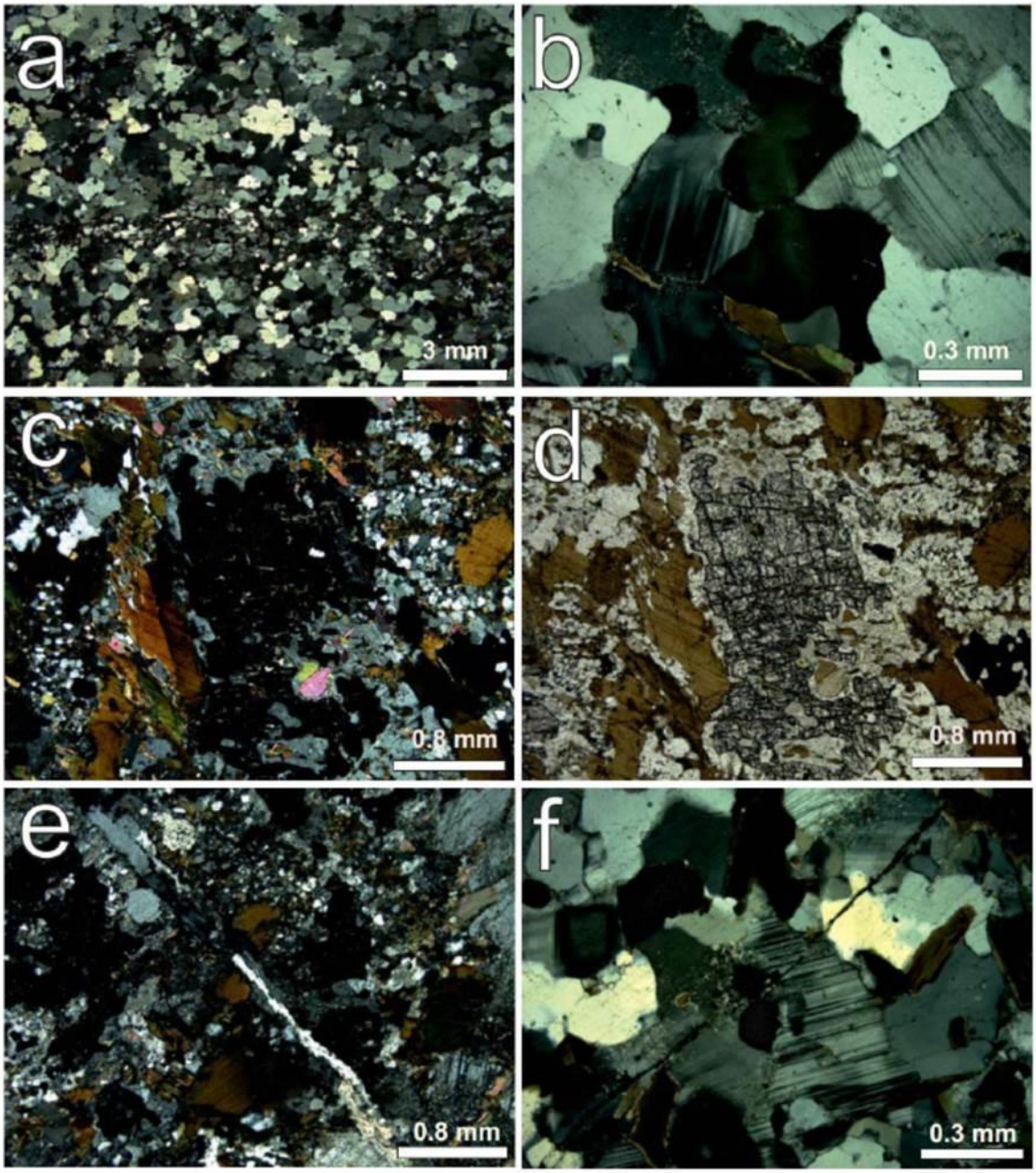

Fig. 9-18: Microphotographs of magmatic biotite plagiogneiss (sample 1319726) under crossed polarizers, apart from (d). (a) Overview of magmatic biotite plagiogneiss. (b) Lobate phase boundaries between quartz and plagioclase, and perpendicular sets of subgrain boundaries (chessboard pattern) in quartz; note the striking deformation twins in plagioclase. (c) Fractured garnet with a corona of plagioclase and biotite; note that biotite is not in direct contact to garnet. (d) the same object like in (c) but with parallel polarizers; note that healed fractures are restricted to garnet. (e) Tension gash filled with K-feldspar, quartz, and calcite. (f) Tension gash mineralized with an opaque phase.

Very high temperature and solid-state diffusion is also indicated by strikingly serrated phase boundaries between quartz and both types of feldspar (Fig. 9-18b). Plagioclase is also relatively isometric in shape and shows both sets of deformation twins. The twins are tapering towards the margins of the crystals (which is characteristic for deformation twins) and are sometimes bent (Fig. 9-18b). Some of the plagioclases are affected by sericitization.

The same holds for K-feldspar, which is also partly replaced by myrmekite. Garnet is up to 10 mm in diameter. It shows fracturing and frequently a double corona, which is up to 5 mm wide. The inner part of these coronas consists of plagioclase, the outer part consists of biotite (Fig. 9-18c,d). Biotite is mostly fresh. Deformation of biotite is restricted to bending or kinking. Some of the biotite crystals are replaced by chlorite. The rock shows relatively large amounts of opaque phases, which, however, could not be determined using a standard microscope. The opaque phases have a roundish shape and are present in the rock matrix (Fig. 9-18d, lower right corner) and are present inside biotite reflecting exsolution.

The macroscopically visible tension gash is mineralized with K-feldspar, quartz, and calcite (Fig. 9-18e). Another tension gash is mineralized with an opaque phase (Fig. 9-18f). The plot voxel frequency vs. grey-scale value confirms that very light phases, such as fluids or air bubbles, are lacking in the magmatic biotite plagiogneiss. Thus, although several extensional veins are present in this rock, open fractures or pore space that are larger than ca. 0.5 mm are not present.

9.2.3 Interpretation and Discussion

The roundish zircons in some of the investigated gneisses suggest that the gneisses and migmatite originate from previous sedimentary rocks, which underwent high-grade amphibolite to granulite facies metamorphism and partial anatexis. These high-grade metamorphic conditions are indicated by (i) the presence of K-feldspar and the lack of white mica (apart from white mica of the leucosome and sericite formed during retrograde metamorphism); (ii) the presence of orthopyroxene; (iii) extremely serrated phase boundaries between K-feldspar and quartz and between plagioclase and quartz; (iv) perpendicular sets of subgrain boundaries in pre-anatectic quartz.

The microfabrics of the high-grade gneisses and migmatites suggest that dislocation creep and volume diffusion operated simultaneously during deformation. Strong waviness of the quartz-feldspar boundaries as well as the lack of perthite lamellae at the K-feldspar margins suggest that diffusional creep has accommodated at least parts of the finite strain. We propose that volume diffusion (Nabarro-Herring creep) in the marginal parts of the crystals was accompanied by high-temperature dislocation creep in crystal cores, resulting in high finite strains (e.g. Gower & Simpson, 1992; Martelat et al., 1999; Zulauf et al., 2002). Dislocation creep in quartz is indicated by the perpendicular sets of subgrain boundaries, which have been observed in all of the studied gneisses and migmatite. One set of subgrain walls is oriented parallel to the prism, the other is parallel to the basal plane, resulting in the so-called ‘chessboard pattern’. The latter suggests prism [c] as an active slip system in the high-quartz field (e.g. Mainprice et al., 1986; Kruhl, 1996). When applying the low quartz/high quartz boundary obtained experimentally by Gross & Van Heege (1973), and assuming deformation in the stability field of sillimanite (that has been observed in the studied rocks), the deformation temperature should have been higher than 650°-750°C. Moreover, quartz is characterized by rectangular (stepped) grain boundaries (partly parallel to the rhombohedral plane) suggesting rhombohedral slip and high mobility of grain boundaries owing to rapid grain boundary migration recrystallization (dislocation creep regime III of Hirth & Tullis, 1992) and secondary grain growth under upper amphibolite to granulite facies conditions (Gapais & Barbarin, 1986; Bunthebarth & Voll, 1991).

The high-temperature deformation fabrics described above pre-date the peak of metamorphism, which led to static growth of randomly oriented laths of orthopyroxene and to partial melting and formation of the leucosomes. The new phases of the leucosomes (quartz, plagioclase, and large white mica) are almost free from deformation fabrics. The same holds for orthopyroxene, which probably developed at the expense of garnet and biotite, although cordierite has not been observed. However, cordierite might have been present, but was replaced by secondary phases during the retrograde metamorphic overprint. This retrograde metamorphic overprint affected all of the studied rocks. Evidence for this overprint is given by (i) replacement of biotite and garnet by chlorite, (ii) sericitization of plagioclase and K-feldspar.

The lack of a metamorphic foliation and related high-grade deformation fabrics suggest that the metadolerite intruded after the high-grade metamorphic event. After its solidification and cooling, it was deformed in the brittle field under metamorphic conditions of the prehnite-actinolite facies, which is related to T = 240-350°C and P <2 kbar (Liou et al., 1987). This deformation led to discrete dilational shear zones and tension gashes, which are mineralized with secondary phases, such as prehnite, actinolite, chlorite, calcite. As the calcite of the mineralized shear fractures of the metadolerite are entirely free from deformation fabrics (no twins!), the differential stress was very low after the calcite had precipitated inside the open vein or shear zone. The age of the brittle event could be dated using K-Ar or ^{39}Ar-^{40}Ar on biotite (of the gneisses) or using fission-track dating of titanite and/or apatite.

Similar dilational shear zones and tension gashes are also present in the gneisses. In the gneisses, however, the number of these structures is much lower than in the metadolerite, as the quartz-bearing gneisses were mechanically weaker under metamorphic conditions of the prehnite-actinolite facies. Under common natural strain rates ($\dot{\varepsilon}$ = 10^{-13}–10^{-14} s^{-1}) quartz starts to recrystallize at T = ca. 300°C. Although the investigated rocks underwent a phase of late brittle faulting and veining, there is no evidence of open fractures or pores. This statement is confirmed by both the microscopic and the computertomographic data. Given that very few amounts of open pore space or open fractures that are larger than ca. 0.5 mm are present in the investigated rocks, these structures would have led to a distinct peak in the logarithmic voxel frequency vs. grey-scale plot. However, these peaks at the left side, where light phases, such as fluids or gas are situated, are entirely missing.

9.3 Laboratory experiments

9.3.1 Petrophysical analyses

On the basis of the geometric characteristics of the rock disc samples, some of the petrophysical properties can be determined. These are the bulk density ρ_b and the effective porosity Φ_{eff}. The bulk density ρ_b is the quotient of the bulk volume V and the mass m of a rock disc:

$$\rho_b = \frac{m}{V}$$

with

ρ_b bulk density [kg m^{-3}],
V bulk volume of the sample [m^3], and
m mass of the sample [kg].

In a first step, the volume of the rock discs was determined via geometric calculation using the sample radius and height. Irregularities in their geometric shape were neglected. The rock discs were dried at 105°C according to DIN 18121-1 (DIN, 1998) and weighted for the determination of their dry mass, density and water content. The mass measurements were conducted before and after the analysis of the thermo-physical properties (chapter 9.3.2),

and their mean was used to calculate the bulk densities. Besides, the bulk density was also determined via immersion weighing (archimedic) for some samples.

By saturating the rock discs with a synthetic solution, their effective porosity can be determined. This was done using synthetic formation water (Tab. 9.3) according to Ozerskiy (2012). The chemical components of the synthetic solution comply with the mineralisation of the groundwater in the considered depth of the potential repository at the Yeniseysky site. The groundwater regime is alkaline and reducing in this area. The groundwater is of Na-Cl-type with a mean Eh-value of 44.8 mV and a mean pH-value of 8. Tab. 9.3 gives an overview on the groundwater mineralisation at the Yeniseysky site according to Ozerskiy (2012).

Tab. 9.3: Groundwater mineralisation in the depth of a potential repository at the Yeniseyskiy site according to Ozerskiy (2012). TDS = Total Dissolved Solids

Component	Concentration [mg l^{-1}]
HCO_3^-	215
Cl^-	5
SO_4^{2-}	16
Ca^{2+}	44
Mg^{2+}	9
Na^+	25
K^+	2.7
Fe	4.1
TDS	**343**

For the preparation of the synthetic solution the substances listed in Tab. 9.4 were used. Targeted and actual net weights are also given in Tab. 9.4. HCO_3^- and Ca^{2+} were used for charge equalisation. The density and the viscosity of the solution were 997.2 kg/m^3 and $1.109 \cdot 10^{-3}$ Pa·s.

Tab. 9.4: Composition of the synthetic formation water (refering to 5 l solution)

Substance	Net weight (target value) mg	Net weight (actual value) Mg
$FeSO_4 * H_2O$	37.3	38.8
$NaSO_4$	85.5	84.4
NaCl	41.2	42
$NaHCO_3$	295	295.7
$CaCO_3$	885	882.9
$Mg(OH)CO_3$	274.4	275.8
$KHCO_3$	34.6	33.6

For the determination of the grain densities, the rock powder provided by BGR was dried at 105°C according to DIN 18121-1 (DIN, 1998). The grain density ρ_b was determined with helium using the comparison pycnometer Quantachrome Ultrapycnometer 1000 V2.4 (Fig. 9-19). For the evaluation of the results, the software Pyc Win 2.03 from Quantachrome Instruments was used.

The total porosities Φ_t were calculated considering the bulk density ρ_b and the grain density ρ_g:

$$\Phi_t = 1 - \frac{\rho_b}{\rho_g}$$

with

Φ_t total porosity [-],
ρ_g grain density [kg m^{-3}], and
ρ_b bulk density [kg m^{-3}].

Fig. 9-19: Quantachrome Ultrapyknometer 1000 V2.4

The water content w of the rock discs was determined when receiving them via weighing and drying according to DIN 18121-1 (DIN, 1998). Additionally, their water content after saturation w_{sat} was determined. Therefore, the rock disks were saturated with synthetic solution in a vacuum exsiccator for four weeks and then weighed.

The water content and the saturated water content are calculated by

$$w = \frac{m_w}{m_s} \quad \text{and} \quad w_{sat} = \frac{m_{w,sat}}{m_s}$$

with

m_w mass of solution [kg],
m_s mass of dry sample [kg], and
$m_{w,sat}$ mass of solution in the saturated sample [kg].

The saturated water content and the volume of the sample can be used to calculate the effective porosity Φ_{eff} by

$$\Phi_{eff} = \frac{V_v}{V_{tot}}$$

with

Φ_{eff} effective porosity [-],
V_v pore volume [cm^3], and
V_{tot} total sample volume [cm^3].

Tab. 9.5 summarises the results for the bulk densities and the grain densities, the total porosities and the effective porosities. As expected, the total porosities are higher than the effective porosities. Negative values of porosities can be explained by inaccuracy of the bulk volumes, geometrically determined. Another reason might be the very high bulk densities of the crystalline rock, which are in a comparable range as the grain densities. Furthermore, the grain densities were determined on grained material obtained during preparation of the core samples. This means that the grained material used for the determination of grain densities was not exactly the same as the investigated rock discs. Insignificant differences in the mineral composition can lead to negative values of the calculated porosities using the bulk

density and the grain density. The water content at reception and the water content of the saturated samples are given in Tab. 9.6.

Tab. 9.5: Results of density and porosity measurements. Total porosity in comparison to effective porosity

Sample	Bulk density		Bulk density	Bulk density	Grain density	Total porosity	Total porosity	Eff. porosity
Depth	ρ_b	ρ_b	ρ_{bm}	ρ_{ba}	ρ_g	Φ_t	Φ_{ta}	Φ_{eff}
[m bgs]	[kg/m^3]	[kg/m^3]	[kg/m^3]	[kg/m^3]	[kg/m^3]	[%]	[%]	[%]
	After dry-ing	After measure-ment	Mean	Archi-medic			Archi-medic	By saturation
166.12	2734	2734	2734	2762	2772	1.37	0.36	0.304
166.34	2655	2655	2655		n.a.			0.443
201.13	3250	3251	3251		3509	7.37		0.194
201.23	3484	3485	3485	3665	n.a.			0.219
347.62	2762	2763	2763	2766	2728	-1.26	-1.39	0.575
347.63	2756	2756	2756		n.a.			0.497
417.75	2856	2856	2856	2826	n.a.			0.155
417.85	2978	2978	2978		2965	-1.12		0.157
443.29	3013	3012	3013		n.a.			0.487
443.39	3005	3002	3004	2997	3060	1.85	2.06	0.439
444.82	2741	2741	2741		n.a.			0.251
444.91	3032	3032	3032	3039	3072	1.08	1.07	0.316
459.33	2699	2698	2699	2709	2782	2.86	2.62	1.490
459.34	2730	2728	2729		n.a.			1.055
476.48	2769	2768	2769	2774	2787	0.66	0.47	0.479
476.58	2779	2778	2779		n.a.			0.543

Tab. 9.6: Results of measurements of the water content and saturated water content

Sample	Water content	Saturated water content
Depth	w	w_{sat}
[m bgs]	[%]	[%]
166.12	0.08	0.11
166.34	0.09	0.16
201.13	0.09	0.06
201.23	0.05	0.06
347.62	0.14	0.20
347.63	0.12	0.19
417.75	0.11	0.05
417.85	0.03	0.05
443.29	0.07	0.17
443.39	0.02	0.14
444.82	0.06	0.09
444.91	0.05	0.10
459.33	0.14	0.56
459.34	0.14	0.37
476.48	0.06	0.17
476.58	0.10	0.20

9.3.2 Thermo-physical properties

Specific heat capacity, thermal conductivity and thermal diffusivity were determined for the dry and the saturated rock disc samples using the “hot disc basic system” of the company Hot Disk AB (Fig. 9-20 and Fig. 9-21 a). Main component of the experimental setup to measure the thermo-physical properties is a heating sensor in the form of a double spiral made from a thin metal foil, which is emplaced in an insulator (e.g. kapton). This sensor is installed in between the regarded sample material (Fig. 9-21 b) and is heated subsequently (Hot Disk

AB, 2007). The principle of the measuring system is shown in Fig. 9-20, measuring sensors are shown in Fig. 9-21c. Logging the change in the resistance of the sensor in time allows quantification of the thermal conductivity of the regarded material. The sensor is the heat source and a dynamic sensor at the same time.

This system delivers the specific heat capacity per volumetric unit in $MJ \cdot m^{-3} \cdot K^{-1}$. Dividing this value by the bulk density of the sample gives the specific heat capacity per mass unit.

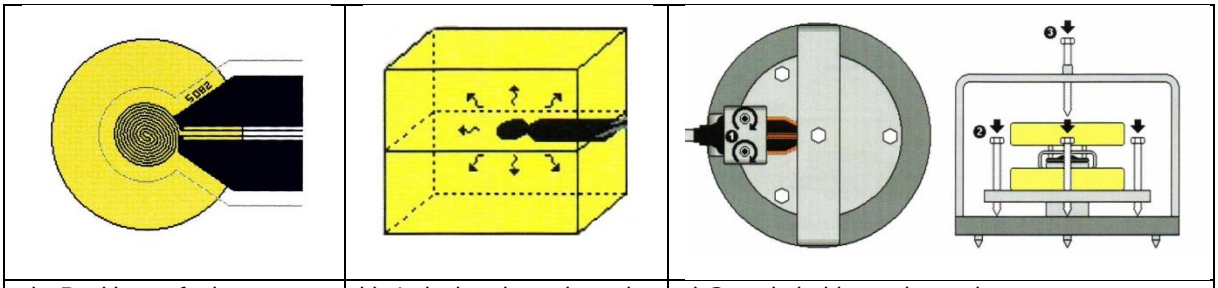

a) Position of the sensor within the sample (yellow)	b) Inducing heat into the sample	c) Sample holder and sample

Fig. 9-20: Experimental principle of the Hot Disk Basic System (Hot Disk AB, 2007)

Fig. 9-21: a) Hot Disk Basic System and vacuum exsiccator, b) Inner chamber and installed sample, c) Measuring sensors of the Hot Disk Basis System

In a first step, the rock discs were dried according to DIN 18121-1 (DIN, 1998). They were fixated in the “hot disc basic system” by applying a slight contact pressure to ensure the coupling between the rock disc and the heat detector. The thermo-physical properties were measured at 25°C and at temperature intervals of 20°C between 50°C and 150°C after applying a constant temperature for two hours for each measurement. Afterwards, the samples were saturated with synthetic solution (Tab. 9.3). Therefore they were placed in a vacuum exsiccator for one week, followed by another four weeks in the exsiccator without application

of a vacuum but with a cover of synthetic solution. Bulk density and effective porosity were determined via weighing during this step. Saturated samples were again placed in the hot disc basic system and their thermo-physical properties were determined at 25°C.

Results for the thermal conductivity, the thermal diffusivity, and the specific heat capacity in dependence on the temperature of the dry samples are given in Tab. 9.7 to Tab. 9.9 and in Fig. 9-22 to Fig. 9-24. The resulting heat and temperature conductivities decrease with increasing temperature for all samples. The specific heat capacity increases with increasing temperature. The samples which stem from ca. 417 m depth below ground surface (biotite-plagiogneiss, banded) show an unspecific trend in the thermal conductivity and specific heat capacity for the middle temperature range, while their thermal diffusivity shows the same trend as the other samples. Repeated measurements at 25°C confirm the first measurements, thus they are not included in the tables and figures presented here.

Tab. 9.7: Results of measurements of the heat conductiviuity of the dry rock disc samples in dependence on the temperature

Temperature	**Thermal conductivity**							
T [°C]	**K [W·m^{-1}·K^{-1}]**							
Depth [m bgs]	**166.12 166.34**	**201.13 201.23**	**347.62 347.63**	**417.75 417.85**	**443.29 443.39**	**444.82 444.91**	**459.33 459.34**	**476.48 476.58**
25	2.879	3.129	2.784	2.545	3.081	2.958	3.869	2.613
50	2.849	3.010	2.681	2.754	3.073	3.026	3.286	2.636
70	2.817	2.985	2.672	2.685	3.047	2.944	3.150	2.578
90	2.720	2.948	2.646	2.598	3.061	2.983	3.147	2.565
110	2.724	2.916	2.603	2.250	3.042	2.952	3.066	2.544
130	2.668	2.857	2.578	2.159	3.023	2.989	2.919	2.527
150	2.647	2.835	2.530	2.233	2.994	2.941	2.815	2.480

Tab. 9.8: Results of measurements of the temperature conductiviuity of the dry rock disc samples in dependence on the temperature

Temperature	**Thermal diffusivity**							
T [°C]	**β [mm^2·s^{-1}]**							
Depth [m bgs]	**166.12 166.34**	**201.13 201.23**	**347.62 347.63**	**417.75 417.85**	**443.29 443.39**	**444.82 444.91**	**459.33 459.34**	**476.48 476.58**
25	1.589	1.004	1.840	1.488	1.126	1.322	2.097	1.373
50	1.357	1.002	1.347	1.576	1.064	1.259	1.769	1.311
70	1.287	0.954	1.308	1.359	0.989	1.268	1.679	1.297
90	1.284	0.930	1.208	1.397	0.990	1.195	1.475	1.243
110	1.229	0.904	1.169	1.400	0.959	1.110	1.329	1.199
130	1.231	0.856	1.117	1.353	0.942	1.079	1.290	1.149
150	1.156	0.8489	1.083	1.291	0.912	1.069	1.273	1.130

Tab. 9.9: Results of measurements of the specific heat capacity of the dry rock disc samples in dependence on the temperature

Temperature	Specific heat capacity							
T [°C]	c [MJ·kg^{-1}·K^{-1}]							
Depth [m bgs]	166.12 166.34	201.13 201.23	347.62 347.63	417.75 417.85	443.29 443.39	444.82 444.91	459.33 459.34	476.48 476.58
25	6.72E-04	9.25E-04	7.28E-04	5.86E-04	9.09E-04	7.58E-04	6.79E-04	6.85E-04
50	7.79E-04	8.92E-04	7.20E-04	5.98E-04	9.59E-04	8.14E-04	6.82E-04	7.24E-04
70	8.12E-04	9.28E-04	7.40E-04	6.77E-04	1.02E-03	7.86E-04	6.90E-04	7.16E-04
90	7.85E-04	9.41E-04	7.93E-04	6.37E-04	1.03E-03	8.45E-04	7.85E-04	7.43E-04
110	8.22E-04	9.58E-04	8.06E-04	5.51E-04	1.05E-03	9.01E-04	7.47E-04	7.64E-04
130	8.04E-04	9.91E-04	8.35E-04	5.46E-04	1.07E-03	9.38E-04	8.33E-04	7.92E-04
150	8.49E-04	9.91E-04	9.16E-04	5.92E-04	1.09E-03	9.32E-04	8.24E-04	7.90E-04

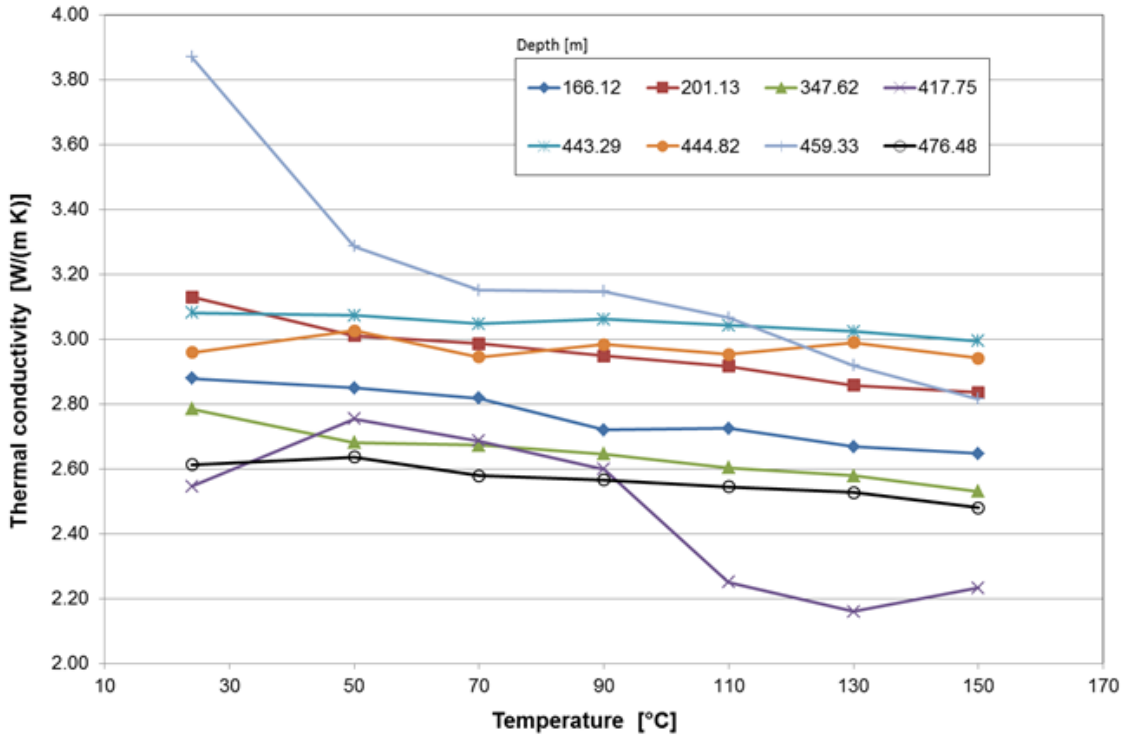

Fig. 9-22: Results of measurements of the thermal conductivity of the dry rock disc samples in dependence on the temperature

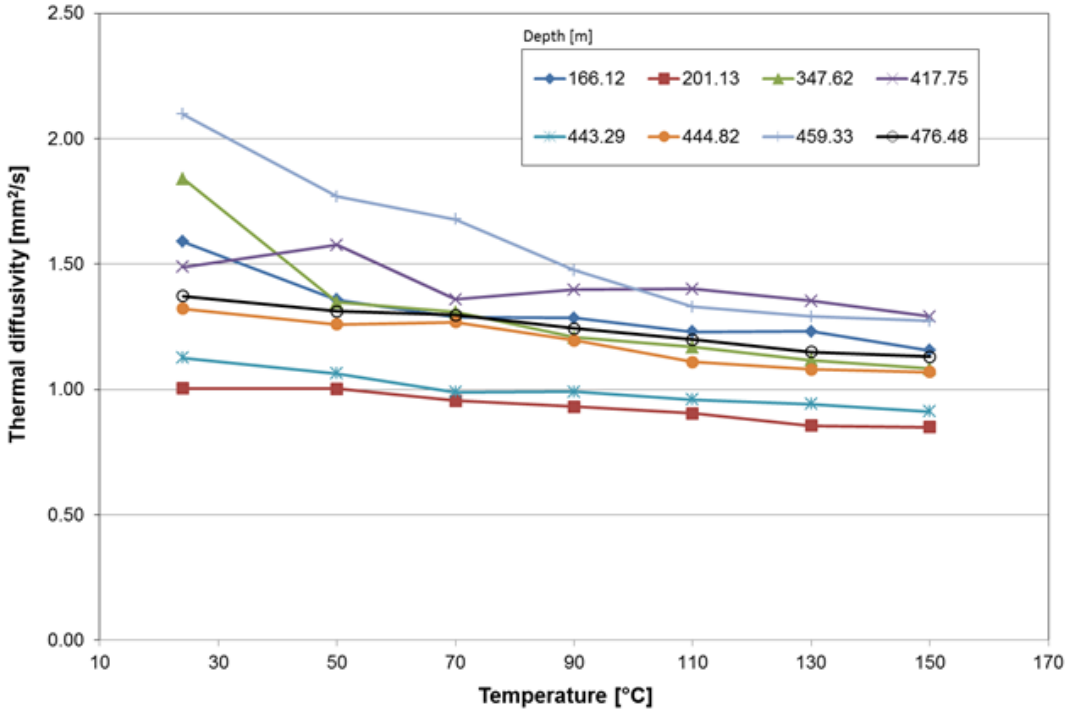

Fig. 9-23: Results of measurements of the thermal diffusivity of the dry rock disc samples in dependence on the temperature

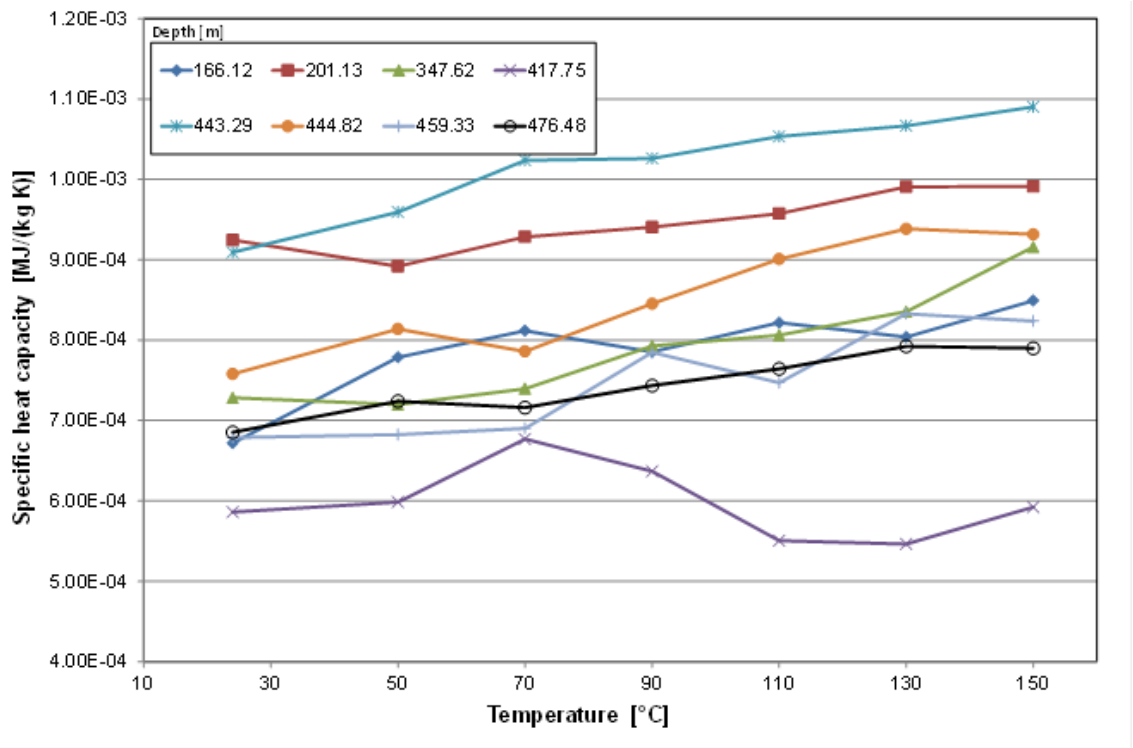

Fig. 9-24: Results of measurements of the specific heat capacity of the dry rock disc samples in dependence on the temperature

Comparing the results for the dry samples with those measured on the saturated samples shows no significant difference between the thermo-physical properties. Obviously, due to the very low porosities and thus low water content of the saturated samples, the rock matrix is the crucial factor for the thermo-physical properties. Results of the measurements are given in Tab. 9.10.

Tab. 9.10: Results of measurements of the thermal conductivity, thermal diffusivity and specific heat capacity of the saturated rock disc samples at 25 °C

Sample	Thermal conductivity	Thermal diffusivity	Specific heat capacity
Depth [m bgs]	K [$W \cdot m^{-1} \cdot K^{-1}$]	β [$mm^2 \cdot s^{-1}$]	c [$MJ \cdot kg^{-1} \cdot K^{-1}$]
166.12 166.34	2.896	1.567	6.85E-04
201.13 201.23	2.905	0.878	9.82E-04
347.62 347.63	2.859	1.329	7.78E-04
417.75 417.85	3.272	1.448	7.74E-04
443.29 443.39	3.158	1.225	8.56E-04
444.82 444.91	2.767	1.289	7.07E-04
459.33 459.34	3.664	3.183	4.22E-04
476.48 476.58	2.803	1.293	7.80E-04

9.3.3 Hydraulic properties

Measurements of the permeability of the samples were performed in permeability cells (Fig. 9-25). Samples are fixated in the stainless steel containers with silicon. The flow through the samples takes place from the bottom to the top. Analyses were run until reaching a steady-state flow through the sample.

Fig. 9-25: Permeability cell used for the determination of the gas and water permeabilities of the samples

9.3.3.1 Gas permeability

The gas permeability was determined with nitrogen. Measurements were conducted at different injection pressures. For the evaluation, the extension of Darcy's law to compressible media was applied for steady-state flow as follows:

$$k_g = \frac{2 \cdot q_g \cdot \mu_g \cdot l \cdot p_0}{A \cdot \left(p_1^2 - p_0^2\right)}$$

with:

kg	gas permeability [m^2]
qg	flow rate of the gas [$m^3\ s^{-1}$]
μg	viscosity of the gas [Pas] = $1.786 \cdot 10^{-5}$ Pas
l	length of the sample [m]
A	cross section of the sample [m^2]
p0	atmospheric pressure [Pa]
p1	injection pressure (absolute) [Pa]

Results of the measurements of the gas permeability are listed in Tab. 9.11.

Tab. 9.11: Gas permeabilities [m^2] at different injection pressures

Injection pressure (gauge) [MPa]	Sample, depth [m bgs]							
	166.12 166.34	201.13 201.23	347.62 347.63	417.75 417.85	443.29 443.39	444.82 444.91	459.33 459.34	476.48 476.58
0.4	3.31E-19	4.06E-20	6.67E-22	2.16E-22	1.61E-21	2.62E-17	4.00E-18	2.05E-19
0.6	2.80E-19	3.80E-20	3.66E-21	n.d	1.16E-21	2.70E-17	3.75E-18	1.45E-19
0.66	n.d	n.d	n.d	3.88E-22	n.d	n.d	n.d	n.d
0.8	2.82E-19	3.93E-20	3.27E-21	n.d	1.17E-21	2.87E-17	3.22E-18	1.34E-19
1.1	n.d	n.d	n.d	6.60E-22	n.d	n.d	n.d	n.d
Mean	2.98E-19	3.93E-20	2.53E-21	4.21E-22	1.31E-21	2.73E-17	3.66E-18	1.62E-19

n.d.: not determined

9.3.3.2 Water permeability

The water permeability was determined using the synthetic formation solution (chapter 9.1.2). It was calculated by the Darcy's law for incompressible media:

$$k_w = \frac{q_w \cdot \mu_w \cdot l}{A \cdot \Delta p}$$

with:

k_w	water permeability [m^2]
qw	flow rate of the water [$m^3\ s^{-1}$]
μw	viscosity of the water [Pas]
l	length of the sample [m]
A	cross sectional area of the sample [m^2]
Δp	pressure difference [Pa]

The viscosity of the synthetic solution was μw =$1.109 \cdot 10^{-3}$ Pas. The results for the water permeability are listed in Tab. 9.12. The water permeability could not be determined for all samples due to the technical limits of the experimental setup. Measurements in the available permeability cell are not feasible at permeabilities lower than ca. 1E-20 m^2.

Comparing the gas and the water permeability of the samples (Tab. 9.12) shows that the water permeabilities are generally lower than the gas permeabilities with a factor of one to three orders of magnitude (Fig. 9-26). Both the gas and the water permeability show a decreasing trend with depth. At a depth between 440 m and 580 m below ground surface, a sudden increase in both permeabilities can be observed. This concerns the contact of the

dolerite with the lamprophyre as well as the migmatite and the migmatized biotite plagiogneiss.

Tab. 9.12: Water permeabilities [m^2] at different injection pressures

Injection pressure (gauge) [MPa]	Sample, depth [m bgs]							
	166.12 166.34	201.13 201.23	347.62 347.63	417.75 417.85	443.29 443.39	444.82 444.91	459.33 459.34	476.48 476.58
0.1	n. d.	n. d.	n. d.	n. d.	n. d.	n. d.	2.86E-18	n. d.
0.2	8.71E-20	n. d.	n. d.	n. d.	n. d.	2.15E-19	6.39E-19	n. d.
0.3	n. d.	n. d.	n. d.	n. d.	n. d.	n. d.	7.96E-19	2.32E-20
0.5	n. d.	n. d.	n. d.	n. d.	n. d.	1.25E-19	5.53E-19	n. d.
0.8	7.27E-20	n. d.	n. d.	n. d.	n. d.	1.72E-19	4.47E-19	3.93E-20
1.0	6.61E-20	n. d.	n. d.	n. d.	n. d.	8.02E-20	3.72E-20	3.94E-20
Mean	6.64E-20	n. d.	n. d.	n. d.	n. d.	1.37E-19	1.28E-18	3.67E-20

n.d.: not determined

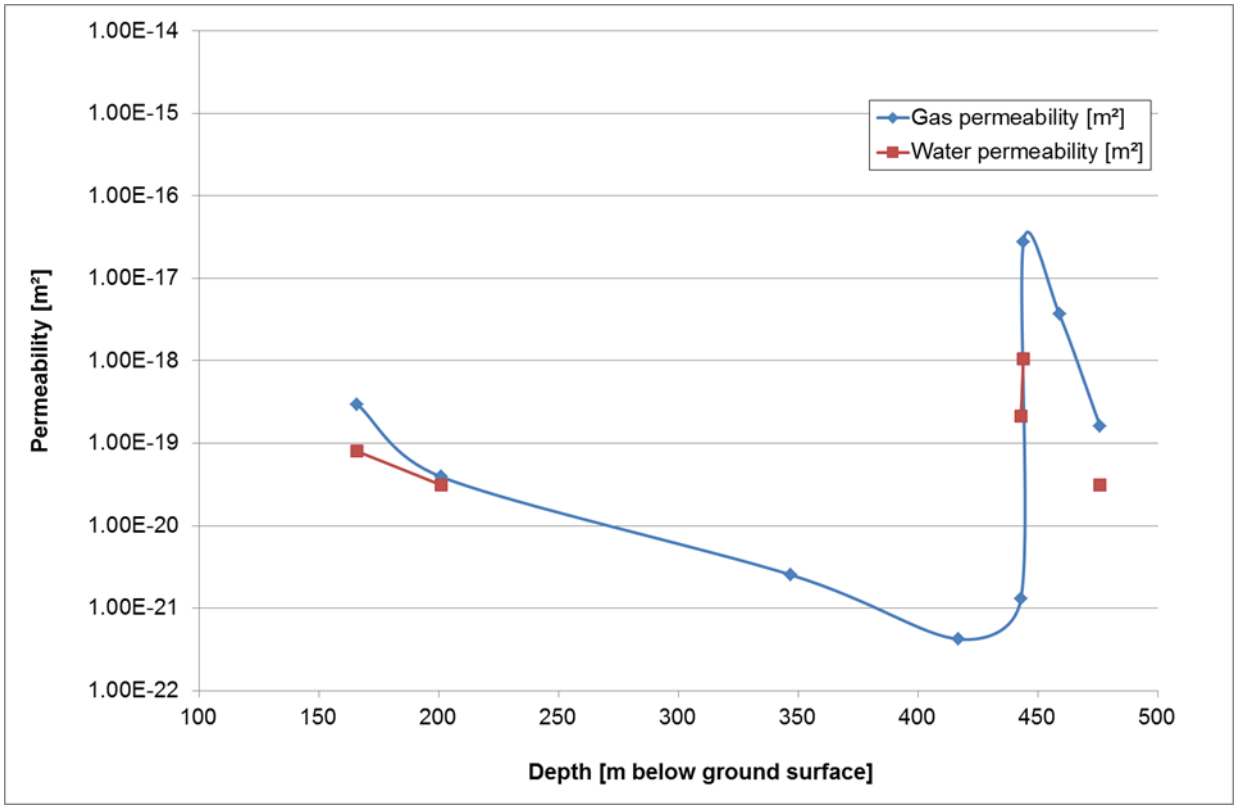

Fig. 9-26: Comparison of gas and water permeability of the considered samples

9.3.4 Mechanical properties

9.3.4.1 Dynamic elastic parameters

The dynamic elastic parameters were determined by means of ultrasonic measurements (Fig. 9-27) for four of the drill core samples (depth bgs: 201.14 m, 347.64 m, 444.82 m, and 476.55 m). These were carried out in radial direction at a distance of 1 cm (Fig. 9-28). Measurements in radial direction were conducted at six different points of each sample, indicated by the yellow circle in Fig. 9-28.

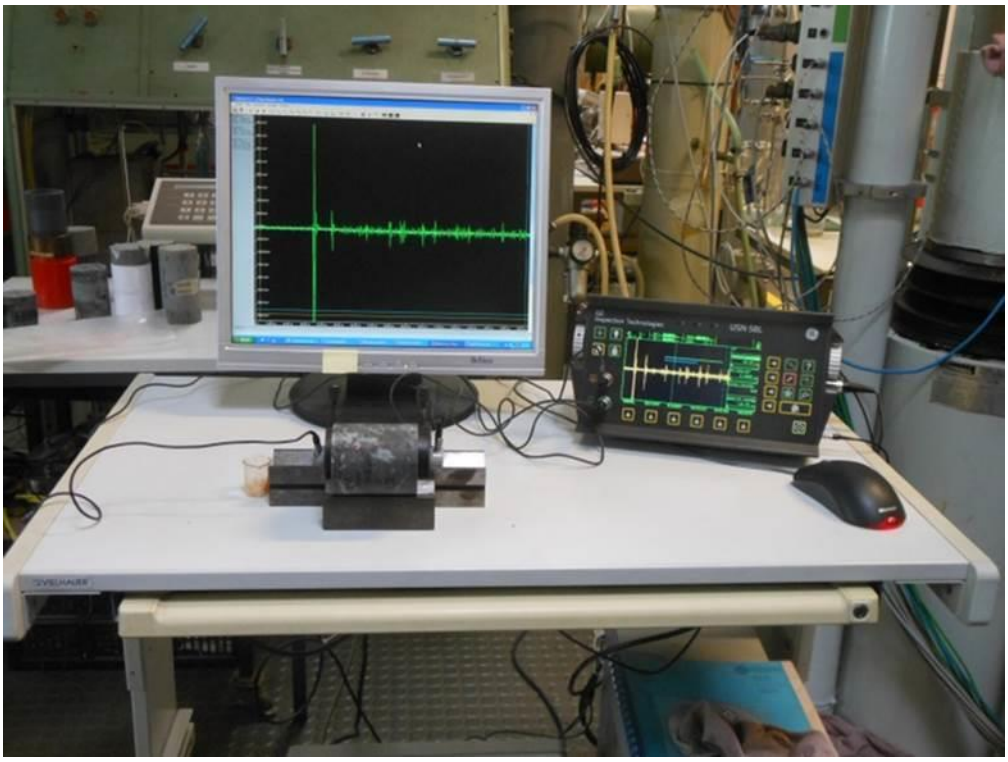

Fig. 9-27: Experimental setup for the ultrasonic measurements of the dynamic elastic parameters

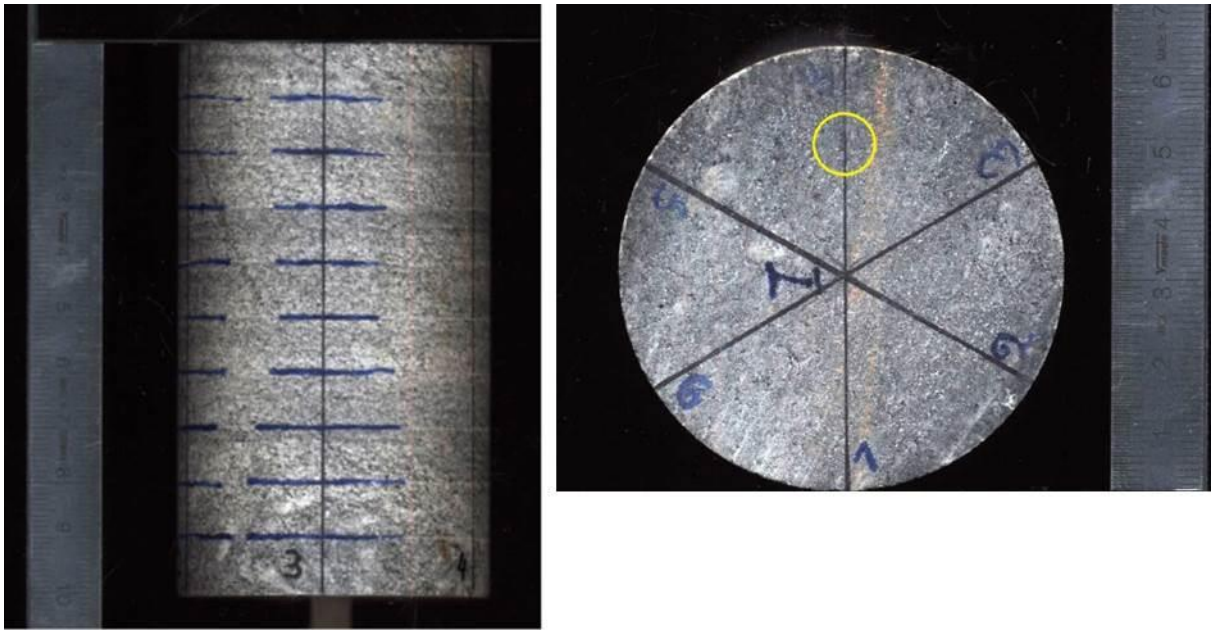

Fig. 9-28: Sample of a biotite plagiogneiss (201.14 m bgs) with marks of the measurement locations in radial direction (left) and axial direction (right, yellow circle)

Measurements were averaged for each sample and dynamic elastic parameters were calculated using the bulk density (Militzer et al., 1987):

Young's modulus E_{dyn}

$$E_{dyn} = \frac{v_S^2 \cdot \rho_{ges} \cdot \left(3v_P^2 - 4v_S^2\right)}{v_P^2 - v_S^2}$$

with

v_s shear wave velocity (longitudinal) [m s^{-1}],

ρ_b bulk density [kg m^{-3}], and

v_p compressional wave velocity [(transversal) m s^{-1}].

The Poisson's ratio ν_{dyn} was calculated by

$$\nu_{dyn} = \frac{v_P^2 - 2v_S^2}{2 \cdot \left(v_P^2 - v_S^2\right)}$$

Results of the measurements are depicted in Fig. 9-29 and Fig. 9-30. Both the axial and the radial measurements deliver similar results for the dynamic elastic parameters for each sample. No correlation can be identified between these results and the depth. Only a slight correlation exists between these results and the petrophysical properties of the samples. Three of the samples are biotite plagiogneisses, while one of the samples is from the contact of the dolerite and the lamprophyre (444.82 m bgs). This sample shows a higher Young's modulus than the other three samples, while for the Poisson's ratio this trend is not observed.

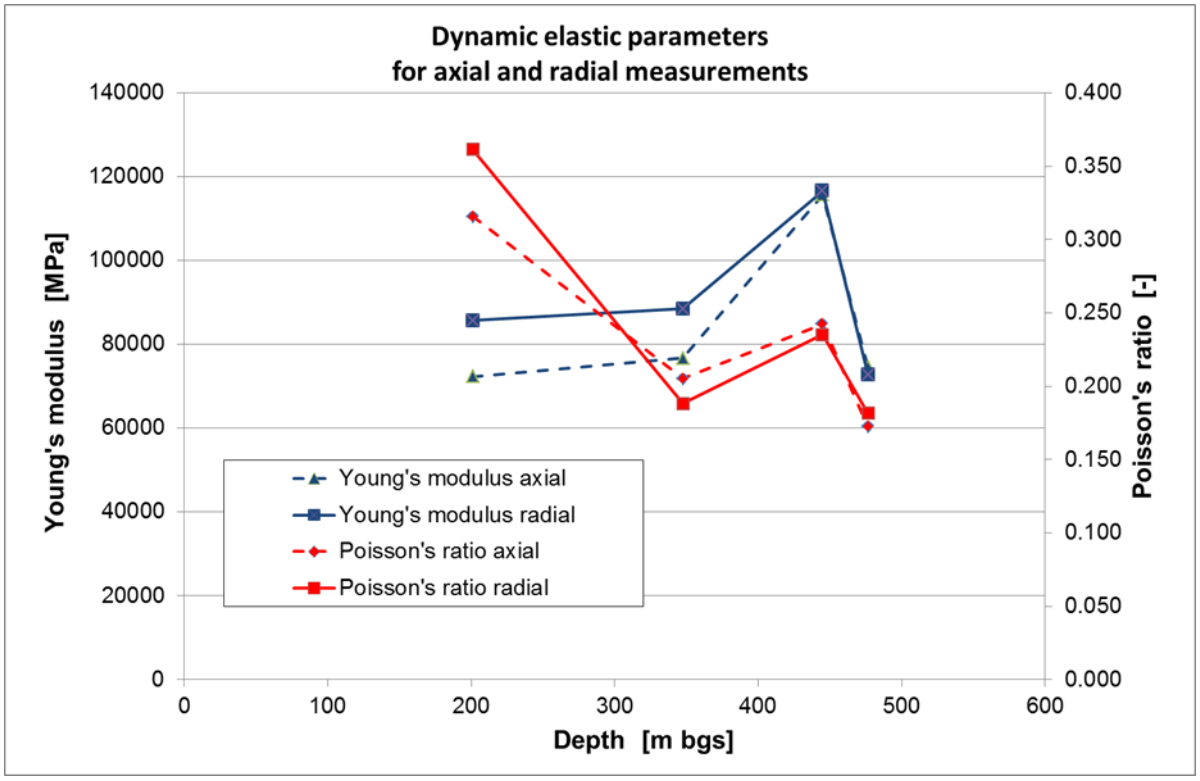

Fig. 9-29: Young's moduli and Poisson's ratio for the axial and transversal measurements

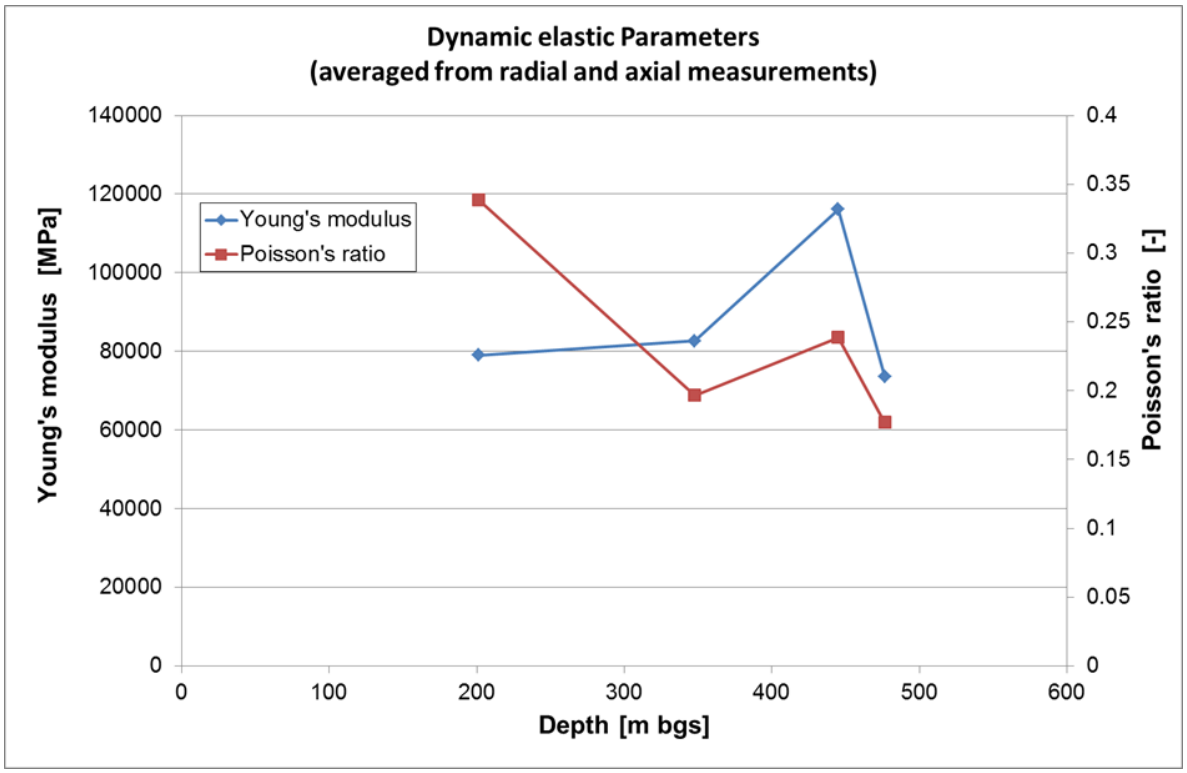

Fig. 9-30: Averaged Young's moduli and Poisson's ratio

9.3.4.2 Static elastic parameters

The static elastic parameters were determined via triaxial tests (Fig. 9-31). With these, it is possible to determine the permeability, deviatoric stress, axial deformation, and Young's modulus. The geomechanical properties of rock samples are dependent on the length of the samples. Available samples showed variable lengths of 54 mm to 100 mm. Thus, all experiments were conducted applying the same confining pressure of 2 MPa. A failure criterion as a function of the variable confining pressure cannot be determined this way. The samples were placed in the triaxial cell. In a first step, the samples were consolidated in a hydrostatic stress condition. The gas permeability was measured simultaneously at a maximum injection pressure of 1 MPa.

Fig. 9-31: Experimental setup for the triaxial measurements of the static elastic parameters

The second step is called the deviatoric phase. The axial deformation was regulated at 0.1 mm min^{-1}. During the loading phase before the failure of the sample, the loading is interrupted by unloading phases in order to determine the static elastic parameters Young's modulus and Poisson's ratio. After failure of a sample, the experiments were terminated.

Figure 9-32 shows the courses of strain and deformation for the four samples in dependence on the deviatoric pressure. Figure 9-33 depicts the change in volume depending on the axial deformation. The first two samples (201.14 m and 347.67 m depth) show a distinct failure behaviour with failures at lower axial deformations than the other two samples. The sample from a depth of 444.82 m shows a higher axial deformation at a medium deviatoric pressure. This is due to the different petrophysical properties of the sample. Beside the different mineralogical composition of this sample (see Tab. 9.2), this drill core sample shows a dissenting fracture network compared with the other three samples. The fourth sample from a depth of 476.66 m shows no distinct failure behaviour. This may be caused by an expansion of the fracture network without a distinct point of failure.

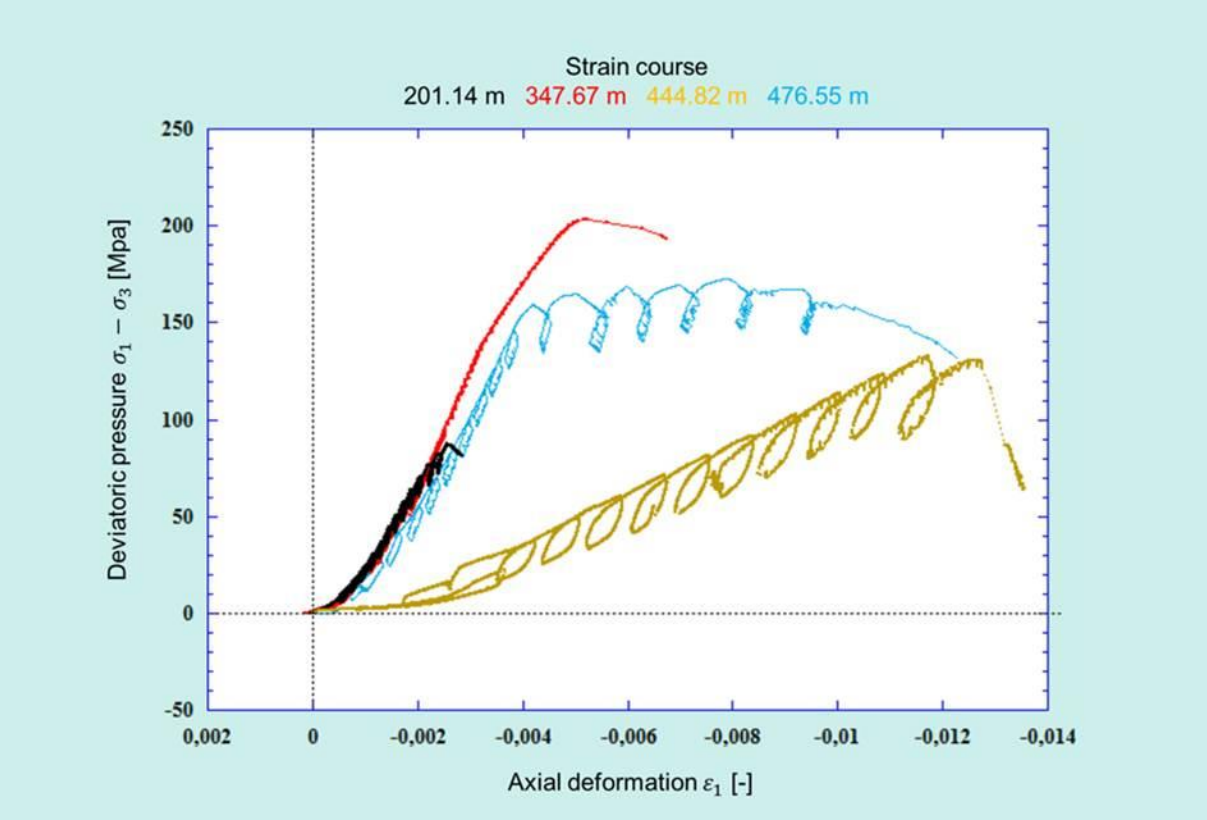

Fig. 9-32: Strain and deformation course of the four samples

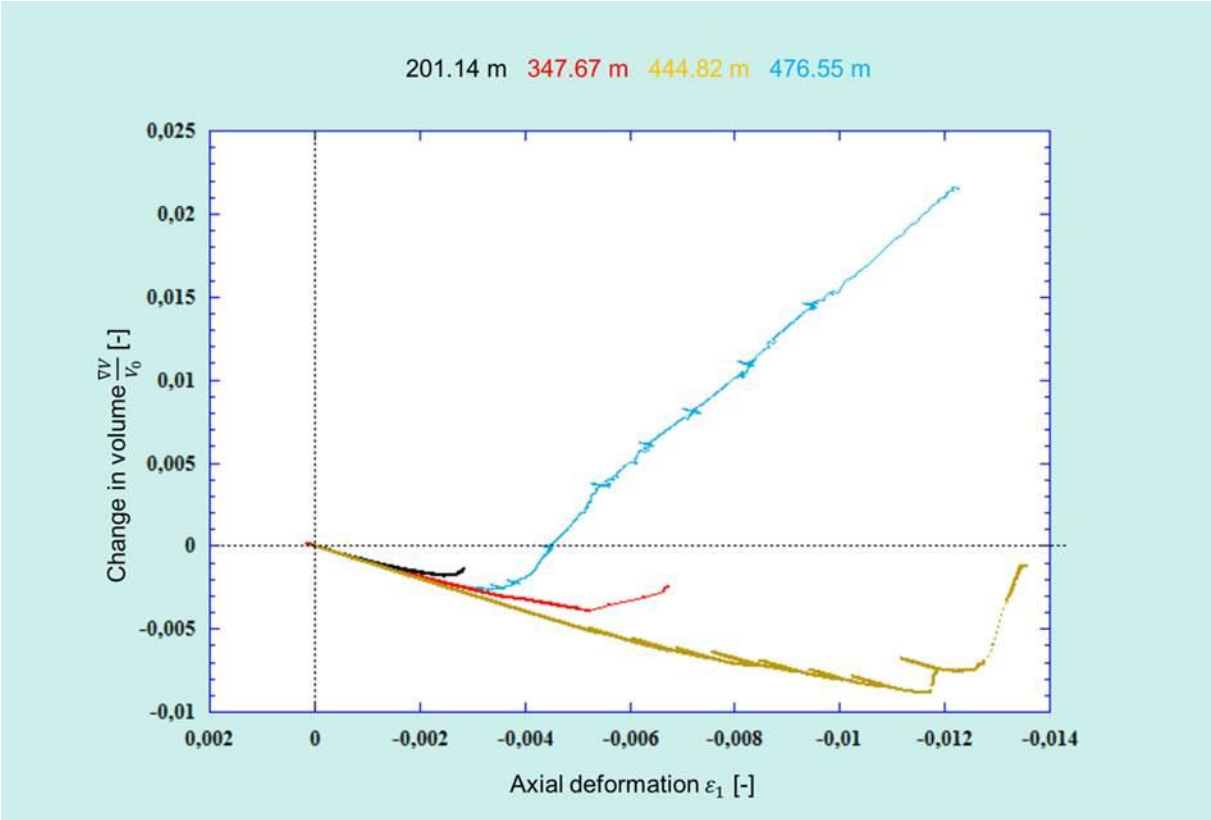

Fig. 9-33: Change in volume of the four samples

The gas permeability of the samples rises during the experiments and shows an abrupt rise at failure (Fig. 9-34). Here, the sample from 476.55 m depth shows a clear rise in the permeability and no divergent behaviour from the other samples. As for the determination of the permeability described in chapter 9.1.4, there is no trend in the permeability depending on the depth of the samples (Fig. 9-35). Excluding the rock sample from the contact between the dolerite and the lamprophyre from the evaluation delivers a decreasing trend of the permeabilities of the biotite plagiogneisses with depth. Comparing the results for the gas permeability of the different analyses (Fig. 9-36) they show the same trend for all methods but higher permeability values for the data collected in the triaxial tests. This may be due to the fact that here, pressure was already applied to the samples and new pathways for flow may have been opened during determination of the parameters.

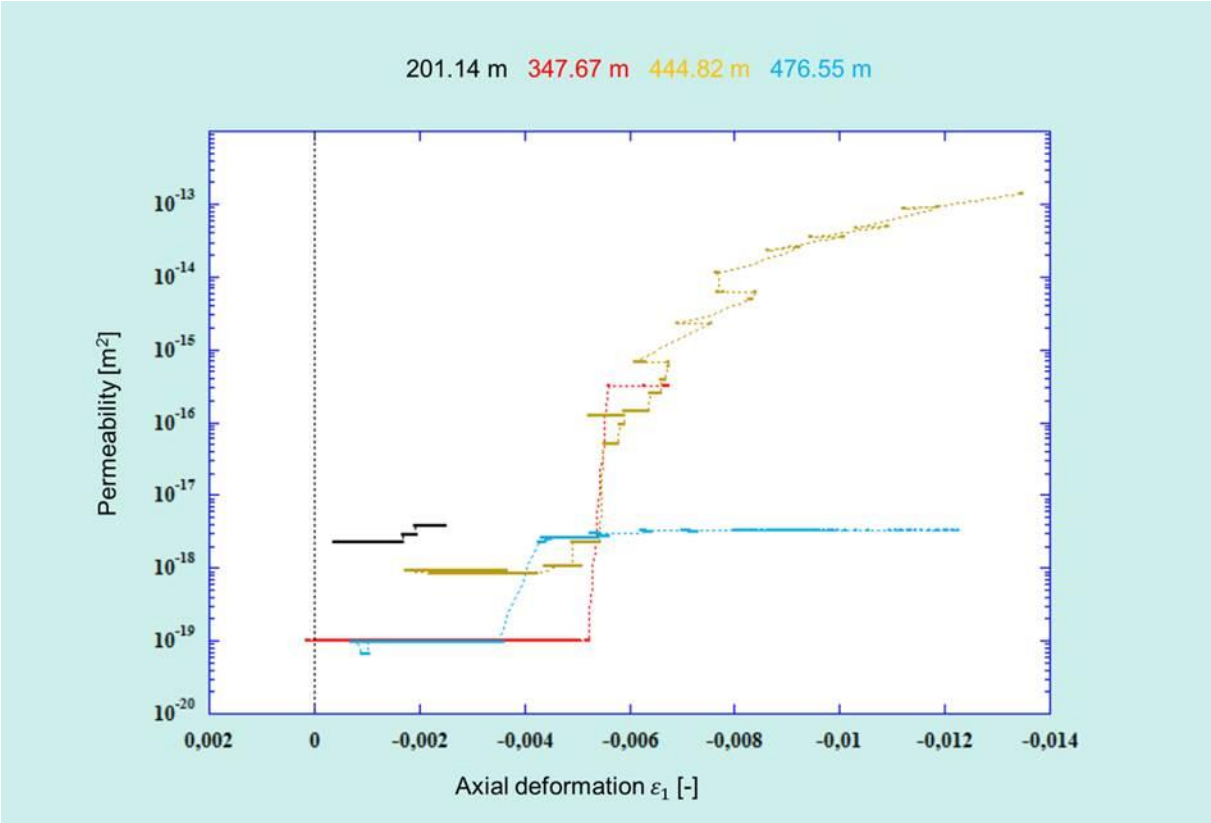

Fig. 9-34: Change in permeability of the four samples

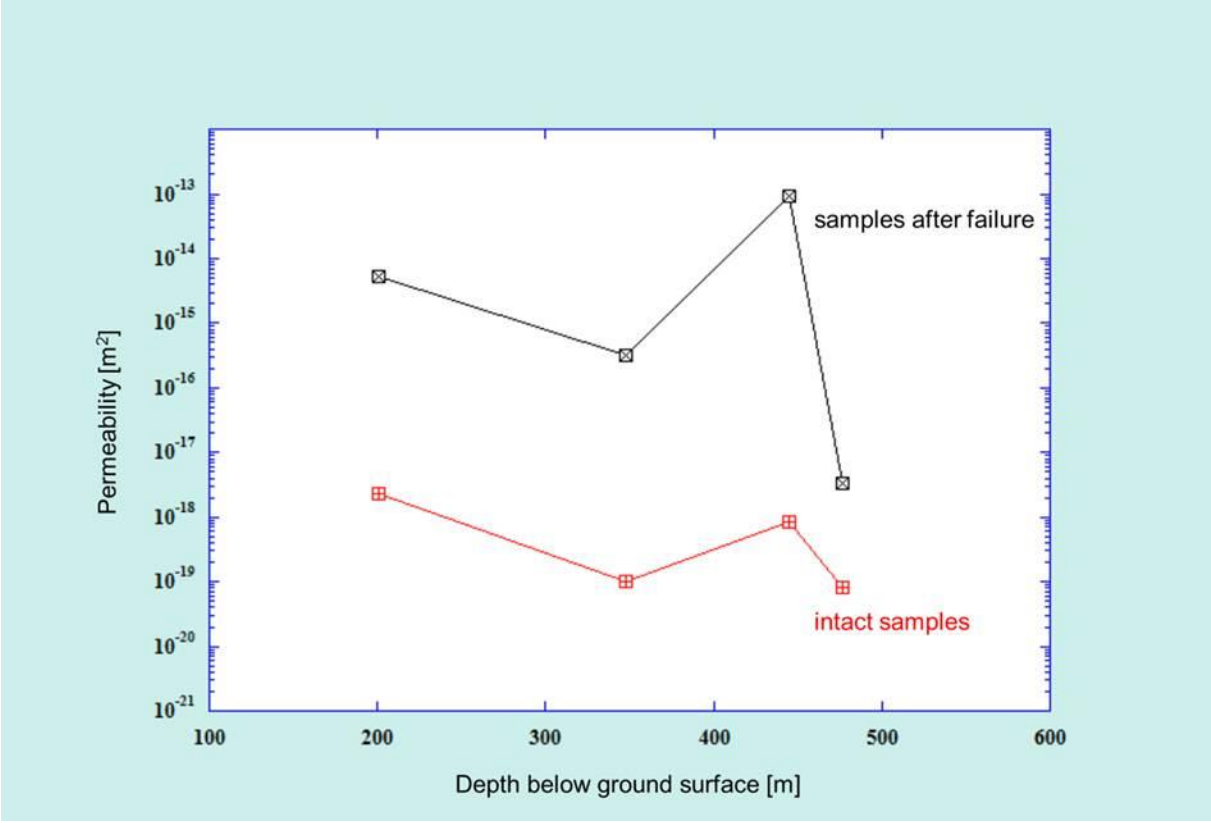

Fig. 9-35: Permeability of the samples before and after failure

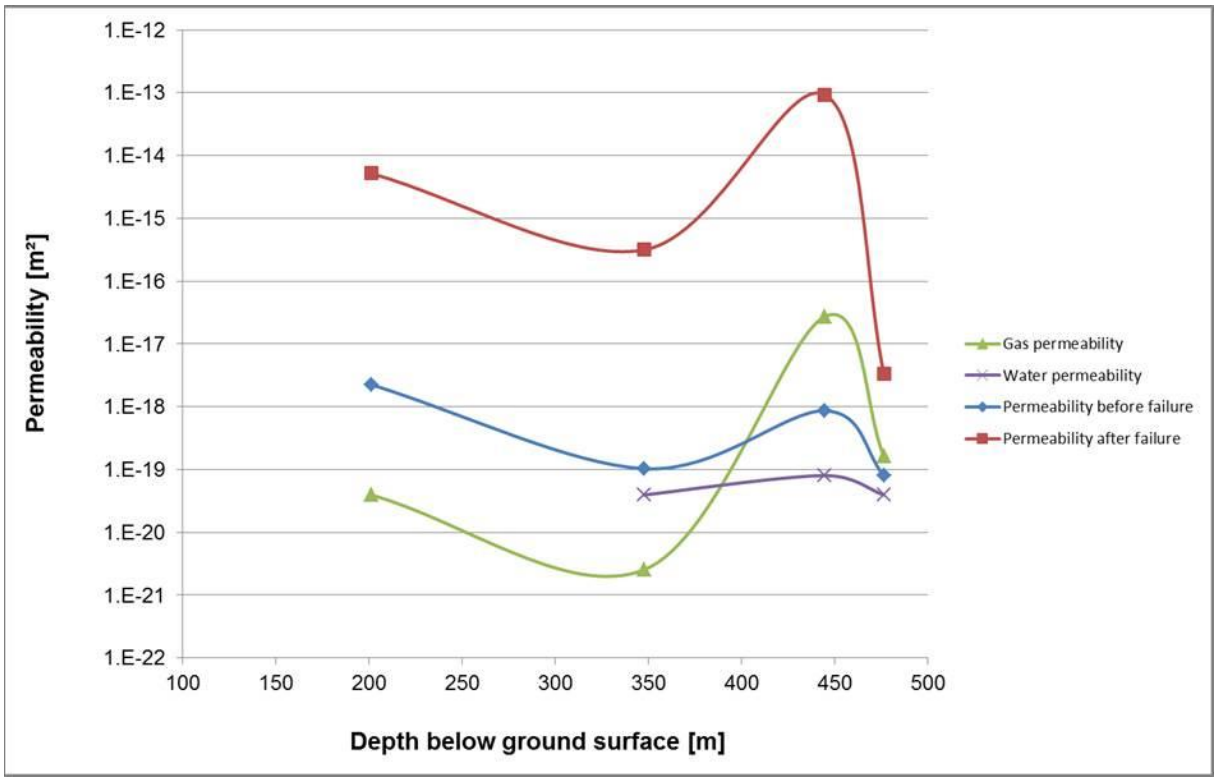

Fig. 9-36: Comparison of all data on the permeability of the rock samples determined during the analyses described in this report

The static Young's moduli are given in Figure 9-37 to Figure 9-40. Generally, the dynamic Young's moduli are higher than the static moduli. During the loading period, open fractures are compressed, leading to an increasing axial deformation and increasing Young's modulus. At low levels of loading, the sample expands radially. Additionally, fractures are compressed. At higher levels of deviatoric pressure, after discontinuities in the sample have been eliminated, the radial expansion gains influence. The sample from depth 476.55 m bgs shows a significantly different behaviour. Before reaching the point of dilatancy, the static Young's modulus rises gradually, which can be observed during loading as well as during unloading. Beyond the point of dilatancy, the static Young's moduli decrease during loading, indicating a rising influence of static deformation. During unloading, the Young's moduli are increasing, but since the sample is already in a state of destruction, these moduli are apparent moduli only. A comparison of the dynamic and static Poisson's ratios shows the same order of magnitude for the two different analyses (Fig. 9-41 to Fig. 9-43). Again, the sample from 476.55 m bgs shows a dissenting shape of curve and order of magnitude for the Poisson's ratio. High apparent values can be observed due to the fact that the sample is already in a state of destruction.

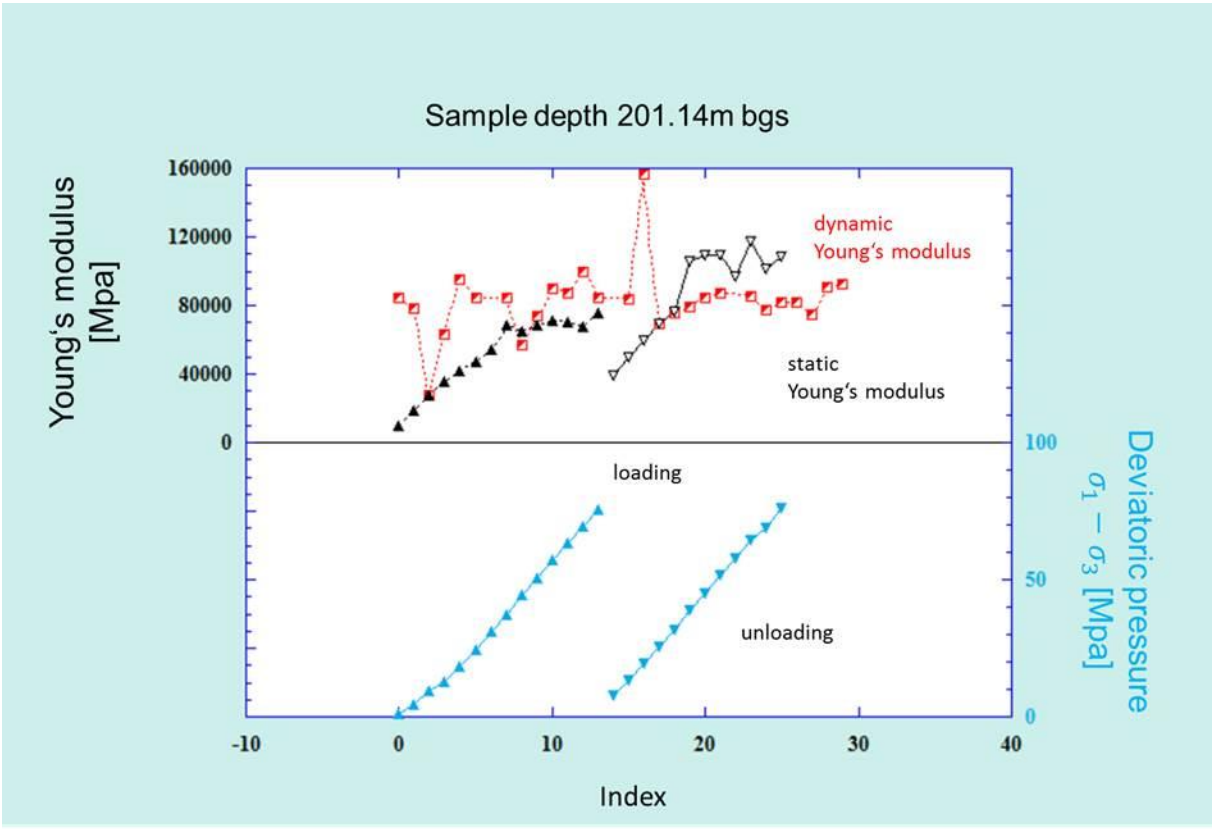

Fig. 9-37: Young's modulus and deviatoric pressure for sample depth 201.14 m bgs

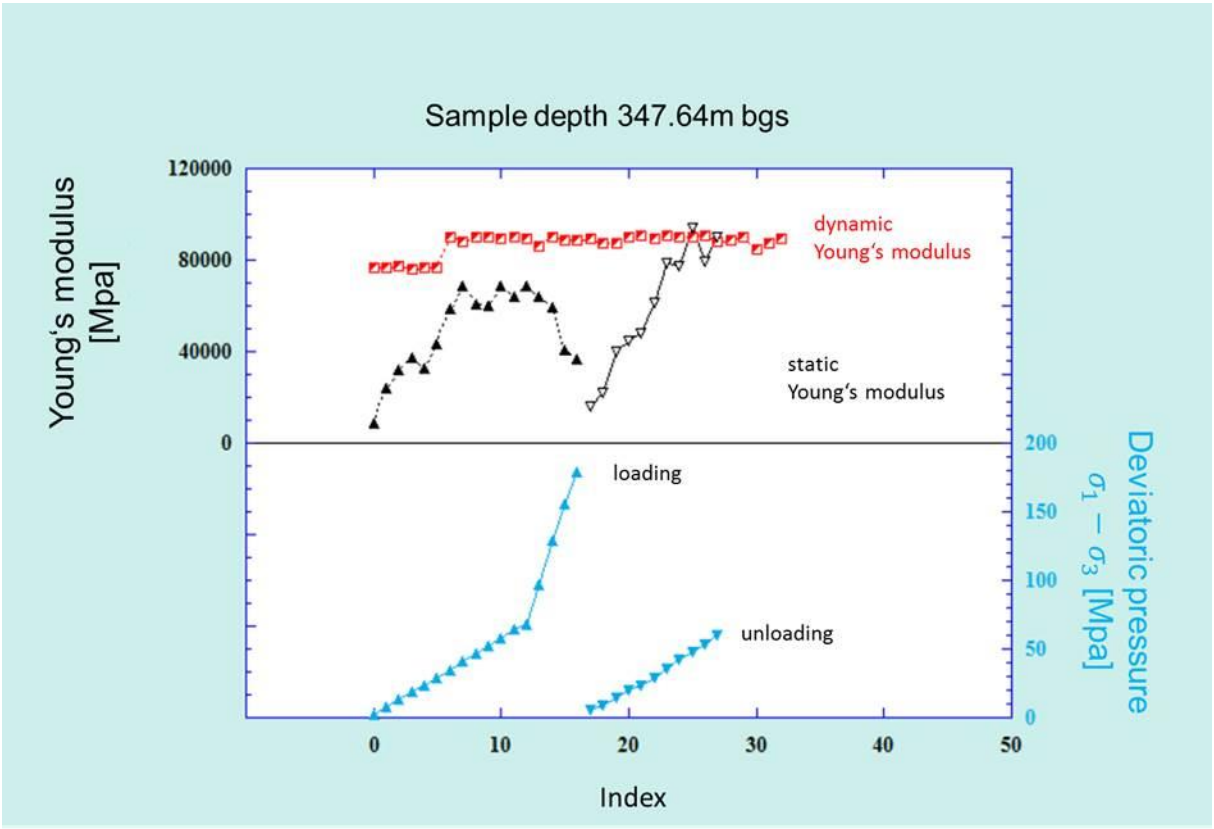

Fig. 9-38: Young's modulus and deviatoric pressure for sample 347.64 m bgs

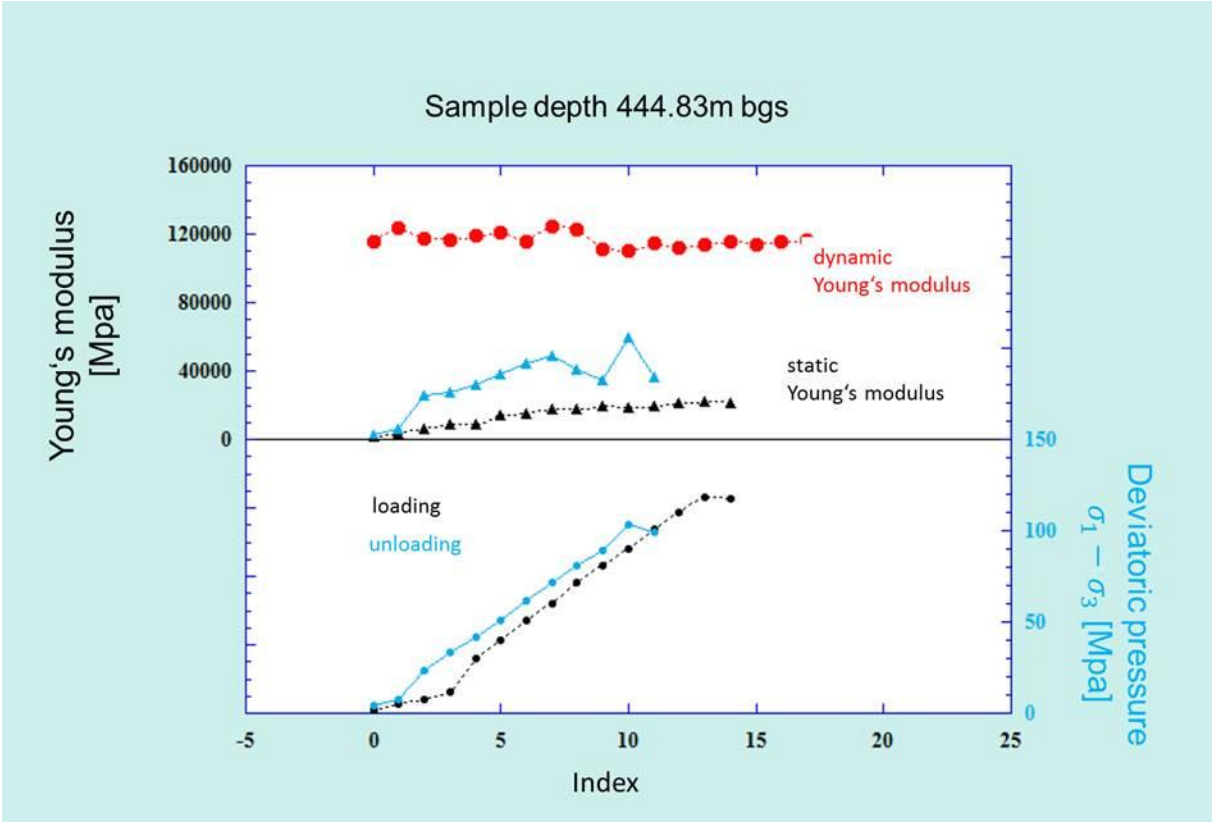

Fig. 9-39: Young's modulus and deviatoric pressure for sample 444.83 m bgs

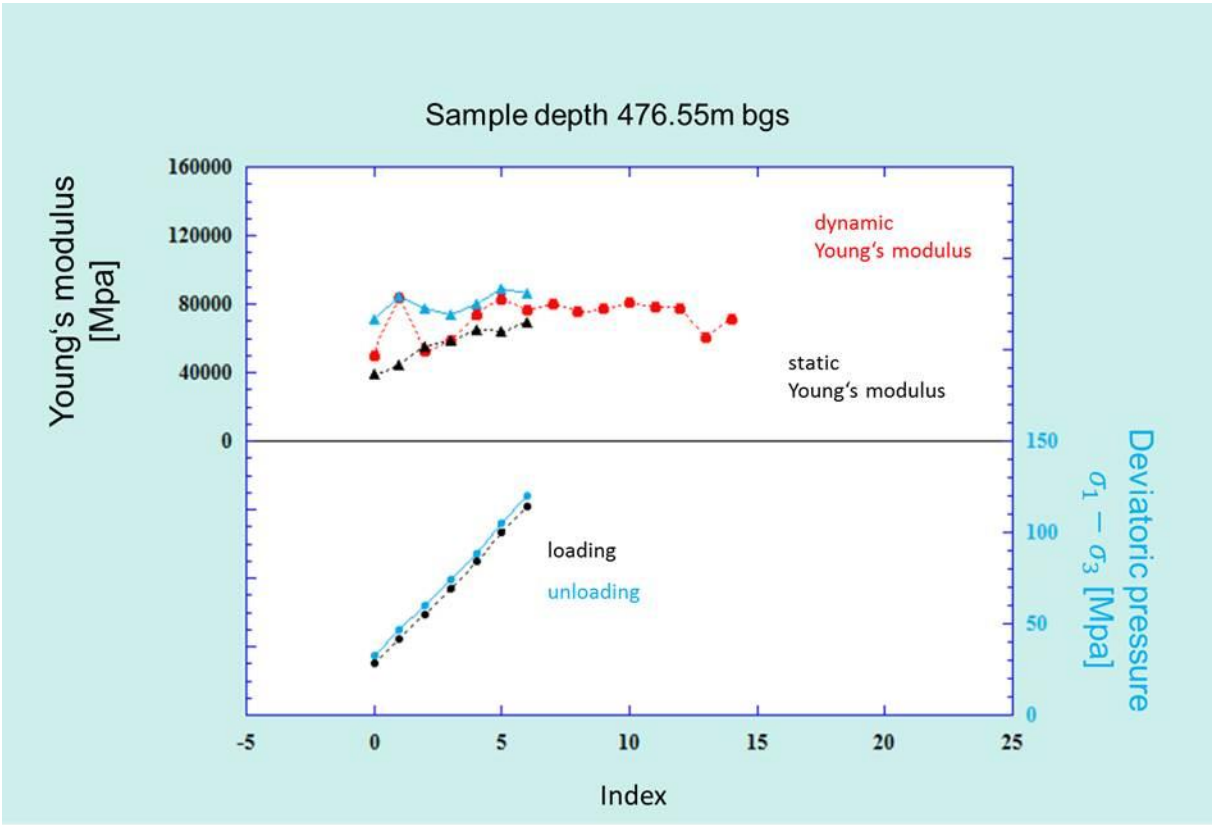

Fig. 9-40: Young's modulus and deviatoric pressure for sample 476.55 m bgs

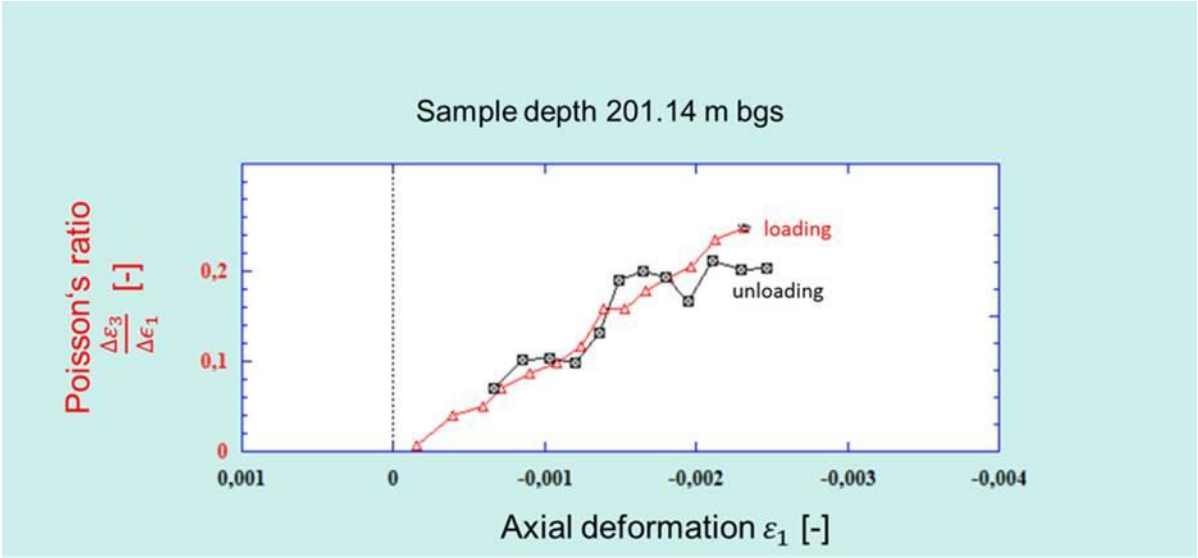

Fig. 9-41: Poisson's ratio and axial deformation for sample depth 201.14 m bgs

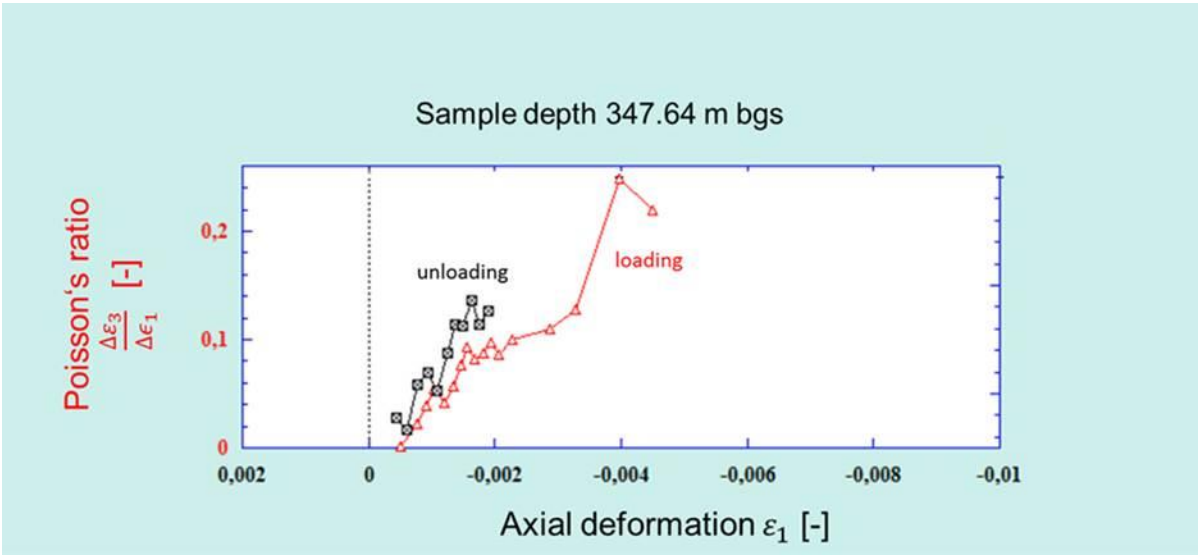

Fig. 9-42: Poisson's ratio and axial deformation for sample depth 347.64 m bgs

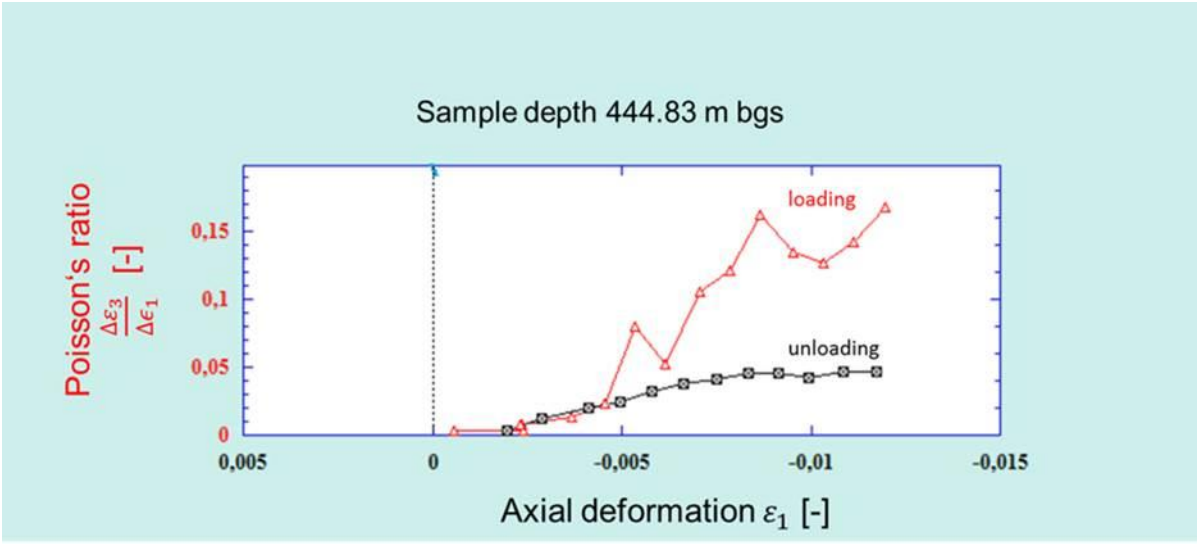

Fig. 9-43: Poisson's ratio and axial deformation for sample depth 476.55 m bgs

9.4 Sorption experiments of radionuclides

9.4.1 Background

According to the Safety Standards of IAEA and the idea of multi-barrier systems, the crystalline rocks are the last barrier to prevent radionuclide release from a repository to the environment. Thus, determination of sorption properties of host rocks towards long-lived radionuclides is essential for a safety assessment of a future HLW repository.

Time dependence of sorption of cesium(I), plutonium(IV), americium (III) and neptunium(V) onto samples of leucogranite, tonalite and granodiorite from Nizhekansky massif (Itatsky and Kamenny areas) was studied earlier (Anderson et al., 2000, 2002). The distribution coefficients are $n \cdot 10^2$ - $n \cdot 10^3$ mL/g for Cs, Pu and Am and only up to 2 mL/g for Np. The drawback of these studies is the aerobic conditions of the experiments that are not relevant for the deep geological media with low oxygen content. The presence of oxygen and other redox active substances (Fe^{2+}, H_2, O_2^{2-} etc.) are controlling the Eh values of the aqueous solutions. The redox conditions are strongly affecting the speciation of such elements as plutonium, neptunium, uranium, selenium and some others that are relevant for high level wastes. Thus, the Eh conditions have to be controlled during experiments.

Sorption of cesium, europium and uranium was studied for rock samples from the Äspö site, Sweden. Stage et al. (2012) used two types of granites for sorption experiments: «oxidized» granite contacted for a few years with atmospheric air and «unoxidized» granite that was freshly extracted from underground in Ar atmosphere. It was shown with X-ray photoelectron analysis that ca. half of the uranium that was initially added in the form of U(VI), after one month of the experiment is located in the form of U(IV) on the surface of «unoxidized» granite. This indicates that even under weakly reducing conditions (Eh ca. 0 V) uranium (and neptunium) can present in lower oxidation state.

Recently Petrov et al. (2012, 2014) studied sorption of cesium for rock samples from two areas of Nizhnekansky massif: “Kamenny” and “Itatsky”. The linear increase of the distribution coefficient of Cs with increasing biotite content in rock samples is visible in Fig 9.44. It can be explained by cation exchange mechanism of cesium, which is the case for radium as well (Huitti et al., 1996). Recently another, «Yeniseysky», site was selected as a final site for URL construction.

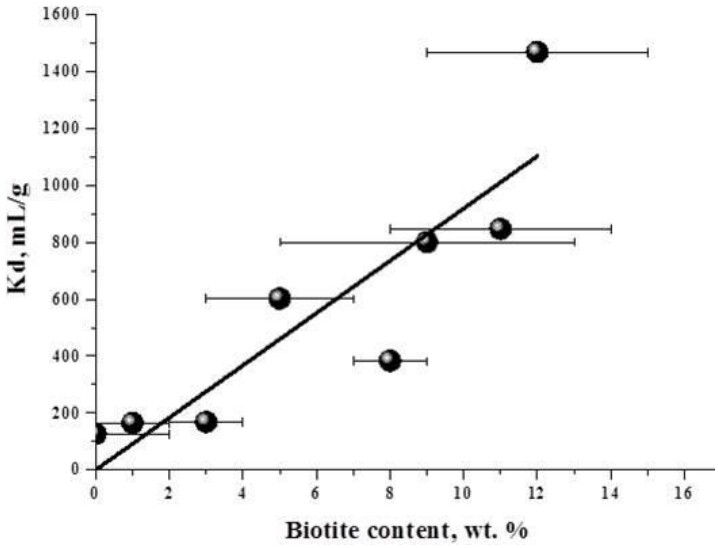

Fig. 9-44: Dependence of the distribution coefficient (Kd) of cesium on biotite content in rock samples (from Petrov et al., 2014).

The aim of the present study is to analyse the sorption behaviour of radionuclides with different chemical properties towards rock samples from Yeniseysky site in the exocontact zone of Nizhnekansky granitoid massif under controlled pH and Eh conditions and with thorough analysis of the rock samples.

9.4.2 Experimental investigations

Five rock samples from different depths (166 m, 417 m, 443 m, 459 m, 476 m) were used in our experiments and can be divided onto three types: 1 – sillimanite-containing plagiogneisses (samples 166 and 417); 2 – migmatized granito-gneisses and plagiogneisses (samples 459 and 476); 3 – intensively metamorphized gabbro-diabase (sample 443). Based on chemical composition determined by X-ray fluorescence spectromentry and on content of silica we can select intermediate (type 1), felsic (type 2) and mafic (type 3) types of igneous rocks.

Rock samples were prepared for two types of sorption experiments: set 1 – determination of distribution coefficients and time-dependencies of sorption; set 2 – determination of spatial distribution of sorbed radionuclides depending on mineral composition, structure and/or degree of metasomatic and deformation transformations. For experimental set 1 rock samples were crushed to grain size of 1-2 mm. Solid to liquid ratio was 1 : 4 in these experiments. Thick plain rock slices with polished sides and size of 8x12x30 mm were used for experimental set 2.

All sorption experiments were performed in glove-box with inert atmosphere (N_2) at room temperature. The total mineralization of simulated ground water (SGW) was 200 mg/L, main cation – Ca^{2+}, main anion – HCO_3^{2-}. SGW solution was pre-equilibrated with bentonite (Khakassiya, Russia) for 3 weeks and further filtrated with 50 nm filter. Absence of bentonite colloids in final SGW solution were determined by scanning electron microscopy with X-ray energy dispersive microanalysis. The Eh value was ca. -200 mV, pH = 7.6.

Initial concentration of all radionuclides was 10^{-9} mol/L. In experimental set 1, suspensions of crushed granites and SGW solutions of individual radionuclides were permanently shaking and aliqouts of solutions were taken after 30 minutes, 1 hour, 4 hours, 8-10 hours, 1 day, 2 days, 4 days, 1 week and 2 weeks of experiment. The specific activities of the radionuclides in solution after centrifugation were analysed by liquid-scintillation counting. The sorption efficiency (%) was calculated as a ratio of specific activity of radionuclide in solution after experiment to its initial specific activity:

$$\Gamma = \frac{I_0 - I}{I_0} \cdot 100\%$$

where I – count rate of the solution after sorption (cpm), I_0 – initial count rate (cpm).

The distribution coefficient Kd was calculated as specific activity of radionuclide sorbed on solid phase (Bq/g) divided by its specific activity in solution (Bq/mL). Spatial distribution of the sorbed radionuclides onto the surface of rock slices was analysed by digital radiography with Cyclone Storage System (PerkinElmer) after their careful washing with deionized water and drying.

9.4.3 Results and discussion

Aliquots of suspensions were taken periodically, centrifuged and measured for radionuclide content. The dependence of radionuclide sorption (%) on time is shown in Fig. 9-45 for all the investigated rock samples. Sorption of metal ions is fast, quantitative and almost independent on rock sample. It reaches 95% within 1 hour for americium, 4 hours – for plutonium and cesium. Fast sorption of actinides can be explained by fast surface complex formation with different hydroxo-groups on the surface of minerals. Sorption of radium reaches steady-state only after 7 days. We don't know for the moment the reason of such behaviour, but can only propose kinetically hindered cation exchange mechanism.

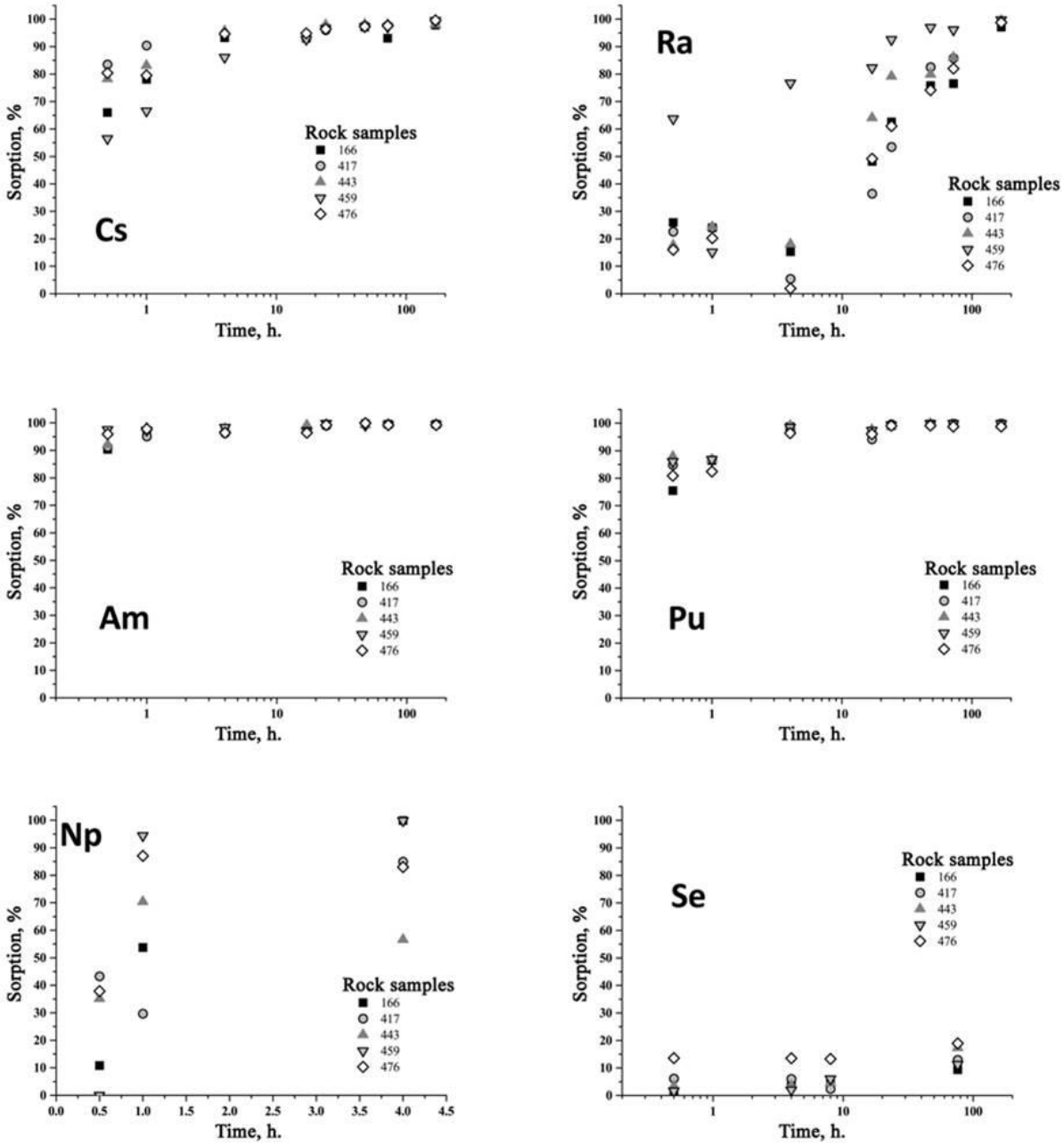

Fig. 9-45: Time-dependence of radionculide sorption onto rock samples from Yeniseysky site.

9.5 References

Anderson E.B., RogozinYu.M., Bryzgalova R.V. et al. (2000). Experimental investigation of sorption-barrier properties of granitoids of the Nizhnekanskiy Massif // Int. Conference on Material Research Society (MRS'2000), Sydney, Australia.

Anderson E.B., Rimski-Korsakov A.A., Savonenkov V.G. et al. (2002). Status of the Nizhnekanskiy Granitoid Massif as a Candidate for HLW Deep Geological Repository in Russia // Sim. on HLW, LLW, Mixed Wastes and Environmental Restoration (WM'02), Tucson, USA, Abstr. 77.

Bunthebarth, G. & Voll, G. (1991). Quartz grain coarsening by collective crystallization in contact quartzites. In: Equilibrium and Kinetics in Contact Metamorphism. The Ballachulish Igneous Complex and its Aureole (eds Voll, G., Töpel, J., Pattison, D. R. M. & Seifert, F.), pp. 251–265. Springer, New York.

DIN Deutsches Institut für Normung e. V. (Ed) (1998). DIN 18121-1: Soil, investigation and testing - Water content - Part 1: Determination by drying in oven (in Germ.). Beuth Verlag.

Gapais, D. & Barbarin, B. (1986). Quartz fabric transition in a cooling syntectonic granite, (Hermitage Massif, France). Tectonophysics, 125, 357–370.

Gower, R. J. W. & Simpson, C. (1992). Phase boundary mobility in naturally deformed, highgrade quartzofeldspathic rocks: evidence for diffusional creep. Journal of Structural Geology, 14, 301–313.

Gross, A. F. K. & van Heege, J. P. T. (1973). The high-low quartz transition up to 10 kbar pressure. Journal of Geology, 81, 717–724.

Hirth, G. & Tullis, J. (1992). Dislocation creep regimes in quartz aggregates. Journal of Structural Geology, 14, 145–159.

Hot Disk AB (2007). Instruction Manual, Hot Disk Thermal Constants Analyser.

ISC (2001). ISC-On-line Bulletin, International Seismological Centre, Thatcham, United Kingdom.

Huitti T., Hakanen M., Lindberg A. (1996). Sorption of cesium, radium, protactinium, uranium, neptunium and plutoniumon Rapakivi granite // Report Posiva-96-23, Helsinki, Finland, 57 P.

Kruhl, J. H. (1996). Prism- and basal-plane parallel subgrain boundaries in quartz: a microstructural geothermobarometer. Journal of Metamorphic Geology, 14, 581–589.

Liou, J.G., Maruyama, S. & Cho, M. (1987.) Very low-grade metamorphism of volcanic and volcaniclastic rocks - mineral assemblages and mineral facies.- In: Frey, M. (ed.): Low temperature metamorphism, 351 pp., New York (Chapman & Hall).

Mainprice, D., Bouchez, J.-L., Blumenfeld, P. & Tubia, J. M. (1986). Dominant c slip in naturally deformed quartz: Implications for dramatic plastic softening at high temperature. Geology, 14, 819–822.

Martelat, J.-E., Schulmann, K., Lardeaux, J.-M., Nicollet, C. & Cardon, H. (1999). Granulite microfabrics and deformation mechanisms in southern Madagascar. Journal of Structural Geology, 21, 671–687.

Militzer, H., Schön, J., Stötzner, U., Stoll, R. (1987). Angewandte Geophysik im Ingenieur- und Bergbau.- VEB Deutscher Verlag für Grundstoffindustrie, Leipzig.

Petrov V.G., Vlasova I.E., Kuzmenkova N.V. et al. (2012). Characterization of rock samples from areas of the proposed HLW and SNF repository in Russia (Nizhnekansky Massive) and first sorption studies // 1st Workshop Proceedings of the Collaborative Project „Crystalline Rock Retention Processes“ (7th EC FP CP CROCK). Vol. 7629 of KIT SCIENTIFIC REPORTS. Karlsruhe Institute of Technology Karlsruhe, Germany, pp. 37–42.

Petrov V., Kuzmenkova N., Petrov V. et al. (2014). Sorption of Cs, Eu and U(VI) onto rock samples from Nizhnekansky Massive // Int. Conference on Radioecology and Environmental Radioactivity 2014 (ICRER'14), Barcelona, Spain.

Stage E., Huber F., Heck S., Schäfer Th. (2012). Sorption/desorption of 137Cs(I), 152Eu(III) and 233U(VI) onto new crock derived Äspö diorite – a batch typestudy // 1st Workshop Proceedings of the Collaborative Project „Crystalline Rock Retention Processes“ (7th EC FP CP CROCK).Vol. 7629 of KIT SCIENTIFIC REPORTS. Karlsruhe Institute of Technology Karlsruhe, Germany, p. 51–62.

Zulauf G, Dörr W, Fiala J, Kotková J, Maluski H, Valverde-Vaquero P. (2002). Evidence for high temperature diffusional creep preserved by rapid cooling of lower crust (North Bohemian shear zone, Czech Republic). Terra Nova, 14: 343-354.

Zulauf, G., Zulauf, J., Hastreiter, P. & Tomandl, B. (2003). A deformation apparatus for threedimensional coaxial deformation and its application to rheologically stratified analogue material. J. Struct. Geol., 25: 469-480